University of Warsaw
Faculty of Physics

Magdalena Furman

Dissertation

Study of nonlinear effects in exciton-polariton condensates

Supervised by:
dr hab. Barbara Piętka, prof. UW

Warsaw, 2025

Abstract

This dissertation presents an experimental study of optical nonlinear effects in exciton-polariton microcavities based on II-VI semiconductors, with cadmium telluride (CdTe) as the main material platform. The work focuses on phenomena such as optical bistability, exciton-polariton condensation, and controlled interactions between polariton condensates. It also develops experimental tools that advance reciprocal- and real-space resolved studies for precise imaging and efficient excitation of microstructures.

First, transmissive CdTe microcavities in the strong coupling regime fabricated by a lift-off process are introduced. The input-output characteristics revealed optical bistability with two distinct types of hysteresis loops, depending on laser detuning: one with the conventional shape and direction reported for other types of microcavities, and a new one, exhibiting a triangular shape and an opposite direction of formation. Angle-resolved measurements demonstrated that the switching mechanism is linked to a thermally induced transition between strong and weak coupling regimes. A theoretical model including thermal redshifts and coupling reduction reproduced the observed bistabilities. The system also provided access to natural exceptional points in the polariton spectrum. Encircling experiments were performed by simultaneously tuning the excitation power, which effectively modulated the coupling strength, and by tracing the in-plane wavevector. Together, these parameters allowed the exploration of the exceptional point topology.

Then, ballistic coupling of condensates in semimagnetic CdTe microcavities is investigated. In this system, the giant Zeeman effect under an external magnetic field modifies exciton-photon detuning and polariton effective masses. Experiments showed that the magnetic field switches the parity of the condensate dyads between in-phase and anti-phase states. The effect was observed in real- and momentum-space interference patterns and was explained using analytical model and spinor Gross-Pitaevskii simulations.

Finally, polymer microlenses fabricated directly on the surface of microcavities using two-photon polymerization are presented. Ray-tracing simulations guided the microlens design. Experiments confirmed that the microlenses extend the accessible in-plane wavevector range, allow parallel measurements in reciprocal space from multiple spots on the sample with microlens arrays, and reduce the laser pulse energy required to achieve condensation threshold by locally concentrating excitation. Their functionality was demonstrated in both dielectric and semiconductor microcavities under cryogenic conditions.

Altogether, the dissertation reports the realization of transmissive CdTe microcavities with novel bistability mechanisms, the appearance and encirclement of natural exceptional points, the magnetic-field induced parity switching of condensate supermodes, and the development of microlenses as tools for single and multiplexed reciprocal space studies. Together, these results document new nonlinear effects in II-VI microcavities and establish novel methods for their systematic investigation.

Streszczenie

W niniejszej rozprawie przedstawiono badania eksperymentalne dotyczące nieliniowych efektów optycznych w mikrownękach polarytonowo-ekscytonowych opartych na półprzewodnikach grup II-VI, z tellurkiem kadmu (CdTe) jako głównym materiałem bazowym. Praca koncentruje się na takich zjawiskach, jak bistabilność optyczna, kondensacja polarytonowo-ekscytonowa oraz kontrolowane oddziaływania między kondensatami polarytonowymi. Opracowuje również narzędzia eksperymentalne, które umożliwiają prowadzenie badań w przestrzeni odwrotnej i rzeczywistej w celu precyzyjnego obrazowania i wydajnego wzbudzania tych mikrostruktur.

Na początku przedstawiono mikrownęki na bazie CdTe w silnym sprzężeniu, wytworzone w procesie lift-off. Charakterystyka wejścia-wyjścia ujawniła bistabilność optyczną z dwoma odrębnymi typami pętli histerezy w zależności od odstrojenia energii lasera: jedną o typowym kształcie i kierunku, opisywanym dla innych typów mikrownęk, oraz nową, o trójkątnym kształcie i przeciwnym kierunku tworzenia. Pomiary z rozdzielczością pędową wykazały, że mechanizm przełączania jest powiązany z termicznie indukowanym przejściem między silnym i słabym sprzężeniem. Model teoretyczny uwzględniający przesunięcia termiczne i redukcję sprzężenia odtworzył zaobserwowane bistabilności. Taki układ zapewnił również dostęp do naturalnych punktów wyjątkowych w widmie polarytonów. Przeprowadzono eksperymenty okrążające punkt wyjątkowy, poprzez jednoczesne dostrajanie mocy pobudzania, co skutecznie modulowało siłę sprzężenia, oraz poprzez śledzenie wektora falowego w płaszczyźnie. Parametry te łącznie umożliwiły zbadanie topologii punktów wyjątkowych.

Następnie zbadano sprzężenie balistyczne kondensatów w półmagnetycznych mikrownękach na bazie CdTe. W tym układzie pod wpływem zewnętrznego pola magnetycznego, pojawiający się gigantyczny efekt Zeemana modyfikował odstrojenie między fotonem a ekscytonem i masy efektywne polarytonów. Eksperymenty wykazały, że zewnętrzne pole magnetyczne przełącza parzystość kondensatu między stanami w fazie i w antyfazie. Efekt ten zaobserwowano we wzorach interferencyjnych przestrzeni rzeczywistej i w przestrzeni pędu i wyjaśniono za pomocą modelu analitycznego oraz symulacji Grossa-Pitaevskiego.

Na koniec przedstawiono mikrosoczewki polimerowe wytworzone bezpośrednio na powierzchni mikrownęk przy użyciu polimeryzacji dwufotonowej. Projekt kształtu mikrosoczewek oparto na symulacjach śledzenia promieni. Eksperymenty potwierdziły, że mikrosoczewki rozszerzają dostępny zakres wektorów falowych w płaszczyźnie, umożliwiają jednoczesne pomiary w przestrzeni odwrotnej z wielu punktów na próbce za pomocą układów mikrosoczewek oraz zmniejszają energię impulsu laserowego wymaganą do osiągnięcia progu kondensacji, poprzez lokalną koncentrację wzbudzenia. Ich funkcjonalność wykazano zarówno w mikrownękach dielektrycznych, jak i półprzewodnikowych w warunkach kriogenicznych.

Całościowo, w pracy opisano realizację mikrownęk CdTe z nowatorskimi mechanizmami bistabilności, pojawienie się i otoczenie naturalnych punktów wyjątkowych, indukowane polem magnetycznym przełączanie parzystości supermodów kondensatu oraz opracowanie mikrosoczewek jako narzędzi do badań przestrzeni odwrotnej, w pojedynczym miejscu, jak i w wielu jednocześnie. Wyniki te dokumentują nowe efekty nieliniowe w mikrownękach II-VI i ustanawiają metody do ich systematycznego badania.

Acknowledgements

Academic work is always the result of the efforts of many people, so I would like to thank everyone who contributed to the creation of this doctoral dissertation.

First of all, I would like to thank my supervisor, Prof. Barbara Piętka, for giving me the opportunity to work and develop, for her guidance during my doctoral studies, for teaching me independence, and for introducing me to a wonderful world of polariton physics.

I would also like to express my sincere gratitude to Prof. Jacek Szczytko, whose kindness, support, and kind words gave me strength throughout all these years.

I am deeply grateful to Prof. Jerzy Łusakowski, whose support proved invaluable not only throughout my doctoral studies but from my very first days at this University.

I am extremely grateful to Mateusz for his constant support, both in my scientific work and in my life. Thank you for our long conversations, countless hours spent on measurements, and above all, for being there.

I would like to thank Rafał for introducing me to the secrets of working in an optical laboratory and for his constant support; Karolina for being there for me in difficult moments and for her kind words; Przemek for his willingness to help and wise advice even in the toughest moments.

I would like to thank Prof. Wojciech Pacuski and Dr. Bartek Seredyński for providing unique CdTe optical microcavities, which made it possible to conduct the research described in this thesis. I would also like to thank Dr. Aleksander Bogucki and Dr. Łukasz Zinkiewicz for introducing me to 3D microprinting and for their help even from the other side of the world.

I would also like to thank Dr. Andrzej Opala, Dr. Helgi Sigurðsson, and Prof. Michał Matuszewski for the many years of cooperation and for their work on theoretical models for my experimental research.

I am also thankful to my friends from the Polariton group, who welcomed me warmly from the very beginning.

I would like to express my heartfelt thanks to everyone at the Department of Solid State Physics, where I have found true friends. Thank you for your support, smiles, and warmth - especially Nilesh, Mateusz, Julka, Kuba, Kuba, and Maciek.

I would also like to thank students, especially Marcin, Marysia, Kuba, Zuzia, Adam, and Nina, for your commitment, patience, and enthusiasm for learning. Working with you has been a great pleasure for me.

I would like to thank my friends from the bottom of my heart for their constant help, support, and patience - for being there for me, even when I could not always find time for you.

I would also like to thank my loving family - my parents, my sister Marysia, and my cousins - for their invaluable support, care, and willingness to help in moments of doubt.

Finally, I would like to give special thanks to Marcin, for the countless hours we spent together, for supporting my ideas, and for your patience. Thank you for always being there.

Tę pracę dedykuję moim Dziadkom,
Babci Jance, Babci Jadzi i Dziadkowi Jankowi.

Contents

Chapter 1

Motivation

In the current Information Age, collecting, processing, and analyzing data has become essential for scientific research, medicine, finance, and technology, as well as for everyday life. The resulting rapid growth of demand for data processing has pushed conventional silicon-based electronics close to its limits. The current approach of continued miniaturization of transistors is reaching the physical boundaries and quantum limitations. Simultaneously, silicon electronics is constrained by resistive losses, leading to high energy consumption and emerging heat dissipation challenges. These limitations have stimulated the search for alternative paradigms for data processing and computation that could provide both higher speed and lower energy requirements.

Among the proposed solutions, photonic platforms stand out because of the intrinsic advantageous properties of light: unparalleled speed, high bandwidth, low latency, and the absence of resistive losses. However, the difficulties in engineering strong nonlinear effects in photonic systems remain a major obstacle for practical implementations of logic and information processing. In those, nonlinearity is essential as it provides the mechanism for signal switching, information storage, and mutual interactions between signals, functions that are at the core of any computing device.

An unique way to engineer a strong nonlinear response in photonics is to couple light with matter. Namely, hybrid light-matter quasiparticles known as exciton-polaritons combine a strong nonlinear response stemming from exciton-exciton interactions with mentioned above advantages of photons. They can be realized in various types of optical microcavities. The most common approach utilizes semiconductor microcavities, where electronic excitations in quantum wells are strongly coupled to the photonic resonances of the cavity. Exciton-polaritons provide a versatile platform for implementing nonlinear photonic functionalities at a low energy cost. Their unique nonlinear functionalities have already been recognized as a potential platform for photonic data processing that supports multiple distinct computational paradigms [1]. Taking this importance as a starting point, the expansion and control of nonlinear properties of exciton-polaritons are the main topics of this dissertation.

The storage and processing of binarized information requires two available stable states. Here, exciton-polaritons bring optical bistability, which enables two robust and switchable states of transmission directly implementing binary memory in the optical microcavity. This work extends the optical bistability into CdTe-based microcavity platform. This led to the

discovery of alternative mechanisms driving the bistable behavior, enabling the implementation of two novel regimes of optical bistability (Chapter 4 and Ref. [2]).

A different paradigm of information processing that has especially recently gained significant attention is neuromorphic computing. This approach requires nonlinear nodes that function as neurons that directly process the information when arranged in interconnected function-specific networks. In this context, non-equilibrium Bose-Einstein condensates of exciton-polaritons have already been established as advantageous neuron-like nodes, offering the required nonlinearity and interconnectivity [3–7].

However, practical applications of neuromorphic computing require low-power operation. In the context of an exciton-polariton platform, it corresponds to reducing the optical excitation power required to reach the condensation thresholds. To address this challenge, this work introduces polymer microlenses printed directly onto the microcavity surface. The optimized design of the microlenses maximizes the efficiency of light injection, significantly reducing the energy required to achieve the condensation threshold. Simultaneously, this approach increases the efficiency of the emitted light collection and brings access to otherwise unreachable high-momenta polariton states, concurrently optimizing angle-resolved emission imaging (Chapter 6 and Ref. [8]). Additionally, arrays of such microlenses enable previously inaccessible parallel imaging of reciprocal space from multiple positions on the sample simultaneously (named here as multiplexed k-space imaging).

Looking beyond the classical information processing paradigms, polariton systems have been recognized as a platform for analog quantum simulators [9]. Coupled condensates network can directly emulate spin models such as the XY Hamiltonian [10], offering an explicit physical solution to complex optimization problems and many-body quantum phenomena. In this approach, the functionality of the network is encoded within the coupling rates between the individual condensate sites. This work explores the adjustability of these rates by the natural fluctuations of the photonic potential inherent in CdTe-based microcavity systems [11] (Chapter 3). Moreover, this dissertation demonstrates a new method for controlling the coupling between individual condensate sites by an external magnetic field. Specifically, benefiting from the unparalleled sensitivity to magnetic field of Mn-doped semimagnetic microcavities, the magnetic field is used to switch the parity of a synchronized collective condensate supermode, thereby providing a novel handle for engineering condensate networks and exploring their use as simulators (Chapter 5 and Ref. [12]).

All of these functionalities, namely optical bistability, polariton condensates and their coupled networks, rely on exploiting the nonlinear interactions of exciton-polaritons. The overarching goal of this dissertation is therefore centered on identification, control, and harnessing those nonlinearities to advance both fundamental understanding and potential applications of polariton physics.

The work is structured as follows:

Chapter 2 is devoted to the theoretical introduction of the basis of polariton physics. Introduces the properties of excitons trapped in semiconductor quantum wells as well as optical resonators, specifically microcavities. Later, strong and weak coupling regimes between those two constituents are discussed. Finally, a non-equilibrium Bose-Einstein condensation of exciton polaritons is presented.

In the following, **Chapter 3** presents experimentally characteristic properties of CdTe-based optical microcavities. It concentrates on the experimental methods for the observation

of a strong coupling regime, which are the basis of the whole dissertation. The following measurements are used to introduce properties of polariton Bose-Einstein condensates, study photonic potential landscapes in CdTe-based microcavities, and demonstrate differences between strong and weak coupling regimes.

Chapter 4 describes the bistable behavior of II-VI semiconductor microcavities. The Chapter begins with the presentation of the method used for the preparation of transmissive microcavities, obtained here by the water-assisted lift-off method. Following investigations of the quasiresonant laser transmission through the cavity as a function of incident light intensity reveal bistability in the power input-output characteristics with two distinct types of hysteresis. The first observed bistability exhibited a hysteresis loop with the typical shape and direction reported in the literature for other types of microcavities, although it appeared for an unusual laser detuning, whereas the second, newly observed "triangular" hysteresis displayed an unusual, opposite direction of formation. The experimental observations are also fully supported by a theoretical model. The Chapter also includes a section showing that a controlled transition between the strong and weak coupling regimes allowed access to a natural exceptional point in polariton dispersion. An additional noteworthy result presented in this Chapter is the observation of a third type of optical bistability in a single QW CdTe-based microcavity, arising solely from the redshift of the photonic mode with increasing transmitted laser power.

Chapter 5 is devoted to ballistically coupled polariton condensates in semimagnetic microcavities in an external magnetic field. The experimental results present switching of the parity of a synchronized polariton condensate dyad with a magnetic field. These results are presented in both real space and momentum (k-) space, where the varying magnetic field leads to a change in the number of interference fringes, which is further confirmed by theoretical modeling.

Chapter 6 introduces polymer microlenses which can be directly printed on top of the microcavities. The numerical methods based on ray-tracing are used to design specific functionalities of the microlenses. Later part details the microlenses printing process. The following optical measurements confirm the applicability of the microlenses for momentum-resolved imaging, also under cryogenic conditions. Additionally, arrays of such microlenses enable simultaneous multi k-space imaging (polariton multiplexing), allowing parallel collection of multiple polariton dispersions. The use of microlenses also leads to a significant reduction in the energy required to reach the condensation threshold.

Chapter 7 presents a summary of the entire dissertation with Appendix I (section 7.1) including details of the structure of the investigated samples and Appendix II (section 7.2) containing an analysis of interactions between three condensates trapped in separate potential minima, observed in a CdTe-based microcavity. In contrast to the dyad system discussed in Chapter 5, where the condensates are synchronized through ballistic propagation, the three-condensate configuration in Appendix II exhibits interactions governed by diffusive propagation.

Chapter 2

Introduction to semiconductor microcavities

Exciton-polaritons are hybrid light-matter quasiparticles, resulting from strong coupling between cavity photons and quantum well excitons. Their dual nature provides them an exceptionally small effective mass and significant nonlinear interactions, making them an interesting platform for exploring nonlinear effects such as non-equilibrium Bose-Einstein condensation or optical bistability.

This Chapter begins with an introduction of the basic concepts necessary to understand the phenomena addressed later in the work. First, the properties of excitons in semiconductor quantum wells will be presented, with emphasis on their binding energies, space confinement, and relevance for optical interactions. Next, the concept of optical microcavities will be introduced, including their design, spectral properties, and role as resonators. Then, by combining these two ingredients, the physics of strong exciton-photon coupling in microcavities will be described, with a distinction between the weak and strong coupling regimes, leading to the formation of exciton-polaritons. The closing section of this Chapter details the process by which such polaritons transition into a non-equilibrium Bose-Einstein condensate.

2.1. Excitons in semiconductor quantum wells

Electrons in atoms can occupy only specific, quantized energy states, known as energy levels. Within a crystal in which many atoms form a regular lattice, these discrete levels overlap and form continuous energy bands of allowed states. Electrons in a given solid state material fill the available states up to a characteristic value known as the Fermi energy. The Fermi energy with respect to the available energy bands determines the electrical properties of the material and allows the classification of solids into three groups: metals, semiconductors, and isolators.

The flow of electric current in solids arises from the directed motion of free charge carriers, which requires the presence of available electronic states. In metals, the Fermi energy lies within a band. As a result, even for an arbitrarily small energy excitation, there are available states contributing to electric conduction.

In semiconductors and insulators, the Fermi energy is located in the forbidden energy range between two accessible bands, known as the valence and conduction bands. The valence

band is completely filled and separated from the conduction band by an energy interval, the so-called band gap (E_g) [13]. It specifies how much energy must be provided to a bound electron in the valence band to become a free carrier in the conduction band.

In insulators, the band gap energy is high, as a result those materials are electrically non-conductive. For insulators, the band gap is generally greater than 4 eV (e.g. boron nitride $E_g \approx 6.0$ eV, sapphire $E_g \approx 8.8$ eV, or diamond $E_g \approx 5.5$ eV). It makes it practically impossible to excite electrons from the valence band to the conduction band under normal conditions [14].

Semiconductors are characterized by significantly lower band gaps compared to insulators, which makes it possible to generate free carriers. In these materials, electrons can be excited from the valence band to the conduction band using an energy at least equal to the band gap. This can be achieved through various mechanisms such as illumination, heating, or the application of an electric field [15]. Typically, the band gap of semiconductors lies in the range of 0.1–3 eV (for example, gallium arsenide $E_g \approx 1.42$ eV, cadmium telluride $E_g \approx 1.5$ eV, or indium phosphide $E_g \approx 1.34$ eV). The listed values correspond to normal conditions, i.e., room temperature and atmospheric pressure, while any change in these parameters leads to a change in E_g. The easiest parameter to tune the band gap is the temperature, which affects the crystal through thermal expansion of the lattice. Typically, as the temperature increases, the band gap decreases [16, 17]. Another external parameter that can be used to modify E_g is the hydrostatic pressure, which alters the band structure of the crystal. Most often, increasing pressure reduces the band gap, while lowering the pressure increases it, although this is not a universal rule [18, 19]. Moreover, doping, mechanical strain, and reduction of dimensionality in nanostructures can also strongly influence the effective band gap of materials.

In semiconductors illuminated by light, when the photon momentum can be conserved (for instance, in a direct band-gap material), absorption of a photon with energy higher than the band gap promotes an electron to the conduction band. This leaves in the valence band an unoccupied electron state. Such a band with an empty state can also be described by introducing a new quasiparticle, called a hole, which carries an effective positive charge. The electrons can interact with holes via Coulomb interactions, leading to the formation of a bound pair known as an exciton. This state has an energy lower than the band gap E_g of the host material, because part of the electron-hole pair's energy is reduced by their Coulomb attraction. The difference between the band gap and the actual energy required to create an exciton is called the exciton binding energy E_b. This energy, as well as the average electron-hole separation, can be estimated using a simple hydrogen-like model, in which the electron plays the role of the light particle orbiting around the much heavier hole. This approach not only provides an approximate value of the binding energy but also introduces the so-called exciton Bohr radius a_B, which defines the average distance between the electron and hole in the bound pair.

Excitons can be classified according to their size, expressed in terms of the exciton Bohr radius. If the Bohr radius is comparable to the lattice constant, the exciton is referred to as a Frenkel exciton. Such excitons exhibit high binding energy and are typically strongly localized on a single atom or molecular bond. They are characteristic of crystalline organic materials and alkali metal halides. The second type, so-called Wannier-Mott excitons, are characterized by a much larger Bohr radius (tens of times larger than the lattice constant). They exhibit a relatively lower binding energy and are characteristic of semiconductors such as cadmium

telluride (CdTe, an important material in this dissertation, which will be discussed in more detail in the following sections) or cadmium selenide (CdSe) [15].

In addition to bulk crystals, excitons are primarily studied in systems with reduced-dimensionality, such as quantum wells (2D), quantum wires (1D), and quantum dots (0D), where the charge carriers are confined in one, two, or all three spatial directions, respectively. This reduced dimensionality strongly enhances Coulomb interactions, which in turn modify the exciton binding energy and radius. For example, in the ideal two-dimensional case, this binding energy is about four times greater than in a three-dimensional material:

$$E_b^{2D} = 4E_b^{3D}. \tag{2.1}$$

This confinement leads to significant changes in their energetic and optical properties [13].

In this work, excitons formed in quantum wells are specifically relevant. A quantum well is created when a thin layer of semiconductor is sandwiched between barrier layers with a larger E_g, as shown in Fig. 2.1. To observe quantum confinement effects, the width of the well must be at least comparable to the exciton Bohr radius in the bulk material. In practice, this corresponds to layer thicknesses of a few to several tens of nanometers, depending on the semiconductor. An example is the CdTe/CdMgTe system, where the width of a single quantum well is usually about tens of nanometers [15].

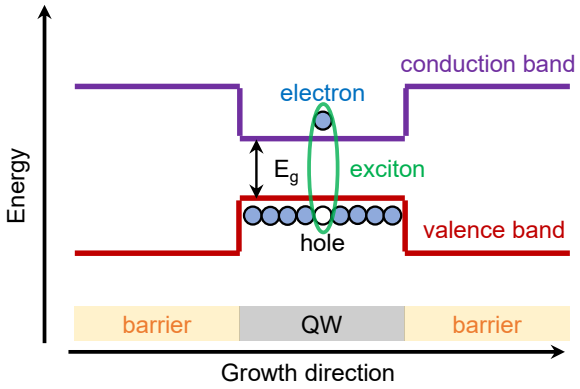

Figure 2.1: **Quantum well exciton.** Schematic representation of a quantum well, showing the exciton, energy gap, barriers, and the valence and conduction bands.

The exciton energy can be described as:

$$E_{ex}(k) = E_g + E_0 + \frac{\hbar^2 k^2}{2m^*}, \tag{2.2}$$

where E_0 includes the electron-hole interaction energy and confinement contributions, and the effective exciton mass is given by:

$$m^* = m_e + m_h. \tag{2.3}$$

The effect of quantum confinement depends on the ratio of the quantum well width to the Bohr radius. In practice, for materials such as CdTe, the typical exciton binding energies

in quantum wells are on the order of several tens of meV, which is sufficient to observe bound excitonic states well above cryogenic temperatures, in some cases even up to room temperature [20–22].

The optical properties of quantum wells are often dominated by excitonic effects. Excitons can be directly excited by light, which gives rise to pronounced features in absorption spectra [23]. Under nonresonant excitation, relaxation frequently occurs through excitonic states, which radiative annihilation dominate the photoluminescence spectra [24]. Due to their enhanced stability in such systems, excitons have found practical applications in optoelectronics, for example, in light emitters [25] or semiconductor lasers [26, 27].

2.2. Optical microcavities

Optical resonators are fundamental components of many photonic devices as they allow the control and confinement of light. In particular, the operation of lasers critically relies on optical resonators, which provide the necessary feedback to preserve stimulated emission.

A Fabry-Pérot resonator is an optical resonator composed of two parallel mirrors between which light undergoes multiple reflections and interference. As a result, standing waves are formed for specific wavelengths, where the radiation fulfilling the resonance condition is strongly localized. The condition for the formation of a standing wave depends on the optical distance between the mirrors, i.e., $n_c L$, is the effective path that light travels inside the cavity considering the refractive index of the medium, and is given by:

$$\lambda = \frac{2n_c L}{N}, \tag{2.4}$$

where L denotes the distance between the mirrors, n_c is the refractive index of the medium inside the resonator, and N is the mode number. Light with a wavelength that does not satisfy this resonance condition is predominantly reflected and does not form a standing wave inside the cavity.

An optical microcavity is a special type of Fabry-Pérot resonator, in which the distance between the mirrors is on the order of the optical wavelength. As a result, the spectral separation between consecutive cavity modes increases significantly, along with the localization of the optical field within the cavity. In practice, the most commonly used mirrors are Distributed Bragg Reflectors (DBRs) [28–30], although in simpler designs high-quality metallic mirrors may also be employed. DBRs can provide a very high reflectivity, typically $R \approx 99\%$. In semiconductor structures, reflectivities as high as $R > 99.9\%$ can be achieved [28, 30], which exceeds the reflectivity of classical metallic mirrors (e.g. silver in the visible range: $R \sim 95$–98% [31]), where, in addition, absorption losses become significant.

A Distributed Bragg Reflector consists of a periodic stack of pairs of layers with alternating refractive indices n_i and thicknesses L_i, which fulfill the condition:

$$n_i L_i = \frac{\lambda_0}{4}, \tag{2.5}$$

where λ_0 is the designed (or central) wavelength. This condition ensures that the reflections from the successive interfaces of the multilayer stack add up in phase, resulting in strongly

enhanced reflectivity. Around the wavelength λ_0, the mirror exhibits a broad spectral region of high reflectivity, also known as the photonic stopband.

The relative width of the stopband in the limit of a higher number of pairs of layers can be estimated from the refractive index contrast between the DBR layers [32, 33]:

$$\frac{\Delta E}{E_\mathrm{c}} \approx \frac{4}{\pi} \arcsin\left(\frac{|n_2 - n_1|}{n_2 + n_1}\right), \tag{2.6}$$

where E_c is the central energy of the stopband ($E_\mathrm{c} = hc/\lambda_0$). The reflectivity of a DBR grows with both the refractive index contrast $\Delta n = |n_2 - n_1|$ and the number of layer pairs. For example, for GaAs/AlAs DBRs characterized by high refractive index contrast, about 15–20 pairs are already sufficient to exceed 99% reflectivity [34]. In practice, further increasing the number of layers provides diminishing returns and becomes limited by technological challenges such as precise thickness control, interface roughness, absorption losses, or strain accumulation during growth.

By placing a layer of refractive index n_c and thickness of L_c between two such DBRs, a microcavity structure is obtained that supports standing optical modes confined between the mirrors.

Figure 2.2(a) shows an example of the simulated, using transfer-matrix method [35], reflectivity spectrum of a single Bragg mirror composed of 22 alternating layers of $Cd_{0.4}Mg_{0.6}Te$ and $Cd_{0.88}Zn_{0.04}Mg_{0.08}Te$, with refractive indices $n_1 = 2.46$ and $n_2 = 2.74$, respectively. The photonic stopband is clearly visible in the spectrum between 1.52 eV to 1.68 eV, with optical modes appearing at its edges (also called Bragg modes), which correspond to standing waves located mainly in the mirrors. Figure 2.2(b) presents the reflectivity spectrum of a complete optical microcavity formed by placing two of such Bragg mirrors around a central cavity layer. In this case, a distinct cavity mode appears within the stopband at the designed central wavelength of $\lambda_0 = 777$ nm (1.596 eV).

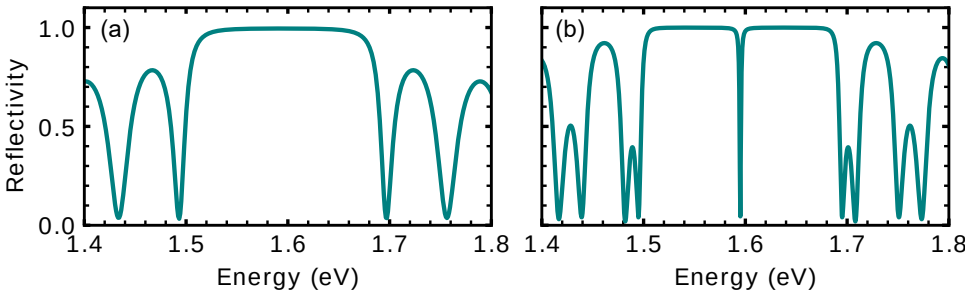

Figure 2.2: **Reflectivity spectra of a single DBR and microcavity.**(a) Simulated reflectivity spectrum of a single Bragg mirror composed of 22 alternating layers of $Cd_{0.4}Mg_{0.6}Te$ and $Cd_{0.88}Zn_{0.04}Mg_{0.08}Te$, with refractive indices $n_1 = 2.46$ and $n_2 = 2.74$. (b) Reflectivity spectrum of a complete optical microcavity formed by placing two such Bragg mirrors around a central cavity layer.

The microcavity photon resonance energy depends on the incidence angle, that is, on the in-plane wavevector of the photon. The photon energy dispersion in such a cavity can be

written as:

$$E_{\mathrm{ph}}(k_{\parallel}) = \frac{\hbar c}{n_c}\sqrt{\left(\frac{2\pi}{L_c}\right)^2 + k_{\parallel}^2}, \tag{2.7}$$

where $k_{\parallel}$ is the in-plane wavevector of the photon. For $k_{\parallel} \ll 2\pi/L_c$, a series expansion leads to a parabolic dependence:

$$E_{\mathrm{ph}}(k_{\parallel}) \simeq E_{\mathrm{ph}}(0) + \frac{\hbar^2 k_{\parallel}^2}{2m_{\mathrm{eff}}}, \qquad m_{\mathrm{eff}} = \frac{E_{\mathrm{ph}}(0)}{c^2/n_c^2}. \tag{2.8}$$

This allows for defining an effective cavity photon mass. Introducing the concept of effective mass in the system of optical microcavities makes it possible to treat the motion of a photon in the cavity analogously to a massive particle, although with an extremely small effective mass on the order of 10^{-5}–10^{-4} of the free electron mass [30, 36].

The finite lifetime of the photon in the cavity is directly related to the linewidth of the cavity resonance. A convenient parameter characterizing the quality of an optical cavity, which is determined by the photon lifetime, is the quality factor Q:

$$Q = \frac{E_{ph}}{\Delta E}, \tag{2.9}$$

where E_{ph} is the resonance energy and ΔE is the full width at half maximum (FWHM) of the resonance. For large values of Q, the resonance linewidth is narrow, which corresponds to a long photon lifetime τ, approximately given by:

$$\tau \approx \frac{\hbar Q}{E_{ph}}. \tag{2.10}$$

2.3. Microcavity exciton-polaritons, strong and weak coupling regimes

Having introduced the concepts of excitons and optical microcavities in the previous sections of this Chapter, the focus now turns to systems in which both phenomena occur together. By placing quantum wells at the maximum of the electric field distribution of the microcavity, the interaction of excitons with cavity photons is enhanced. Depending on the relative strength of this interaction compared to the losses of the system, two distinct regimes can be distinguished.

In weak coupling regime the rate of coherent energy exchange between excitons and cavity photons is slower than their respective decay rates. In this regime, the microcavity primarily modifies the emission properties of the emitter. Characteristic manifestations include the Purcell effect (enhancement of spontaneous emission due to the cavity), photonic lasing, or redshift [28–30, 37].

In contrast, when the rate of coherent energy exchange between the excitonic and photonic modes exceeds their decay rates, the system operates in the strong coupling regime. Here, separate bare exciton and photon modes are no longer observed as the system instead exhibits two new hybrid eigenstates of the upper and lower polaritons.

The system in the strong coupling regime can be modeled as two coupled oscillators, described by the Hamiltonian [30, 38]:

$$\mathrm{H} = \begin{pmatrix} E_{\mathrm{ph}}(k_\parallel) & \frac{\hbar}{2}\Omega_R \\ \frac{\hbar}{2}\Omega_R & E_{\mathrm{ex}}(k_\parallel) \end{pmatrix},$$

where $E_{\mathrm{ph}}(k_\parallel)$ and $E_{\mathrm{ex}}(k_\parallel)$ denote the bare photon and exciton energies, and $\hbar\Omega_R$ is the Rabi splitting. Diagonalization of the Hamiltonian yields the polariton eigenenergies:

$$E_\pm(k_\parallel) = \frac{E_{\mathrm{ph}}(k_\parallel) + E_{\mathrm{ex}}(k_\parallel)}{2} \pm \frac{1}{2}\sqrt{\left[E_{\mathrm{ph}}(k_\parallel) - E_{\mathrm{ex}}(k_\parallel)\right]^2 + \hbar^2\Omega^2}. \tag{2.11}$$

corresponding to the upper (+) and lower (–) polariton branches. The equation describes characteristic for the strong coupling regime energy levels repulsion (anticrossing) of the polariton states as a function of the energies of bare exciton and cavity photon modes.

The associated eigenvectors of H define the Hopfield coefficients, which quantify relative contributions to a polariton mode, photonic $C(k_\parallel)$ and excitonic $X(k_\parallel)$. This is described by the following equations:

$$|C(k_\parallel)|^2 = \tfrac{1}{2}\left(1 + \frac{E_{\mathrm{ph}}(k_\parallel) - E_{\mathrm{ex}}(k_\parallel)}{\sqrt{[E_{\mathrm{ph}}(k_\parallel) - E_{\mathrm{ex}}(k_\parallel)]^2 + \hbar^2\Omega^2}}\right), \tag{2.12}$$

$$|X(k_\parallel)|^2 = \tfrac{1}{2}\left(1 - \frac{E_{\mathrm{ph}}(k_\parallel) - E_{\mathrm{ex}}(k_\parallel)}{\sqrt{[E_{\mathrm{ph}}(k_\parallel) - E_{\mathrm{ex}}(k_\parallel)]^2 + \hbar^2\Omega^2}}\right). \tag{2.13}$$

These coefficients are real and positive, and satisfy the normalization condition:

$$|C(k_\parallel)|^2 + |X(k_\parallel)|^2 = 1, \tag{2.14}$$

ensuring that each polariton is a normalized superposition of photon and exciton basis states.

An important parameter when discussing exciton-polaritons is the exciton-photon detuning, defined as the difference between the cavity photon energy and the exciton energy at $k_\parallel = 0$:

$$\delta = E_{\mathrm{ph}}(0) - E_{\mathrm{ex}}(0). \tag{2.15}$$

Figures 2.3(a)–(c) show exemplary dispersion relations of exciton, photon, and polariton branches for negative, zero, and positive detuning, respectively. Figures 2.3(d)–(f) present the corresponding Hopfield coefficients, which quantify the excitonic and photonic fractions of the lower polariton branch in each case.

For negative detuning [$\delta < 0$, Figs. 2.3(a,d)], where the minimum energy of the photon mode is tuned below the exciton energy, the polariton states are more photonic, and the point of equal contributions is shifted to higher values of $k_\parallel$. In the case of zero detuning [$\delta = 0$, Figs. 2.3(b,e)], exactly at $k_\parallel = 0$ the photonic and excitonic contributions to the lower polariton are equal, but the excitonic fraction increases with $k_\parallel$. For positive detuning [$\delta > 0$, Figs. 2.3(c,f)], the photon mode energy is higher than the exciton energy, resulting in a lower polariton branch with a stronger excitonic character.

Strongly coupled systems exhibit remarkable properties derived from their hybrid light-matter nature [30, 36, 39, 40]. Experimental observations include polariton lasing, collective phenomena such as non-equilibrium Bose-Einstein condensation [41, 42], quantum vortices [43], superfluidity [44], and the formation of solitons [30, 45].

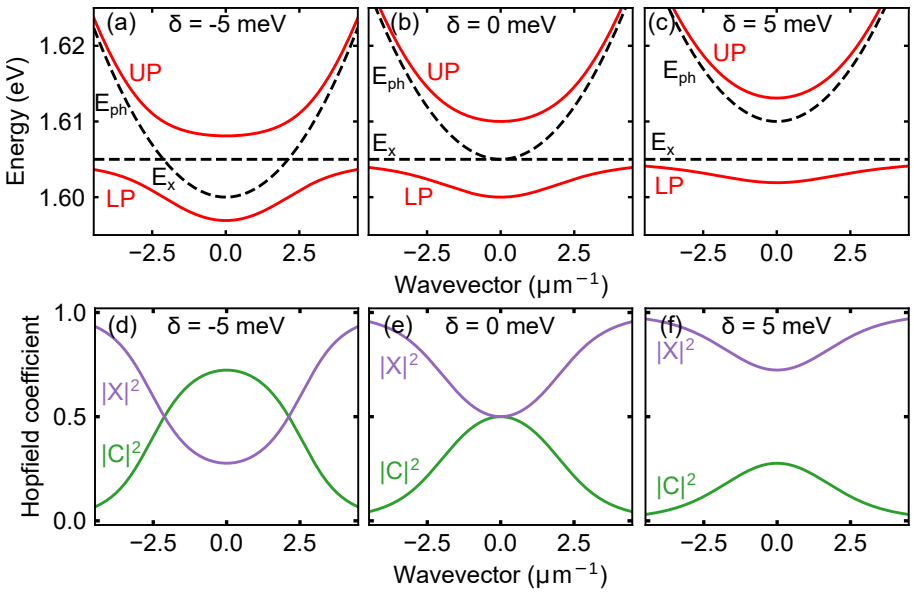

Figure 2.3: **Illustration of how the detuning between exciton and photon modes changes the dispersions.** (a)–(c) Dispersion relations for negative, zero, and positive detuning, showing the bare exciton and photon modes (black dashed lines), and the resulting polariton branches (solid red lines). (d)–(f) Hopfield coefficients of the lower polariton branch for the three detuning, indicating the excitonic (purple) and photonic (green) fractions.

2.4. Non-equilibrium Bose-Einstein condensation of exciton-polaritons

The Bose-Einstein condensate (BEC) is a quantum state of matter, theoretically described by S. N. Bose and A. Einstein in 1924-1925. Einstein, based on Bose's work on the quantum statistics of photons, demonstrated that bosons, that is, particles with integer spin, can macroscopically occupy the lowest quantum state at temperatures close to absolute zero. As the system is cooled, the particles begin to macroscopically populate a single state at the energy minimum. The first experimental confirmation of creating a BEC in atomic gases was achieved by E. Cornell and C. Wieman [46] in 1995 for rubidium atoms and shortly afterwards by W. Ketterle for sodium atoms [47]. However, this required extreme cooling conditions, since condensation was observed only at temperatures on the order of hundreds of nanokelvins. This results from the very large atomic mass and the necessity of creating a highly dilute gas, which, according to the formula for the critical temperature ($T_c \propto n^{2/3}/m$), leads to values in the nanokelvin range.

In 2006, J. Kasprzak and collaborators demonstrated for the first time the experimental observation of exciton-polariton BEC in a semiconductor microcavity [42]. Polaritons, as a hybrid light-matter quasiparticles, possess an extremely small effective mass (about 10^{-5} of the free electron mass [48]), compared to atomic gases. As a result, condensation occurs at temperatures much higher than those in atomic systems. Initially, observations were only

possible under cryogenic conditions, but further research led to the realization of condensation at room temperature, including organic materials [49,50], polymers [51,52], perovskites [53–55], and transition metal dichalcogenides (TMDs) [56, 57]. The possibility of observing exciton-polariton condensation at room temperature is related to the properties of excitons. In conventional inorganic semiconductors (e.g., GaAs or CdTe), the exciton binding energy is only a few meV, which limits the stability of excitonic states to low temperatures. In organic materials, perovskites, or TMDs, this binding energy is significantly higher (up to tens to hundreds of meV), making excitons stable even at room temperature [58].

It should be noted that exciton-polariton condensation is a non-equilibrium process. Due to the finite lifetime of polaritons, maintaining the condensate requires external pumping, here, pulsed excitation, so the system typically does not reach thermal equilibrium. Consequently, the term "condensate" used throughout this work refers to a non-equilibrium, driven-dissipative condensate, distinct from equilibrium Bose-Einstein condensation observed in ultracold atoms systems.

The creation of a polariton condensate requires an appropriate excitation scheme. Typically, as can be seen in Fig. 2.4, nonresonant pumping is used. In this excitation scheme, the laser energy is set higher than the energy of the polariton modes, optimally near the upper Bragg minimum. Photon absorption creates high energy free charge carriers, which then relax into excitonic states, forming the so-called excitonic reservoir. The reservoir is made of high-wavevector excitons, which upon subsequent interactions with phonons undergo rapid scattering processes (on the picosecond timescale), enabling polaritons to relax to lower energy states [42]. For their high densities, polaritons as bosonic particles undergo a stimulated scattering process that enables efficient population transfer toward the lowest-energy polariton states once the occupation threshold is reached. Condensation occurs when the macroscopic population of the ground state of the polariton is reached.

The condensation process can be observed as a nonlinear increase in emission intensity, a blueshift of the emission energy, and linewidth narrowing [41, 42]. The blueshift originates from the interactions of matter component, which manifest as repulsive contributions to both polariton-polariton and polariton-excitonic reservoir interactions, leading to an overall increase in the condensate energy with growing density. Although exciton-polariton condensates can form at pump powers significantly lower than the lasing threshold of conventional semiconductor lasers, research is ongoing to further reduce it even further.

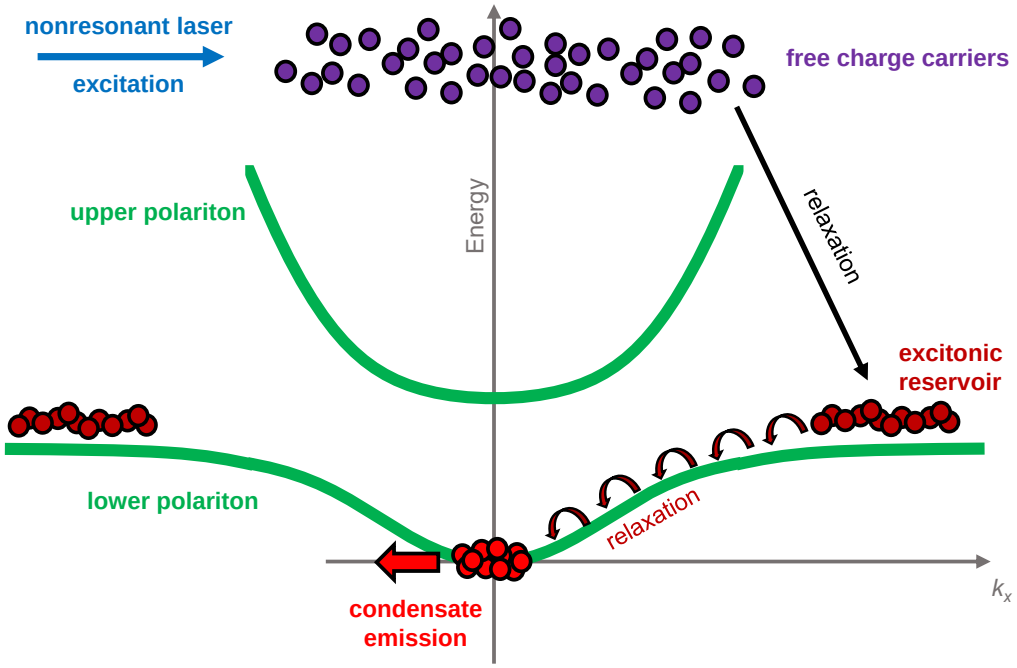

Figure 2.4: **Scheme of exciton-polariton condensate formation.** Nonresonant absorption leads to the generation of free carriers, which then relax into the excitonic reservoir, from where polariton states can become populated, and under appropriate conditions the ground state can reach macroscopic occupation of the ground state forming the condensate.

Chapter 3

Optical properties of CdTe-based semiconductor microcavities

Before discussing the physical effects observed in strongly coupled systems, this Chapter introduces the experimental aspects of the work. It describes the growth method of the optical microcavities, presents their preliminary characterization, and outlines the experimental setup used in the optical studies.

3.1. Molecular Beam Epitaxy growth of optical microcavities

All semiconductor samples investigated experimentally in this work were grown using Molecular Beam Epitaxy (MBE). The microcavity structures based on cadmium telluride (CdTe), which constitute most of the samples studied in this thesis, were designed and fabricated in the Molecular Beam Epitaxy Laboratory of the Faculty of Physics, University of Warsaw, by Prof. Wojciech Pacuski and Dr. Bartłomiej Seredyński.

MBE is one of the most precise crystal growth methods, allowing thickness control at the level of an atomic monolayer. Heated effusion cells containing high-purity metals or compounds, typically 7N purity or higher, are used as atom sources for growth. The purity of source materials is described by the N-grade notation, where the number preceding 'N' indicates how many nines appear in the fractional purity. The high material purity minimizes point defects and directly translates into improved optical properties. During heating, the elements evaporate, producing atomic fluxes directed toward the substrate placed in the growth chamber. Substrates in this technique are wafers, flat monocrystalline plates, most commonly with a diameter of 2-3 inches. A wafer is mounted in a dedicated holder, first introduced into the load-lock chamber, then transferred to the preparation chamber, and after proper pumping, finally moved into the growth chamber.

The entire process takes place under ultra-high vacuum (UHV), on the order of 10^{-11} mbar. Such conditions are achieved using a combination of pumps. A membrane pump feeding a turbomolecular pump (providing a high vacuum of about 10^{-8} mbar in the load-lock), an ion pump (maintaining vacuum in the preparation chamber at $\sim 10^{-9}$ mbar), and a cryogenic pump allowing for UHV conditions in the growth chamber at $\sim 10^{-11}$ mbar [59]. In addition, the walls of the growth chamber are cooled with liquid nitrogen, which promotes the trapping

of residual contaminants and helps maintain process cleanliness.

During growth, parameters such as substrate temperature, effusion cells temperatures, and the resulting atomic fluxes are precisely controlled. A key tool for monitoring crystalline quality is Reflection High-Energy Electron Diffraction (RHEED). This technique enables evaluation of the surface crystallinity, growth mode (layer-by-layer or three-dimensional), and growth rate. A beam of electrons with energies of several keV is directed toward the surface at a small angle. The electrons are diffracted on atomic rows, producing characteristic patterns on a detector. Depending on the appearance of the diffraction image, one can determine whether the grown structure is amorphous, polycrystalline, or of high-quality monocrystal character. Furthermore, oscillations of the RHEED intensity provide direct information on the growth rate, allowing calibration with monolayer precision.

The typical growth temperature of group II-VI semiconductor microcavities is around 300–350 °C, with a deposition rate of about one monolayer per second. This process requires highly precise temperature control because elements such as tellurium exhibit high vapor pressures, and even small deviations may lead to significant changes in atomic fluxes. In MBE, several atomic species can be supplied simultaneously from different effusion cells, which makes it possible to grow complex multilayer structures with controlled composition and doping. During growth, magnetic ions, such as manganese, can be incorporated into Bragg mirrors [60] or quantum wells [61–65]. In the mirrors, magnetic ions primarily modify the refractive-index profile; in an external magnetic field the index becomes field-dependent, thereby shaping the dispersion of the photonic modes, while doping the quantum wells modifies the magnetic properties of excitons. This approach enables the realization of magnetic or semimagnetic microcavities, which are unique compared to other studied systems, and allows the observation of new phenomena related to the interaction with an external magnetic field [61–67].

3.2. Strong coupling regime in II-VI microcavity

The thesis concentrates on experimental investigation of the optical properties of semiconductor microcavities. All of the spectroscopic measurements were performed at the Polariton Laboratory at the Faculty of Physics, University of Warsaw. The general scheme of the experimental setup used for the reflectivity and photoluminescence measurements is shown schematically in Fig. 3.1.

All experimental results were obtained using microcavities based on semiconductors made of elements from groups III-V and II-VI of the periodic table and, unless stated otherwise, collected at a temperature of 4.5 K, in a cryostat cooled with liquid helium. During measurements, the sample chamber was evacuated to a vacuum of 10^{-6}-10^{-7} mbar to prevent condensation of water vapor on the sample surface. The sample was mounted on a so-called "cold finger" – a copper plate with high thermal conductivity, directly connected to the flow of liquid helium. To ensure proper thermal contact, the sample was attached to the cold finger using a silver paste. The entire system was located in a vacuum chamber.

The optical measurements were performed in the visible and near-infrared spectral range. Reflectivity measurements were performed using a halogen lamp. This lamp covered the entire spectral range relevant to all investigated microcavities. For photoluminescence measurements, a pulsed Ti:sapphire laser was used (Coherent Mira-900 laser, pulse duration 4 ps, repetition

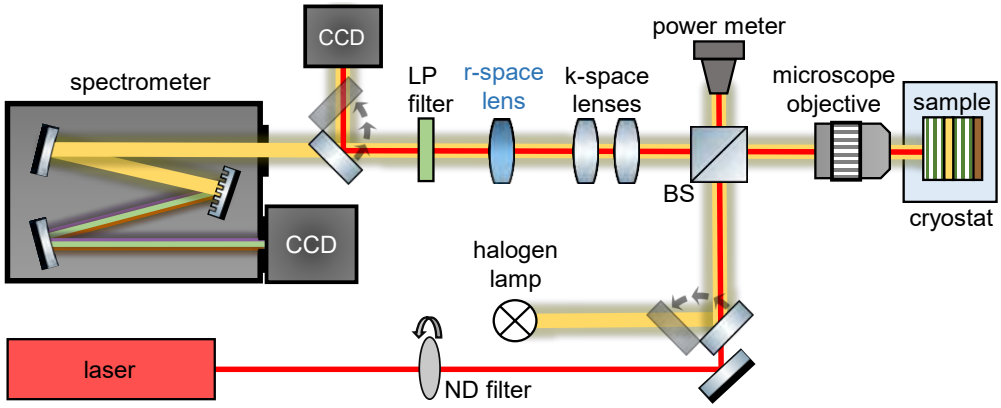

Figure 3.1: **Experimental setup for measuring semiconductor optical microcavities.** The setup allows for measurements of both reflectivity and photoluminescence. Microscope objective was used to focus light on the sample surface, and then the signal from the sample was collected using the same microscopic objective and lenses appropriately positioned in the detection path, either in real space or in reciprocal configuration.

rate of 76 MHz, tunable wavelength range approx. 700-850 nm).

As indicated in the experimental setup scheme (Fig. 3.1), the laser and the halogen lamp could be directed into the sample from the reflectivity side. Light was directed to a microscope objective and then focused onto the sample surface. The reflected light (together with emission from the sample in photoluminescence measurements) was collected with the same microscope objective and directed to the spectrometer slit, equipped with 2D CCD camera or directly to the CCD camera sensor. The laser power was adjusted using a rotating neutral density filter, and the power incident on the sample was measured with a power meter. In the detection path, two lenses were used to observe the Fourier plane (k-space) on the spectrometer or camera, or a single lens was used to image the real space of the sample.

A scheme of these imaging configurations is presented in Fig. 3.2(a). The observation of reciprocal space requires a microscope objective that collects the signal from the sample and performs a Fourier transform of that signal. The Fourier transform is realized at the back focal plane of the objective (BFP) also known as the Fourier plane (FP), i.e. the surface where rays emitted at the same angle from different positions on the sample intersect. The Fourier transformed signal then passes through two appropriately aligned lenses, of which the first is the so-called Bertrand lens (named after the mineralogist Émile Bertrand, the inventor of this configuration), and the second is an imaging lens. The Bertrand lens (sometimes called the Fourier lens) allows observation of the BFP of the objective, while together these two lenses form a relay system that projects the Fourier plane onto the detector sensor.

The momentum of the photons can be decomposed into components perpendicular and parallel to the sample. In the microcavity the perpendicular component is quantized and directly dependent on the cavity width. The in-plane momentum of polaritons is continuous and conserved after optical recombination. Angle-resolved imaging provides access to the angle at which light exits the sample, and thus to the polaritons in-plane momentum. The relation between the emission angle and the in-plane wavevector is given by:

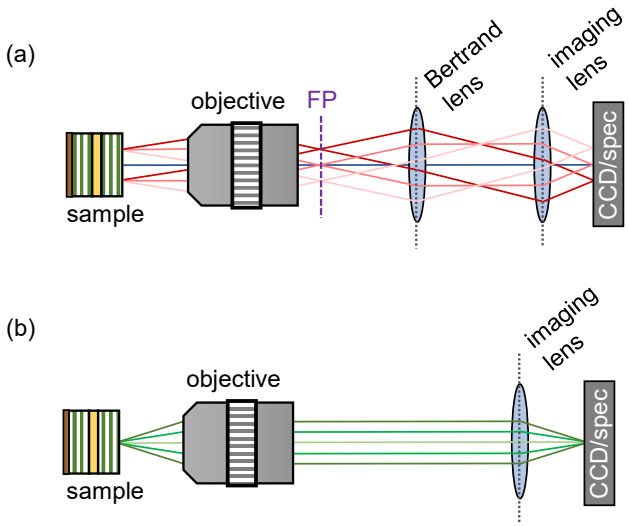

Figure 3.2: **Optical setups showing how light rays are directed in reciprocal and real space imaging configurations.** (a) The reciprocal space imaging setup consists of a microscope objective, a Bertrand lens, and an imaging lens, and (b) the real space imaging setup uses a microscope objective to collect the signal and a lens to focus it onto a camera or spectrometer slit.

$$k_{\parallel} = \frac{E}{\hbar c} sin\theta, \tag{3.1}$$

where E is the energy of the photon emitted from the cavity. Since all measurements presented in this work are referenced to the in-plane component $k_{\parallel}$, it will be referred to simply as k throughout the text.

A schematic experimental configuration illustrating the propagation of light rays in the real-space imaging setup is shown in Fig. 3.2(b). Imaging of the real space of the sample employs an optical setup consisting of two optical elements. The first element, which is typically a microscope objective or a short-focal length lens, collects the reflected or emitted signal from the sample and collimates it. The second focusing lens is positioned so that it precisely focuses the collimated signal on the spectrometer slit or camera sensor, enabling the real-space (spatial) image of the sample to be captured.

The presence of strong coupling in a semiconductor microcavity system can be experimentally demonstrated by measuring the polariton dispersion relation. Using the experimental setup described above, both white-light reflectivity and photoluminescence momentum-resolved spectra were measured from a CdTe-based semiconductor optical microcavity (Sample C.3, for more details on the structure, see Appendix I, 7.1). The results were collected at a temperature of 4.5 K and are presented in Fig. 3.3. Figures 3.3(a,b) were measured at the same position on the sample, while the maps shown in Figs. 3.3(c,d) were collected at a different position with different detuning. These two measurements demonstrate the possibility of tuning the cavity photon mode energy across the sample. This tuning arises from the intentional thickness wedge of the cavity layer introduced during MBE growth, which modifies the optical path

length and shifts the cavity photon energy. As a result, measurements at different sample positions allow access to various detuning values.

The map shown in Fig. 3.3(a), presents white-light reflectivity from the microcavity, with clearly visible lower and upper polariton modes in the dispersion map. The lower polariton is observed in the energy range between 1.60 eV and 1.62 eV, while the signal from the upper polariton appears above 1.62 eV. The coupled oscillator model described above in Eq. (2.11), was overlaid on the experimental dispersion relation. The modeled lower and upper polariton branches are shown with red dashed lines. The dispersion observed in reflectivity agrees very well with the model. The modeling allows for the determination of the Rabi energy $\hbar\Omega_R$ as 12 meV as well as the bare exciton and cavity photon energies, indicated in Fig. 3.3(a) with white dashed lines. From the modeling, the exciton-photon detuning at the investigated position was determined as $\delta = -17.7$ meV (E_{ph}=1.6023 eV, E_{ex}=1.602 eV).

Additionally, as described above, photoluminescence from the sample can be excited using a laser tuned to the first Bragg minimum of the studied structure. For these measurements, the laser wavelength was tuned to 730 nm, corresponding to an energy of 1.70 eV. The photoluminescence spectrum in Fig. 3.3(b) was obtained at the same sample position as the reflectivity map in Fig. 3.3(a), for a laser pulse energy of 20 pJ. The results show a homogeneous population of the lower polariton branch, while no signal from the upper polariton is observed. The upper polariton retains a substantial excitonic fraction and a broader resonance, which suppress its visibility. In contrast, the lower polariton has a larger photonic fraction (particularly near $k \approx 0$), which enhances its coupling to the external electromagnetic field and enables for more efficient light emission.

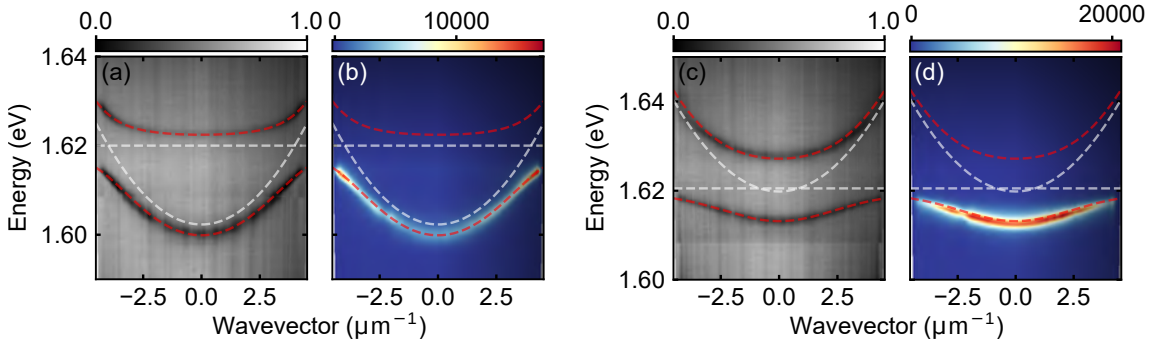

Figure 3.3: **Strong coupling regime observed for two detunings on a Sample C.3 microcavity.** (a) White-light reflectivity at the first sample position, showing clear branches of the lower and upper polaritons. (b) Photoluminescence from the same position, revealing only emission from the lower polariton branch under nonresonant excitation. (c) White-light reflectivity at a second position on the sample, corresponding to a different detuning, with both polariton branches visible. (d) Photoluminescence from the second position.

To demonstrate the effect of a different detuning, additional measurements were performed at another position on the sample, and presented in Figs. 3.3(c,d). At this position, the lower polariton signal is observed between 1.61 eV and 1.62 eV, while the upper polariton signal appears above 1.625 eV. The white-light reflectivity map in Fig. 3.3(c) was modeled with the coupled oscillator model, yielding a detuning of $\delta = -7$ meV. Similarly to the previous

case, the photoluminescence map was collected at a pulse energy of 20 pJ and presented in Fig. 3.3(d), which shows only the lower polariton emission. This spatial dependence of the detuning will be utilized in the following sections of the thesis.

3.3. Non-equilibrium Bose-Einstein condensation in CdTe-based microcavity

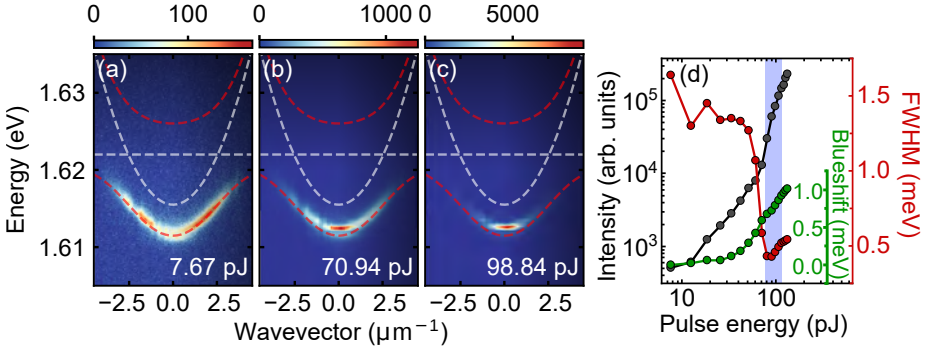

Figure 3.4: **Polariton condensation from Sample C.3 under nonresonant pulsed excitation.** (a) Momentum-resolved PL spectra collected at low excitation energy (7.67 pJ), with visible a uniform population of the lower polariton branch. (b) Map collected near the condensation threshold (70.94 pJ), and (c) above the threshold (98.84 pJ). (d) Extracted parameters of Lorentzian fits to the photoluminescence spectra at $k = 0$, with integrated emission intensity, blueshift of the emission energy, and linewidth narrowing of the lower polariton mode.

As described above, polariton condensation can be achieved under nonresonant excitation. The experiment was carried out using the setup shown in Fig. 3.1, with a pulsed Ti:sapphire laser. Measurements were performed on Sample C.3, under conditions analogous to those described above, with photoluminescence collected for increasing excitation density.

The results are shown in Fig. 3.4. The momentum-resolved spectra in Fig. 3.4(a), collected at a pulse energy of 7.67 pJ, shows a uniform population of the entire lower polariton branch, visible between 1.61 eV and 1.62 eV. Then, the coupled oscillator model was modeled to the dispersion map, yielding a detuning value of $\delta = -7.5$ meV between the photonic and excitonic modes. When the excitation pulse energy was increased, a redistribution of the population along the lower polariton branch was observed. At a pulse energy of 70.94 pJ, corresponding to the condensation threshold [Fig. 3.4(b)], lower-polariton mode becomes macroscopically occupied around $k = 0$ and undergoes an interaction-induced blueshift. After exceeding the threshold and further increasing excitation, the condensate state was still observed, which was confirmed by the map shown in Fig. 3.4(c), obtained at 98.84 pJ.

A more detailed analysis of the signal was carried out by extracting cross-sections of the maps at $k = 0$ for successive excitation energies. Lorentzian fitting were performed to the emission peaks, from which the intensity, energy blueshift, and spectral linewidth were extracted as functions of increasing pulse energy, as shown in Fig. 3.4(d). The observed

nonlinear increase of the emission intensity reflects the onset of polariton condensation. The energy blueshift originates from repulsive polariton-polariton interactions, which increase the effective potential energy of the condensate. In turn, the linewidth narrowing indicates the build-up of macroscopic coherence in the system. Together, these signatures confirm the realization of non-equilibrium Bose-Einstein condensation in the investigated CdTe-based microcavity sample.

3.4. Photonic potential fluctuations in CdTe-based microcavity

Despite the very high precision of MBE growth, CdTe-based structures exhibit a significant degree of photonic disorder, which arises from crystalline defects and spontaneous strain relaxation. This disorder results in local fluctuations of the photonic potential energy, which distinguishes CdTe-based microcavities from their GaAs-based counterparts. In GaAs-based cavities, the photonic potential is typically flat, which allows for relatively longer-range propagation of polaritons and their condensates (which in extreme cases reach several tens of micrometers [68]). In contrast, in CdTe-based microcavities the disorder leads to strong spatial modulation of the photonic potential.

As a consequence, polariton condensates in CdTe structures are typically strongly localized in potential minima rather than freely propagating [42, 63]. This localization strongly affects the condensation dynamics, as the condensate emission predominantly originates from these local minima.

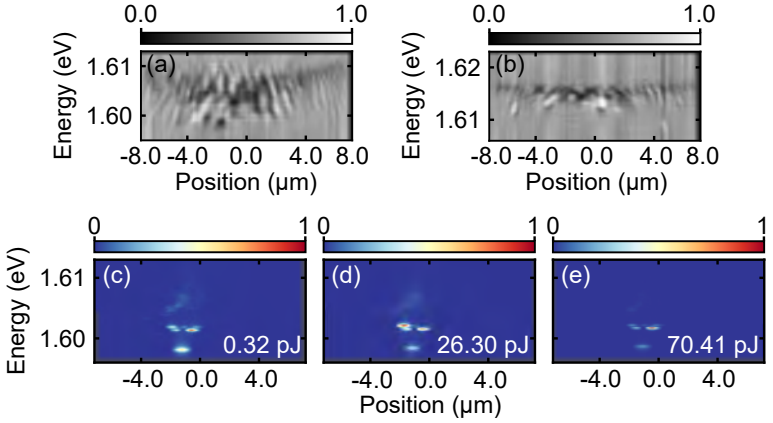

Figure 3.5: **Effect of photonic disorder on polariton states in a CdTe microcavity.** (a,b) White-light spatially-resolved reflectivity spectra at two different sample positions, corresponding to different detuning values [cf. Figs. 3.3(a)–(d)], showing local fluctuations of the lower polariton energy. (c) Spatially-resolved photoluminescence spectra below the condensation threshold (0.32 pJ), where localized states appear on top of a broad emission background. (d) At higher excitation power (26.30 pJ), the localized states become more pronounced while the background signal decreases. (e) Above the condensation threshold (70.41 pJ), condensation occurs into localized states, visible as spectrally narrow emission peaks. A redistribution of intensity between different localized states is observed with increasing excitation.

This effect can be clearly observed in the spatially-resolved experiments shown in Figs. 3.5. The reflectivity map in Fig. 3.5(a) corresponds to the detuning presented in Figs. 3.3(a,b), while the map in Fig. 3.5(b) corresponds to the position with detuning shown in Figs. 3.3(c,d). The reflectivity maps reveal that the energy of the lower polariton fluctuates differently depending on the local detuning. For more negative detuning [Fig. 3.5(a)], the polariton has a larger photonic fraction, and fluctuations occur between 1.595 eV and 1.612 eV. For less negative detuning [Fig. 3.5(b)], the fluctuations are observed in a smaller energy range, between 1.612 eV and 1.618 eV.

The influence of disorder is also visible in photoluminescence. At the position of Fig. 3.5(a), even well below the condensation threshold (0.32 pJ), Fig. 3.5(c) already shows several localized states that appear on top of a broad emission background. As the excitation power increases, as shown in Fig. 3.5(d), for 26.30 pJ, the intensity of these localized states increased as well, while the broad background fades. Once excitation exceeds the condensation threshold in Fig. 3.5(e), for 70.41 pJ, the emission spectrum narrows, confirming condensation in localized states. Interestingly, with higher excitation, the emission shifts between different localized states. In the last two panels, the initially dominant state on the left weakens, while the state on the right becomes stronger.

As shown, photonic disorder in CdTe-based microcavities not only suppresses long-range polariton propagation but also determines the localization sites of the condensates by the built-in potential landscape. This feature is fundamental for understanding the behavior of condensates in this material platform and will remain an important theme in the following Chapters.

3.5. Exciton-photon coupling dependence on temperature

A practical demonstration between the strong and weak coupling regime can be obtained experimentally by tracing polariton dispersion relations as a function of temperature. The measurements were obtained on a Sample C.3.

The measured white-light reflectivity spectra in reciprocal space are presented in Fig. 3.6. As shown in Fig. 3.6(a), measured at a temperature of 5 K, the lower and upper polariton modes are clearly visible in the dispersion map. The map was modeled with the coupled oscillator model, where the bare photonic mode and the exciton mode are indicated with white dashed lines, and the lower and upper polariton branches are shown with red dashed lines. From the modeling, the detuning at the investigated position was determined as $\delta = -19.2$ meV. The subsequent maps were collected for the higher temperatures, indicated in the lower right corner of each panel. As can be seen, within the temperature range of 5 K to 130 K, corresponding to Figs. 3.6(a)–(l), polariton modes remain clearly visible and the modeling procedure was straightforward, since the full wavevector range available on the maps was well resolved. As the temperature increased, the polariton modes were observed to move closer to each other, approaching a detuning value of zero. With increasing temperature, the polariton modes were also observed to broaden, accompanied by a gradual decrease in the contrast between the polariton modes and the background signal. This broadening mainly reflects stronger exciton-phonon scattering at higher temperatures, which shortens the exciton coherence time and by exciton-photon interactions, widens the polariton resonances. As

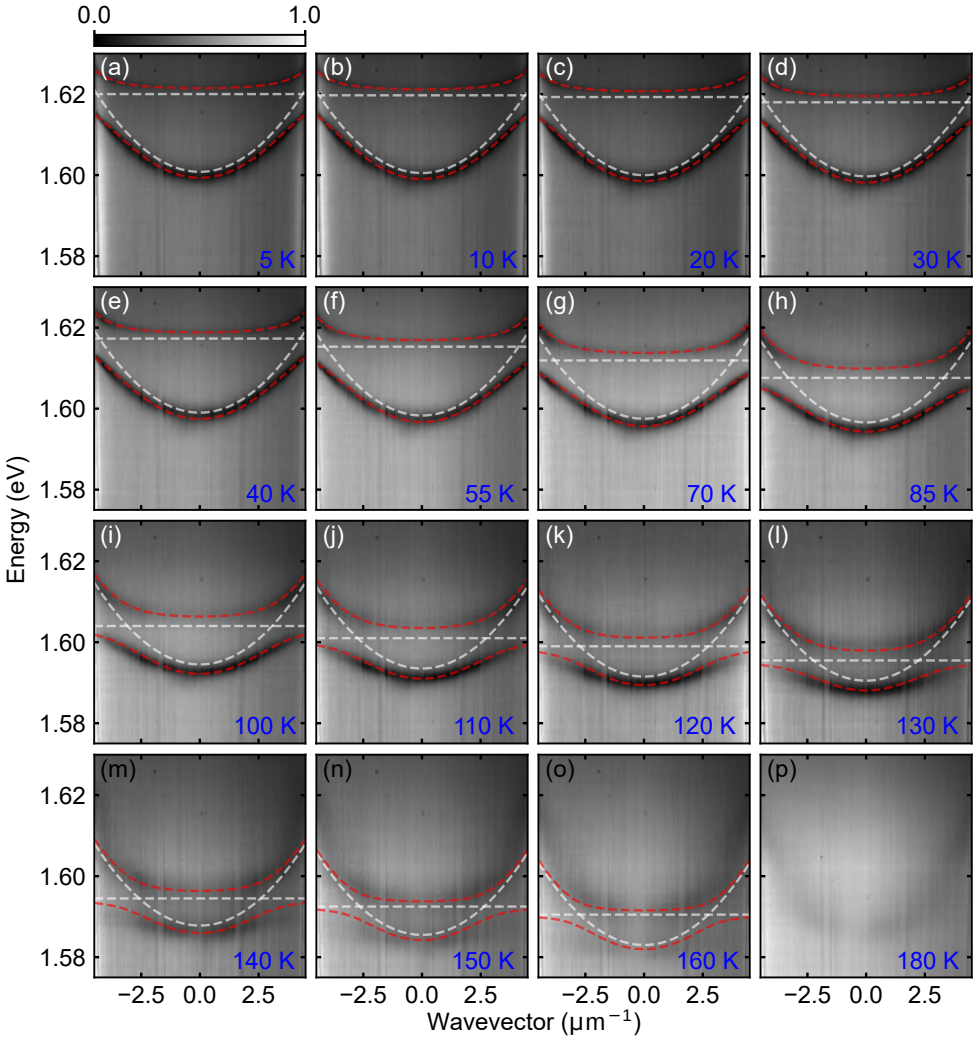

Figure 3.6: **Temperature dependence of polariton dispersion in experiment on a CdTe-based microcavity.** White-light reflectivity maps in reciprocal space for Sample C.3 at selected temperatures, as indicated in each panel. The data were modeled using a coupled oscillator model. White dashed lines mark the bare photonic and excitonic modes, while red dashed lines indicate the upper and lower polariton branches. Polariton modes remain clearly visible up to 130 K [panels (a)–(l)], while at higher temperatures the modes broaden and disappear. At 180 K [panel (p)], only a broad photonic resonance is observed, indicating the transition from strong to weak coupling regime.

the detuning approaches zero, at normal incidence ($k = 0$) the lower polariton gains more excitonic character and broadens strongly. The upper polariton, remains spectrally broad as it retains a substantial excitonic fraction. As the excitonic resonance broadens, its peak amplitude decreases, which reduces the visibility on the reflectance spectrum.

The reliable modeling became difficult above 130 K, where the linewidth of the polariton modes significantly increased and their depth relative to the background decreased. Moreover,

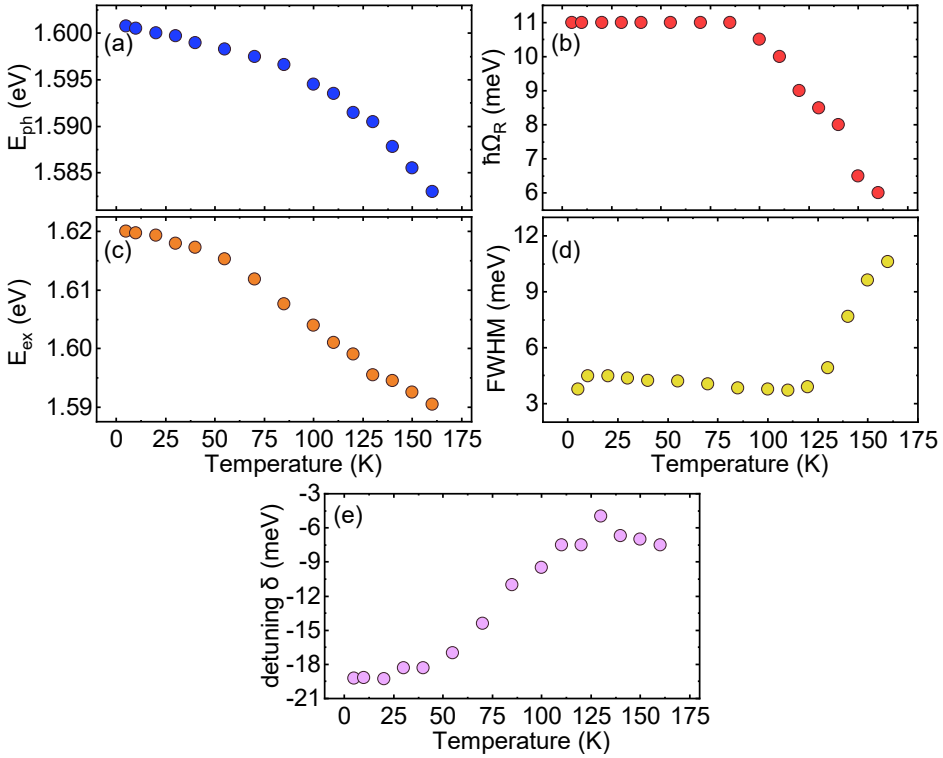

Figure 3.7: **Extracted parameters of the coupled oscillator model from the reflectivity maps and from the Lorentzian fitting to the data as a function of increasing temperature.** (a) Bare cavity photon energy E_{ph}, (b) Rabi energy $\hbar\Omega_R$, and (c) exciton energy E_{ex} as a function of temperature. (d) Temperature dependence of the lower polariton mode linewidth (FWHM) at $k = 0$, obtained from Lorentzian fits. (e) Evolution of the detuning during heating. A consistent increase in detuning is observed up to 130 K, above which the results are less reliable due to broadening and reduced spectral contrast of the modes.

an additional signal appeared in the spectral range between approximately 1.608 eV and 1.625 eV, with an effective mass different from that of the polariton modes, which, based on its energy range, can be attributed to the coupling with the light-hole exciton. At 180 K [Fig. 3.6(p)], only a spectrally broad photonic mode is observed. Therefore, it can be concluded that at a temperature of about 180 K the system no longer exhibits the strong coupling regime.

The parameters obtained by applying the coupled oscillator model are plotted as a function of temperature in Fig. 3.7. The extracted parameters include E_{ph}, $\hbar\Omega_R$, and E_{ex}, presented in Figs. 3.7(a)–(c), respectively. In addition, Lorentzian profile was fitted to the spectra at $k = 0$ to extract the linewidth of the lower polariton mode, as shown in Fig. 3.7(d). Finally, Fig. 3.7(e) illustrates the change of detuning during the measurements. Between 5 K and 130 K detuning smoothly increases, whereas above this temperature the results are less reliable due to the difficulties in applying the model to the raw spectra. As the temperature increases,

the optical path length increases because the refractive index rises (and the cavity undergoes thermal expansion). Consequently, the cavity photon energy decreases and the cavity mode shifts to lower energy. The exciton energy decreases more strongly as a result of the band-gap shrinkage with the temperature. Here, as the system starts at strongly negative detuning, the detuning shifts toward zero value. The lower polariton spectrally broadens as it inherits the increased linewidth of the excitonic resonance. In addition, the broadened excitonic resonance results in lowered coupling efficiency with the cavity mode, which is observed as a decrease of the Rabi splitting. These measurements confirm that in white-light reflectivity the strong coupling regime can be observed in CdTe-based microcavities up to temperatures as high as 130 K.

Chapter 4

Optical bistability in transmissive II-VI microcavities

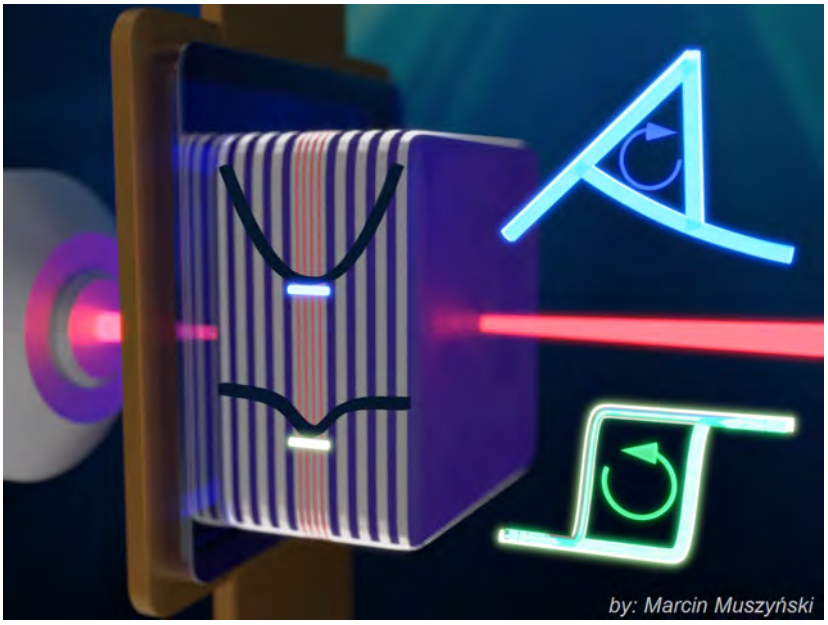

The results described in this Chapter are published in:
1. M. Furman, et al., "Inverted optical bistability and optical limiting in coherently driven exciton-polaritons" (2023), APL Photonics, 8, 046105 [2]
and
2. A. Opala, M. Furman, et al., "Natural exceptional points in the excitation spectrum of a light-matter system" (2023), Optica 10, 8 [69].

One of the most important phenomena originating directly from the nonlinear properties of exciton-polariton systems is optical bistability. It is a direct manifestation of polariton-polariton interactions which can be used for the realization of all-optical logic elements and switches. This Chapter demonstrates optical bistability in a CdTe-based microcavity, a material system in which this effect had not been previously reported in the transmission geometry. This achievement was only possible because of the development of novel sample fabrication methods that enabled direct access to the transmission geometry in strongly coupled CdTe-based microcavities, thus opening new possibilities for probing nonlinear effects.

To this end, a transmissive CdTe-based microcavity was fabricated using a specially developed lift-off method. In this process, the epitaxial growth is extended by an additional water-resolvable sacrificial layer. This allows for the separation of the actual microcavity stack from its original substrate. For ease of further experiments, the exfoliated free-standing microcavity was transferred onto a transparent sapphire support, allowing for transmission measurements. This approach not only preserved the optical quality of the microcavity but also provided a unique experimental configuration for investigating the nonlinear dynamics of polaritons under resonant excitation.

The optical quality of the structure after the lift-off process was verified using momentum-resolved reflectivity and photoluminescence measurements. These confirmed that the system remained in the strong coupling regime and supported the formation of a non-equilibrium Bose-Einstein condensate of polaritons.

Subsequent quasiresonant laser transmission experiments revealed clear signatures of optical bistability in the input-output power characteristics. Importantly, two new distinct types of hysteresis loops depending on the excitation conditions were discovered. These bistable behaviors differ qualitatively from those reported in other semiconductor microcavity systems, showing unique features arising from the interplay between thermal effects and the transition between strong and weak coupling regimes. Subsequent observations resolved in reciprocal space, showed a redshift of the polariton modes and a reduction of the Rabi splitting, while real-space emission patterns exhibited spatial reorganization between bistable states.

Finally, a theoretical model was developed to fully support both types of bistabilities observed experimentally. The model incorporated the experimentally confirmed effects of energy redshift and the reduction of the Rabi splitting. Both of those effects drove the transition from strong to weak coupling. The model successfully captures the newly identified forms of optical bistability. In addition, the theoretical analysis proves that in the investigated CdTe-based microcavities, the underlying nonlinear mechanisms differ fundamentally from those previously established in other polaritonic materials.

4.1. Introduction to bistability in optical microcavities

Optical bistability is a well-known example of a nonlinear phenomenon in optics. It occurs when the system exhibits two different stable stationary states under the same excitation conditions depending on the history of the system. The appearance of this effect is possible when the output of an optical system (for example transmission or reflection of light) is not directly proportional to the incident field but requires a presence of a nonlinear effect [70, 71].

Two necessary requirements for observing the bistability are the presence of a nonlinear medium, which provides an excitation intensity-dependent refractive index or absorption, and a feedback mechanism, which is most often realized in an optical resonator [72, 73]. Experimentally, this behavior is most often observed as the formation of a hysteresis loop in the input-output power characteristic, when the pump power is adiabatically increased and decreased [70].

Since its first observation, optical bistability has attracted much interest due to the possibility of realizing optical switches and memory elements based on bistable systems [74,75]. In later years, this phenomenon has been demonstrated in a wide range of nonlinear optical platforms, from semiconductor lasers [76–78], through cold atom systems [79–81], to cavities filled with nonlinear materials [73, 82], and photonic crystals [83, 84]. Optical bistability has also been observed in VCSELs [85–87], in layered semiconductor materials [88], and in plasmonic systems [89]. These examples highlight the universality of the bistability effect.

A particularly interesting system exhibiting optical bistability is a semiconductor optical microcavity operating in the strong coupling regime. There, the excitonic component of polaritons leads to strong nonlinear effects [40, 90].

In the literature, two explanations can be found for the occurrence of optical bistability in strongly coupled microcavity systems. The first theoretical proposal [91] suggested that the transition from the strong to weak coupling regime can lead to hysteresis, what was confirmed experimentally [92]. However, the better known mechanism responsible for bistability in optical microcavities is based on the polariton-polariton interactions, which act as a Kerr-type nonlinearity [40, 90, 93–95]. In such a system, the polariton mode shifts to higher energies with increasing polariton density as a result of repulsive polariton-polariton interactions, thereby modifying the resonance condition with respect to the pumping laser.

Recently, optical bistability in polariton systems has also been reported in device-oriented structures such as polariton diodes [96], confirming its relevance for future applications in optical switching and information processing.

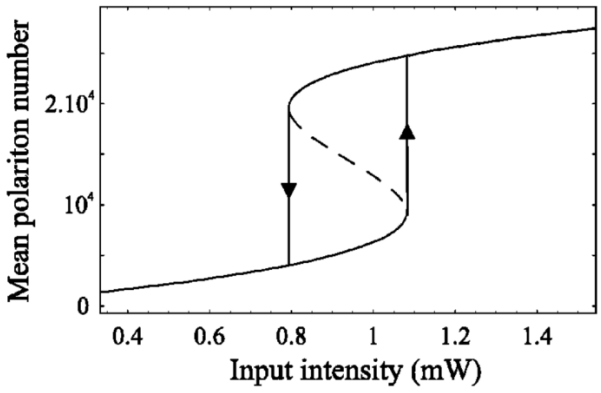

Figure 4.1: **Model of S-shaped optical bistability in a strongly coupled microcavity.** The calculated transmission intensity in a function of excitation power exhibits a S-shaped dependence with a hysteresis loop between low- and high-transmission states. Adapted from Ref. [93].

The experiments reported in [93, 97] presented a direct experimental demonstration of the optical bistability. In their realization, the energy of the laser reflected or transmitted through the microcavity was tuned slightly above the energy of the lower polariton mode.

A theoretical model explaining this behavior is described in Baas et al. [93]. The mean field model includes a Kerr-type nonlinear contribution stemming form repulsive polariton-polariton interactions which results in an energy blueshift of the polariton resonance energy under strong excitation. Figure 4.1 presents the solution of the model, demonstrating a S-shaped dependence of transmission on the excitation intensity. At low excitation powers, the transmission remains weak due to the significant energy detuning between the laser and the polariton mode. As the excitation power increases, the transmission intensity increases until it reaches the bottom turning point of the S-shaped characteristic. Here, the middle branch of the characteristic is physically unstable, leading to a rapid switch from the low- to the high-transmission branch. Physically, this jump coincides with the bringing of the polariton mode in resonance with the laser, providing sudden increase of transmittance.

Upon decreasing the laser power, the system follows the high-transmission branch down to the top turning point of the S-shaped curve. Here, the transmission intensity suddenly drops as the system returns to the low-transmission state, forming a characteristic counterclockwise hysteresis loop in the input-output intensity plane.

This characteristic bistable behavior of the system depends on the laser-polariton detuning $\Delta = E_{\mathrm{L}} - E_{\mathrm{LP}}$, where E_{LP} is the energy of the lower polariton branch, and E_{L} the excitation laser energy compared with the linewidth of the lower polariton mode γ_{LP}. In particular, the model predicts that the bistability appears only when the laser detuning Δ is greater than $\sqrt{3}\,\gamma_{\mathrm{LP}}$. For smaller laser detunings the bistability disappears and the system realizes either the so-called optical limiter regime or for the $\Delta = \sqrt{3}\,\gamma_{\mathrm{LP}}$ the optical discriminator regime. In these regimes, the transmission varies smoothly with excitation power without the formation of two distinct stable branches.

The model introduced by Baas et al. provides a useful reference for interpreting bistable phenomena observed in strongly coupled microcavities. In this work, its conceptual framework serves as a starting point for understanding of optical bistability. However, the behavior observed here of CdTe-based transmissive microcavities deviates significantly from the predictions of this model, suggesting other underlying mechanisms and demonstrating a necessity for developing a specific theoretical description.

4.2. Exfoliation of II-VI semiconductor microcavities

The transmission configuration is especially convenient for the observation of bistability in optical microcavities. For CdTe-based microcavities, the structure can be grown by MBE on two types of substrates, CdTe substrates [98–100] and GaAs substrates [11, 101], however, both these materials are nontransparent in the energy range corresponding to excitons in CdTe quantum wells. However, there are documented methods for fabricating semiconductor optical microcavities suitable for measurements in transmission. Such approaches include mechanical polishing [102] and chemical etching of selected material layers [103].

In this work, another method was used to separate the nontransparent GaAs substrate from the CdTe-based microcavity. It was realized by introducing an additional, hygroscopic

'sacrificial' buffer layer between the microcavity and the substrate. This so-called lift-off method, already applied to CdTe-based optical microcavities, was developed at the Faculty of Physics, University of Warsaw, and described in Ref. [104, 105].

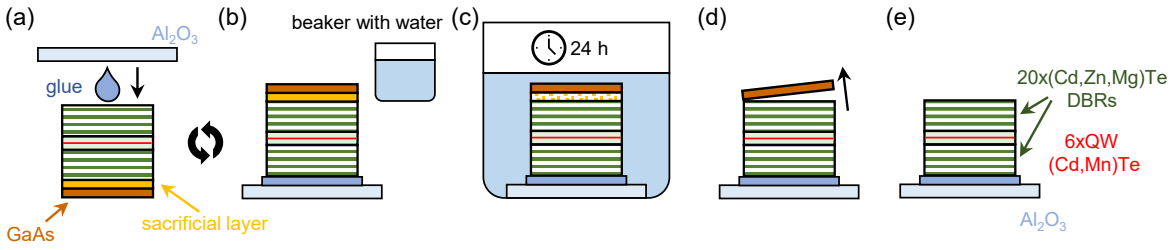

Figure 4.2: **The process of creating a transmissive, CdTe-based semiconductor microcavity, using the lift-off method.** (a) A transparent sapphire (Al_2O_3) substrate attached to the CdTe microcavity grown on a nontransparent GaAs substrate. The sacrificial MgTe layer is marked in yellow. (b) A microcavity glued to the transparent substrate with a beaker with demineralized water prepared for the MgTe oxidation process. (c) Submerging the microcavity in water for approximately 24 hours. (d) Detachment of the GaAs substrate from the microcavity. (e) The microcavity on the new transparent substrate after the water-based exfoliation process.

Figure 4.2 presents a schematic procedure of the fabrication process of the transmissive CdTe-based optical microcavity with the lift-off method. During MBE growth of the microcavity on the nontransparent GaAs substrate, a 90 nm-thick magnesium telluride (MgTe) sacrificial layer was grown between the substrate and the microcavity structure. It is shown in Fig. 4.2(a) as a yellow layer. MgTe is a hygroscopic material that dissolves easily in water, thus allowing for the separation of the microcavity structure from the substrate. After the growth, the sample was prepared for immersion in water. A new, transparent substrate was attached to the top Bragg mirror with a glue. After attaching the new substrate to the top surface of the microcavity, the sample was placed in a beaker with demineralized water and left for approximately 24 hours [Fig. 4.2(c)]. After that time, the oxidation of the MgTe layer was completed and the sample was removed from the water and dried. The GaAs substrate was pushed from the side with a wooden toothpick. Then, as seen in Fig. 4.2(d), the old substrate detached without significant resistance and was removed. The resulting transmission microcavity, presented schematically in Fig. 4.2(e), was finally dried using a stream of nitrogen gas.

The described procedure was tested using various transparent substrates and glues. Figure 4.3(a) shows an image of different trial samples. Both glass and sapphire substrates were tested, along with various gelfilms and glues to attach the sample. Finally, sapphire (Al_2O_3) was chosen because of the ease of cutting to match the sample dimensions, as it easily breaks along the crystallographic planes. Sapphire also did not crack upon cooling, unlike some glass substrates.

The tested glues behaved differently in water and under cryogenic conditions. Some of the tested glues became opaque in water, while the gelfilms detached together with the sample during measurements. The final choice for measurements was a Marabu-fixogum glue, a photo

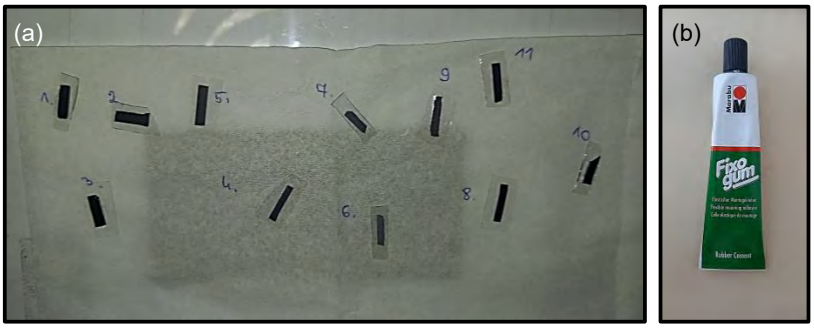

Figure 4.3: **Process of fabricating a CdTe-based transmissive microcavity via water-based exfoliation.** (a) Tested CdTe-based optical microcavities used for optimizing the exfoliation procedure, employing various substrates, glues, and soaking times in distilled water. (b) Photography of the final glue selected for bonding the sample, which met all requirements for cryogenic temperatures and transmission measurements.

of which is presented in Fig. 4.3(b).

During the exfoliation process, it was especially important to properly attach the microcavity to the transparent substrate. It was crucial to avoid blocking the access of water to the MgTe layer. If the layer of glue was too thick and spread over the edges of the microcavity when pressing the new substrate onto the sample, the glue can restrict the water access during the oxidation process. It can completely block the process and disallow the separation of the microcavity from the substrate. If necessary, excess glue has to be carefully removed, e.g. with a wooden toothpick.

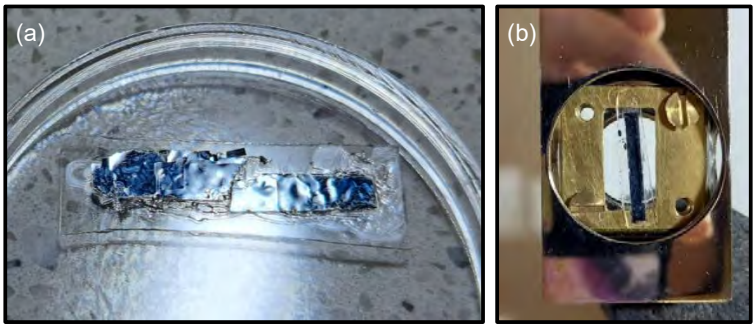

Figure 4.4: **CdTe-based optical microcavity prepared for transmission measurements.** (a) Transmissive sample on the new substrate after water-based exfoliation. (b) The sample mounted on a transmissive cold finger inside the cryostat.

Following this optimized procedure produced a CdTe transmission microcavity. Figure 4.4 presents photographs of the final transmissive microcavity. Figure 4.4(a) shows the microcavity immediately after the exfoliation process, transferred onto a new substrate and placed in a laboratory Petri dish. Subsequently, Fig. 4.4(b) shows the transmissive microcavity attached to the cold finger inside the cryostat. A detailed description of the full structure of the sample

can be found in Appendix I, 7.1, under the name Sample C.1.

4.3. Strong coupling regime and polariton BEC after exfoliation

After completion of the water-based exfoliation process, the optical quality of the microcavity was checked to verify whether the system exhibited a strong coupling regime at T = 4.5 K. For this purpose, a white-light halogen lamp was used to measure the momentum-resolved reflectivity spectrum, as shown in Fig. 4.5(a). In the reflectivity map obtained in this way, two modes corresponding to the lower and upper polariton branches are visible. For wavevector values above $\pm 2.5\ \mu m^{-1}$, a characteristic anticrossing of the modes can be observed, confirming that the sample is in the strong coupling regime. In Fig. 4.5(b), a cross-section at $k = 0$ (marked with a red dashed line) was extracted from the reflectivity map, and the resulting spectrum was fitted with a double Lorentzian profile. The parameters obtained from this fit were used to determine the Q-factor of the microcavity, with a value of $Q = 345$.

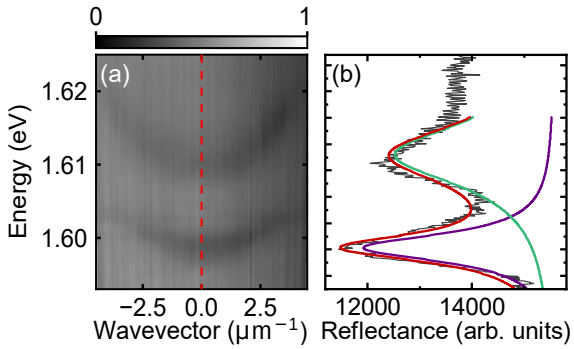

Figure 4.5: **White-light reflectivity from a transmissive CdTe microcavity, showing the lower and upper polariton modes.** (a) Momentum-resolved dispersion measured on a spectrometer for transmissive Sample C.1. (b) Cross-section at $k = 0$ [red, dashed line in (a)] with a double-Lorentzian fit. The linewidth of lower polariton branch $\gamma_{\mathrm{LP}} = 4.63$ meV and its energy of $E_{LP} = 1.599$ eV extracted from the fit were used to determine the cavity Q-factor of $Q = 345$.

The next stage of the characterization measurements was to investigate the photoluminescence of the transmissive microcavity and to observe the transition of exciton-polaritons into a non-equilibrium Bose-Einstein condensate. Photoluminescence measurements were performed using the experimental setup described in Chapter 3, and shown in Fig. 3.1. The microcavity was excited nonresonantly with a pulsed Mira-900 laser with the energy of 1.746 eV, tuned to the first Bragg minimum of the cavity. Measurements were carried out with the sample inside a cryostat at a temperature of 4.5 K.

A series of measurements was taken for increasing excitation laser pulse energy. Figs. 4.6(a)–(c) presents momentum-resolved photoluminescence spectra. The pulse energy values for each map are indicated in the lower right corner. The dispersion obtained for low pulse energy ($E_{\mathrm{pulse}} = 0.03$ pJ) is presented in Fig. 4.6(a). Here, the entire lower polariton branch is populated, exhibiting nonuniform occupation, typical for inhomogeneous CdTe-based samples.

As the pulse energy increased, as presented in Fig. 4.6(b) for $E_{\text{pulse}} = 2.70$ pJ, gradual relaxation of polaritons from a broader range of wavevectors toward the bottom of the lower polariton branch near $k = 0$ was observed. Due to the inhomogeneous photonic potential in the CdTe samples, the condensate did not perfectly localize around $k = 0$. After exceeding the condensation threshold ($E_{\text{pulse}} = 3.30$ pJ), the dispersion shows only a spectrally narrow line, as presented in Fig. 4.6(c). Furthermore, the spectrum below the condensation threshold was modeled with a coupled-oscillator model, with the resulting coupling strength of 12 meV.

The collected spectra were then analyzed using Lorentzian fits to cross-sections of each dispersion map at k characterized by the highest signal intensity. From the fits, the integrated intensity, linewidth of the polariton mode (FWHM), and energy shift of the signal were extracted for each pulse energy. The results are summarized in Fig. 4.6(d), where intensity is shown in black, blueshift in green, and FWHM in red, as a function of increasing excitation pulse energy. The transition to non-equilibrium polariton condensate occurred at a pulse energy of approximately 3.30 pJ, where the nonlinear increase of the emission intensity coincides with the sudden narrowing of the spectral linewidth.

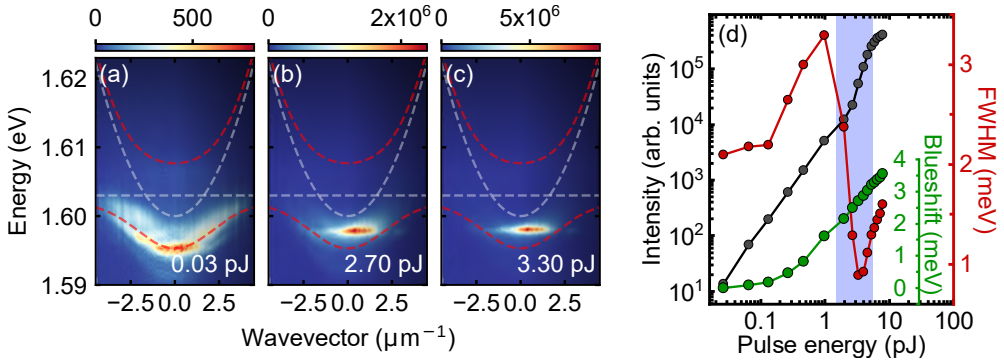

Figure 4.6: **Non-equilibrium Bose-Einstein condensation on transmissive, exfoliated CdTe-based microcavity.** (a) Momentum-resolved emission spectra collected below the condensation threshold, at excitation energy $E_{\text{pulse}} = 0.03$ pJ, with a relatively broad lower polariton mode populated along the entire polariton branch. A coupled oscillator model was modeled to the data, with the following parameters: $E_{\text{ph}} = 1.6$ eV, $E_{\text{ex}} = 1.603$ eV, $\hbar\Omega = 0.012$ eV and $m^*_{\text{ph}} = 1.71 \times 10^{-5}\ m_{\text{e}}$. (b) Momentum-resolved emission spectra showing the onset of condensation, where polaritons start to accumulate mainly near the dispersion minimum at the excitation energy of $E_{\text{pulse}} = 2.70$ pJ. (c) Momentum-resolved emission spectra of the condensate, spectrally localized in energy, collected at excitation energy of $E_{\text{pulse}} = 3.30$ pJ. (d) Condensation characteristics obtained from Lorentzian fits to cross-sections of the maps at successive excitation powers, showing the intensity, blueshift, and FWHM.

These characterization measurements demonstrate that the exfoliation method provides microcavity samples operating in the strong coupling regime and exhibiting BEC of exciton-polaritons. After confirmation of the high quality of the transmissive samples, it is possible to investigate optical bistability.

4.4. Optical bistabilities in exfoliated microcavities

4.4.1. Bistable laser transmission through exfoliated microcavities

The experimental configuration for measuring optical bistability was designed to collect the total intensity of light transmitted through the sample for the varying intensity of the incident laser. The measurement system, shown in simplified form in Fig. 4.7, is based on two separate photodetectors (power meters), independently measuring the incident and transmitted laser intensity.

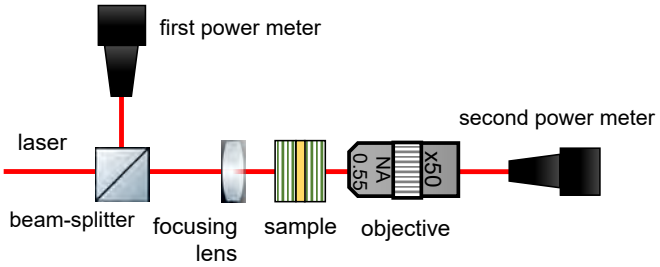

Figure 4.7: **Measurement setup with two detectors for optical bistability experiments.** The system consists of two power meters: one placed before the sample to monitor the input power beam, and another positioned after the sample to measure the transmitted light intensity.

In this experiment, the sample was excited quasi-resonantly, which means that the incident laser energy was tuned close to the energy of the polariton modes. A tunable, linearly polarized, continuous-wave Ti:sapphire laser (Coherent MBR) was used as the laser source.

The laser beam power was controlled using a set of a linear polarizer, a half-wave plate, and a second linear polarizer. The two linear polarizers were oriented perpendicular to each other (crossed polarizers), while the rotation of the half-wave plate modified the laser transmission through the system. The half-wave plate was mounted on a motorized, computer-controlled rotational stage, allowing for precise and automated adjustments. The angle of the half-wave plate was varied in the range from 0° to 45°, enabling continuous control of the transmitted laser intensity. As a result, the laser power could be continuously tuned over a broad range, from a few microwatts to several tens of milliwatts.

With this method, the dependence of the transmitted light intensity on the half-wave plate angle θ is described by:

$$I(\theta) = I_0 \sin^2(2\theta), \tag{4.1}$$

where I_0 is the incident light intensity.

The laser power incident on the sample was monitored after a 90:10 beam splitter. The weaker, reflected part of the beam was directed to the power meter. The remaining 90% was focused on the sample, placed in the transmissive configuration cryostat using a lens with a focal length of $f = 25.4$ mm. The beam spot on the surface of the sample was approximately 12 µm in diameter. The light transmitted through the sample was collected by a microscope objective (Nikon, TU-Plan, 50×, NA = 0.55) and sent to the second power meter.

This configuration allowed for measurement of the transmitted power as a function of the input power (input-output characteristics). For each laser detuning relative to the polariton mode energy, a separate transmission characteristic was collected.

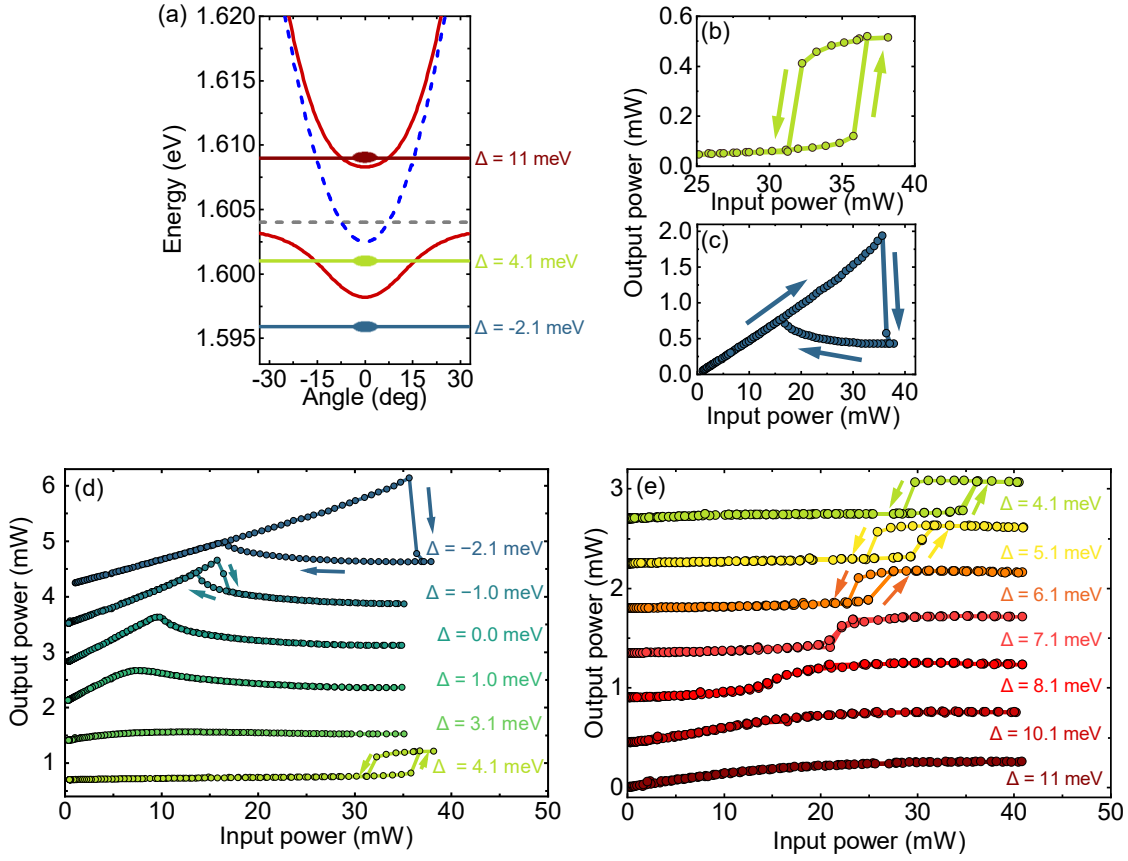

Figure 4.8: **Observation of new types of hysteresis in CdTe-based microcavity.** (a) Exciton-polariton dispersion relation for the CdTe-based microcavity, with marked laser detunings of $\Delta = -2.1$ meV, $\Delta = 4.1$ meV and $\Delta = 11$ meV between which the laser transmission was measured. (b)–(e) Input-output characteristics collected for successive laser detunings. (b,c) Transmission intensity dependences showing novel types of bistabilities: for positive $\Delta = 4.1$ meV (b), and negative detuning $\Delta = -2.1$ meV (c). (d) Input-output characteristics for successive detunings of the laser energy from the bottom of the lower polariton branch (between $\Delta = -2.1$ meV and $\Delta = 4.1$ meV). (d) Input-output characteristics collected for successive laser detunings collected between $\Delta = 4.1$ meV and $\Delta = 11$ meV.

All measurements were performed at 4.5 K. Each analyzed position was scanned with a laser power, collecting the input-output power characteristics, and then the laser energy was changed and the scan was repeated. At the position that had the appropriate detuning for observing bistability, the white-light reflectivity spectrum from the detection side was collected to determine the local detuning between the photon and exciton modes. Figure 4.8(a) shows the dispersion of the polariton modes obtained from a coupled oscillator model applied

to the reflectivity spectrum, which at this position revealed a slightly negative detuning of $\delta = -1.5$ meV. This result differs from earlier reports, where optical bistability was typically observed for positive or near-zero detuning [93, 97]. The dispersions of the upper and lower polariton branches are marked with solid red lines, while the photon mode is shown with a navy blue dashed line, and the bare exciton with a dark gray dashed line.

The transmission measurements presented in Figs. 4.8(b)–(e), were performed for different energies of the incident laser, quantified by the laser-to-lower polariton detuning Δ.

The first case corresponds to the laser energy set 4.1 meV above the minimum of the lower polariton branch. The energy of the laser with respect to the polariton modes is presented in Fig. 4.8(a) with a light-green line and labeled $\Delta = 4.1$ meV. Figure 4.8(b) presents the obtained input-output characteristic. At low laser powers up to 35 mW, the transmitted intensity increased almost linearly with the incident power. However, around 36 mW the transmission rapidly switched to a higher transmission state. As the incident power was further increased, the transmission intensity remained stable. When laser power was reduced, the system remained in the high-transmission state up to 32 mW, after which it switched back to the low-transmission state. Switching up at 36 mW and down at 32 mW resulted in the formation of a closed hysteresis loop with a counterclockwise direction of evolution. The direction of the hysteresis is indicated by the arrows marking the direction of the change in the incident laser power.

The observed bistability resembles the behavior known in microcavity systems operating in the strong coupling regime [93, 97]. However, there were also significant differences. Firstly, it occurred at much higher excitation powers. Moreover, the behavior at high laser powers was unexpected. Once the system switched to the higher transmission state, upon further increasing of the input laser power, the transmitted light intensity decreased, instead of increasing. In addition, the condition $\Delta > \sqrt{3}, \gamma_{\mathrm{LP}}$ described by the theory for the observation of optical bistability was not met, since the linewidth of the lower polariton mode was $\gamma_{\mathrm{LP}} = 4.63$ meV. This unexpected behavior led to further investigation of this system.

The aim of the following measurements was to investigate the bistable behavior at different laser-polariton detunings. The experimental results of the input-output power dependence for successive laser energies are summarized in Figs. 4.8(d,e). The plots are labeled by the detuning Δ. A positive Δ indicates that the laser energy was set above the lower polariton energy, while a negative Δ corresponds to excitation below. The extreme excitation energies between which systematic measurements were collected are also indicated by lines in Fig. 4.8(a), and their detunings are equal to $\Delta = 11$ meV (marked with a dark red line) and $\Delta = -2.1$ meV (marked with blue).

The characteristics were measured starting from the position of the laser energy at $\Delta = 11$ meV, as shown in Fig. 4.8(e). This is the position where the laser energy exceeded the upper polariton energy. The measurement at $\Delta = 11$ meV exhibited a nonlinear dependence of the transmitted light intensity, but it did not show a separation into two distinct states between which the system could switch. For detunings above $\Delta = 7.1$ meV, the system still exhibited nonlinear transmission. At $\Delta = 7.1$ meV, a closed hysteresis loop was observed. At this point, the input-output characteristic resembled the optical discriminator regime, with both low- and high-transmission states being degenerate. Moving the laser energy closer to the lower polariton branch ($\Delta = 6.1$ meV and $\Delta = 5.1$ meV), an opening of the hysteresis loop was observed and the optical bistability with counterclockwise hysteresis orientation

was shifted towards higher input powers. Additionally, the hysteresis width increased with decreasing laser energy.

The characteristic already described was collected at $\Delta = 4.1$ meV. Subsequently, further input-output power characteristics were measured for successive laser energies approaching the minimum of the lower polariton branch, which are collectively presented in Fig. 4.8(d). At $\Delta = 3.1$ meV no bistable behavior was observed, in contrast to the expected narrowing of the hysteresis width. In the input-output curve, the transmitted laser power increased, but with a slower rate above 10 mW. This effect became more pronounced as the laser energy was tuned closer to the polariton minimum, for example, at $\Delta = 1.0$ meV. When the laser energy was set resonant with the lower polariton energy ($\Delta = 0$ meV), the input-output curve consisted of two regimes. Up to approximately 10 mW the transmission increased linearly with the laser power. At higher powers, the transmitted intensity started to decrease.

Further, the laser energy was tuned below the lower polariton dispersion. For $\Delta = -1.0$ meV, the transmission increased linearly with excitation power until a critical value of 15 mW. At this point, the system exhibited a sudden drop in transmission to a lower transmission state, after which the transmitted signal continued to decrease steadily. When the laser power was reduced, the signal did not follow the same curve as during the power increase. The characteristics met the linear part of the curve at around 13 mW, forming a new type of hysteresis loop. As the laser energy was tuned further below the polariton minimum, at $\Delta = -2.1$ meV, the width of this hysteresis loop increased and ranged between 17 mW and 38 mW [this hysteresis case was additionally placed on a separate panel in Fig. 4.8(c)]. Notably, this new type of hysteresis loop was oriented clockwise, in contrast to the counterclockwise direction of the standard optical hysteresis observed in strongly coupled microcavity systems.

In the following sections, measurements aimed at explaining this behavior are presented. As a comment on the observed phenomenon, the results indicate that the microcavity imposes an upper limit on the transmitted intensity: when the input signal exceeds a certain threshold, depending on the type of the bistability, the transmission saturates or decreases. Such a self-limiting response is characteristic for so-called optical limiters [106–108], devices designed to restrict transmission and protect detectors or optical components from excessively intense light. Similar optical limiting effects have been demonstrated across a wide range of photonic structures, including waveguides [109, 110], photonic crystals [111], microcavities [112, 113], and strongly coupled microcavity systems [40, 114].

4.4.2. Microcavity properties under strong resonant laser illumination

In order to gather more insights into the observed bistable behavior, the emission from the sample was analyzed during the input power cycle loops. The detection setup for measurements in real and momentum spaces was extended by adding three short-pass filters, marked in the schematic Fig. 4.9 as SP filters. The use of multiple filters was necessary because of the very high intensity of the transmitted laser. In the quasi-resonant measurements, the laser is tuned directly near the polariton modes, and its intensity is several orders of magnitude stronger than the photoluminescence from the sample. Therefore, it was crucial to efficiently suppress the laser by adjusting the angle-tunable filters, so that the laser light was blocked while the emission from the sample was preserved.

Since the measurements were demanding and required several days to complete, the

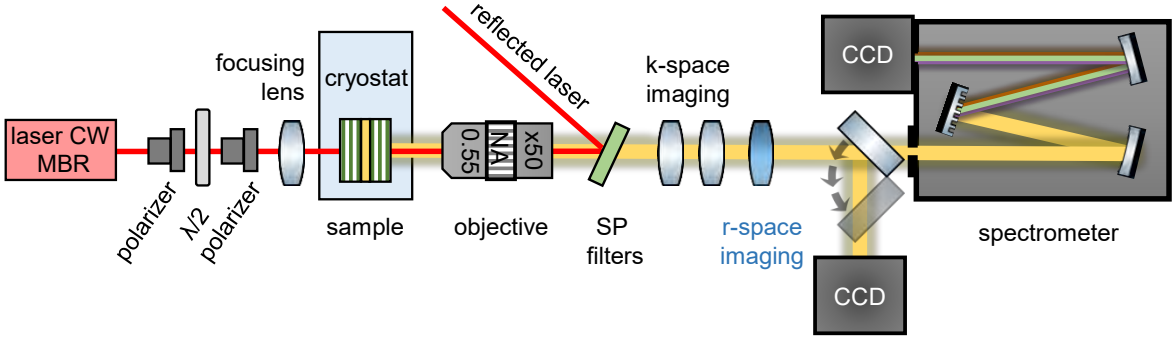

Figure 4.9: **Experimental setup used for photoluminescence measurements of the sample, under quasi-resonant laser transmission.** Along the detection path, additional SP filters were introduced to suppress the transmitted laser while allowing the sample emission to be collected on a detector (CCD camera or spectrometer).

positions on the sample at which the input-output characteristics were collected were not identical across different datasets. The crucial points of reference were always the detuning value Δ for a given measurement and the shape of the corresponding input-output power characteristic. In practice, this meant ensuring that the characteristic measured with the power meters consistently matched the expected laser energy relative to the polariton minimum.

Momentum-resolved photoluminescence spectra corresponding to each type of hysteresis (each laser energy detuning) were measured using the setup shown in Fig. 4.9. These measurements focused on determining the shape of the dispersion of the modes rather than the signal intensity.

Figure 4.10 presents the results for the first energy detuning, tuned to the minimum of the lower polariton branch ($\Delta = 0\,\mathrm{meV}$). The corresponding input-output power dependence is presented in Fig. 4.10(a). It shows maximum transmitted power at 18 mW, followed by a sharp decrease in output intensity, but importantly without bistable behavior.

The corresponding dispersion maps under resonant transmission of the laser through the polariton mode can be seen in Figs. 4.10(b)–(g). The gray area on the maps marks the inaccessible spectral region due to the filtering of the strong incident laser beam. All photoluminescence maps were modeled with the coupled oscillator model, with the resulting parameters summarized in Table 4.1.

For the lowest investigated power of 504 µW in Fig. 4.10(b), a clear emission from the lower polariton was observed around 1.6 eV. Based on this signal, the coupled oscillator model was applied. The extracted exciton-photon detuning equal to $-1.5\,\mathrm{meV}$ was consistent with the previous bistability measurements in this system. Four subsequent dispersion maps [Figs. 4.10(c)–(f)] were collected along the linear part of the input-output power characteristic. In Fig. 4.10(c), measured at 2.67 mW, the emission from the lower polariton branch was stronger and still well reproduced by the initial coupled oscillator model. Additionally, a weak signal from the upper polariton became visible near $k = 0$, close to the energy of 1.605 eV, consistent with the modeled dispersion relation.

At 6.9 mW [Fig. 4.10(d)], the emission broadened spectrally. Moreover, both the lower and upper polariton modes shifted to lower energies, indicating a decrease of both the bare

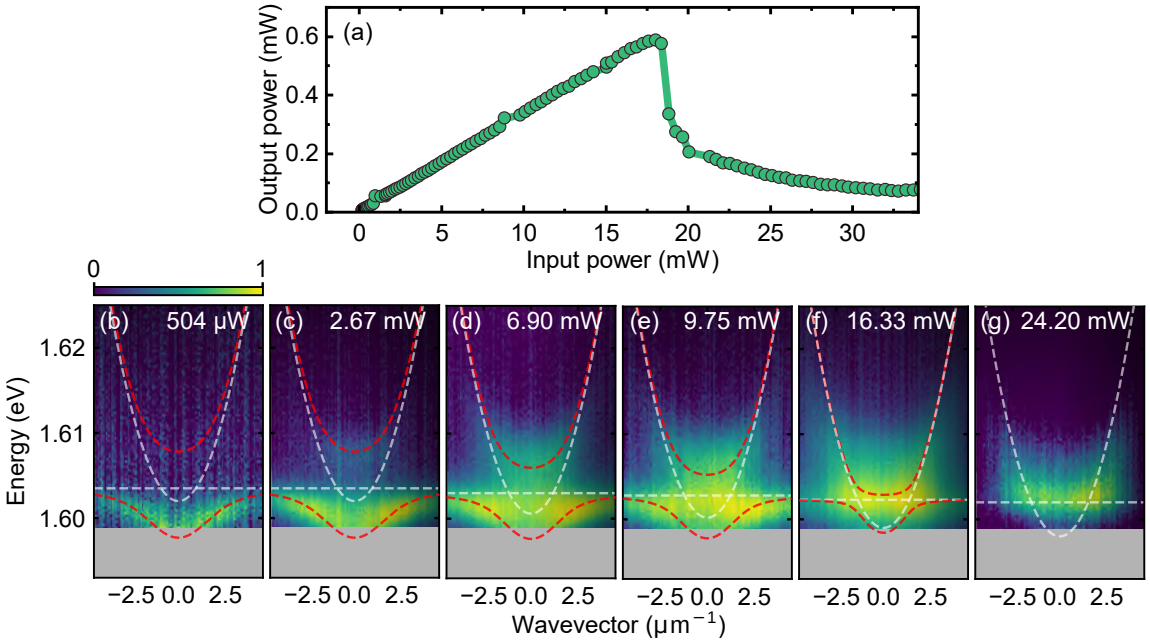

Figure 4.10: **Momentum-resolved photoluminescence spectra with laser energy tuned exactly at the lower polariton energy minimum.** (a) Input-output power characteristic measured with the excitation laser tuned to the minimum of the lower polariton branch. (b)–(g) Photoluminescence dispersion maps collected under resonant excitation for increasing laser powers, with the spectral region of the laser masked on gray. The coupled-oscillator model was applied to the emission, allowing extraction of photon and exciton energies, effective photon mass, and Rabi splitting, as summarized in Table 4.1.

photon and bare exciton energies. The intensity distribution along the modes also changed. It concentrated more around $k = 0$, suggesting a reduction of the Rabi splitting $\hbar\Omega_R$. This was confirmed by the applied coupled oscillator model. At the higher input power of 9.75 mW [Fig. 4.10(e)], a further redshift of both polariton modes was observed. The signal from the upper polariton, visible near 1.603 eV, became significantly broader in momentum compared to Fig. 4.10(d). A further reduction in Rabi splitting was also indicated by the even stronger emission at low momenta. At an even higher power of 16.33 mW [Fig. 4.10(f)] the reduction of both upper and lower polariton energies and Rabi splitting became clearly visible.

The most significant change appears at the powers after the sudden intensity drop at the input-output power characteristic around 18 mW. At 24.2 mW [Fig. 4.10(g)], lower polariton mode was no longer visible, and the emission around the energy range of the upper polariton became very broad in k-space. These two observations suggest that, at this input power, strong coupling is lost. The modeled bare photon and exciton energies for this dispersion map support the hypothesis of a transition from the strong to weak coupling regime. Additionally, the continued redshift of both polariton modes suggests the presence of thermal effects, which induce a decresing energies of both the photon and exciton components and a progressive reduction of the Rabi splitting.

Table 4.1: Parameters of the coupled oscillator model for successive maps in Fig. 4.10.

Map	E_{ph} [eV]	E_{ex} [eV]	$\hbar\Omega$ [eV]	$m^*_{\mathrm{ph}}/m_{\mathrm{e}}$
(b)	1.602	1.6035	0.010	1.71×10^{-5}
(c)	1.602	1.6035	0.010	1.71×10^{-5}
(d)	1.6006	1.6030	0.008	1.71×10^{-5}
(e)	1.6002	1.6028	0.007	1.71×10^{-5}
(f)	1.599	1.6023	0.003	1.71×10^{-5}
(g)	1.598	1.6020	0.000	1.71×10^{-5}

The next results were obtained for the input laser energy tuned below the bottom of the lower polariton branch ($\Delta = -1.7\,\mathrm{meV}$). In this regime, the input-output characteristic shows a bistable behavior with a clockwise hysteresis loop, shown in Fig. 4.11(a). For this measurement, the transmission initially linearly increased with laser power up to 24 mW, after which a sudden drop to a lower-transmission state occurred. In this state, further increase of the laser power led to only a slight growth in transmission. When the power was subsequently decreased, the transmission intensity did not followed the same characteristic. Instead, the transmission was lower within 25 mW to 17 mW range, forming a triangular hysteresis loop.

The white-light reflectivity map collected at this position is shown in Fig. 4.11(b). The laser energy is indicated with a red solid line, along with the applied coupled-oscillator model. From the reflectivity spectrum and the model, the photon-exciton detuning of $\delta = -2.8$ meV was extracted. Figure 4.11(c) presents the reflectivity map that indicates the spectral regions cut out by the filters during the photoluminescence measurements. The filters were used to suppress the very strong laser signal, and additionally to weaken the lower polariton emission, thus allowing the observation of the PL from the upper polariton. The filter operating limit is marked with an orange dashed line and marked as "SP".

The photoluminescence maps shown in Figs. 4.11(d)–(h) display the results obtained while increasing the laser power from 0 mW to 30 mW, whereas Figs. 4.11(i)–(m) present the data collected during the reverse sweep, with the power decreasing from 30 mW to 0 mW.

An additional polarizer was introduced on the detection line to filter out the laser light transmitted through the sample. As in the previous measurement series, all maps were intensity normalized, and the analysis was focused on the shape and curvature of the polariton modes.

At the lowest power of 5 mW [Fig. 4.11(d)], both the lower and upper polariton modes are visible. The lower polariton branch is observed around 1.60 eV, while the upper polariton appears near 1.61 eV. The observed intensity of the upper polariton is significantly higher than that of the lower polariton branch. However, this is a result of additional filtering of the lower polariton spectral range with the short-pass (SP) filters. The actual emission intensities of both the laser and the lower polariton were much stronger than those of the upper polariton, and the filters were applied to enable simultaneous observation of the curvature of both polariton branches.

Figures 4.11(e)–(g) present the measured photoluminescence from the system under increasing excitation power for a series of subsequent laser powers following the linear part of the input-output characteristic shown in Fig. 4.11(a). In Fig. 4.11(e), taken at 11.44 mW, both

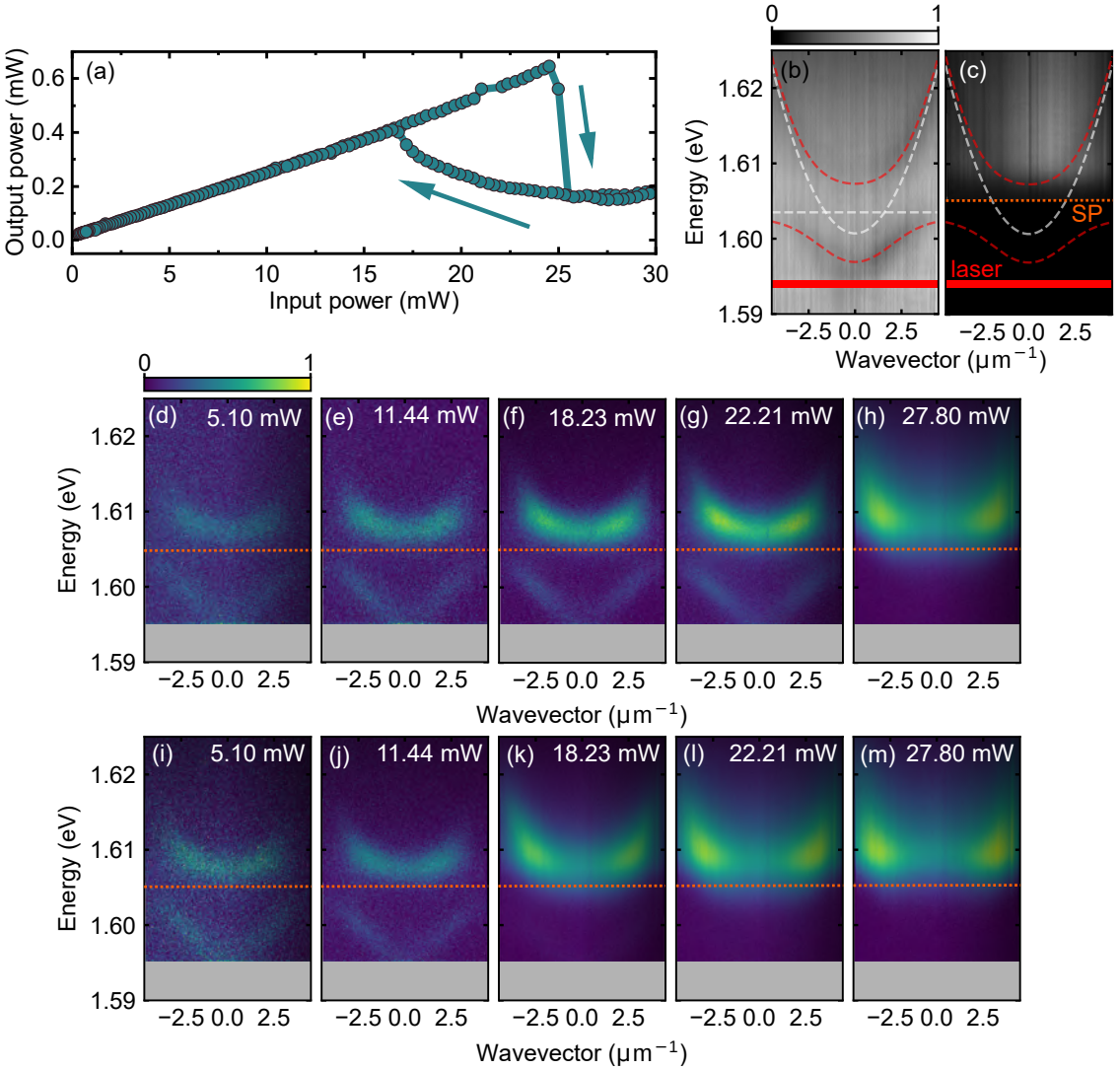

Figure 4.11: **Momentum-resolved photoluminescence spectra with laser energy tuned below the bottom of the lower polariton energy.**(a) Input-output power characteristic measured with the laser tuned slightly below the bottom of the lower polariton branch with $\Delta = -1.7$ meV, showing optical bistability with a clockwise hysteresis loop. (b) White-light reflectivity map with applied coupled-oscillator model. (c) Reflectivity map with the model, indicating the spectral regions cut by filters during the photoluminescence (PL) measurements. (d)–(h) PL dispersion maps collected while increasing the excitation power from 0 to 30 mW, and (i)–(m) corresponding maps obtained during the reverse power sweep.

upper and lower polaritons are clearly visible. Further increase in laser power, Fig. 4.11(f) (18.23 mW) reveals a slight redshift of the upper polariton mode. The further redshift is noticeable in Fig. 4.11(g), collected at 22.21 mW, just before the transition to the lower transmission state. It is worth noting that with the increasing input laser power, the emission

intensity of the upper polariton branch increased faster than that of the lower polariton branch.

The last photoluminescence map on the increasing input power ramp was collected at 27.80 mW [Fig. 4.11(h)], above the bistable region. Compared with the previous dispersion maps, a clear difference was observed. The lower polariton branch was no longer visible, while the signal above 1.608 eV broadened both spectrally and in momentum. The disappearance of the emission from the lower polariton mode combined with a significant drop in the transmitted laser power suggests that in this regime strong coupling was lost. The photoluminescence signal visible above 1.608 eV can then be attributed to a spectrally broadened exciton emission weakly coupled to the cavity mode.

In the next step, momentum-resolved photoluminescence was investigated for the same excitation powers, but in reversed order. This enabled a direct comparison of differences in the dispersion at the same input powers but corresponding to two bistable transmission states of the input-output characteristic. Beginning from 30 mW, when the system was in the low-transmission state, the power was gradually reduced. Figure 4.11(m) presents the map collected at 27.8 mW, reproducing the dependence observed in panel (h). The emission signal was most intense at larger wavevectors, as the system, being in the lower-transmission state, occurred in the weak-coupling regime.

The next investigated laser power of 22.21 mW corresponds to the bistable range of input-output characteristics. The collected photoluminescence map presented in Fig. 4.11(l) shows dispersion branches that are strongly populated at higher wavevectors. It more resembles the higher excitation power in Fig. 4.11(m), than the same input power, but collected during the intensity increase power ramp in Fig. 4.11(g). There is no trace of the lower polariton mode, through which the laser could be transmitted, which may indicate that the system remains in the weak-coupling regime. Compared to panel (m), intensity of both bright arms now begin slowly to move towards $k \approx \pm 2.5\ \mu\text{m}^{-1}$. This may suggest that as the power decreases, the photon mode shifts towards higher energies. Such a redistribution of emission towards higher k can also originate from the loss of coupling with light-hole excitons. Instead of the step-like dispersion characteristic of multiple exciton resonances in the weak-coupling regime, the system evolves towards the smooth bare cavity-photon dispersion.

This trend is confirmed in Fig. 4.11(k), which shows the signal collected at 18.23 mW [same as panel (f)]. The power remains within the bistable range, but near the point where the input-output characteristic switches back from the lower-transmission state to the linear characteristic. The signal observed here reveals that the curvature of the emission in the upper polariton energy range begins to resemble more that of the polariton mode. However, the more intense arms at larger wavevectors are still dominant and spectrally broad. The lower polariton branch is still not visible; thus, the system is in the weak-coupling regime (detected emission comes from the photon mode). Once again, the photoluminescence signal significantly differs from the one collected at the same input power for the power increase ramp.

Figure 4.11(j), collected at 11.44 mW, presents the photoluminescence after the system has returned from the lower-transmission state to the linear part of the input-output characteristic. Clear emission from both the upper and lower polariton modes reappear, and the dispersion matches the one collected at the same power in panel (e). A similar situation is observed in Fig. 4.11(i), measured at 5.1 mW, where the upper and lower polariton modes are again

visible, fully reproducing the behavior from panel (d).

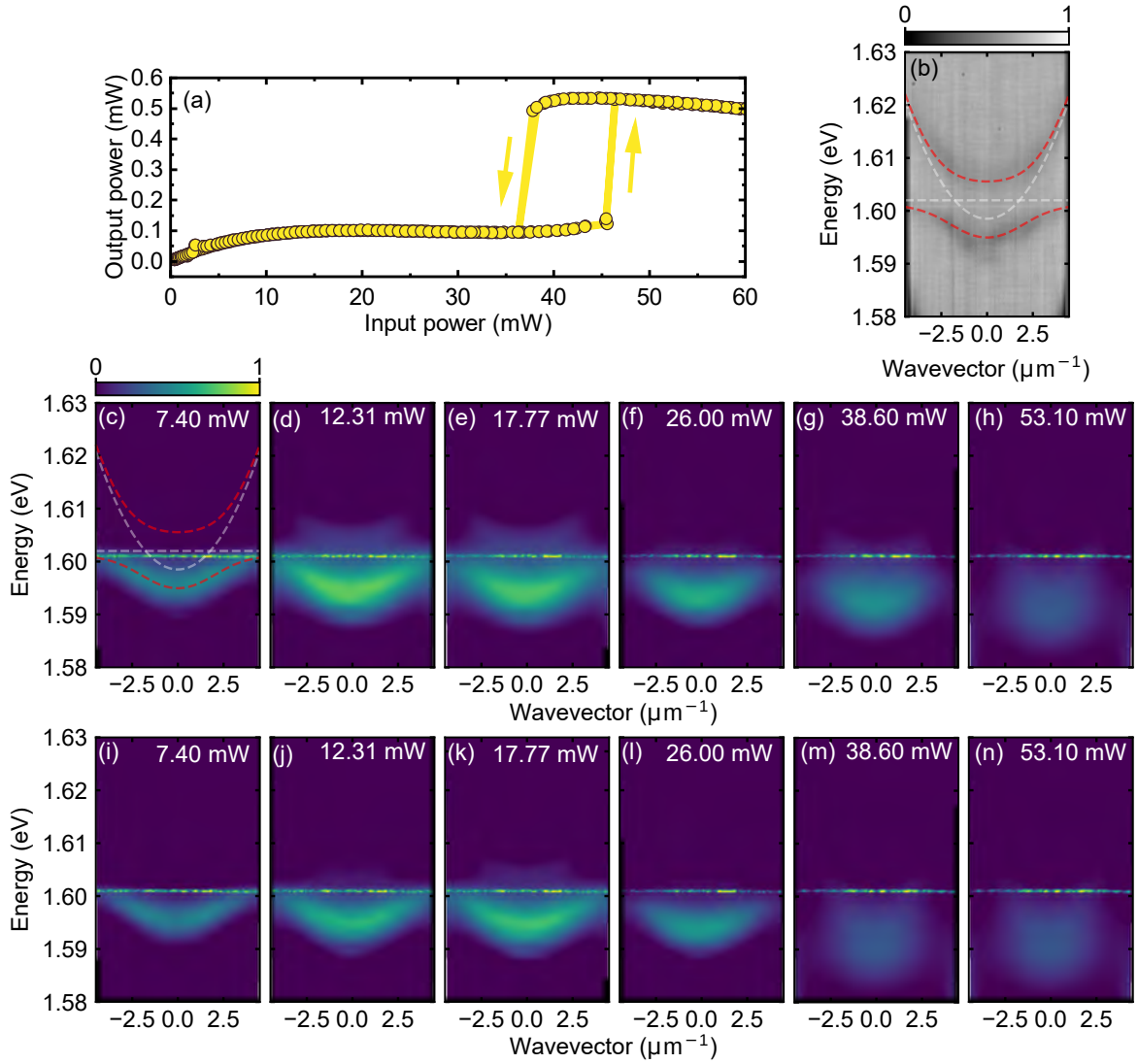

Figure 4.12: **Polariton dispersion relations under quasi-resonant laser transmission, for the laser energy above the lower polariton mode.** (a) Input-output power characteristic for positive laser detuning, showing optical bistability with a counterclockwise hysteresis loop. (b) White-light reflectivity map with applied coupled-oscillator model. (c)–(h) Corresponding photoluminescence dispersion maps collected for increasing laser power. (i)–(n) PL maps obtained for the reverse sweep (decreasing power).

The dispersion maps collected at selected laser powers along the input-output characteristic, on both the increasing and decreasing power sweeps, reveal how the polariton modes evolve with respect to the fixed laser energy. The photoluminescence observations show that with the laser energy detuned below the lower polariton branch, the emerging clockwise hysteresis corresponds to the transition between the strong and weak coupling regimes. This means

that each of the bistable states of the hysteresis differs by the presence or absence of strong coupling in the system.

The last investigated configuration corresponded to the transmitted laser energy tuned above the minimum of the lower polariton branch with $\Delta = 6.5$ meV. The collected input-output power characteristic is shown in Fig. 4.12(a). In this case, the hysteresis loop exhibited a counterclockwise orientation, with two well-defined states of high and low transmission. As the laser power increased, the system remained in the low-transmission state from 0 mW up to about 45 mW, after which it switched to the high-transmission state. While decreasing the laser power, the return to the low-transmission state occurred around 26 mW, thereby forming a hysteresis loop.

The corresponding white-light reflectivity map is shown in Fig. 4.12(b). Two modes are clearly visible, the lower polariton around 1.595 eV and the upper polariton near 1.61 eV. A coupled-oscillator model was applied to this map, allowing determination of the photon-exciton detuning of -3.5 meV. During photoluminescence measurements with the laser transmitted through the sample, a crossed polarizer was used to suppress the laser intensity. As in previous measurements, the maps were intensity normalized, since different filters and acquisition times were used, and the focus of the analysis was on the curvature of the dispersion rather than the signal intensity.

Figures 4.12(c)–(g) present photoluminescence maps collected while increasing the laser power, but still along the lower-transmission branch of the input-output characteristic. In Fig. 4.12(c), taken at 7.40 mW, the emission was well described by the coupled-oscillator model obtained from the reflectivity map. At this power, only the emission from the lower polariton was observed. In Fig. 4.12(d), measured at 12.31 mW, an additional weak signal from the upper polariton appeared at higher energies. A redshift of both modes was also observed. The trend continued in Fig. 4.12(e), collected at 17.77 mW, and in Fig. 4.12(f), taken at 26 mW, with both polariton modes shifting further to lower energies. A significant change occurred in Fig. 4.12(g), collected at 38.60 mW. The lower polariton shifted substantially to lower energy, and its curvature changed compared to previous measurements, while the upper polariton remained visible. As can be seen, at this input power the upper polariton is in resonance with the laser energy. At 53.10 mW [Fig. 4.12(h)], corresponding to the high-transmission state of the input-output characteristic, the modes shifted further to lower energies, and the laser energy was higher than the upper polariton, at $k = 0$. Additionally, the linewidth of the lower polariton mode broadened, its curvature significantly changed, and the emission intensity weakened at high emission angles. All of these effects can again be attributed to heating at higher excitation powers.

The same set of measurements was performed while decreasing the laser power incident on the sample. Figures 4.12(i)–(n) show the dispersion maps collected for the same transmitted laser powers as in the increasing-power sequence. Starting from Fig. 4.12(n), collected at 53.10 mW, the dispersion corresponds to the high-transmission state and is identical to the map in Fig. 4.12(h). The following laser power of 38.60 mW corresponded to the bistable range. The emission spectra shown in Fig. 4.12(m) exhibited the same shape as in panel (n). Importantly, despite being collected at the same power as the map in panel (g), the visible difference shows that the system was in a different transmission state depending on the measurement sequence. The subsequent maps [Figs. 4.12(l)–(i)] lie outside the bistable power range. The photoluminescence maps correspond to those obtained in the increasing-power run

but collected in the reverse power ramp direction. They show a gradual recovery of the lower polariton energy back to its initial position. Finally, at 7.40 mW [Fig. 4.12(i)], the system returned to the original configuration of the lower polariton mode, similar to the map shown in panel (c).

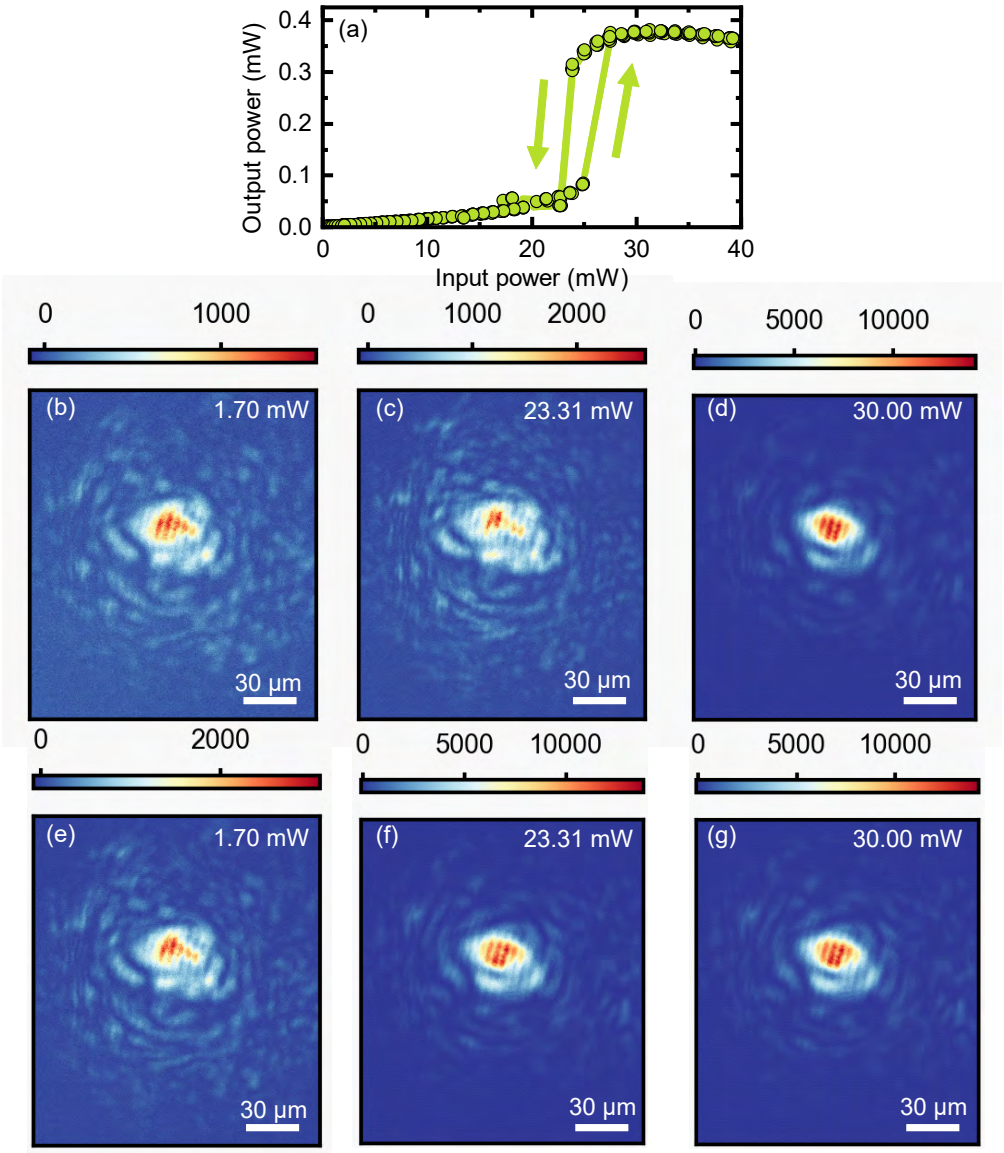

Figure 4.13: **Real-space emission measurements collected with the laser tuned above the lower polariton branch at $\Delta = 5.5$ meV.** (a) Input-output power characteristic of transmitted laser for the laser tuned above the lower polariton branch, showing a counterclockwise hysteresis loop. (b)–(d) Real-space emission maps collected at 1.7 mW, 23.31 mW, and 30 mW during the power-increasing scan, illustrating the transition from the low- to the high-transmission branch. (e)–(g) Corresponding maps obtained at the same powers during the power-decreasing scan.

These measurements demonstrate that, in the regime of optical bistability with counterclockwise hysteresis, thermal effects also play a key role, inducing a redshift of the polariton modes and spectral broadening. The switching to the high-transmission state occurs when the laser energy crosses the upper polariton branch.

Additional measurements were performed in real-space emission under quasi-resonant excitation. To extend the observation area, the focusing lens was replaced with a focal length of $f = 75$ mm. All of the incident laser light was fully blocked off by the appropriate filters. Specifically, when the laser energy was tuned below the minimum of the lower polariton branch, a short-pass filter was used, which allowed observation of emission from both the lower and the upper polariton (presented in Fig. 4.15). Similarly, for excitation at the minimum, both branches were visible, with the signal from the lower polariton dominating at larger wavevectors (Fig. 4.14). In contrast, when the laser energy was set above the lower polariton minimum, the laser signal was suppressed by a long-pass filter, transmitting only the emission from the lower polariton while cutting off the contribution from the upper branch (Fig. 4.13). The measurements focused on comparing the photoluminescence within the bistable regime, examining how the emission behaved at the same excitation power depending on whether the measurement was performed during the increase or the decrease of the laser power.

In the first measurement, the laser energy was tuned above the lower polariton branch at $\Delta = 5.5$ meV. As shown in Fig. 4.13(a), the input-output power characteristic shows the formation of a hysteresis loop with a counterclockwise orientation. During the increase of laser power, the transmission gradually rose up to about 25 mW, followed by a sudden switch from the low- to the high-transmission branch. The return to the low-transmission state occurred around 23 mW, thereby forming the hysteresis loop.

Figures 4.13(b)–(d) present real-space emission maps collected during power increase scan. The data correspond to three excitation powers: 1.7 mW, within the low-transmission state, 23.31 mW, still in the low-transmission state and at 30 mW, after switching to the high-transmission state. As can be seen, the real-space patterns were similar within the same transmission state. In addition, interference fringes appeared in this regime, whose origin is not yet fully understood. They are suspected to arise either from phase coupling within the emission itself or from interference between the transmitted laser and the emission. In the high-transmission state, the emission became more spatially localized, while the interference fringes remained visible.

Figures 4.13(e)–(g) show the emission maps collected at the same excitation powers during the power-decreasing scan. Importantly, the emission map collected at 23.31 mW, within the bistable region, shows clear differences in the real-space patterns, depending on the direction of the power ramp. The low- and high-transmission states are thus distinguishable also by their real space emission profiles.

The second analyzed real-space measurement series corresponded to the case where the laser energy was tuned exactly to the minimum of the lower polariton branch ($\Delta = 0.0$ meV). The input-output power characteristic shown in Fig. 4.14(a), featured a drop in transmission around 11 mW, but no hysteresis loop was observed in this measurement. The response of the system was the same, regardless of whether the measurement was performed during the increase or decrease of the laser power.

Figures 4.14(b)–(d) present spatial emission maps collected for three selected excitation powers (1.84 mW, 8.87 mW, and 26 mW) during the power increasing scan. The emission

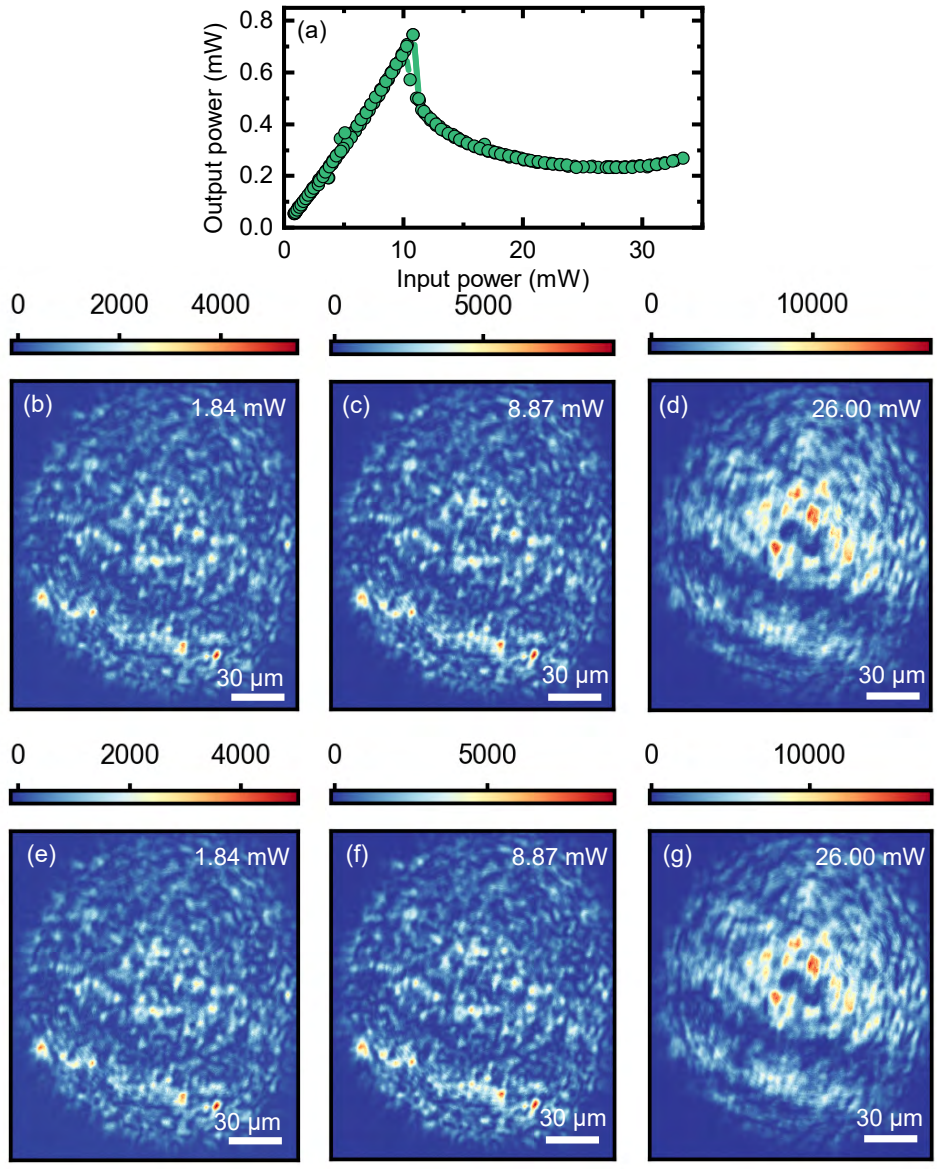

Figure 4.14: **Real-space emission measurements collected with the laser tuned to the lower polariton branch at $\Delta = 0.0$ meV.** (a) Input-output power characteristic of transmitted laser for the laser tuned to the minimum of the lower polariton branch, showing a nonlinear transmission response regime without hysteresis. (b)–(d) Real-space emission maps collected at 1.84 mW, 8.87 mW, and 26 mW during the power-increasing scan. (e)–(g) Corresponding maps obtained at the same powers during the power-decreasing scan.

profile in Fig. 4.14(b) consisted of randomly distributed, densely packed, small ($< 5\,\mu$m) emission spots. The emission intensity increased with the incident laser power in Fig. 4.14(c), but preserved the spatial profile. However, the spatial emission pattern changed significantly at powers above 11 mW [Fig. 4.14(d)] (corresponding to the intensity drop in input-output

curve). Figures 4.14(e)–(g) show the corresponding emission maps collected at the same powers but during the power-decreasing scan, starting from 35 mW. No significant differences were observed between the maps obtained at the same excitation powers in the two scan directions.

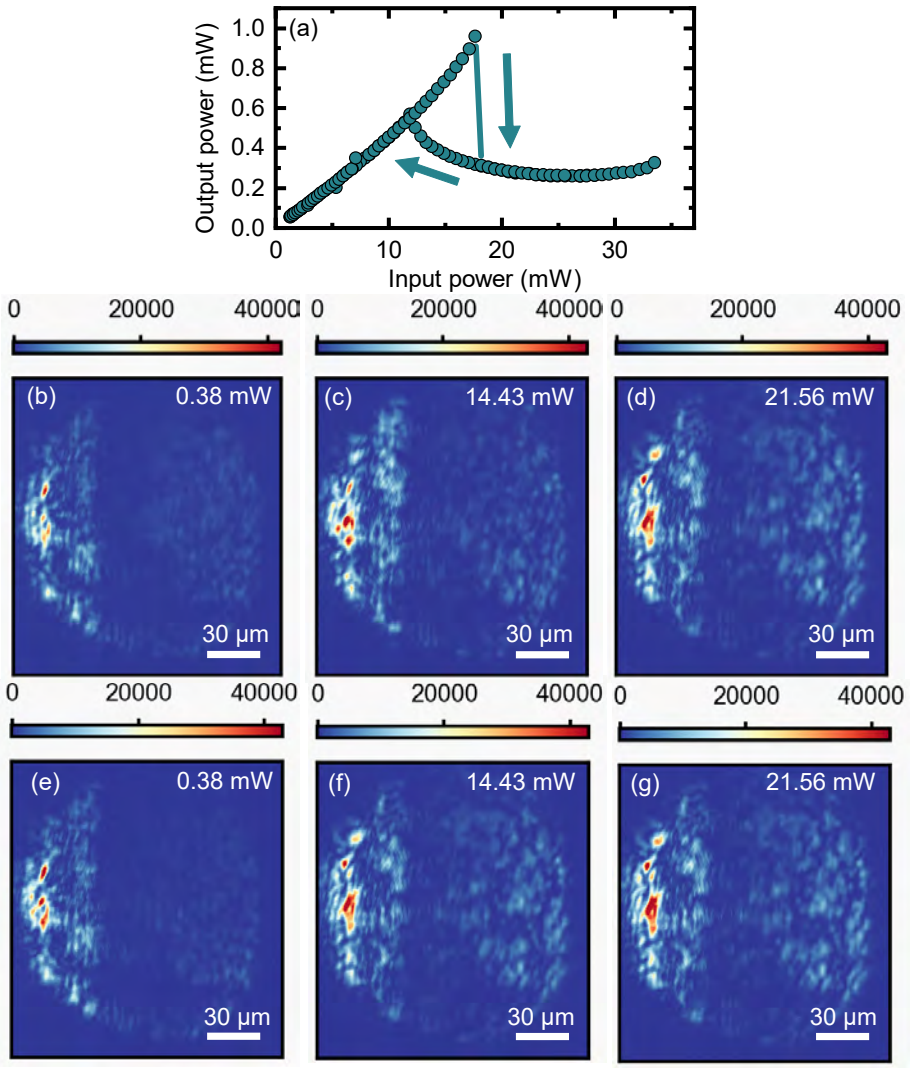

Figure 4.15: **Real-space emission measurements collected with the laser tuned below the lower polariton branch at $\Delta = -1.5$ meV.** (a) Input-output power characteristic of transmitted laser for the laser detuned below the lower polariton minimum, showing the formation of a clockwise hysteresis loop. (b)–(d) Real-space photoluminescence maps collected at 0.38 mW, 14.43 mW, and 21.56 mW during the power-increasing scan. (e)–(g) Corresponding maps obtained at the same powers during the power-decreasing scan.

Figure 4.15(a) shows the last input-output power characteristic collected for a laser detuned below the lower polariton minimum at $\Delta = -1.5$ meV. During the increase of laser power, a

linear growth of transmission was observed up to approximately 17 mW, followed by a sudden drop to a lower-transmission branch. When the power was decreased, the transmitted signal did not follow the same trajectory, but remained on the lower-transmission returning to the linear dependence at 13 mW.

Figures 4.15(b)–(d) present the real-space photoluminescence collected at three representative excitation powers of the transmitted laser: at 0.38 mW, corresponding to the linear increase of transmission, at 14.43 mW, still within the linear regime and at 21.56 mW, where the system followed the lower-transmission state. With the change of excitation power, a brightening of the potential minima on the sample was observed for the two lower powers. After the rapid transmittance drop, the emission pattern switched, with enhanced luminescence originating from different regions on the sample. Figs. 4.15(e)–(g) show analogous measurements collected for the same laser powers but during a gradually decreasing laser power scan. For the emission maps collected at 14.43 mW, depending on the scan direction (increasing or decreasing laser power), the emission maps exhibited distinct patterns, reflecting whether the measurement was performed on the high- or low-transmission branch.

Importantly, all three series of measurements were carried out at the same position on the sample, with the only parameter changed between the scans being the laser energy. This variation alone significantly altered the appearance of the real-space emission: from a strongly localized spot [Fig. 4.13], through a partially illuminated region [Fig. 4.15], to an entirely brightened real-space field [Fig. 4.14].

To summarize the experimental results, the k-space spectra track the evolution from strong to weak coupling in every bistability regime (depending on the Δ value) and the switch between the transmission states. The real-space maps confirm this by showing distinct spatial patterns at the same input power on the two sides of the hysteresis loop (and identical patterns in the no-hysteresis case). Together, these observations demonstrate that the two bistable states correspond to different coupling regimes, distinguished by the presence or absence of strong coupling.

4.4.3. Theoretical description of both types of optical bistability

The theoretical model describing the experimentally observed effects was proposed and developed by Dr. Andrzej Opala and Prof. Michał Matuszewski. The theory aiming to explain the appearance of two new types of hysteresis in a CdTe-based semiconductor optical microcavity system was based on the standard two-component model. This model is commonly used in polariton systems to describe Rabi splitting [115] and Rabi oscillations [116–119], Bose-Einstein condensation with long-range phase coherence [39], as well as nonlinear excitonic effects such as the formation of solitons [120,121] or the observation of multistability [122,123]. It has also been applied to the analysis of the propagation and dissipation processes in microcavities [124,125]. In this model, it is assumed that the pumping laser energy lies within the spectral range of the polariton mode energies.

The entire analysis aimed at creating a model that fully reproduces the observed effects began with the presentation of the standard two-component model, which couples the mean-field equations [126, 127] describing the evolution of the photonic and excitonic components of polaritons. These equations take the form:

$$\begin{aligned} \mathrm{i}\hbar\frac{\mathrm{d}}{\mathrm{d}t}\psi_{\mathrm{C}} &= \left(E_{\mathrm{C}}(\mathbf{k}) - \mathrm{i}\hbar\gamma_{\mathrm{C}}\right)\psi_{\mathrm{C}} + \frac{\hbar\Omega_{\mathrm{R}}}{2}\psi_{\mathrm{X}} + F\mathrm{e}^{-\mathrm{i}\omega_{\mathrm{L}}t}, \\ \mathrm{i}\hbar\frac{\mathrm{d}}{\mathrm{d}t}\psi_{\mathrm{X}} &= \left(E_{\mathrm{X}}(\mathbf{k}) - \mathrm{i}\hbar\gamma_{\mathrm{X}} + g_{\mathrm{X}}|\psi_{\mathrm{X}}|^2\right)\psi_{\mathrm{X}} + \frac{\hbar\Omega_{\mathrm{R}}}{2}\psi_{\mathrm{C}}, \end{aligned} \tag{4.2}$$

where $E_{\mathrm{C}}(\mathbf{k}) = E_{\mathrm{C}}^0 + \frac{\hbar^2\mathbf{k}^2}{2m_{\mathrm{C}}^*}$ is the dispersion relation of cavity photon, and $E_{\mathrm{X}}(\mathbf{k}) = E_{\mathrm{X}}^0 + \frac{\hbar^2\mathbf{k}^2}{2m_{\mathrm{X}}^*}$ is the dispersion relation of excitonic states in the quantum well. The parameters γ_{C} and γ_{X} represent the loss coefficients of the photonic and excitonic components, respectively. The Rabi splitting $\hbar\Omega_R$ describes the coupling strength between photons and excitons, while the term $Fe^{-\mathrm{i}\omega_{\mathrm{L}}t}$ corresponds to the external pumping of the system, with F determining the amplitude of the laser pump and $E_{\mathrm{L}} = \hbar\omega_{\mathrm{L}}$ the pump energy. Moreover, the parameter g_{X} denotes exciton-exciton interactions strength, originating from Kerr-type third-order nonlinearities. This contribution was crucial for describing the standard bistability known from microcavity systems based on group III-V materials [93].

Calculations were performed to determine the system response to laser excitation by solving Eqs. (4.2) and analyzing the steady-state density of the photonic component, $|\psi_{\mathrm{C}}^{\mathrm{SS}}|^2$, which is proportional to the transmitted optical intensity. In this model, the laser field amplitude F was slowly increased from zero to a chosen maximum value and then decreased back to zero, which allowed to obtain complete hysteresis loop.

Figure 4.16(a) shows the result obtained for the laser energy close to the lower polariton branch ($\Delta = 2.09$ meV). In this case, a typical S-shaped hysteresis loop was obtained, formed between the pump field (laser power) and the photonic response. This dependence is known in the literature and has been analyzed both theoretically and experimentally [40, 90, 93]. Although this hysteresis may appear similar to that experimentally observed square-shaped loop with a counterclockwise orientation, it is not a correct description of the experimental results. It will be obvious when we investigate different laser energies, leading to predictions contrary to the experimental results.

Figure 4.16(b) presents the results of the model obtained for a pumping laser energy located slightly above the upper polariton branch ($\Delta = 12.34$ meV). For this detuning, an unusual triangular hysteresis loop with a counterclockwise orientation was obtained. This result was not observed experimentally for such a laser detuning between the lower polariton mode.

The appearance of this hysteresis was explained by a nonlinear blueshift induced by exciton-exciton interactions. Figs. 4.16(c,d) show the calculated polariton dispersions for two laser pump amplitudes: (c) lower F_1 and (d) higher F_2. For low input power (c), the shift $\Delta_{\mathrm{B}} = g_{\mathrm{R}}|\psi_{\mathrm{X}}^{\mathrm{SS}}|^2$ was insignificant and the energy difference between the photon and exciton modes at $\mathbf{k} = 0$ was about 2 meV. The solid red lines indicate analytically determined dispersions of the lower and upper polaritons, including the exciton energy shift, and the dashed orange lines indicate the positions of the uncoupled photon and excitonic modes. Panel (d) shows the situation for higher laser power, where a significant blueshift strongly modified the polariton branches.

Furthermore, Fig. 4.16(e) shows the Hopfield coefficients C_{U} and X_{U}, which describe the photonic and excitonic fractions of the upper polariton [128]. It was calculated that for the larger laser power F_2, the upper polariton becomes significantly more excitonic, with the excitonic fraction at $\mathbf{k} = 0$ being higher by about 0.26 compared to the F_1 case. This explains the observed decrease in photonic density with increasing laser power. What can be also seen in Fig. 4.16(a), when a laser energy was closer to the lower polariton minimum, the opposite mechanism was observed, leading to an enhancement of the photonic component.

The triangular hysteresis loop shown in Fig. 4.16(b) was thus interpreted as an effect of the change in polariton composition with increasing laser power.

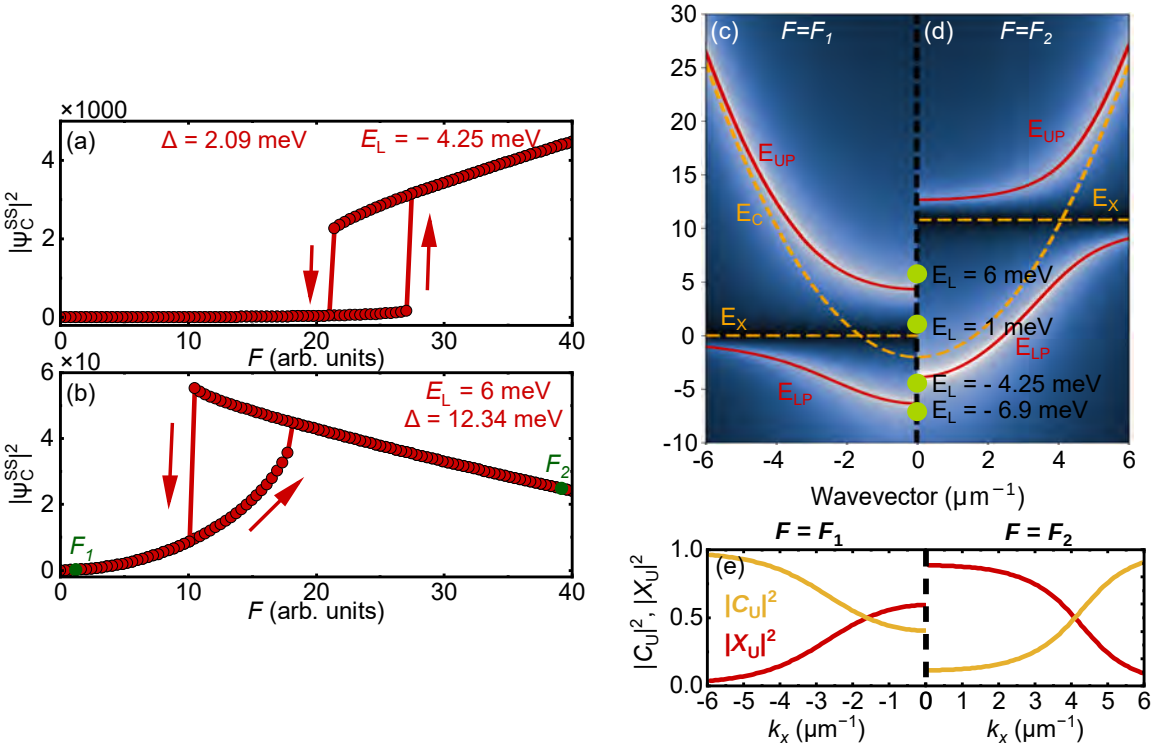

Figure 4.16: **Theoretical simulations of optical bistability in a microcavity system with nonlinearities from exciton-exciton interactions.** (a) Calculated input-output characteristic for a pump energy close to the lower polariton branch ($E_{\mathrm{L}} = -4.25$ meV, $\Delta = 2.09$ meV), showing a typical S-shaped hysteresis loop. (b) Input-output characteristic for a higher value of laser energy ($E_{\mathrm{L}} = 6$ meV, $\Delta = 12.34$ meV), resulting in a triangular hysteresis loop with a counterclockwise orientation. (c,d) Calculated polariton dispersions at two laser pump amplitudes: (c) low F_1, where the blueshift Δ_{B} is insignificant, and (d) higher F_2, where a significant blueshift modifies the polariton branches. (e) Hopfield coefficients of the upper polariton, showing the increase of the excitonic fraction for larger laser amplitudes.

As can be seen, the initially proposed model successfully reproduced the effects observed in strongly coupled polariton systems that exhibit Kerr-like nonlinearities. However, it fails for the hysteresis loops observed in this CdTe-based transmissive microcavity. Therefore, in order to reproduce the experimentally observed characteristics, the model was extended to

include additional effects.

Specifically, the redshift of the polariton modes induced by thermal processes, as well as the transition of the system from the strong to the weak coupling regime through a reduction of the Rabi splitting [124] $\hbar\Omega_R$. The modified equations take the form:

$$\begin{aligned} \mathrm{i}\hbar\frac{\mathrm{d}}{\mathrm{d}t}\psi_\mathrm{C} &= (\tilde{E}_\mathrm{C} - \mathrm{i}\hbar\gamma_\mathrm{C})\psi_\mathrm{C} + \frac{\hbar\tilde{\Omega}}{2}\psi_\mathrm{X} + F\mathrm{e}^{-\mathrm{i}\omega_\mathrm{L}t}, \\ \mathrm{i}\hbar\frac{\mathrm{d}}{\mathrm{d}t}\psi_\mathrm{X} &= (\tilde{E}_\mathrm{X} - \mathrm{i}\hbar\gamma_\mathrm{X} + g_\mathrm{X}|\psi_\mathrm{X}|^2)\psi_\mathrm{X} + \frac{\hbar\tilde{\Omega}}{2}\psi_\mathrm{C}. \end{aligned} \tag{4.3}$$

In this extended two-component model, the effective photon dispersion $\tilde{E}_\mathrm{C}$ and exciton dispersion $\tilde{E}_\mathrm{X}$ include a correction for the redshift induced by thermal effects [129,130]. It was assumed that the thermal effects scale quadratically with the laser pump amplitude, leading to the equations:

$$\begin{aligned} \tilde{E}_\mathrm{C} &= E_\mathrm{C} - \beta_\mathrm{C}|F|^2, \\ \tilde{E}_\mathrm{X} &= E_\mathrm{X} - \beta_\mathrm{X}|F|^2, \end{aligned} \tag{4.4}$$

where β_C and β_X are phenomenological coefficients that describe the strength of thermal effects. Although phenomenologically both modes shift by similar amounts ($\beta_\mathrm{C} \approx \beta_\mathrm{X}$) for a given pump power, in real semiconductor materials these values may differ significantly depending on the material properties [129].

The model was further extended by adding a decrease of the Rabi splitting, which leads to a gradual loss of strong coupling at high exciton densities with high laser powers. This effect arises from phase-space filling (Pauli exclusion principle) [126]. The effective Rabi frequency was therefore written as:

$$\tilde{\Omega} = \Omega_\mathrm{R}^0\,\mathrm{e}^{-(\beta_1 n_\mathrm{R} + \beta_2|\psi_\mathrm{X}|^2)}, \tag{4.5}$$

where $|\psi_\mathrm{X}|^2$ denotes the coherent exciton density and $n_\mathrm{R} \approx \alpha\,\dfrac{|F|^2}{\gamma_\mathrm{X}}$ describes the density of incoherent, thermally excited carriers. Here, α is a scaling parameter and Ω_R^0 is the bare Rabi splitting in the absence of saturation. The coefficient β_1 defines the influence of incoherent carriers, while β_2 describes the role of coherent carriers with loss of strong coupling.

Figure 4.17 presents the optical bistability characteristics with hysteresis loops obtained from the extended model described by Eqs. (4.3). In this extended model, the main source of nonlinearity was assumed to be the loss of strong coupling, rather than exciton-exciton interactions as in the standard model. This condition is satisfied when $g_\mathrm{X} \ll \beta_2\Omega_\mathrm{R}$. In Fig. 4.17(a), optical bistability with a hysteresis loop is shown for a pump energy close to the upper polariton branch ($\Delta = 7.34$ meV, $E_\mathrm{L} = 1$ meV). The loop shape and counterclockwise orientation correspond to the experimental results obtained for excitation near the upper polariton branch [as shown in Fig. 4.8(b)]. In Fig. 4.17(b), optical bistability with a clockwise hysteresis loop is observed for a laser energy below the lower polariton branch ($E_\mathrm{L} = -6.9$ meV, $\Delta = -0.55$ meV). In this case, a triangular hysteresis loop was obtained, where a rapid depletion of the photonic field density above the critical laser power led to a drop into a lower transmission state. This type of bistability is attributed to the dominant contribution of loss

of the strong coupling in the system, compared to exciton-exciton interactions, together with the thermally induced redshift of the photon and exciton modes.

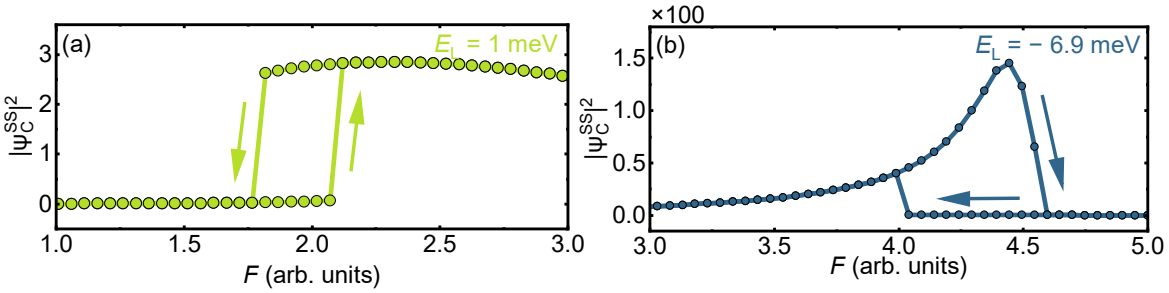

Figure 4.17: **Optical bistability in the extended two-component model.** (a) Calculated input-output characteristic for a pump energy close to the upper polariton branch ($\Delta = 7.34$ meV, $E_L = 1$ meV), showing a counterclockwise hysteresis loop consistent with the experimental observations. (b) Input-output characteristic for a pump energy below the lower polariton branch ($\Delta = -0.55$ meV, $E_L = -6.9$ meV), displaying a triangular hysteresis loop with clockwise orientation.

The extension of the standard two-component model by including experimentally observed effects such as the thermally induced redshift of polariton modes and the reduction of the Rabi splitting enabled reproduction of the hysteresis loops observed in the experiment. The modified model captures the transition between strong and weak coupling regimes, as well as explains the appearance of unconventional hysteresis shapes and their orientation. This demonstrates that thermal effects and phase-space filling effects play a role in determining the nonlinear response from the CdTe-based transmissive microcavity system, which extends the range of optical bistability types observed so far in microcavity systems.

4.5. Observation of exceptional points during the transition of the system from strong to weak coupling regime

Optical microcavities are lossy systems in which photons and excitons exhibit limited lifetime. Such a system can therefore be described by a non-Hermitian Hamiltonian where loss or gain are introduced via imaginary parts of the energy. Non-Hermitian systems allow for a specific degeneracies in parameter space, exceptional points (EPs), where not only the eigenvalues (energies) but also the eigenvectors (states) coalesce. EPs are also characterized with specific, winding topology, resembling a Möbius strip. After an adiabatic encirclement of an EP the state switches to the other branch, and only two full loops return it to the initial state.

In the theory proposed by Dr. Andrzej Opala and Prof. Michał Matuszewski, it was shown that such exceptional points can arise naturally. This means that they can appear without intentional tuning loss imbalances or polarization degrees of freedom. In this case, natural exceptional points occur exactly at the boundary between strong and weak coupling regimes. Importantly, the EP does not coincide with the photon lasing threshold. The theoretical explanation of this naturally occurring exceptional point was the generation of so-called

Bogoliubov excitations (fluctuations on top of the polariton fluid). In this way the effective coupling strength can be weakened and encircle the EP in a two-parameter space spanned by the coupling strength and the particle wavevector.

The work considered a non-Hermitian model of two polariton modes:

$$\hat{H} = \begin{pmatrix} E_{\mathrm{C}} - \mathrm{i}\hbar\gamma_{\mathrm{C}} & \frac{\hbar}{2}\Omega_{\mathrm{R}} \\ \frac{\hbar}{2}\Omega_{\mathrm{R}} & E_{\mathrm{X}} - \mathrm{i}\hbar\gamma_{\mathrm{X}} \end{pmatrix}, \tag{4.6}$$

where $E_{\mathrm{C}}(\mathbf{k}) \approx E_{\mathrm{C}}^0 + \dfrac{\hbar^2 k^2}{2m_{\mathrm{C}}}$ denotes the dispersion of the cavity photon, $E_{\mathrm{X}}(\mathbf{k})$ is the (approximately flat) exciton dispersion, $\hbar\Omega_{\mathrm{R}}$ is the Rabi splitting, and γ_{C} and γ_{X} are the photon and exciton loss rates, respectively.

The eigenenergies of this Hamiltonian are

$$E_{\pm} = \frac{1}{2}\Big(E_{\mathrm{C}} + E_{\mathrm{X}} - \mathrm{i}\hbar(\gamma_{\mathrm{X}} + \gamma_{\mathrm{C}}) \pm \sqrt{\left(\delta - \mathrm{i}\hbar(\gamma_{\mathrm{C}} - \gamma_{\mathrm{X}})\right)^2 + (\hbar\Omega_{\mathrm{R}})^2}\Big), \quad \delta(\mathbf{k}) = E_{\mathrm{C}}(\mathbf{k}) - E_{\mathrm{X}}(\mathbf{k}), \tag{4.7}$$

where the real part $\mathrm{Re}(E_{\pm})$ sets the positions of the energy branches, with the imaginary part $\mathrm{Im}(E_{\pm})$ - the decay rate that describes their losses.

From these expressions it follows that an anticrossing (characteristic for strong coupling regime) occurs when:

$$\Omega_{\mathrm{R}} > |\gamma_{\mathrm{C}} - \gamma_{\mathrm{X}}|, \tag{4.8}$$

and an exceptional point appears precisely when the square root in the eigenenergies vanishes at zero detuning, i.e.,

$$\Omega_{\mathrm{R}} = |\gamma_{\mathrm{C}} - \gamma_{\mathrm{X}}| \quad \text{and} \quad \delta = 0. \tag{4.9}$$

The Hamiltonian also implies that the EP is unrelated to the photon lasing threshold. Lasing requires positive feedback and gain exceeding losses, whereas the Hamiltonian describes even vacuum fluctuations. This distinction is consistent with theoretical predictions [131, 132].

The dynamics of a coherently pumped system are governed by

$$\mathrm{i}\hbar\frac{\mathrm{d}}{\mathrm{d}t}\psi_{\mathrm{C}} = (E_{\mathrm{C}}(\mathbf{k}) - \mathrm{i}\hbar\gamma_{\mathrm{C}})\psi_{\mathrm{C}} + \frac{\hbar\tilde{\Omega}_{\mathrm{R}}}{2}\psi_X + F\,\mathrm{e}^{-\mathrm{i}\omega_p t}, \tag{4.10}$$

and

$$\mathrm{i}\hbar\frac{\mathrm{d}}{\mathrm{d}t}\psi_{\mathrm{X}} = (E_{\mathrm{X}}(\mathbf{k}) - \mathrm{i}\hbar\gamma_{\mathrm{X}})\psi_{\mathrm{X}} + \frac{\hbar\tilde{\Omega}_{\mathrm{R}}}{2}\psi_{\mathrm{C}} + g_{\mathrm{X}}|\psi_{\mathrm{X}}|^2\psi_{\mathrm{X}}. \tag{4.11}$$

Here, $F\mathrm{e}^{-i\omega_p t}$ is a coherent laser pump at frequency ω_p, and g_{X} represents the exciton-exciton nonlinearity, which was negligible in the main analysis.

Experimentally, the effective coupling $\tilde{\Omega}_{\mathrm{R}}$ was observed to decrease with increasing laser power, i.e., with increasing reservoir density due to saturation (phase-space filling and formation of an incoherent reservoir). To first order,

$$\tilde{\Omega}_{\mathrm{R}} = \Omega_{\mathrm{R}}^0\Big(1 - \beta n_{\mathrm{R}}\Big) \approx \Omega_{\mathrm{R}}^0\left(1 - \frac{\beta}{\gamma_{\mathrm{R}}}|F|^2\right), \tag{4.12}$$

where n_{R} is the reservoir density and γ_{R} its decay rate. Thus, by increasing the pump power $|F|^2$ one can optically reduce $\tilde{\Omega}_{\mathrm{R}}$.

Next, by analyzing small fluctuations (Bogoliubov excitations) on top of the fluid and moving to a frame rotating with ω_p, one obtains the Hamiltonian:

$$\hat{H}_{\mathrm{Bog}} = \begin{pmatrix} E_{\mathrm{C}}(k) - \hbar\omega_p - \mathrm{i}\hbar\gamma_{\mathrm{C}} & \frac{\hbar}{2}\tilde{\Omega}_{\mathrm{R}} \\ \frac{\hbar}{2}\tilde{\Omega}_{\mathrm{R}} & E_{\mathrm{X}} - \hbar\omega_p - \mathrm{i}\hbar\gamma_{\mathrm{X}} \end{pmatrix}. \tag{4.13}$$

Structurally, this is the same model as the Hamiltonian introduced above, but with the parameter $\tilde{\Omega}_{\mathrm{R}}$ and an overall energy shift by $\hbar\omega_p$. Therefore, the Bogoliubov excitations inherit the EP and the transition between strong and weak coupling regimes.

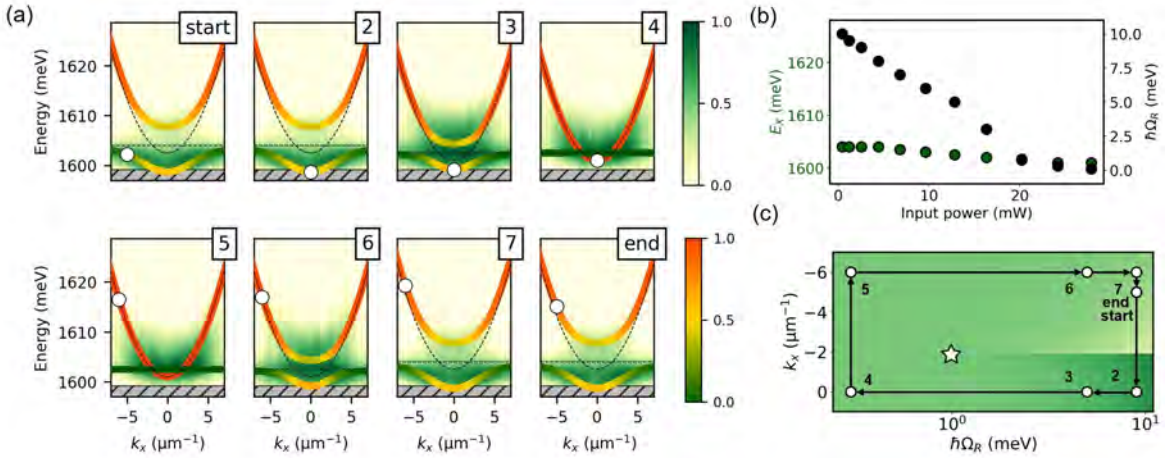

Figure 4.18: **Natural exceptional point appearing between strong and weak coupling regimes via optical tuning.** (a) Momentum-space photoluminescence under resonant excitation at the minimum of the lower polariton branch for increasing laser power. Colored thick curves are fits to the two polariton branches and color encodes Hopfield coefficient. As the power increases, the effective coupling $\tilde{\Omega}_{\mathrm{R}}$ decreases, and the system passes through the vicinity of the EP into the weak coupling regime. Reducing the power restores strong coupling and mode splitting. (b) Parameters extracted from fits with increasing laser power, coupling strength $\tilde{\Omega}_{\mathrm{R}}$ and exciton energy E_{X}. (c) Trajectory in $(k, \tilde{\Omega}_R)$ encircling the EP (white star). A single loop transfers the state between polariton branches, whereas two loops return it to the initial branch.

The geometry of the spectrum near an EP resembles a two-sheeted Riemann surface on which the two branches glue together at the exceptional point. Encircling the EP along a loop in the parameter space of the wavevector and the coupling $\tilde{\Omega}_{\mathrm{R}}$, a single full loop transfers the state to the other branch, and only after two full loops the state returns to the initial position.

Figure 4.18(a) shows photoluminescence maps in reciprocal space under resonant excitation with the laser set at the minimum of the lower polariton, for different laser powers. In the experiment associated with the observation of the new type of optical bistability, it was noticed that increasing the power of the laser transmitted through the microcavity led to the loss of

strong coupling. This revealed an additional degree of control over the coupling strength via the excitation power, which was subsequently utilized to probe exceptional points. As the power increases, the effective coupling $\tilde{\Omega}_{\mathrm{R}}$ decreases, as was already demonstrated in main part of this Chapter. The colored thick curves overlaid on the maps correspond to fits of the energies of the two polariton branches, with the color indicating the photonic Hopfield coefficient. At low power a clear branch splitting characteristic of strong coupling is observed. With increasing power, the splitting diminishes; the system passes through the vicinity of the EP into the weak-coupling regime, seen as branch crossing as for non-interacting modes. Reducing the power restores strong coupling and the mode splitting.

Figure 4.18(b) presents the values of $\tilde{\Omega}_{\mathrm{R}}$ and the exciton energy E_{X}, extracted from fits to the experimental data, as functions of increasing laser power. One can tune $\tilde{\Omega}_{\mathrm{R}}$ by more than an order of magnitude using the laser power alone, whereas E_{X} shows no significant energy shift. Hence, the spectral changes arise not from an energy shift but from a weakening of the coupling strength.

Encircling of the exceptional point in this system is shown in Fig. 4.18(c), which presents a visualization in the $(k, \tilde{\Omega}_{\mathrm{R}})$ plane with a loop whose points correspond to the white circles in Fig. 4.18(a). The white star marks the position of the EP. The dispersion maps in panel (a) are labelled with the same numbers as the points in panel (c). Starting from the map marked "start", where the white circle lies on the lower polariton branch at $k \approx -5\ \mu\mathrm{m}^{-1}$, the corresponding position in panel (c) is also labeled "start". As the laser power increases from maps "2" to "4", the white circle shifts to $k = 0$, while the coupling strength $\tilde{\Omega}_{\mathrm{R}}$ decreases and eventually vanishes, leading to a transition from the polaritonic anticrossing to the crossing of bare photon and exciton modes (weak coupling). In map "5" the system remains in the weak-coupling regime, but the white circle moves towards $k \approx -6\ \mu\mathrm{m}^{-1}$, as also indicated in panel (c). With further decrease of the laser power, $\tilde{\Omega}_{\mathrm{R}}$ increases again and the strong coupling regime is restored, visible in maps "6", "7", and "end". Importantly, after completing this closed trajectory around the exceptional point, the white circle ends up on the upper polariton branch in panel (a), even though in the $(k, \tilde{\Omega}_{\mathrm{R}})$ space of panel (c) it returns to the same point.

In summary, it was shown that by tuning the excitation power the effective coupling strength can be optically controlled, allowing the system to cross between strong and weak coupling regimes. It was demonstrated that this transition gives rise to a natural exceptional point, appearing without the need for engineered asymmetries or loss imbalance. The measurements revealed the collapse and reopening of the polariton splitting, and the trajectory in $(k, \tilde{\Omega}_{\mathrm{R}})$ space confirmed the characteristic topology of the EP, where one encirclement transfers the system from the lower to the upper polariton branch. In this way, experimental evidence was provided that Bogoliubov excitations can weaken the coupling and lead to the emergence of EPs, establishing CdTe-based microcavities as a platform for studying non-Hermitian physics and topological mode switching under fully optical control.

4.6. Observation of optical bistability from a redshift of photonic mode in CdTe-based microcavity

The main goal of these studies was to investigate the optical properties and strong coupling behavior of a simplified microcavity structure containing only a single quantum well. The results presented in this section concern measurements of a CdTe-based microcavity, not previously described in this thesis, grown as part of a separate project. It was the first microcavity structure containing a single 10 nm CdTe quantum well, grown by MBE by Prof. Wojciech Pacuski and M.Sc. Adam Szczerba, which exhibited strong coupling even after exfoliation and transfer onto a transparent substrate.

Unlike previously discussed samples containing multiple quantum wells, the presence of only one QW significantly affects several parameters of the system. In particular, it reduces the overall oscillator strength and thus the Rabi splitting compared to multi-QW structures. However, it also allows for a clearer interpretation of exciton-photon interactions, minimizes inhomogeneous broadening due to well-to-well variations, and provides a well-defined platform for studying the intrinsic properties of a single excitonic resonance. This makes the sample an important reference system for understanding the role of quantum well density in determining the strength of polariton coupling.

It was a CdMnTe/CdMgTe microcavity consisting of 25 pairs of Bragg reflector layers, with a $\lambda/2$ CdMgTe cavity containing a quantum well. A MgTe buffer layer was grown between the microcavity structure and the substrate, allowing the water exfoliation process and transfer onto a transparent substrate. After exfoliation, the microcavity operated in the strong coupling regime. As shown in Fig. 4.19(c), reflection map in reciprocal space revealed polariton modes. In the energy range from 1.615 eV to 1.620 eV, a signal originating from the lower polariton was observed, mainly within the in-plane wavevector range -2.5 μm^{-1} to 2.5 μm^{-1}. For energies above 1.620 eV, a signal from the upper polariton was visible in the wavevector range extending up to ± 4.5 μm^{-1}. The experimental data were modeled with a coupled-oscillator model, from which the Rabi splitting was determined as $\hbar\Omega = 6$ meV, with detuning $\delta = -5.2$ meV. A Lorentzian fit of the $k = 0$ cross-section yielded the lower polariton energy $E_{\mathrm{LP}} = 1.615$ eV and FWHM = 2.43 meV, giving a cavity quality factor of $Q = 665$.

The prepared microcavity was mounted in a cryostat and cooled down to 4.5 K. The first measurement was performed in a setup with two power meters, shown in Fig. 4.7, to study the total transmitted light intensity through the polariton modes. As presented in Fig. 4.19(a), scanning the laser energy around the lower polariton minimum revealed nonlinear behavior and optical bistability. The laser-lower polariton detuning values, labeled as Δ in the figure, define the position of the laser relative to the lower polariton minimum. A positive value indicates that the laser energy was above this minimum.

For $\Delta = 1.0$ meV, a nonlinear increase in transmission was observed, starting from the lowest laser powers on the input-output characteristic up to approximately 6 mW. When the laser was tuned exactly to the minimum ($\Delta = 0.0$ meV), first a linear increase in transmission was detected up to about 5 mW, above which the transmitted intensity remained flat. For negative detuning values, i.e., when the laser was tuned below the lower polariton energy, a hysteresis loop opened at the transition point between the two linear transmission regimes. Interestingly, the hysteresis exhibited a counterclockwise direction of formation, which had not

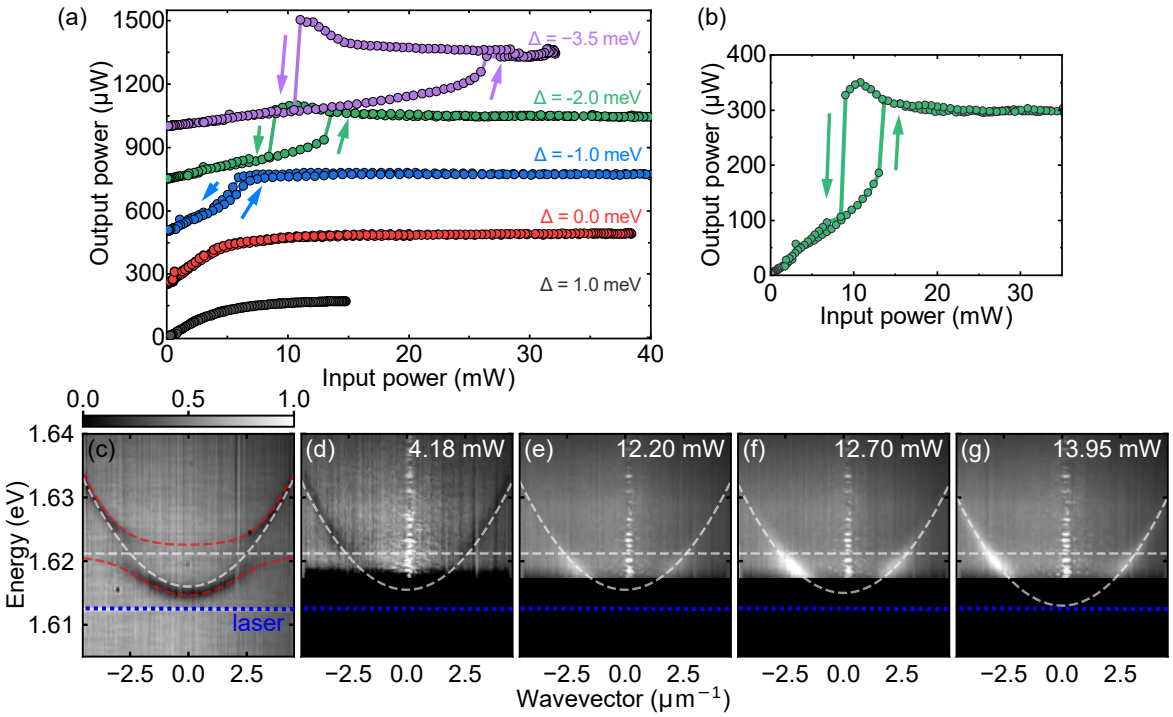

Figure 4.19: **Optical bistability and hysteresis in a CdTe-based transmissive microcavity with a single QW**. (a) Input-output power characteristics of the CdTe-based microcavity showing the creation of optical bistability at different laser detunings Δ relative to the lower polariton minimum. (b) Hysteresis loop collected at $\Delta = -2.0$ meV, with arrows indicating the switching direction. (c) Reciprocal space white-light reflectivity map of the microcavity with overimposed coupled-oscillator model (white dashed lines indicates bare photon and exciton modes, red dashed lines polariton modes). The dark-blue dashed line marks the laser energy. Extracted parameters from the modeling: Rabi splitting $\hbar\Omega = 6$ meV, detuning $\delta = -5.2$ meV, photon energy $E_{\mathrm{ph}} = 1.616$ eV, exciton energy $E_{\mathrm{ex}} = 1.621$ eV, and effective photon mass $m_{\mathrm{ph}} = 2.3 \times 10^{-5} m_{\mathrm{e}}$. (d)–(g) Reciprocal space maps at different laser powers showing the photon-like mode and its redshift due to thermal effects.

been observed in the previously described results. In the previously studied microcavity, tuning the laser below the lower polariton minimum led to a "triangular" hysteresis with a clockwise formation. However, here the hysteresis was not triangular but rather "square-shaped". For the more negative laser-polariton detuning, the bistable range grew.

To investigate this phenomenon in more depth, detailed measurements of the hysteresis at $\Delta = -2.0$ meV were performed, as shown in Fig. 4.19(b). In the power range from 0 to 13 mW, a linear increase in transmission was observed, after which the system switched to a higher-transmission state that persisted despite increasing laser power, with no further growth in transmission. When decreasing the laser power, transmission increased within the bistable range from about 13 mW to 11 mW, followed by a drop between 11 mW and 9.5 mW. Below 9.5 mW, the system switched back to the lower-transmission branch. The counterclockwise

direction of the hysteresis is indicated with arrows in the figure.

Next, quasi-resonant transmission measurements in reciprocal space were carried out. In Fig. 4.19(c), where the coupled-oscillator model was superimposed, the energy of the laser was additionally marked by a dark-blue dashed line. Spectral filters (SP) were used, as indicated by shaded regions from around 1.617 eV to the 1.605 eV in Figs. 4.19(d)–(g). Additionally, white-light illumination was applied from the reflection side to track the dispersion of the modes. Since emission from the sample was weak, simultaneous collection of emission and white-light reflection were possible. At 4.18 mW [Fig. 4.19(d)], corresponding to the lower-transmission state, the signal resembled the photon mode curvature rather than the polariton mode. At higher powers, still within the lower-transmission state [Figs. 4.19(e,f)], photoluminescence from the photon mode was observed, with the model fit showing a redshift of the mode energy, suggesting thermal effects in the system. In Fig. 4.19(g), collected after switching to the higher-transmission state, the photon mode energy dropped more abruptly, reaching the laser energy.

These results indicate that even at a relatively low laser power of 4.18 mW, the cavity was no longer operating in the strong coupling regime. This suggests that the observed hysteresis originates from transmission changes through the bare photon mode in the weak coupling regime crossing the energy of the incident laser.

4.7. Summary

The studies presented in this Chapter provide new insights into nonlinear phenomena in exciton-polariton systems. They demonstrate that optical bistability in optical microcavities can arise from mechanisms fundamentally different from the well-known description based on Kerr-type nonlinearities. The bistable response observed in this work originates from the interplay between thermal effects and a transition between strong and weak coupling regimes, revealing a qualitatively new form of nonlinear behavior in CdTe-based microcavities.

To enable direct access to transmission characteristics and allowing for precise tracing of input-output power dependencies, a transmissive CdTe-based microcavity was employed. This configuration, made possible by the development of a reliable lift-off approach, opened a new experimental pathway for exploring nonlinear polariton dynamics in II-VI semiconductor systems. The observations revealed two distinct novel types of hysteresis loops, whose properties could not be explained by the literature model based on polariton-polariton interactions. The additional momentum-resolved experimental results demonstrated a mechanism in which the two bistable states correspond to strong and weak coupling regimes. This conclusion was also confirmed by measurements in real space. Depending on the type of hysteresis loop, the transition between the low- and high-transmission states is accompanied by a switching between strong and weak coupling regimes, driven by thermally induced redshifts and a reduction of the Rabi splitting. The observed here bistability in CdTe-based microcavities arises not only from nonlinear interactions but also from a switching between strong and weak coupling regimes, mediated by thermal effects.

Theoretical modeling supported this interpretation, showing that the inclusion of thermal energy shifts and coupling reduction reproduces the experimentally observed hysteresis loops. The developed framework extends the understanding of bistability in polaritonic systems and

identifies temperature- and coupling-controlled mechanisms as new degrees of freedom for manipulating nonlinear optical responses.

In addition, the observed possibility of tuning the exciton-photon coupling strength with the incident laser power opened access to phenomena related to non-Hermitian physics. Specifically, exactly at the crossing between strong and weak coupling regimes the system exhibits Exceptional Point (EP), a spectral singularity unique for non-Hermitian systems. This work experimentally explored the nontrivial winding topology of EP by encircling it in momentum–coupling strength plane.

In a broader perspective, all of these findings establish CdTe-based transmissive microcavities as an experimental platform for studying and controlling nonlinear polariton phenomena. The discovered form of bistability enriches the landscape of polariton nonlinearities and may provide a basis for novel photonic functionalities such as optical switching, logic operations, and tunable polariton devices driven by coupling transitions. In addition, the effective tunability of the coupling strength opens the access to non-Hermitian physics.

Chapter 5

Magnetic field control of exciton-polaritons condensate supermode parity

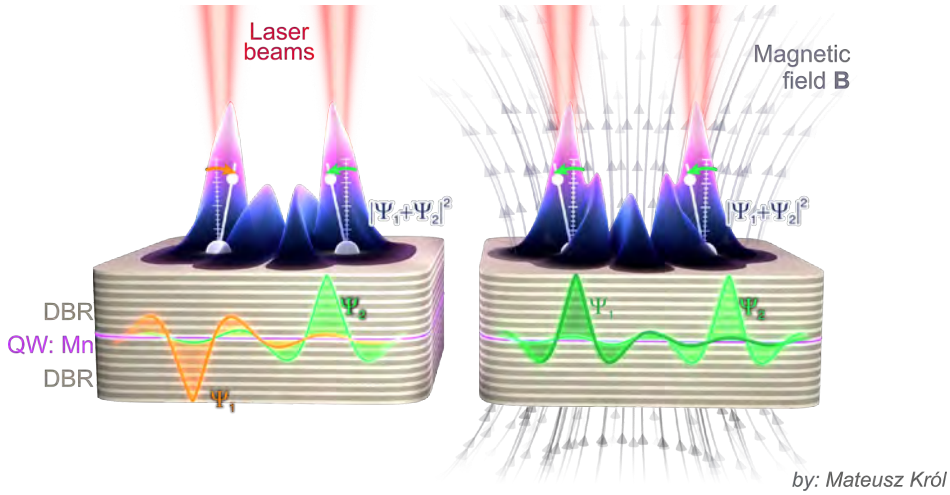

The results described in this Chapter are published in:
M. Furman, et al., "Magneto-optical induced supermode switching in quantum fluids of light" (2023), Communications Physics, 6, 196.

Controlling the spatial organization of coherent light fields is a challenge in polaritonics, closely related to the rapidly growing field of polariton-based quantum simulators [10,133–135]. In such systems, engineered potentials allow for the realization of lattice configurations and control over coupling between individual sites, enabling the emulation of complex many-body Hamiltonians. While magnetic fields are routinely used to manipulate the polarization of light in magnetooptical systems, introducing them as an additional degree of control over the coupling between condensate sites offers a novel way to tune the spatial configuration and interactions within polaritonic lattices. The aim of this Chapter is to demonstrate that an external magnetic field can serve as a control parameter for the spatial state of a polariton condensate, specifically enabling switching between distinct parities of a condensate supermode. This represents a new magnetooptical effect, which acts not on the spin (polarization) but on the spatial degree of freedom of light.

To demonstrate this effect, we used a specially designed CdTe-based semimagnetic optical microcavity incorporating semimagnetic quantum wells doped with Mn ions. The presence of magnetic ions enhances the sensitivity of the system to external magnetic fields through the giant Zeeman effect. That provided the necessary energy shift for modifying the polariton dispersion and condensate properties.

In the following, the phenomenon of magnetic-field-induced supermode parity switching is presented and analyzed both in real and reciprocal space. The experiments reveal how the Zeeman splitting alters the effective masses and dispersion of the spin-polarized polariton branches. This led to a change in the phase relation between two coupled condensates and, consequently, to a reversal of the supermode parity. The observations are supported by theoretical modeling and numerical simulations based on the spinor Gross–Pitaevskii equation, which reproduce the switching behavior.

This work provides the first experimental evidence for a magnetooptical effect that reconfigures the spatial state of a polariton condensate. Beyond its fundamental significance, this result introduces a new pathway for magnetic control of coherent states of light in microcavity systems, opening perspectives for tunable polaritonic circuits and hybrid magneto-optical devices where both spin and spatial degrees of freedom are actively manipulated.

5.1. Introduction to ballistically coupled polariton condensates

Particles in the exciton-polariton condensate created by a nonresonant laser can propagate ballistically over significant distances. Depending on the sample properties, such propagation can occur with only weak scattering, reaching tens or even hundreds of micrometers across the sample [68, 136]. Ballistic condensates have been observed in microcavities with energetically homogeneous photonic potentials exhibiting long polariton lifetimes. In such structures, at the excitation laser spot, a reservoir of hot excitons is created. This reservoir feeds the condensate and generates a repulsive potential because of strong exciton-exciton interactions. Because of the high homogeneity of the cavities, the reservoir does not trap the condensate at the same position. Instead, the ballistic condensate is repelled and spreads away from the laser spot [136, 137]. This phenomenon has been observed, among others, in planar GaAs/InGaAs microcavities [138].

When the microcavity is excited by multiple laser beams, the resulting condensates can

couple between each other by ballistic exchange of particles. This allows for the realization of so-called polariton dyads (formed from a pair of condensates) or triads (formed from three coupled condensates) [139]. In a polariton dyad, the system establishes a common phase, and the condensates at individual sites can lock either in-phase or in anti-phase. In such configurations, interference fringes arise in the area between the excitation sites. These two states can be distinguished by the parity of the interference pattern, which manifests itself through the number of observed fringes [10, 139, 140]. The parity of the interference pattern originates from whether the ballistically propagating polaritons arrive at the opposite site in-phase or anti-phase. The parity of the supermode can be thus changed by controlling this phase. It can be realized by tuning physical parameters such as the distance between the excitation beams, additional pumping, or the exciton-photon detuning of the cavity. Moreover, it has been shown that introducing additional sub-threshold laser spots can create effective barriers, enabling control over both the sign and strength of the coupling between condensates and thereby switching the system between ferromagnetic (in-phase) and antiferromagnetic (anti-phase) configurations [140].

Ballistic condensates can be arranged in entire networks of mutually interacting condensates [10,138,139,141,142]. Specifically, such networks can be used as quantum simulators. For example in [10] networks of several dozen condensate nodes were used to find solutions of XY Hamiltonians. The authors showed that the system spontaneously selects a configuration of relative phases (ferromagnetic or antiferromagnetic), which was confirmed by the observation of interference patterns in real space.

The aim of this Chapter was to demonstrate a novel method of controlling the parity of coupled polariton condensates using an external magnetic field. Semimagnetic optical microcavities provide an especially suitable platform for exploring magnetic-field induced effects. These structures contain quantum wells doped with magnetic ions and are known for their pronounced magnetic-field-dependent properties. Photoluminescence from such microcavities has revealed several magnetic field dependent effects, including lowering of the condensation threshold in magnetic field [61]. It was also demonstrated that even relatively small magnetic field lead the condensate to acquire strong circular polarization [64], and concluding with the observation of the giant Zeeman effect [65] of exciton-polaritons.

As shown in Fig. 5.1, which contains results taken from Ref. [65], applying a magnetic field in the Faraday configuration to such a microcavity leads to the energy splitting of excitons into states with opposite spin projections, corresponding to circular polarizations σ^+ (spin $+1$) and σ^- (spin -1). The behavior of the system in the magnetic field is dominated by heavy-hole excitons, which are the primary contributors to the observed strong coupling. Light-hole excitons lie at higher energies and possess both a smaller oscillator strength and a weaker Zeeman splitting.

In the polariton dispersion maps in Fig. 5.1(a), after applying the magnetic field, the lower polariton branch splits into branches with σ^+ and σ^- polarizations. The magnitude of this polariton splitting depends on the detuning between the bare cavity photon mode and the exciton, the larger the excitonic fraction of the polariton, the stronger the observed splitting.

Figure 5.1(b) additionally shows how the magnetic field up to 5 T induces a Zeeman splitting of the heavy-hole exciton energies, while the cavity photon mode remains essentially unchanged. As a result, the exciton-photon detuning becomes field-dependent. Furthermore, Fig. 5.1(c) presents how the Rabi splitting energy changes as a function of the applied external

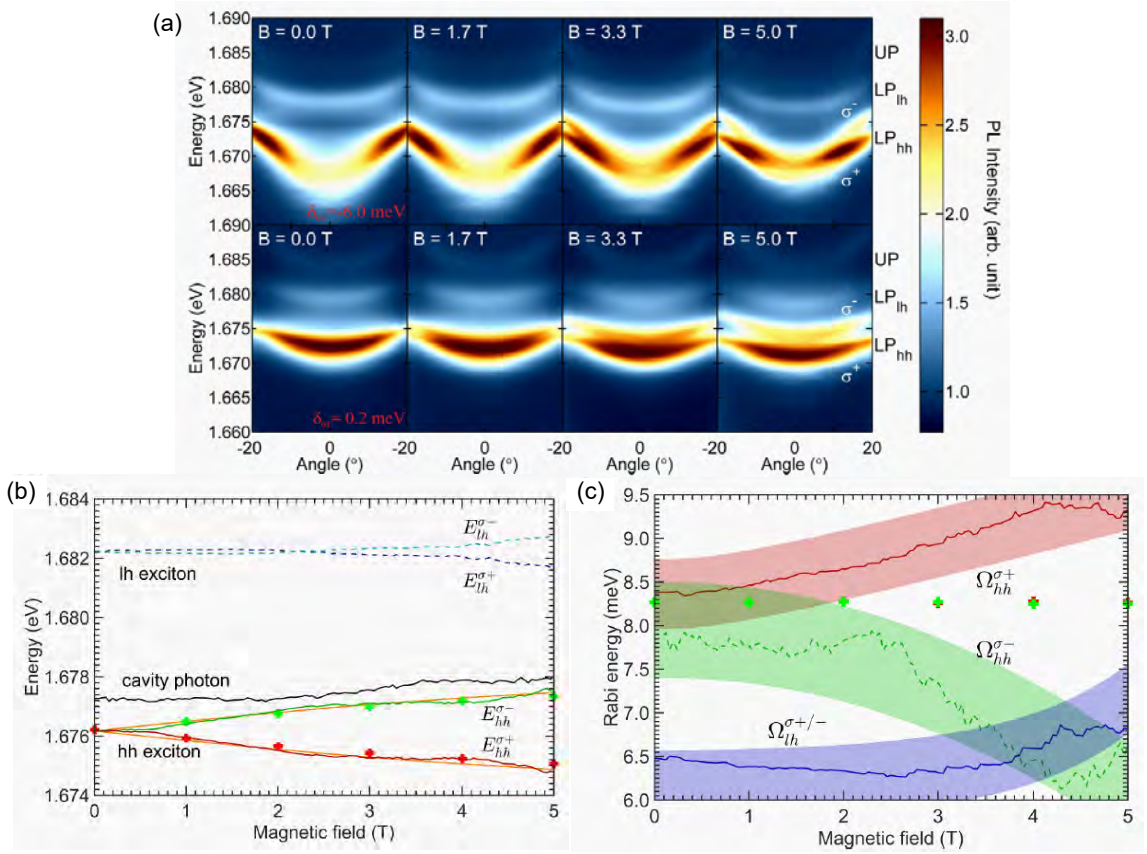

Figure 5.1: **Magnetically induced Zeeman splitting of exciton-polaritons in a semimagnetic microcavity.** (a) Exciton-polariton dispersion relation photoluminescence maps showing the splitting of the lower polariton branch into σ^+ and σ^- polarized components under applied magnetic field up to 5 T. (b) Evolution of heavy-hole exciton and cavity photon energies as a function of magnetic field up to 5 T. (c) Dependence of the Rabi splitting energy on the applied magnetic field. Data adapted from [65].

magnetic field.

The giant Zeeman splitting influencing exciton-photon detuning and the excitonic component of polaritons also affects the effective mass of the lower polariton branch. As illustrated schematically in Figs. 5.2(c,d), these changes modify the curvature of the dispersion relation: without magnetic field the lower polariton branch has a certain effective mass [panel (c)], whereas under applied field the dispersion becomes changed [panel (d)]. Such a modification of the dispersion affects the phase relation of ballistically propagating polaritons between two excitation sites, and thereby provides a mechanism for switching the parity of the condensate supermode using a magnetic field. Confirming this prediction is the main goal of the studies described in this section. To this end, the experiment was designed to excite a condensate supermode using two spatially separated laser beams in a semimagnetic semiconductor microcavity based on CdTe, as schematically shown in Fig. 5.2(a). Figure 5.2(b) further illustrates the experimental concept, where the application of a magnetic field is expected to enable

switching of the condensate supermode parity. In this work, this phenomenon was investigated primarily in the real space of the sample, and the observed effects were further confirmed in reciprocal space.

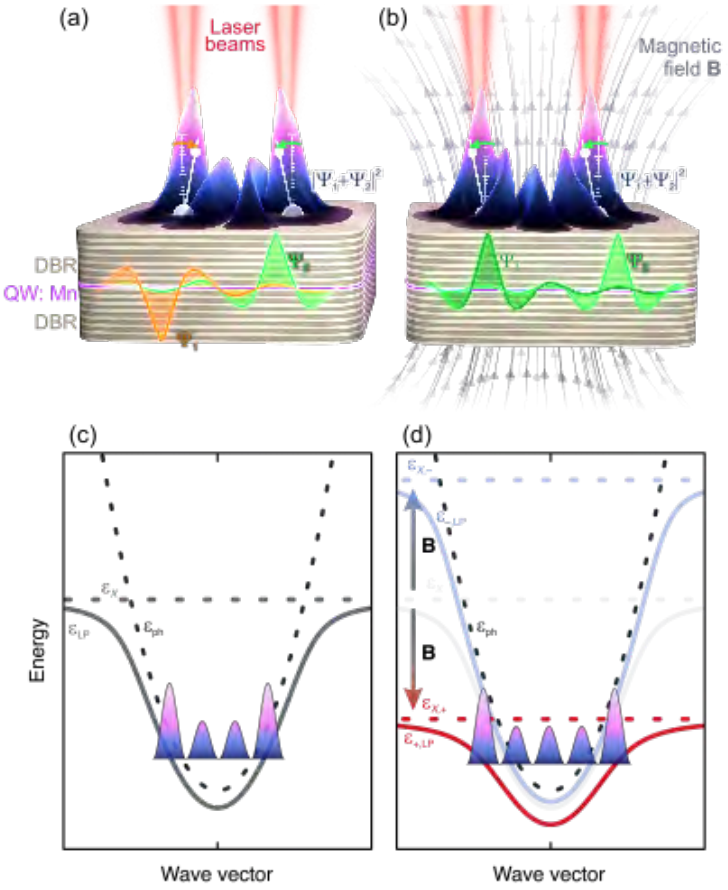

Figure 5.2: **Concept of condensate supermode control in a semimagnetic CdTe-based microcavity.** (a) Two spatially separated laser beams generate interacting polariton condensates. (b) Applying an external magnetic field enables switching of the condensate supermode parity. (c) Schematic polariton dispersion without magnetic field. (d) Magnetic field induced splitting of the heavy-hole exciton into σ^+ and σ^- states; the σ^+ state couples to the cavity photon, modifying the polariton effective mass and allowing parity switching. The image was made by Dr. Mateusz Król.

As an aside, it is worth recalling that the use of magnetic fields to control other properties of light is known in optics. Well-known magneto-optical phenomena include the Faraday effect, in which the polarization plane of linearly polarized light rotates when passing through a medium under an applied magnetic field. Another example is the Kerr effect, where the polarization changes after reflection from a magnetized surface. These classical effects primarily modify the polarization state of light, which is in contrast with the effect proposed here, where the magnetic field affects the spatial mode of the electromagnetic field.

5.2. Polariton condensate supermode in magnetic field

The constructed experimental setup is presented in Fig. 5.3. In the experiment a picosecond laser (Mira-900) was used with a pulse duration of 4 ps and a repetition rate of 76 MHz. The sample was excited nonresonantly. The laser wavelength was tuned to the first Bragg minimum and set to 710 nm, corresponding to a photon energy of approximately 1.75 eV. The laser was divided into two beams using a 50:50 beam splitter. The power of both beams was separately controlled with neutral density (ND) filters.

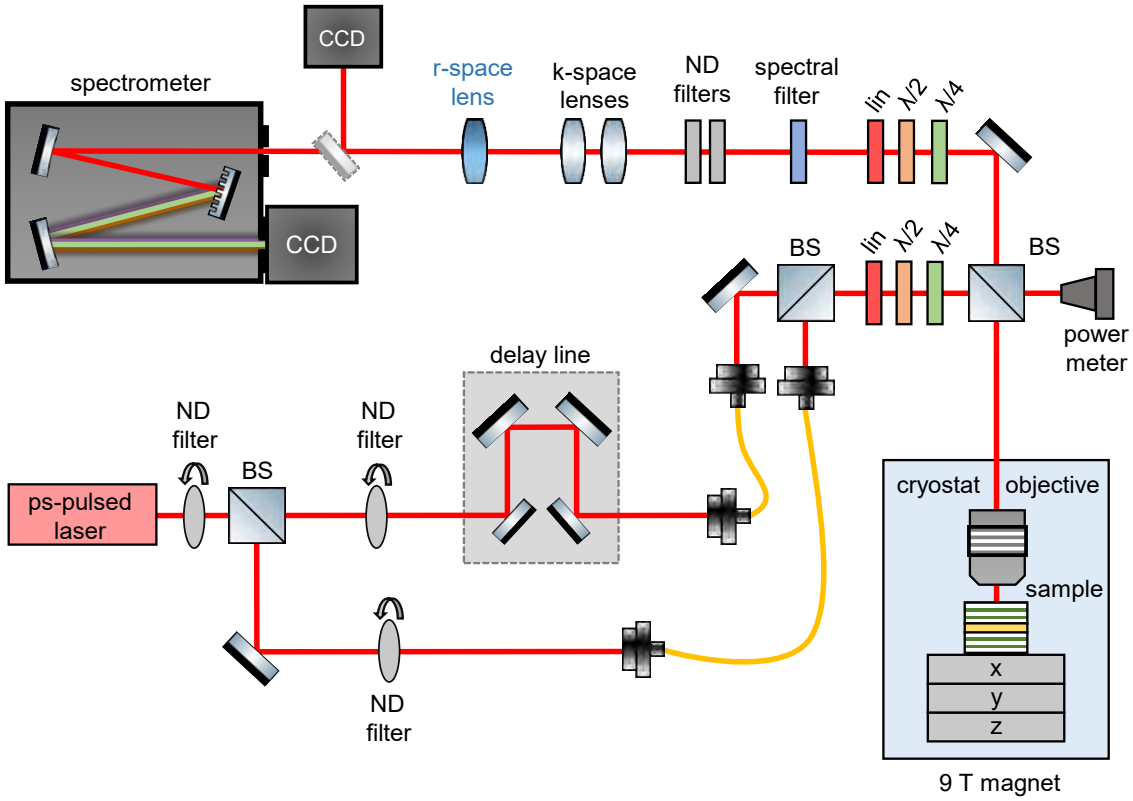

Figure 5.3: **Scheme of the experimental setup used for measurements in magnetic field up to 9 T, in Faraday geometry using two nonresonant excitation beams of CdTe-based microcavity.** The experiment was performed using a picosecond laser, a delay line, and polarization optics at excitation and detection sides. The photoluminescence signal was collected in a confocal geometry at 4.5 K under a magnetic field of up to 9 T.

After splitting, the first beam was coupled to an optical fiber. The second beam, before coupling to another optical fiber, was directed onto a delay line consisting of mirrors mounted on translation stages. The delay line allowed to precisely control the relative arrival time at the sample between the laser pulses from both arms. In these measurements it was essential to align the two beams so that they reached the sample simultaneously. After passing through the fibers, both beams were recombined at another beam splitter and directed towards the cryostat.

A linear polarizer, half-wave plate, and quarter-wave plate were used on the excitation path to set the desired linear polarization of the beams. The optical power of each beam was verified before the sample using a power meter placed in front of the cryostat.

The experiments were carried out in an AttoCube bath cryostat equipped with a 9 T superconducting magnet. A magnetic field was applied to the sample in the Faraday geometry, which means that the field was parallel to the optical axis, i.e., along the direction of light propagation. The sample was mounted on an xyz piezo translation stage, which allowed precise positioning and focusing.

Excitation and collection of the emitted light were performed with a high numerical aperture microscope objective. The collected light entered a polarization selection setup. In the measurements, σ^+-polarized emission was detected, corresponding to the field orientation. Next, a spectral filter then blocked the reflected laser light and transmitted only the photoluminescence signal. Lenses were used to project the signal either on a camera or onto a spectrometer slit, with one lens for real space or with two lenses for reciprocal space imaging. Additional ND filters in the detection path allowed the light intensity incident on the photodetectors to be reduced when necessary.

All measurements were carried out at the temperature of 4.5 K. The investigated structure was a semimagnetic CdTe-based optical microcavity (Sample C.2), containing quantum wells doped with 0.5% Mn ions.

5.2.1. Condensate supermode parity switching

Semiconductor microcavities based on II-VI materials are characterized by a highly inhomogeneous photonic potential, as discussed previously in Chapter 3, Section "Photonic potential fluctuations in CdTe-based microcavity". Despite this inhomogeneity, ballistically propagating condensates can still be observed, although over much shorter distances, and they are rare and difficult to identify experimentally.

A single ballistic condensate propagates without forming interference fringes, but when two condensates are created simultaneously they can couple into a polariton supermode. In such a case interference fringes arise from the superposition of two polariton waves, giving rise to quantized standing-wave modes visible in dispersion maps and in the real-space emission profile. Particular care was therefore taken to ensure that the observed fringes were not due to local potential traps, but indeed originated from ballistic coupling of condensates. The position on the sample was carefully tested to exclude the influence of strong inhomogeneities of the photonic potential.

The main goal of this part of the study was to observe magnetic-field induced switching of the spatial interference pattern (parity) of a polariton supermode. The results studied in real space by collecting x-y maps on a CCD camera are presented in Fig. 5.4.

Figure 5.4(a) presents the real-space photoluminescence map of the condensate excited with a single beam. The excitation beam had a FWHM of about 2 μm on the sample, and the pulse energy was set to 3.3 pJ. The emission observed from this region was strongly inhomogeneous, considerably broader and more diffuse than the excitation spot. The FWHM of the photoluminescence signal was about two times larger than that of the laser beam. The approximate position of the observed signal on the map was indicated by a red dashed circle. Figure 5.4(b) presents the real-space photoluminescence map from the second excitation beam,

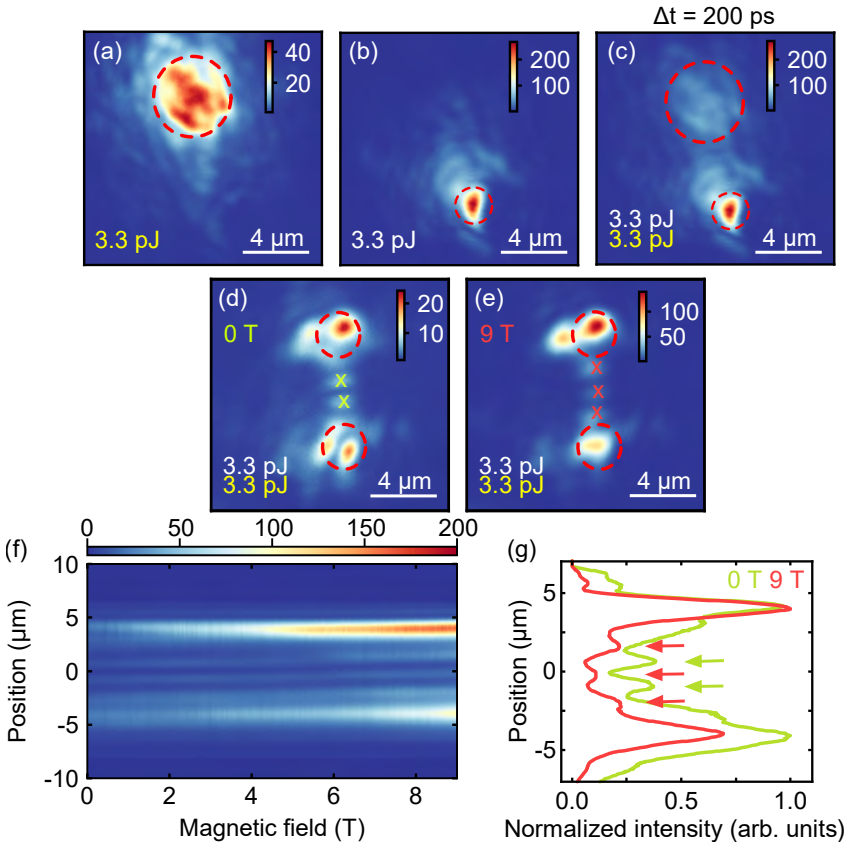

Figure 5.4: **Real-space photoluminescence maps of supermode polariton condensate.** (a,b) Emission patterns for each excitation beam measured separately. (c) Two excitation spots delayed by 200 ps show no interference fringes, confirming the finite coherence time. (d) Synchronized beams create two condensates forming a supermode, with two interference fringes between them. (e) Real-space emission at $B = 9$ T with enhanced intensity and a change in the number of fringes. (f) Evolution of interference fringes with increasing magnetic field. (g) Cross-sections at $B = 0$ and $B = 9$ T demonstrating the field-induced shift of fringe positions.

measured under the same excitation pulse energy of 3.3 pJ, but separated by about 7 μm from the first beam. Although the laser spot size at this position was the same as in Fig. 5.4(a), the emission was considerably more confined. A single well-localized emission spot with an FWHM of about 1.5 μm was detected, surrounded by a weaker spatially extended background signal. The emission area was also marked with a red dashed circle for clarity. Because the photonic potential in CdTe-based microcavities is highly inhomogeneous, the emission patterns from two positions on the sample look different, even if both beams have the same spatial profile. Figure 5.4(c) presents the combined result obtained when the microcavity was excited by two laser beams, with pulse energy of 3.3 pJ each. Here, one beam reaches the sample about 200 ps later than the other, realized by extending the optical path by 60 mm in the delay line. In this case, the resulting photoluminescence map resembled a simple sum of

the signals obtained from the two individual excitation spots. This indicates that the delay time of 200 ps was much longer than the condensate lifetime (about 12 ps in CdTe-based microcavities [11]), and therefore the phase coherence could not be preserved.

When the excitation pulses in two beams were synchronized in time, interference fringes appeared, as shown in Fig. 5.4(d). The intensity maxima are located directly under the two excitation spots, which are indicated by dashed red circles. The presence of two interference fringes between them confirms that the condensate crates a single supermode synchronized in anti-phase. The fringes are indicated in Fig. 5.4(d) by light green crosses. This measurement was performed without any external magnetic field. When a field of $B = 9$ T was applied, the real-space PL map changed, as shown in Fig. 5.4(e). The intensity of both condensates increased. More importantly, in the region where two interference fringes were observed without the magnetic field, three fringes appeared under $B = 9$ T. This indicates that the relative phase between the two condensates forming the supermode changed, and that they became locked in-phase. The positions of the three fringes are marked by red crosses.

To follow the evolution of the condensate supermode, cross-sections were extracted from the PL maps at successive magnetic fields between 0 T and 9 T and presented in Fig. 5.4(f). This representation allows for identification of the field at which phase synchronization is lost and the field at which the parity of interference fringes changes. Although the total signal shows only a relatively low amplitude of the fringes, a characteristic evolution can be observed in the range of $B \approx 3 - 4$ T, where the fringe initially located near 3 μm gradually merges with the outer fringe around 4.5 μm. For clarity, Fig. 5.4(g) presents cross-sections for two extreme field values. The light green curve corresponds to zero magnetic field, with the two fringes marked by light green arrows. The red curve shows the result at $B = 9$ T, with three red arrows marking the positions of the fringes. Although the lack of energy resolution leads to limited visibility of the interferences in the integrated signal, the change in the fringe positions between the two field values confirms the effect of the magnetic field on the real-space interference pattern.

5.2.2. Condensate supermodes switching resolved in energy

Next, the real-space signal was directed to the entrance slit of the spectrometer to obtain energy-resolved data, allowing to spectrally resolve different modes of the condensate. As in the previous section, photoluminescence was measured for each excitation beam separately and also for two beams with one delayed in time relative to the other. The results are presented in Fig. 5.5.

Figs. 5.5(a,b) show the PL signal from two different excitation spots measured independently. The emission was spectrally broad, with no dominant emission energy. In Fig. 5.5(b), localized states appear near 1.603 eV, showing the inhomogeneous photonic potential typical for CdTe-based microcavities.

For two beams incident on the sample but one delayed by 200 ps [Fig. 5.5(c)], no interference fringes were observed in the energy-resolved map between two excitation spots. When the time delay was reduced, a condensate formed simultaneously at both excitation sites, and their phases became synchronized [Fig. 5.5(d)], both beams crossed the condensation threshold. A strong emission appeared at 1.606 eV, marked on the map with a dashed red line. At this energy, two condensates located around $x = \pm 3$ μm with two interference fringes between

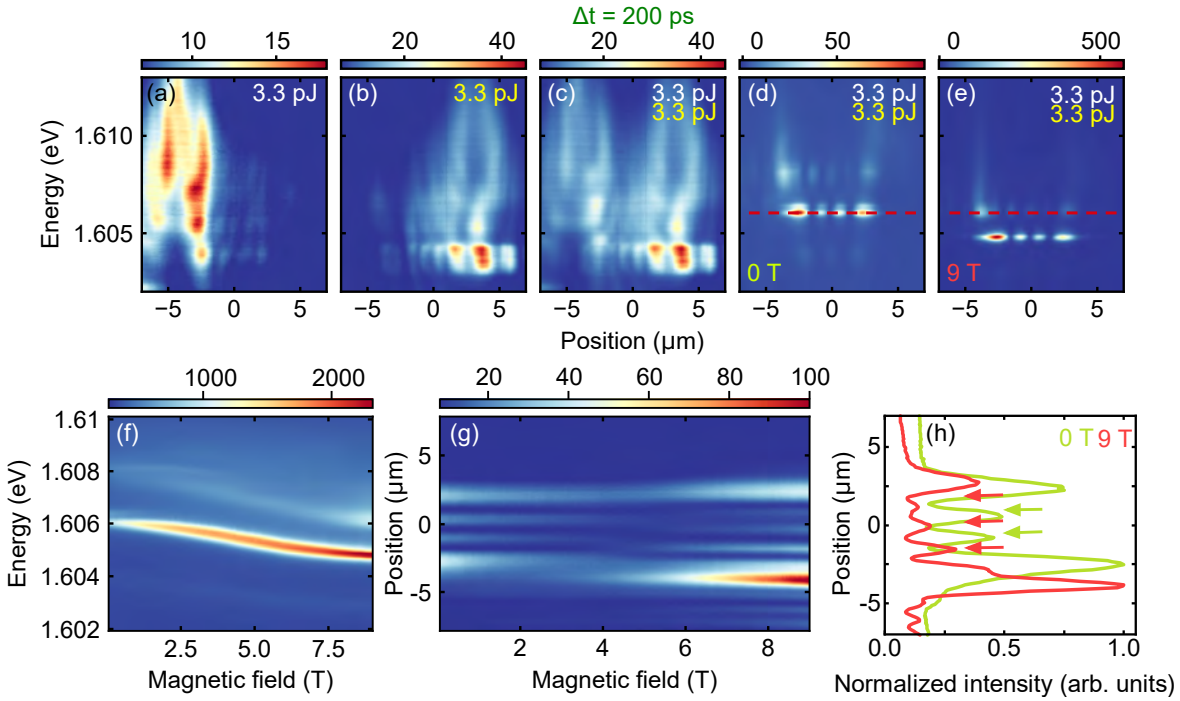

Figure 5.5: **Spectrally resolved photoluminescence in real space of coupled polariton condensates.** (a,b) Real-space emission from two excitation spots measured independently at a pulse energy of 3.3 pJ. (c) Two beams delayed by 200 ps show no interference fringes. (d) Phase-synchronized emission from a condensate supermode with two interference fringes at 1.606 eV. (e) Emission at $B = 9$ T shows an energy shift of the supermode and the appearance of a higher-order mode. (f) Evolution of mode energies with increasing magnetic field. (g) Cross-sections at energy of 1.606 eV demonstrating phase desynchronization around $B = 5$ T and the transition from two to three interference fringes. (h) Line profiles at 1.606 eV for $B = 0$ T (green, two fringes) and $B = 9$ T (red, three fringes).

them form a polariton condensate supermode. A higher-energy mode at 1.608 eV with three interference fringes was also observed, but with a much lower intensity. All these measurements were performed at zero magnetic field. When a magnetic field of $B = 9$ T was applied, the emission pattern changed, as shown in Fig. 5.5(e). The main supermode redshifted to about 1.604 eV, while at 1.606 eV a second mode of opposite parity appeared. The energy evolution is shown in Fig. 5.5(f), presenting spatially integrated emission versus magnetic field. The strongest signal, starting at 1.606 eV for $B = 0$ T, shifted to 1.6045 eV at the highest magnetic field, with simultaneous increase in emission intensity. The weaker higher-energy mode was also visible from energy of 1.608 eV for $B = 0$ T, to energy of 1.606 eV for $B = 9$ T, moving in energy with the field.

To study the supermode phase behavior, cross-sections were extracted at the energy corresponding to the strongest mode at zero magnetic field (1.606 eV), with the results shown in Fig. 5.5(g). At this energy, it was possible to identify phase desynchronization range and the change in the parity of interference fringes. The parity change occurred around $B \approx 5$ T.

Above this value, the system shift from supermode with two fringes (anti-phase) to supermode with three fringes (in-phase) at higher magnetic fields.

Finally, Fig. 5.5(h) presents cross-sections through the maps in panels (d) and (e) at 1.606 eV. The light green cross-section (0 T) shows two interference fringes, indicated by arrows. The red ones (9 T) reveals three fringes, whose positions are shifted compared to the zero-field case and located in between the original fringes.

5.2.3. Condensate supermode in reciprocal space

The same position that was analyzed in real space in the previous section was investigated in momentum space using the spectrometer.

Figures 5.6(a,b) present the polariton dispersion collected for each excitation beam separately. Individually, each beam was below the condensation threshold. The maps show the emission from the lower polariton branch around 1.605 eV. For both beams, the dispersions exhibit similar behavior, with a higher polariton population at higher wavevectors. The vertical interference fringes visible at $k = 0$, most likely originating from the additional reflection from the beam splitter in the detection system.

Figure 5.6(c) shows the polariton dispersion when both excitation beams were present simultaneously and together exceeded the condensation threshold, creating a coupled ballistic condensate. The time delay between the beams was adjusted so that both laser beams reached the sample simultaneously. The pulse energies of both beams are indicated at the top of the maps. Figure 5.6(c) shows the photoluminescence dispersion map without external magnetic field. Several discrete modes appear around 1.606 eV with constructive interference fringes. The number of fringes depends on the detuning and the momentum range at which the modes are observed. The most visible signal is from the central mode, highlighted with a dashed red line at 1.606 eV. Here, two condensates at ± 2.5 µm^{-1} are visible, with two interference fringes between them.

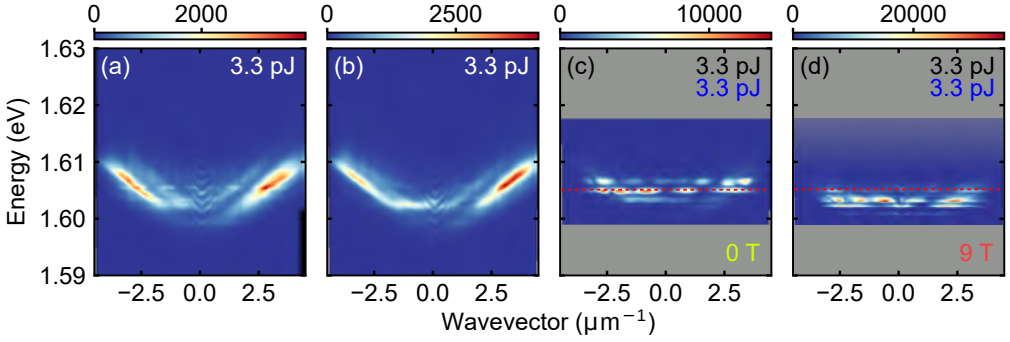

Figure 5.6: **Polariton dispersion maps for individual and coupled condensates.** (a,b) Dispersion of the lower polariton branch measured for each excitation beam separately. (c) Formation of a polariton supermode from two ballistic condensates without external magnetic field. (d) Dispersion of the supermode in a magnetic field of $B = 9$ T, showing an energy shift and a change of the effective polariton mass.

Next, a magnetic field of $B = 9$ T was applied to the sample [Fig. 5.6(d)]. The first visible

effect was a shift of all modes to lower energies. Also, the wavevector range over which the supermode emission was observed broadened. These results confirm the mechanism described in the introduction, where the Zeeman splitting shifts the exciton energy, thereby modifying the exciton-photon detuning and consequently the lower polariton dispersion. Because the measurements focused on the energy range of the lower polariton mode, the condensate supermode measurements were taken on a more detailed grating on the spectrometer, so the observed spectral range is narrower.

5.3. Theoretical description of the condensate supermode in magnetic field

The theory used to describe the observed phenomena was developed by Dr. Helgi Sigurðsson. The basis of the theory is the change in the polariton dispersion and polariton-polariton interactions under an external magnetic field. In addition, a spin-reservoir model was included to account for the spin imbalance in the presence of a magnetic field. Next, it is shown that this allows one to change the synchronization conditions of two condensates and to switch their supermodes. A condition for the critical magnetic field B_{crit} was also derived. In addition, numerical simulations were carried out to confirm the mode switching.

The model is explained step by step. The discussion begins with how the applied external magnetic field affects the polariton mode. The lower polariton branch, considered for both spins:

$$\epsilon_{\pm}(\mathbf{k}) = \frac{\epsilon_{\mathrm{ph}}(\mathbf{k}) + \epsilon_{X,\pm}}{2} - \sqrt{\Omega_{\mathrm{R}}^2 + \left(\frac{\epsilon_{\mathrm{ph}}(\mathbf{k}) - \epsilon_{X,\pm}}{2}\right)^2}, \tag{5.1}$$

where $\epsilon_{\mathrm{ph}}(\mathbf{k}) = \hbar^2 k^2/2m$ is the energy of the cavity photon, which scales quadratically with momentum $\mathbf{k}$. When an external magnetic field is applied, the heavy-hole exciton energy changes due to the Zeeman effect and a spin splitting is observed, what can be written as $\epsilon_{X,\pm} = \epsilon_0 \mp \mu_B g_{\mathrm{eff}} B$, where ϵ_0 is exciton energy in a zero magnetic field ($B = 0$), μ_B is Bohr magneton, and g_{eff} is an effective factor g of the exciton. Ω_{R} in denotes the Rabi energy, i.e., the light–matter coupling strength.

Furthermore, the photonic and excitonic fractions of the polariton, are given by Hopfield coefficients. The excitonic fraction is equal to:

$$|X_{\pm}|^2 = \tfrac{1}{2}\left(1 - \frac{\epsilon_{X,\pm} - \epsilon_{\mathrm{ph}}(\mathbf{k})}{\sqrt{[\epsilon_{X,\pm} - \epsilon_{\mathrm{ph}}(\mathbf{k})]^2 + 4\Omega_{\mathrm{R}}^2}}\right), \tag{5.2}$$

while the photonic fraction can be written as:

$$|C_{\pm}|^2 = \tfrac{1}{2}\left(1 + \frac{\epsilon_{X,\pm} - \epsilon_{\mathrm{ph}}(\mathbf{k})}{\sqrt{[\epsilon_{X,\pm} - \epsilon_{\mathrm{ph}}(\mathbf{k})]^2 + 4\Omega_{\mathrm{R}}^2}}\right). \tag{5.3}$$

It is evident that the polariton composition depends on the magnetic field through the heavy-hole exciton energy. This means that the larger the exciton fraction, the stronger the magnetic field influence.

Another important effect is that the effective mass of the polaritons depends on their photonic/excitonic fraction. If the polariton is more photonic, i.e., when $|C_\pm|^2$ is larger, the polariton has a lower effective mass. If the polariton is more excitonic, its effective mass is higher. Applying a magnetic field changes these proportions and makes the masses ($m_\pm$) of spin-up and spin-down polaritons different, as expressed by:

$$m_\pm \simeq \frac{m}{|C_\pm|^2}, \tag{5.4}$$

where m denotes the effective photon mass of the optical cavity.

The theory can be used to determine the condition for supermode switching. Two polariton condensates were considered that originate from from two laser spots and can synchronize, forming the supermode. During propagation between the excitation sites, polaritons accumulate phase equal to:

$$\Delta\phi \approx k_c d, \tag{5.5}$$

where k_c is the mean wavevector of the propagating polaritons and d is the distance between the laser excitation spots.

If $\Delta\phi = 0 \pmod{2\pi}$, the condensates are in phase and an even supermode is observed in emission, whereas if $\Delta\phi = \pi \pmod{2\pi}$, the condensates are out of phase and an odd supermode is observed. The magnetic field changes k_c, and can therefore switch the parity of the supermode from even to odd or vice versa.

The value of k_c can be estimated, assuming that the interaction energy of the condensate is equal to its kinetic energy. This assumption provides only an estimate of the order of magnitude, because it depends on parameter such as exciton reservoir density $n_{X,\sigma}$, which is not directly accessible experimentally, and can be written as:

$$k_{c,\sigma} \approx \sqrt{\frac{4g_0 m}{N_{\mathrm{QW}}\hbar^2}\frac{|X_\sigma|^2}{|C_\sigma|^2}n_{X,\sigma}}, \tag{5.6}$$

from which it follows that k_c depends on the ratio of Hopfield coefficients ($|X_\sigma|^2/|C_\sigma|^2$), i.e., it depends on the magnetic field as well as on the exciton reservoir density $n_{X,\sigma}$, where $n_{X,\sigma}$ is excitonic reservoir density for a given spin projection σ. In short, the magnetic field increases $k_{c,+}$, which can trigger a change of the supermode parity.

For the system to switch to a mode of different parity, the difference of wavevectors (before and after turning on the field) must yield a phase of π over the distance d, what can be written as:

$$\pi = |k_{c,\sigma}(B_{\mathrm{crit}}) - k_{c,\sigma}(0)|\, d. \tag{5.7}$$

In this way, the critical magnetic field B_{crit} at which the switching occurs can be determined.

The behavior of the polariton condensate supermode in magnetic field can be also simulated using the Gross–Pitaevskii equation (for the condensate), coupled to equations for the exciton reservoir:

$$\mathrm{i}\hbar\frac{\partial\psi_\pm}{\partial t} = \Big[\epsilon_\pm(-\mathrm{i}\nabla) + \tfrac{\mathrm{i}\hbar R n_{A,\pm}}{2} + \alpha_\pm|\psi_\pm|^2 + G_\pm(n_{A,\pm} + n_{I,\pm})\Big]\psi_\pm, \tag{5.8}$$

where R is the stimulated scattering rate of excitons from the reservoir to the condensate, $n_{A,\pm}$ is density of active excitons in the reservoir with spin $\pm$, $n_{I,\pm}$ is the density of inactive excitons, $\alpha_\pm$ means nonlinear interaction coefficient between polaritons with spin $\pm$ (condensate self-interaction energy), $G_\pm$ is interaction coefficient between the condensate and the exciton reservoir (condensate-reservoir interaction constant).

To closely reproduce the experiment, equations for the exciton reservoir were added:

$$\frac{\partial n_{A,\pm}}{\partial t} = -\left(\Gamma + \Gamma_{s,\pm} + R|\psi_\pm|^2\right) n_{A,\pm} + \Gamma_{s,\mp} n_{A,\mp} + W n_{I,\pm}. \tag{5.9}$$

which describe how the population of excitons with a given spin evolves in the reservoir, where $\Gamma_{s,\pm}$ is the spin relaxation rate, and W is exciton flow rate from the inactive reservoir to the active reservoir. The magnetic field splits these rates and leads to an excess of one spin over the other, which subsequently affects the condensate.

These equations describe how the polariton condensate wavefunction evolves in time under losses, gain from the reservoir, and interactions. The results of the simulations, presented in Fig. 5.7, show that for small magnetic fields the supermode is parity is odd. Upon increasing the magnetic field, the parity switches to even, in agreement with the initial predictions. Overall, the results summarized in Fig. 5.7, show the transition of supermode parity as a function of increasing magnetic field.

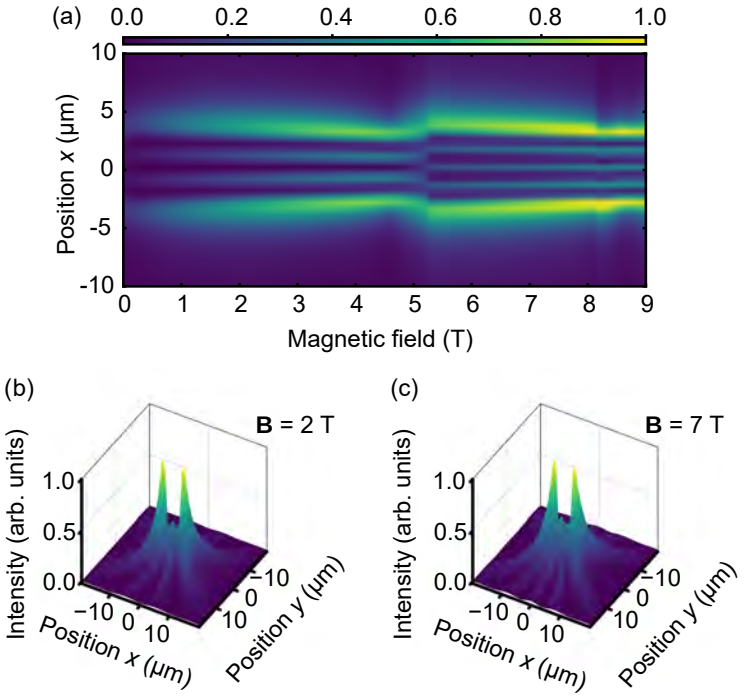

Figure 5.7: **Numerical Gross-Pitaevskii simulation showing the change of supermode parity with increasing magnetic field.** (a) Time-integrated profile of the total condensate density along $y = 0$, calculated for increasing magnetic field. (b,c) Corresponding density maps in the x-y plane for $B = 2$ T and after the switching at $B = 7$ T.

5.4. Summary

The results presented in this Chapter expand the toolbox for one of the main goals in polaritonics of achieving external control over the spatial organization of coherent light. It is demonstrated that a magnetic field can be used not only to tune the polarization of light (as in most magnetooptical effects), but also to reconfigure its spatial mode structure, and coherent coupling between distant sites. This represents the first experimental realization of a magnetically induced parity control of polariton condensate supermodes.

The experiments revealed that an applied magnetic field modifies the spatial interference pattern between two coupled ballistic condensates forming a synchronized supermode. As the field increases, synchronization between the condensates is first lost and later restored in a supermode of opposite parity. This transition was directly observed in the real-space emission as a change in the number of interference fringes and was confirmed in reciprocal space by the corresponding modification of the polariton dispersion.

The experimental observations are consistent with the developed theoretical model. The giant Zeeman splitting in the semimagnetic microcavity modifies the excitonic contribution to polaritons, alters the effective masses and wavevector of the condensate. These changes shift the phase synchronization conditions between the individual condensate sites and define a critical magnetic field at which the mode parity switching occurs. Numerical simulations based on the spinor Gross–Pitaevskii model reproduce the observed behavior, confirming the microscopic mechanism of the transition.

This work introduces a new degree of freedom in the control of the coherent coupling between polariton condensates, by means of magnetic field–tuning of their spatial supermodes. Beyond its fundamental importance for understanding light-matter coupling in semimagnetic microcavities, this finding opens a route toward magnetically reconfigurable polaritonic devices, where both spin and spatial coherence can be manipulated on demand.

Chapter 6

Polymer microlenses for optical microcavities: reciprocal space imaging and lowering condensation threshold

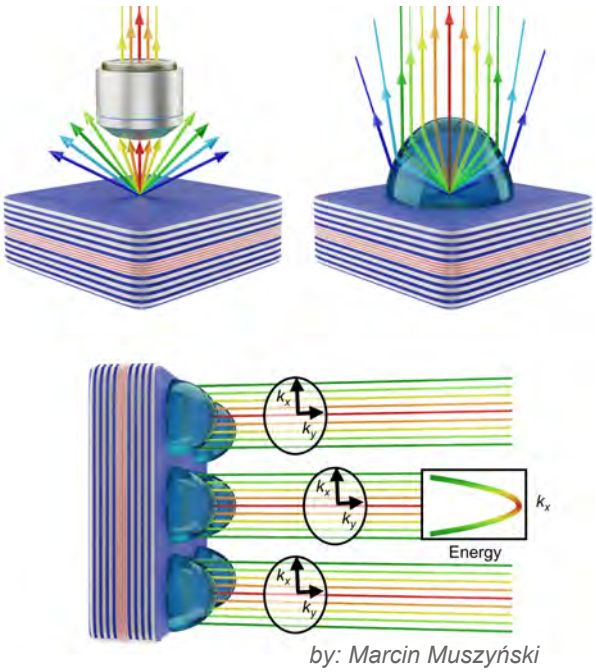

The results described in this Chapter are published in:
M. Furman, et al., "Multiplexed back focal plane imaging with on-chip integrated microlens array" (2025), arXiv, in review.

Efficient coupling of light into and out of the cavity is essential for microcavity systems, as exciton-polaritons are optically created and their properties are determined from the emitted light. One of the challenges for polariton applications is thus the efficient excitation and detection of light within microcavities because it directly affects the energy cost of condensation and the feasibility of nonlinear optical operations. The aim of this Chapter is to develop an approach that enables lower excitation thresholds and enhanced control of polariton systems through improved optical coupling. Here, elliptical polymer microlenses are proposed, designed, and fabricated directly on top of microcavities to demonstrate the improved efficiency of light injection and collection. By exploiting their immersion-like properties and because of their optimized high numerical aperture, these microlenses allow extraction of emission that would otherwise not couple out from the structure. Simultaneous tight focusing of the excitation lowered the threshold of the nonlinear effects, all of which were provided by compact, microscale polymer structures.

The microlenses act here as integrated high-performance micro-objectives, extending the accessible range of emission wavevectors. Simultaneously, they preserved the Fourier-plane imaging capability typical of conventional microscope optics and essential for investigations of polariton systems. This makes them a powerful tool for studying polariton dispersion, condensation dynamics, and nonlinear interactions in regimes where the use of bulky high-NA external optics is impractical, especially at cryogenic temperatures.

The Chapter begins with the description of the microlens design process. Ray-tracing simulations were employed to optimize their geometry for their specific function, e.g. for efficient reciprocal space imaging. The subsequent section presents the fabrication procedure based on two-photon polymerization, detailing the methods required to achieve optical-grade surfaces and precise alignment with the microcavity. Then, the optical performance of the produced microlenses is compared with conventional microscope objectives, showing not only their higher NA, improved light collection efficiency, but also simplification of the detection setup.

The advantages of the microlenses are confirmed in different types of microcavities, ranging from a simple dielectric system to GaAs- and CdTe-based structures operating in the strong coupling regime at cryogenic temperatures. It is shown that microlenses enable imaging of polariton dispersion relations with high resolution and an extended wavevector range to reveal states and features inaccessible to standard microscope objectives. Moreover, microlenses arranged in arrays were used for polariton dispersion multiplexing: collecting multiple momentum-resolved images simultaneously within a single measurement. Finally, it is demonstrated that integrating microlenses with microcavities reduces the excitation threshold for the localized exciton-polariton condensates, paving the way for compact and energy-efficient polariton networks operating in the low-power regime.

6.1. Introduction to the microprinting of polymer microstructures

As can be already seen from the previous chapters, momentum-resolved spectroscopy is an exceptionally practical tool for the investigation of microcavity systems. Reciprocal space imaging, also referred to as k-space analysis or back focal plane (BFP) imaging, is a technique

that allows mapping the angular distribution of light emitted or transmitted by a sample. This distribution directly corresponds to the in-plane wavevector of photons or other quasi-particles. The access to the energy-momentum relation (dispersion relation) is important to understand optical phenomena in nanophotonics [143–145], plasmonics [146], layered materials [147, 148], and optical cavities [42, 149, 150]. Fourier plane imaging was used, among other applications, to study the nature of dipole transitions in single emitters [151, 152], and to map band structures in photonic crystals and metamaterials [153–156].

Momentum space imaging is based on a specific property of a convex lens, which creates Fourier transform of the signal at its back focal plane. Traditionally, k-space imaging is performed in microscopic systems, where a high numerical aperture objective is used to perform the Fourier transform. However, this approach has some limitations. Obtaining a wide range of emission angles requires high numerical aperture (NA) and short focal length objectives, which are typically characterized by a short working distance (WD). Unfortunately, this makes them difficult to use in low-temperature measurements, where the sample is located deep inside the cryostat. In such situations, angle-resolved ellipsometry techniques are sometimes used as an alternative [157], but they also have limitations. The available range of emission angles in this method is narrow, and it is still difficult to implement with samples placed in a cryostat [158]. To overcome these challenges, recent advances in polymer microprinting have been used to extend the capabilities of momentum-space imaging, for example by enabling access to wavevector ranges that were previously inaccessible with other experimental techniques.

The development of 3D microprinting techniques, particularly two-photon lithography, has opened the way for the fabrication of complex optical structures with sub-micrometer and micrometer dimensions [159]. This method has been used, among others, to form light couplers [160], optical fiber micro-connectors [161], waveguides [162], metamaterials composed of polymers [163, 164], optical antennas [165], as well as microlenses [166]. Microlenses in particular are beginning to play an important role in photonics, as they enable efficient collection of the emitted light from the investigated structure. Polymer lenses with optimized geometry enabled improved coupling with weak emitters, such as quantum dots or transition metal dichalcogenide (TMD) materials, increasing the intensity of detected signals [166].

Polymer microlenses printed directly on the sample surface have already been demonstrated as a miniaturized alternative for microscope objectives [166], as shown in Fig. 6.1. They collimate light emitted from the structure into a parallel beam while simultaneously providing access to a broader set of wavevectors than in standard setups with microscope objectives. According to the principles of Fourier optics, such a microlens should also form a back focal plane, meaning it could be used for reciprocal space imaging. Printing the microlens directly on the sample removes the restriction of a limited working distance and enables its use in cryostats, where optical access with the external optics is especially challenging. At the same time, because each microlens collimates light locally, a set of them can be used as a series of independent micro-objectives. This enables simultaneous access to reciprocal space from multiple spatial points on the sample, without the need for mechanical scanning or changing the detection setup. This is especially useful capability for large-scale k-space mapping under cryogenic conditions.

Moreover, the large numerical aperture of such microlenses opens new possibilities in nonlinear effects in semiconductor microcavities. The higher NA of a microlens allows for a

tighter focusing of the excitation beam in the active layer, leading to an increase in polariton density and and thereby allowing the condensation threshold to be reached with effectively lower power.

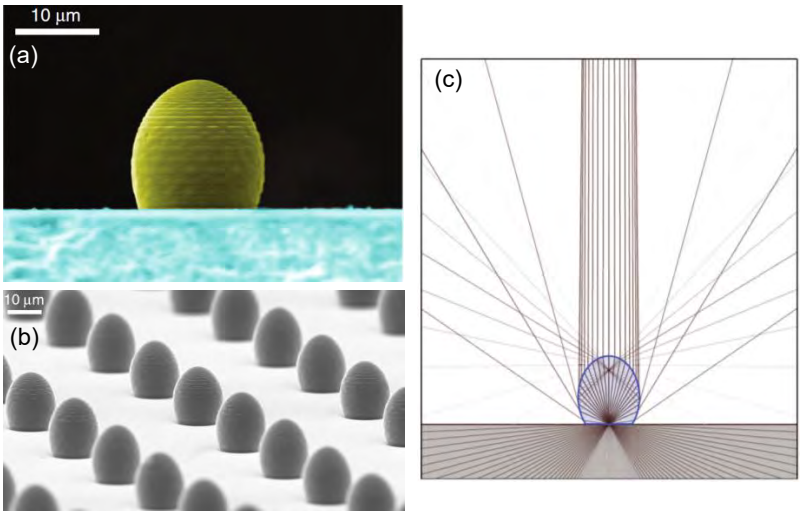

Figure 6.1: **SEM images and the operating principle of an ellipsoidal microlens designed for collecting emission from quantum dots and transition metal dichalcogenide monolayers.** (a) A SEM image of single solid immersion microlens printed on a flat substrate, and (b) a SEM image of an array of such microlenses. (c) Ray-tracing simulation illustrating propagation of the emitted light. The images were taken from the article [166].

6.2. Ray-tracing analysis of microlenses (for Fourier plane imaging)

In the literature [166], the focus was only on the collimation of light emitted from the structure and did not address the properties of the resulting Fourier plane. For this reason, this project began with a theoretical analysis of the Fourier planes in such microlenses.

A custom ray-tracing program was written in Python to analyze the propagation of light in polymer microstructures. This script, created in collaboration with M.Sc. Przemysław Oliwa, is based on classical geometric optics, where light propagation is determined by Snell's law of refraction. The program simulated the trajectories of light rays emitted at various angles and originating from different points within the structure, what allowed for evaluation of the optical performance for different microlens geometries.

The investigated microlenses had the shape of a solid rotational ellipsoid, cut off from the bottom by a plane perpendicular to its major axis (the plane marked gray on the panel), as presented in Fig. 6.2(a). In the simulations, the geometry was analyzed in cross-section along this major axis, which gave an ellipse, as shown in Fig. 6.2(b). Such ellipse is characterized by two dimensions: the major axis of total length $2a$, composed of two equal semi-axes a oriented along the z-direction, and the minor axis of length $2b$, composed of two equal semi-axes b

along the x-direction. In addition, the simulations included parameter d, which defined the vertical offset of the cut off plane relative to the center of the ellipse along the z-axis. This parameter could take positive or negative values. A positive d indicated that the ellipse was cut above its center, resulting in a microlens shorter than a half-ellipsoid. A negative d indicated the cut below the center, giving an elongated microlens shape. $d = 0$ corresponded to an exact half-ellipsoid, as indicated in Fig. 6.2(a). Adjusting d therefore directly controlled the microlens "height".

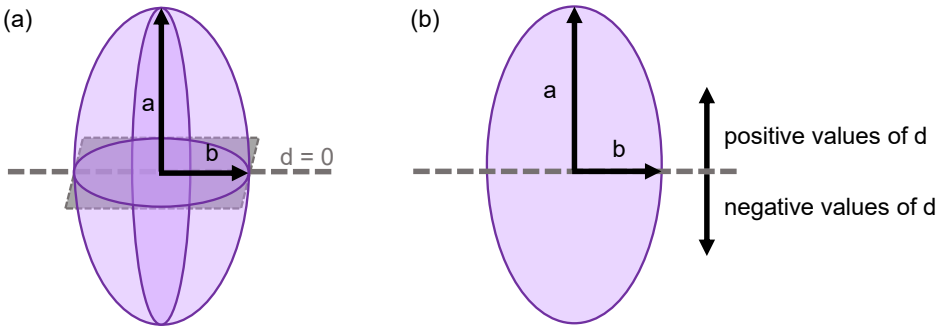

Figure 6.2: **Schematic illustration of the microlens shape and the definition of its geometrical parameters.** (a) Microlens as a rotational ellipsoid with the semi-axes a and b indicated, along with a gray plane representing the cut off of the ellipsoid to form the microlens d. Here, the cut off occurs at $d = 0$, i.e., exactly in the middle of the microlens height. (b) Cross-section through the center of the ellipsoid along its major axis, showing the semi-axes a and b and the variation of the parameter d. Shorter microlenses correspond to larger positive d values, while longer ones correspond to larger negative d values.

The simulations used real values of the optical parameters of the materials. The microlenses were made from a photocurable resin with a refractive index of $n = 1.52$. Refractive indices of the various layers that compose the optical microcavity, including Bragg reflectors (DBRs), barriers, and quantum wells, were also considered in the program. For SiO_2/TiO_2 and CdTe-based microcavities, the thicknesses of layers, barriers, and quantum wells, as well as refractive indices, were provided directly by the growers. For the GaAs-based microcavity, the layer thicknesses were determined from a scanning electron microscope (SEM) image, while the refractive indices at $T = 4.5$ K were taken from Ref. [167]. The paths of light rays propagating through the DBR layers, the microlens, and finally into the air were calculated using Snell's law at each material interface.

Figure 6.3 presents the operating principle of the Python program used to determine the Fourier plane. As shown in Fig. 6.3(a), the light source was located at the position of the quantum wells within the microcavity. To accurately reconstruct the Fourier plane, five to ten emission points were chosen within the quantum wells, separated along x-axis by approx. 0.01 µm. From each of these points, light rays were propagated in multiple directions, covering a wide range of emission angles. Rays emitted at the same angle [marked as red lines in Figs. 6.3(a)–(c)] from different starting positions intersected at points that were close to each other. In theory, only two such rays intersect exactly at the same point, but in the simulation several rays per one angle value were used. For each emission angle, the program calculated

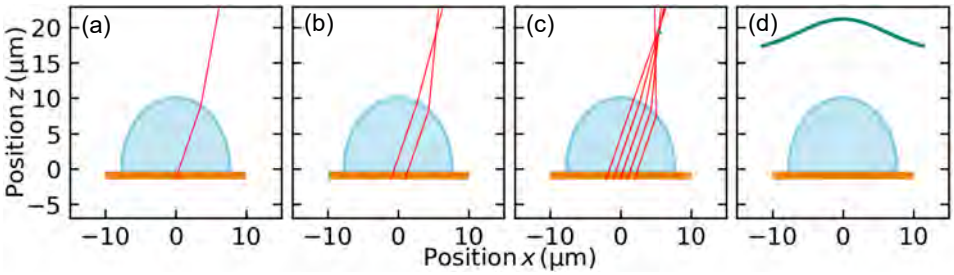

Figure 6.3: **Frames from the ray-tracing program illustrating steps in constructing the Fourier plane.** (a) A single ray (dark red line) propagating from the source, located at the center of the microcavity, through the DBR layers and the microlens. (b) Two rays emitted at the same angle, passing through the Bragg mirror and microlens, and intersecting at a single point. (c) Five rays emitted at the same angle from the structure, intersecting after exiting the microlens. The center intersection point is marked in teal. (d) The complete Fourier plane for the microlens, obtained by combining the intersection points determined for all considered emission angles.

the center intersection position of the rays [teal dot in Fig. 6.3(c)], which defined a single point of the Fourier plane for a given microlens geometry. Only the rays that intersected were taken into account. As shown in Fig. 6.3(d), repeating this procedure for all the emission angles considered results in the full Fourier plane (teal curve visible at a height of approx. 20 µm).

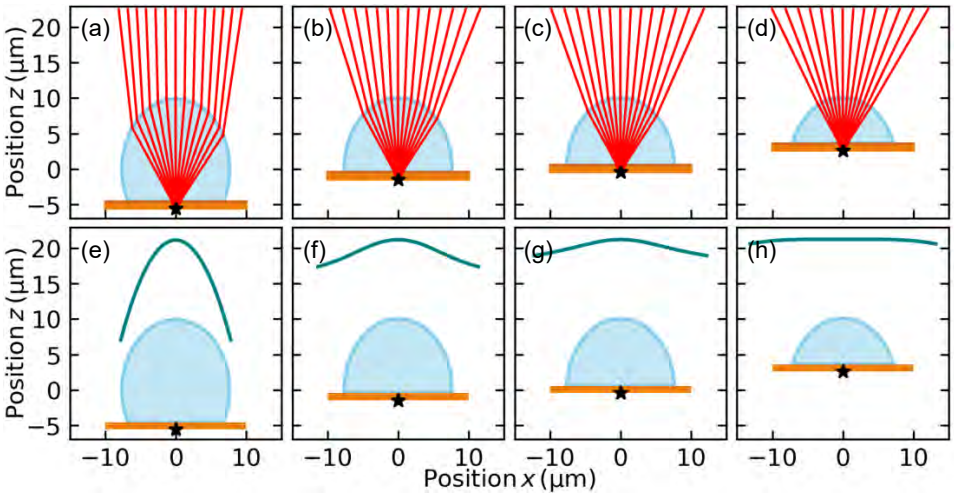

Figure 6.4: **Images generated using a ray-tracing simulation program.** The modeled microlenses have established values of semi-axes named a and b, while the cutting depth parameter d is varied. Panels (a)–(d) show how rays emitted at different angles from a single point within the structure propagate through the cavity and microlens with values of d from more negative (a) to more positive (d). (e)–(h) Corresponding shape of the Fourier plane (shown in teal).

The shape of the Fourier plane was investigated with varying parameter d, which controls the "height" of the microlens, while the parameters a and b were kept constant. This procedure is illustrated in Fig. 6.4, where the analysis began with microlenses having negative d values, corresponding to high geometries, and ended with the analysis of positive d values, corresponding to short microlenses. Figures 6.4(a)–(d) present trajectories of rays (dark red lines) emitted from the center of the microcavity (marked with a star). Figures 6.4(e)–(h) show the reconstructed Fourier plane (teal curves) of each microlens.

As seen in Fig. 6.4(a), very good collimation of rays is obtained. However, for the same microlens geometry, the Fourier plane shown in Fig. 6.4(e) is strongly elongated along the z axis, spanning more than 10 µm. On the other hand, in the opposite limit of large negative d [Fig. 6.4(h)], the Fourier plane becomes nearly flat, but at the cost of poor ray collimation, as visible in Fig. 6.4(d). These two extreme cases demonstrate that both ray collimation and Fourier plane shape vary significantly with d.

Based on the results of the simulations, it was found that overly convex microlenses (high positive values of d) produced an elongated Fourier plane and are characterized with limited angular collection range. In comparison, large negative values of d produced a broader k-vector range but resulted in a strongly curved Fourier plane. The optimal d range of -0.5 µm to 0.6 µm corresponded to a Fourier plane located approx. 7–13 µm above the top of the microlens [as shown in Figs. 6.4(f,g)], with the Fourier surface fitting within the depth of focus of the detection optics. This enabled the fabrication of microlenses that simultaneously provided a wide collection angle (NA $\approx$ 0.95) and minimal image distortion in reciprocal space.

The final dimensions of the microlenses, defined by the parameters a, b, and d for each investigated structure, are listed in the corresponding sections, where they are discussed in detail. With a numerical aperture of approximately 0.95, these microlenses offer a substantial advantage over conventional microscope objectives, whose numerical aperture values typically reach only about 0.6 (for those with WD $>$ 10 mm).

6.3. Printing of the microlenses by two-photon polymerization

The microlenses were fabricated directly on the surfaces of the investigated structures using two-photon photolithography. This process relies on the simultaneous absorption of two photons (typically in the infrared range) by a resin molecule. The combined energy of these two photons exceeds the threshold required to initiate the polymerization process. Due to the nonlinear nature of two-photon absorption, polymerization occurs only in the center of the focal point where the light intensity is the highest. As a result, the effective volume of such a 3D pixel, called a voxel, is smaller than the diffraction-limited focal point. This enables the fabrication of highly precise 3D structures with a resolution down to hundreds of nanometers [168, 169].

In this work, a *Photonic Professional* system (Nanoscribe, GmbH), shown in Fig. 6.5(a), was used, specifically designed for the high-precision fabrication of micro- and nanostructures using two-photon technology. As presented in Figs. 6.5(c,d), a photosensitive material, Nanoscribe's proprietary IP-Dip resin (refractive index $n = 1.52$) was used. This resin is optimized for use with high-numerical aperture oil-immersion objectives and is fully compatible

with the system's optics.

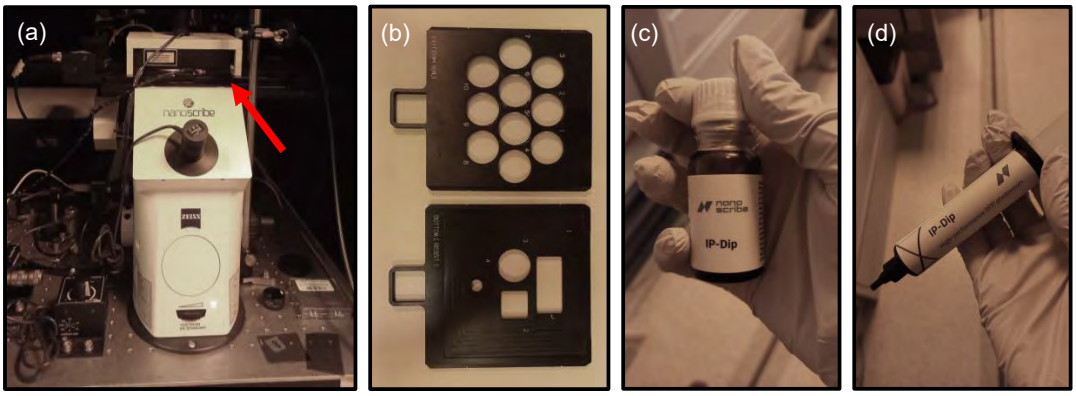

Figure 6.5: **Photographs showing the Nanoscribe system, sample holders, and the IP-Dip resin used for printing.** (a) The Nanoscribe system, in which the laser beam enters the device from below, and the red arrow indicates the location of the sample holder with the glued sample. (b) Sample holders used for attaching microscope slides, the one shown in the bottom part of the photo was used in this printing. (c, d) Packaging of the IP-Dip resist. The glass vial (c) contains the older version of the resin, equipped with a built-in measuring cup. The newer version of packaging (d) comes with a syringe-style dispenser for easier dosing.

The sample fabrication process begins by mounting a microscope slide in a dedicated sample holder [example holders are shown in Fig. 6.5(b)]. The sample is attached to the slide using a transparent glue. Once the glue cures, a single drop of IP-Dip resin is applied to the sample surface. The entire holder is then inverted and inserted into the printer mounting stage [marked with a red arrow in the photo from Fig. 6.5(a)]. A rotating turret allows for the selection of the objective. In this case, a Zeiss oil immersion microscopic objective of 100× magnitude with a NA of 1.3 was used. The scheme and the photography of the objective are shown in Figs. 6.6(a,b). The objective is designed to operate within the resin and provides both high resolution and a tightly focused beam, which is essential for efficient two-photon absorption.

As the microscope objective approaches the sample, it gradually immerses in the resin. Full immersion is critical for achieving correct beam focusing and ensuring that polymerization occurs only at the intended focal point. Once the focus is precisely adjusted along the z-axis (the printing depth), the microlens can be printed.

For the polymerization process, an external fiber-coupled femtosecond laser (Calmar Laser Mendocino) was integrated with the Nanoscribe system. The laser parameters used for polymerization were: wavelength $\lambda = 785$ nm, pulse duration of approximately 100 fs, and repetition rate of 50 MHz.

Before the printing process, the desired microlens geometry must be converted into a print-path .gwl file. It describes the trajectory that the laser follows within the resin (in the actual experimental configuration, the laser position is fixed while the sample holder is moving) to accurately reproduce the desired microlens shape. The print-path files were generated using a Python script initially written by Dr. Aleksander Bogucki and Dr. Łukasz

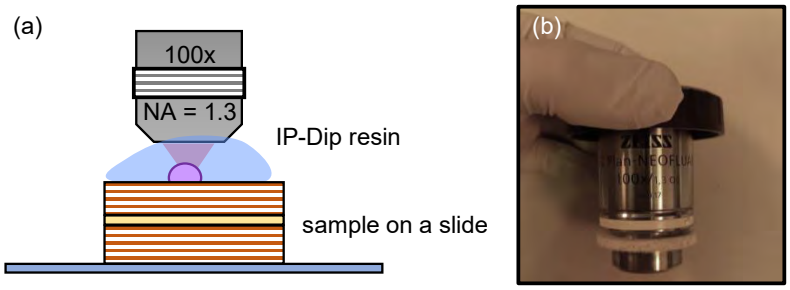

Figure 6.6: **Immersion microscopic objective used for printing in photoresist.** (a) Schematic illustration of how such a microscope objective enables microstructure fabrication inside the resin. (b) Photograph of the immersion objective used for microlens printing.

Zinkiewicz, and later modified by me to microlenses optimized for back focal plane imaging. As illustrated in Figs. 6.7(a)–(c), the microlens is printed using a spiral scanning pattern, with the spiral radius dynamically adapted to the shape of the structure.

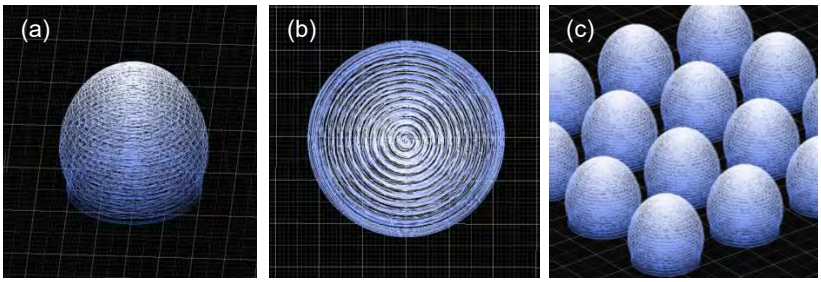

Figure 6.7: **Design of microlens printing based on a spiral pattern. The visualization was created in the DeScribe software.** (a) Close-up of a single microlens design, (b) top view showing the spiral trajectory used for layer-by-layer fabrication, (c) microlens array prepared in DeScribe for printing.

The generated print-path file is then imported into DeScribe, Nanoscribe's dedicated software. DeScribe allows for planning the layout consisting of multiple components, e.g. arrays of microlenses, markers, calibration grids, text labels, and other structures. The software also determines the laser power during polymerization. Next, the DeScribe software generates a complete file in .stl format, ready to be loaded into the device control program (NanoWrite).

In the next step, in NanoWrite, the control software for the Nanoscribe-printer, additional parameters affecting the printing precision can be configured, including print speed, axial resolution, initial coordinates, and tilt correction. The tilt correction is especially important when the sample is not perfectly flat. This procedure takes height measurements at 25 reference points and adjusts the focal plane during printing to maintain optimal focus throughout the entire microlens array area.

After all settings are confirmed, the laser initiates selective polymerization of the resin. Once printing is complete, the sample is developed by immersing it in appropriate solvents. The sample was immersed for 20 minutes in di(propylene glycol) methyl ether and then in

isopropanol. In our case, a magnetic stirrer was used to aid in the process. Finally, the sample was air-dried.

However, initial attempts at printing did not yield fully functional structures, primarily due to alignment issues within the optical system. For an extended period, the Nanoscribe printer had not been used, and the optical path required realignment. Ensuring that the laser beam entered the objective precisely along its axis and focused into a clean Gaussian spot was essential to achieve reproducible polymerization. The laser power also had to be recalibrated for the specific structures. Depending on the underlying material and geometry, the thermal conductivity of the substrate varied, requiring individual adjustment of the laser power. When the power was too low, the resin did not fully polymerize. However, if the power was too high, the resin overheated and even boiled, resulting in burned or damaged areas within the structure, which can be observed as black spots in the optical microscope images in Figs. 6.8(a)–(c). To remedy this, the central part of each microlens (inner spirals) was printed using one power level, while the outer layer of the spiral was printed twice using a slightly higher power to ensure that the structure was fully cured and mechanically stable.

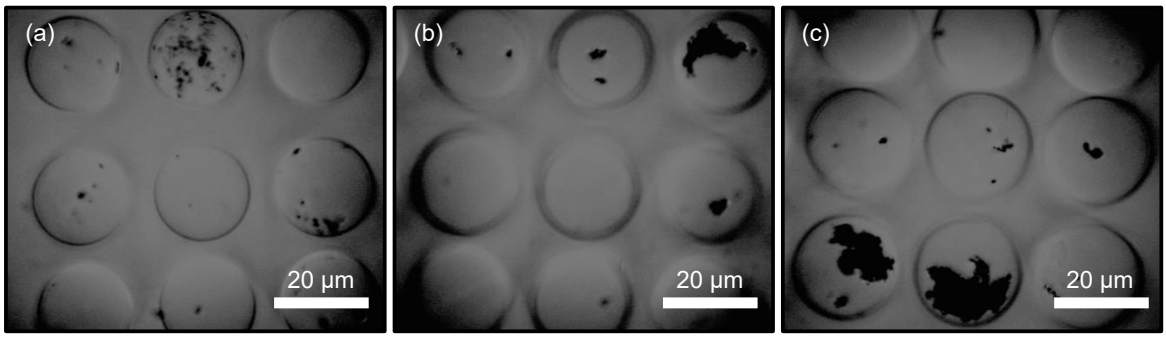

Figure 6.8: **Three example images of a microlens sample damaged during laser polymerization.** (a)–(c) Each black spot corresponds to resin that was burnt due to excessive laser power.

Initial prints, conducted after optical alignment was corrected, were performed on silicon substrates. The structures appeared to be printed correctly, judging by the images from the optical microscope. However, when they were examined under the scanning electron microscope (SEM), they resembled craters, only the outer layer was polymerized, whereas the inner volume remained as unpolymerized resin. This indicated improper laser power settings. To verify the quality of the print in detail, a thin gold layer (between 80 and 120 nm) was sputtered onto the sample surface to allow charge dissipation during SEM imaging. Selected SEM images of these early microlenses prints are presented in Fig. 6.9.

After appropriate laser powers were determined, print quality still required further optimization. The parameters selected within the software environment had a substantial effect on the final result. The most critical parameter was the print speed, which could be adjusted using the PerfectShape option. This feature offers three main modes: *Quality* – the slowest but most precise, providing the highest fidelity and smoothest surfaces, *Intermediate* – offering a less accurate printings compared to *Quality* mode and *Fast* – the fastest option, significantly reducing the total print time (by more than 50% compared to *Quality*), but at the expense of

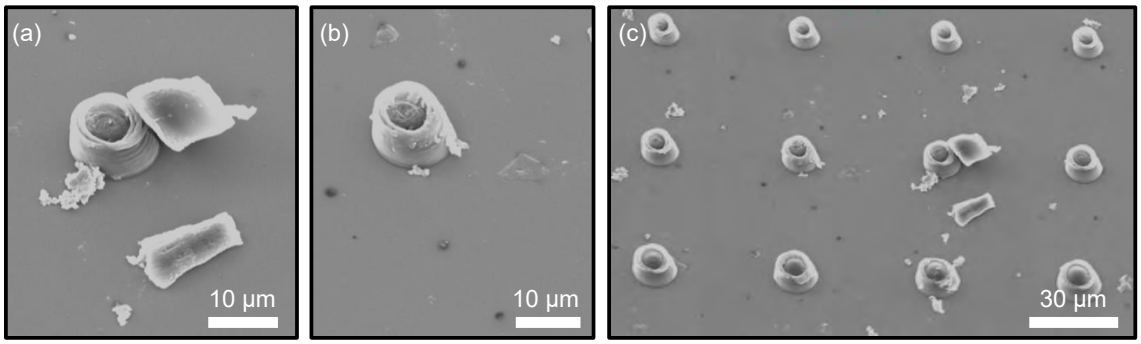

Figure 6.9: **First printed structures after initial laser beam alignment.** SEM images show craters and visible dirt around the printed area, resulting from incomplete polymerization. Only the outer resin layer was hardened, leaving unpolymerized fragments around the print.

fine detail reproduction and surface smoothness. The choice of mode directly affected the fabrication time and the quality of the printed structures.

Another issue encountered was related to the stitching at the point at which the spiral printing path ended. These artifacts were linked to mismatches between the spiral termination and the overall print speed, particularly when using the 'Fast' or 'Intermediate' modes. As shown in Figs. 6.10(a,b), if the process terminated too early, the outer layer of the microlens was incomplete. If it ended too late, excess material accumulated or distorted the structure's profile, what is visible in Figs. 6.10(c,d). To compensate, the spiral trajectory was artificially extended or shortened in the code, effectively allowing the spiral to "overlap" or end slightly before the nominal final radius.

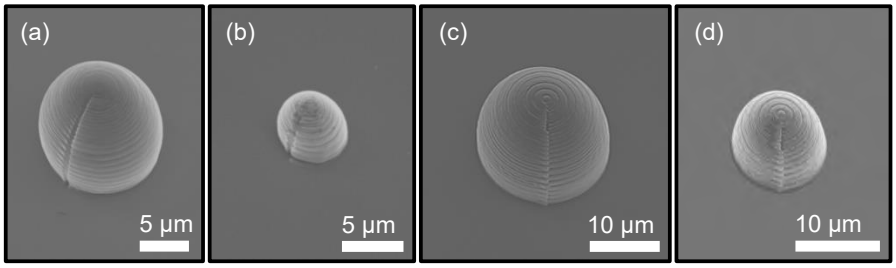

Figure 6.10: **Examples of prints requiring parameter tuning in the Nanoscribe software.** SEM images show stitching artifacts, in panels (a, b) the printing process ended too soon, and in panels (c, d) the process ended too late.

Figure 6.11 shows the final results, when the printing procedure was optimized by carefully selecting laser power, print speed, exposure modes, and stitching corrections. The resulting microlenses exhibited high surface quality, precise curvature, and minimal defects, as demonstrated in the final SEM images.

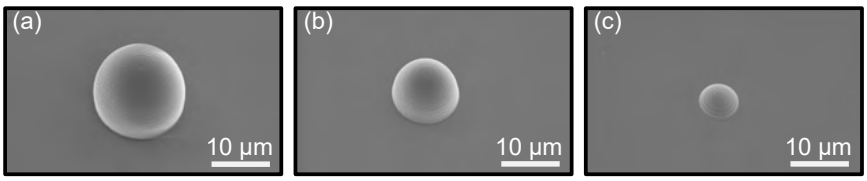

Figure 6.11: **Final, functional prints.** (a)–(c) Microlenses of different parameter d, fabricated using optimized laser settings and fine-tuned parameters in the Nanoscribe software.

6.4. Reciprocal space imaging with microlenses

Typically, reciprocal space (k-space) imaging uses high numerical aperture microscope objectives that perform a Fourier transform of the emitted light. In the resulting Fourier (back focal) plane, rays emitted at the same angle overlap to form the angular (momentum) representation of the emission. In a typical reciprocal space setup [Fig. 6.12(a)], the FP is projected onto the slit of a spectrometer or camera using so-called Bertrand lens followed by an imaging lens which forms the final image. This configuration has some limitations, especially in cryogenic experiments, where optical access to the sample is limited. In such cases, long working distance microscope objectives are used, which offer lower NA and therefore restrict the accessible emission angle range, resulting in reduced wavevector range.

In our case, the conventional microscope objective was replaced with an ellipsoidal microlens, directly printed on the sample. Each microlens collimates the locally emitted light, performing the same role as the microscopic objective. Its main advantage is the ability to collect light at emission angles up to 80 degrees in air (NA ≈ 0.95), by being directly attached to the sample surface. Such microlenses can also operate inside cryostats under cryogenic temperatures. The remaining optical components in the detection path follow standard configurations. In such a setup [Fig. 6.12(b)], the Bertrand lens in conjunction with the imaging lens projects the Fourier plane onto the detection element.

The main difference between using a conventional microscope objective and a polymer microlens lies in the physical size of the Fourier plane (FP). For a microscope objective, the FP diameter can be estimated as:

$$D_{\mathrm{FP}} = 2 \times \mathrm{NA} \times f, \tag{6.1}$$

where NA is the numerical aperture of the objective and f is its effective focal length. For typical objectives, this results in FP dimensions on the order of millimeters, in contrast to the micrometer-scale FP obtained with a microlens. This large discrepancy naturally suggests that using a microlens requires short focal length Bertrand lens. It is optimal to use high magnification microscope objectives to serve as the Bertrand lens. Proper microscope objectives also bring additional benefits, such as correction of chromatic and other optical aberrations, high optical quality, and improved field flatness. Although conventional microscope objectives can also play the role of the Bertrand lens, we tested both microscope objectives (5×, 10×, 20×, 50×) and standard biconvex lens (e.g., $f = 25.4$ mm) as Bertrand optics.

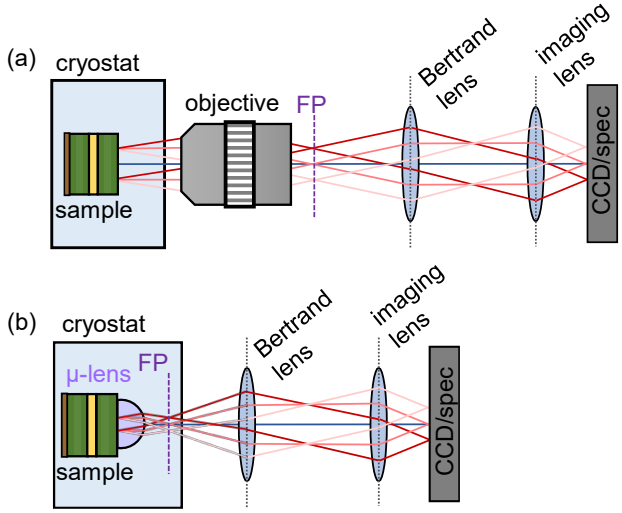

Figure 6.12: **Comparison of setups used for reciprocal space measurements.** (a) In the conventional configuration, a microscope objective collects the signal and performs a Fourier transform, with the Fourier plane (FP) located outside the cryostat. (b) In the modified configuration, a microlens acts as the microscopic objective, generating the Fourier plane inside the cryostat.

6.4.1. Dielectric SiO_2/TiO_2

The performance of the fabricated microlenses was tested using a reference SiO_2/TiO_2 microcavity structure. A detailed description of this structure (named Sample A) can be found in Appendix I, 7.1. This structure exhibits a distinct, deep cavity photon mode visible at room temperature. Because of that, it can be treated as a convinient model system for the experimental characterization of the accessible range of in-plane wavevectors (k) using microlenses.

Based on ray-tracing simulations, a microlens with parameters $a = 10.06$ μm, $b = 7.64$ μm, and $d = -0.44$ μm was selected. To experimentally validate the simulations, a series of microlenses was printed with similar values of a, b, and d, which are listed in Table 6.1. Halogen lamp reflectance dispersion maps were collected for each Fourier plane shape shown in Figs. 6.13(e)–(h). The corresponding experimental results are presented in Figs. 6.13(a)–(d), in each case, the upper panel presents the measured reflectivity dispersion relation, while the lower panel shows the corresponding Fourier plane. For the microlenses that are too tall [as shown in Figs. 6.13(a),(e)], corresponding to strongly negative values of the parameter d, the full dispersion curve cannot be captured in a single measurement. The curvature of the calculated Fourier plane in Fig. 6.13(e) extends significantly outside of the approx. 1 μm depth of focus of the Bertrand objective microscope (NA = 0.55, $f = 4$ mm and magnification 50×). The higher wavevector regions of the dispersion could be accessed by the adjustment of the focus of the Bertrand lens (microlens no. 1 in Table 6.1). A similar limitation was encountered for microlenses that were too flat [as in Figs. 6.13(d),(h)], i.e., with large positive values of d, where the smaller numerical aperture of the microlens caused a significant portion

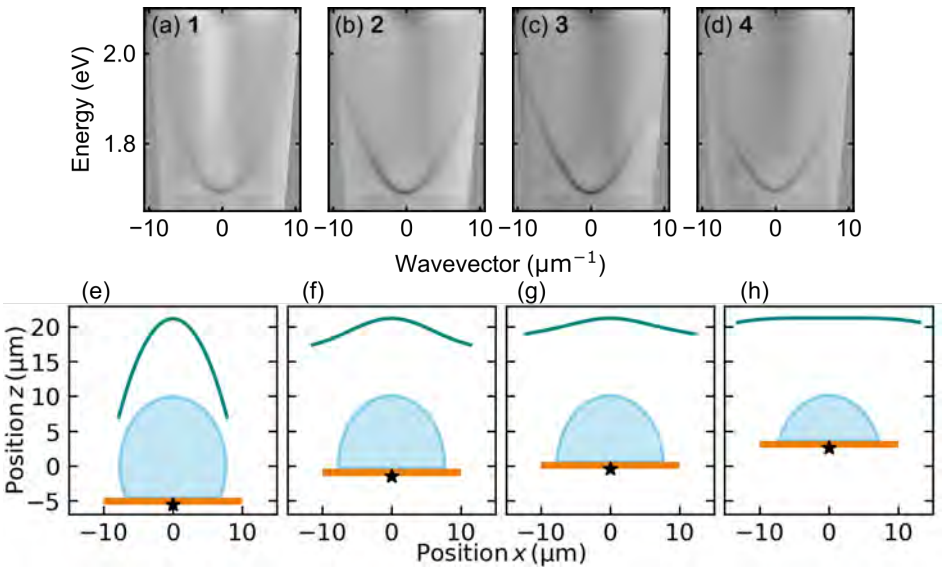

Figure 6.13: **Comparison of experimental reflectivity maps obtained for microlenses of varying heights. For each microlens, the corresponding Fourier plane profile is also shown.** (a) Reflectivity map for the tallest microlens (no. 1), corresponding to the Fourier plane shown in panel (e). Subsequent maps for microlenses no. 2 to 4 are presented in panels (b)–(d), with their respective Fourier planes shown in panels (f)–(h). Panels from (e) to (h) have already been shown in Fig. 6.4.

of rays to be lost, and the dispersion was again only partially visible (microlens no. 4). The most advantageous results were obtained for microlenses no. 2 and 3, which allowed clear observation of the dispersion, including for high in-plane wavevectors. It was demonstrated that the designed microlens (no. 2) provides the broadest angular (momentum) collection range while maintaining an appropriate Fourier plane profile.

The reflectivity dispersion obtained using the microlens was compared with that measured on planar (not fabricated) part of the cavity, using a long working distance microscope objective (NA = 0.55, magnification 50×) in a setup, which functioned as the Bertrand lens in the microlens-based configuration. The results are presented in Figs. 6.14(b,c). Additionally, as shown in Fig. 6.14(a), theoretical dispersion was calculated using the Berreman Method [170, 171]. To compare the experimental data more precisely, cross-sections of both

Table 6.1: Parameters of the microlenses printed on Sample A, from which dispersion was observed in white-light reflectance maps in reciprocal space.

No.	$a\,[\mu\mathrm{m}]$	$b\,[\mu\mathrm{m}]$	$d\,[\mu\mathrm{m}]$
1	9.92	7.62	−4.58
2	10.06	7.64	−0.44
3	10.07	7.65	0.58
4	10.11	7.66	3.61

the reflectivity maps were fitted with Lorentzian profiles to extract cavity mode energy at the corresponding wavevectors. A parabola was fitted to the data extracted from the photon dispersion in the planar structure. These were then plotted alongside the values extracted from the microlens-based measurements. As shown in Fig. 6.14(d), the data from the microlens setup align well with the fitted dispersion, validating the design and alignment of the system. The wavevector range accessible in the microlens system was equal to $(-10.12, 10.12)$ μm^{-1}, compared to $(-4.91, 4.91)$ μm^{-1} with the microscope objective. The figures also include dashed lines defining the numerical aperture range for the objective and microlens. The navy blue lines indicate the NA = 0.55 for the microscope objective, while dark red indicate the microlens aperture of approximately NA = 0.95.

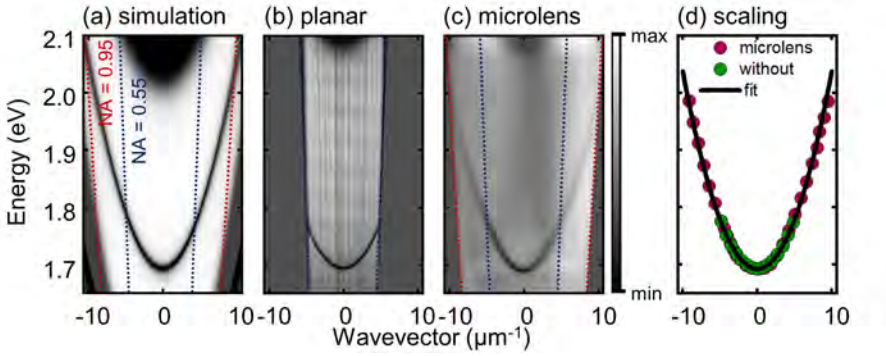

Figure 6.14: **Comparison of white-light reflectivity maps in reciprocal space for Sample A.** (a) Simulation performed using the Berreman Method, showing the numerical aperture of the microlens with dark red dashed lines and the numerical aperture of the objective with navy blue dashed lines (simulation by M.Sc. Przemysław Oliwa). (b) Dispersion relation for the planar structure, collected using the objective with the NA marked on the map, (c) dispersion collected using the microlens with its NA marked with dark red dashed lines, and, for comparison, the NA range of the objective from panel (b), overlaid with navy blue dashed lines. (d) Plot showing the extracted energies from the Lorentz fitting from both dispersions and the parabola fitted to the results of the planar structure. The dark green points come from the fitting to the mode from the planar structure, while the pink points come from the fit to the results collected using the microlens.

These results confirm that the microlens-based system enabled efficient imaging of a wide range of reciprocal space, including high-angle emission that is inaccessible via standard long-working-distance microscope objectives, typically used in cryogenic measurements. Here, Sample A microcavity served as an applicable reference system for evaluating microlens performance, and the used procedure provides a reliable calibration of the in-plane wavevector scaling for subsequent studies of more complex microcavity structures.

Importantly, the glass substrate of Sample A is transparent in the spectral range corresponding to its photonic cavity mode. This enables optical characterization not only in reflection but also in transmission geometry. To demonstrate the feasibility of working with microlenses in a transmission configuration, the sample was integrated into a measurement setup that allowed light to propagate through the structure. A schematic diagram of the

experimental setup is shown in Fig. 6.15(a). A halogen lamp served as the broadband light source for illumination. On the transmission side of the sample, a magnifying lens and a microscope objective with a magnification of 60× and numerical aperture NA = 0.7 were used to focus the transmitted light on the sample. The numerical aperture of this objective defined the maximum range of accessible in-plane wavevectors k, limiting the angular range that could be transmitted through the structure. On the detection side, an array of microlenses was printed directly onto the surface of the sample. A Dove prism on the detection line was used to precisely align the row of microlenses along the entrance slit of the spectrometer. A 10× microscope objective, which acts as a Bertrand lens, was used to image the Fourier plane of the microlenses.

The dispersion map acquired using this configuration is presented in Fig. 6.15(b). The resulting measurement clearly reveals distinct parabolic dispersions, corresponding to the transmission of white-light through individual microlenses. The signal visible between the parabolic dispersions corresponds to the light directly transmitted through the planar parts of the sample, outside of the microlenses. Importantly, this configuration revealed the coexistence of both real and reciprocal space information within a single dataset. While the light transmitted from regions outside the microlenses corresponded to a defocused, global real-space image of the sample, the signal collected through each microlens was Fourier-transformed, providing momentum-space information. This dual character requires interpreting such measurements within two coordinate systems: one describing the global real-space imaging and the other corresponding to the local reciprocal space generated by each microlens.

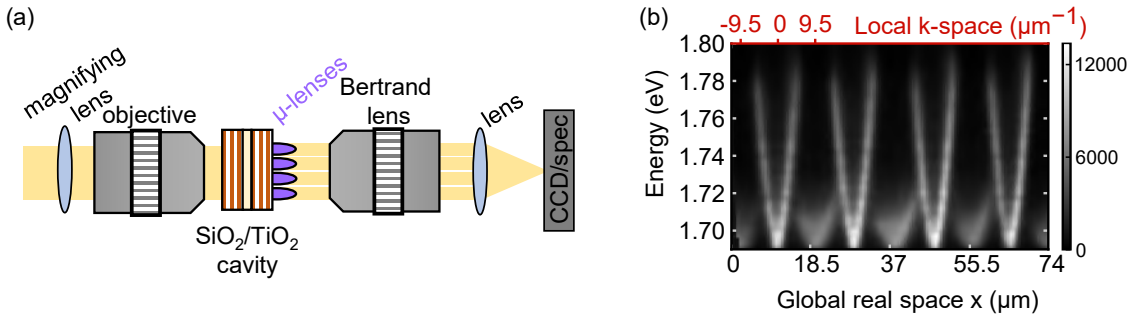

Figure 6.15: **Measurement of white-light transmission through microcavity Sample A, with a row of printed microlenses, conducted at room temperature.** (a) Schematic of the experimental setup used in the measurement. White-light was introduced into the cavity through a microscope objective. An additional magnifying lens was placed in front of the objective to increase the illuminated area. (b) Experimental results showing four dispersions measured simultaneously from four microlenses positioned vertically with respect to the spectrometer slit. A parasitic signal from the planar region of the cavity is visible between the microlenses, resulting from the uniform excitation of the entire sample surface.

6.4.2. Strongly coupled GaAs-based microcavity

Following the successful measurements of microlenses integrated with a dielectric microcavity structure, where they enabled high-momentum reciprocal space imaging and showed compatibility with standard microscope setups, the next step was to test their applicability in a more complex system. Specifically, the goal was to apply them in a GaAs-based microcavity system operating in the strong coupling regime at cryogenic temperatures.

For this purpose, measurements were performed on Sample B, which consisted of a GaAs/AlGaAs distributed Bragg reflector cavity with 12 $In_{0.05}Ga_{0.95}As$ quantum wells embedded between the mirrors. More details on the structure of the Sample B can be found in Appendix I, 7.1. This sample is characterized by very distinct and spectrally narrow polariton modes. The photoluminescence experiments were conducted under nonresonant excitation using a pulsed Ti:sapphire laser (Mira-900) with a wavelength of 785 nm (1.5794 eV) with the sample cooled to 4.5 K.

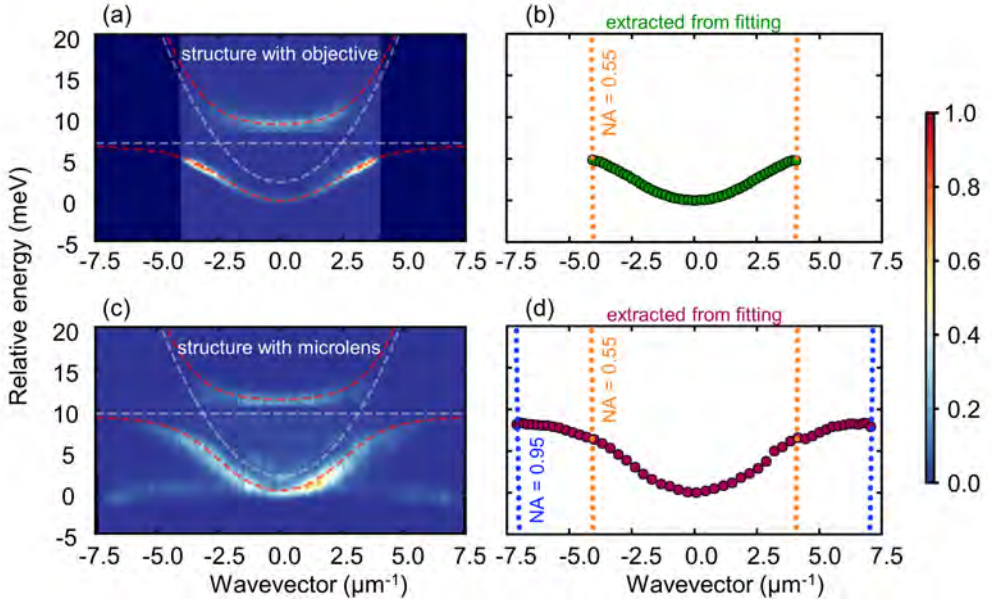

Figure 6.16: **Comparison of photoluminescence reciprocal space maps for Sample B between the planar microcavity measured using microscope objective and the microcavity structure with a printed microlens.** (a) PL map obtained from the planar structure using a microscope objective with NA = 0.55, with an applied coupled oscillator model. (b) Energy in the function of wavevectors parameters extracted by Lorentzian fitting of the lower polariton branch from panel (a) with numerical aperture of the objective marked with the orange dashed lines. (c) PL map of the microcavity with printed microlens, together with an applied model. (d) Emission maxima from Lorentzian fitting for the data shown in panel (c), with both marked numerical apertures of the objective (orange dashed lines), and microlens (navy dashed lines).

The initial measurements were carried out on the planar structure without any microlens. The collected signal was analyzed using a standard reciprocal space imaging configuration,

where a 50× microscope objective with a numerical aperture of NA = 0.55 was used to form the Fourier plane. Reciprocal space PL map is shown in Fig. 6.16(a). On the vertical axis the relative energy is shown, defined with respect to the minimum of the lower polariton branch. As seen in the map, a clear signal from the lower polariton branch appears in the range from 0 meV to about 5 meV. The wavevector range where this signal is visible extends between approximately $\pm 4.08\ \mu m^{-1}$. Outside this region the map is uniformly colored with dark-blue background, reflecting the absence of detectable signal beyond the numerical aperture of the objective. Notably, the signal from the lower polariton is much stronger at higher wavevector values, a phenomenon known in polariton physics as the bottleneck effect. It arises from the excitonic component of polaritons interacting with phonons, which are unable to provide sufficient energy and momentum transfer, causing particles to accumulate predominantly at large wavevectors. Above the relative energy of 9 meV, a signal originating from the upper polariton branch is observed over the same wavevector range. The intensity on the spectrum above 9 meV was multiplied by a factor of 20 due to the significantly weaker intensity of the upper polariton signal compared to that of the lower polariton. Characteristic anticrossing of the polariton modes, typical of the strong coupling regime, is visible in the spectrum. The data were then modeled using a coupled oscillator model (red dashed lines define polariton branches, and white dashed lines define photon and exciton modes), from which the Rabi splitting energy of 8 meV was extracted, along with the detuning between the bare photon mode and the exciton, $\delta = -4.7$ meV. Subsequently, the cross-sections along constant wavevector directions were fitted with Lorentzian profiles to extract the energy and in-plane momentum of the lower polariton (LP) branch. The obtained results are shown in Fig. 6.16(b). Only the LP branch was analyzed due to its higher visibility in PL spectra, which allowed for precise determination of the maximum detectable wavevector value which defines the numerical aperture of the collection optics. Unlike the upper polariton, the LP branch flattens near the exciton energy and signal extends over a broader k-space range. In this plot, the numerical aperture range of the objective (NA = 0.55) is also indicated with dotted orange lines, showing excellent agreement with the values obtained from Lorentzian fitting.

Subsequently, analogous measurements were performed on a region of the sample with a printed microlens on the surface. The microlens geometry had been previously optimized via ray-tracing simulations to match the structure. This time the 50× objective was used as the Bertrand lens to image the Fourier plane from the microlenses. Figure 6.16(c) presents the angle-resolved PL spectrum obtained in the configuration with a printed microlens on the microcavity surface. As in the measurement performed with the microscope objective, the vertical axis shows the relative energy, with its zero set at the minimum of the lower polariton branch. It was observed that printing the polymer structure on the microcavity surface introduced strain, resulting in a shift of the bare photon mode energy by 3.7 meV and of the exciton energy by 6.6 meV, therefore, the energy scales on the vertical axis were unified for both measurements. In this case, the signal from the lower polariton was observed in the range from 0 meV to about 9 meV. An important outcome was the much broader accessible wavevector range for the lower polariton compared to the dispersion measured with the microscope objective, the signal extended between $\pm 7.13\ \mu m^{-1}$. Furthermore, in contrast to the previous measurement, the lower polariton signal did not exhibit a bottleneck effect. This may be a result of the modified detuning caused by strain, which alters the curvature of the dispersion and changes the efficiency of phonon-assisted relaxation. As in the case of the

objective-based measurement, in order to extract the upper polariton signal, the intensity on the spectrum above 10 meV was multiplied, this time by a factor of 4. In the map obtained under excitation through the microlens, an additional symmetric signal was observed on both sides of the lower polariton dispersion, starting at approximately 0 meV and decreasing to approximately -2 meV at the edges of the map. This originates from the strain-induced photonic potential under the microlens, from which part of the polaritons relax into the planar cavity minimum.

Additionally, a coupled oscillator model was applied to the PL spectrum, yielding the dispersions of the upper and lower polariton branches (red dashed lines), along with the bare photon and exciton modes (white dashed lines). From this model, the detuning was determined as $\delta = -7.6$ meV, and the Rabi splitting energy as $\hbar\Omega = 8$ meV. Subsequently, as in the objective-based results, Lorentzian fits were applied to cross-sectional profiles, and the extracted LP energies as the function of wavevectors were plotted in Fig. 6.16(d). In this plot, the numerical aperture of the microscope objective used in the planar cavity measurement (orange dashed lines) and to NA = 0.95 expected for the microlens configuration (blue dashed lines) are also indicated. As can be seen, the LP signal obtained with the microlens matched perfectly with the theoretical calculation of the numerical aperture.

The results revealed a substantial extension of the accessible wavevector range with the microlens. While the planar configuration enabled observation of wavevectors within the range ± 4.08 µm^{-1} (corresponding to NA = 0.55 of the microspoce objective), the microlens allowed access up to ± 7.13 µm^{-1}, equivalent to NA ≈ 0.95.

An important feature of the microlenses is that they remain fully operational under cryogenic conditions, at vacuum levels of the order of 10^{-7} mbar, reliably withstanding such hard environments. After their robustness was confirmed, it was also verified that the use of microlens allowed efficient momentum-resolved detection of strong coupling regimes on the microcavity samples.

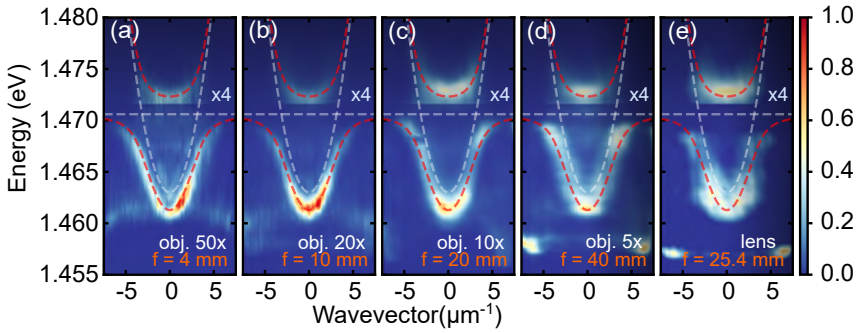

Figure 6.17: **Momentum-resolved photoluminescence maps of a GaAs-based microcavity measured at 4.5 K, with different Bertrand optics.** (a) Measurement using a microscope objective with focal length $f = 4$ mm (50× magnification). (b) Measurement using a microscope objective with $f = 10$ mm (20×). (c) Measurement using a microscope objective with $f = 20$ mm (10×). (d) Measurement using a microscope objective with $f = 40$ mm (5×). (e) Measurement using a simple biconvex lens with focal length $f = 25.4$ mm.

The next step involved evaluating the resilience of microlens Fourier plane measurements

on the imaging optics. Specifically, the use of microscope objective with high NA and short focal length (NA = 0.55, $f = 4$ mm, 50×) as a Bertrand lens in the detection path was replaced with microscope objectives or lens of increasing focal length and decreasing magnification. The motivation behind this was to enable the use of simple optical components. Typically, microscope objectives become increasingly expensive with magnification, while a simple focusing lens is significantly more affordable. These tests also allow to explore the limits of working distance achievable with microlenses, demonstrating that they can operate effectively even with long-distance optics. Due to the microscopic scale of the Fourier plane formed by the microlens (about 20 µm), its imaging required lenses or microscopic objectives with a relatively short focal length in order to obtain magnified image on the sensor.

Measurements were carried out using Bertrand optics with microscope objectives with effective focal lengths $f = 4$ mm (50×), $f = 10$ mm (20×), $f = 20$ mm (10×), $f = 40$ mm (5×), and a spherical bi-convex lens with $f = 25.4$ mm. The results of the measurements are presented in Fig. 6.17. The first measurement, shown in Fig. 6.17(a), displays the reciprocal space photoluminescence obtained using a 50× microscope objective with a focal length of $f = 4$ mm (the shortest tested in this series). As can be seen, both the lower and upper polariton branches are clearly visible. The lower polariton signal spreads between the energies of approximately 1.46 eV to 1.47 eV, while the upper polariton, which for better visibility was multiplied by a factor of 4, appears above 1.47 eV. The applied coupled oscillator model shows excellent agreement with the experimental data, and the same set of fitted parameters was used for the subsequent panels. The next result, obtained with a 20× microscope objective used as the Bertrand lens with $f = 10$ mm, is shown in Fig. 6.17(b). The observed polariton dispersion closely resembles that of the previous panel. No significant deterioration of the emission was observed, a broad wavevector range was still visible, and the polariton modes retained sufficient accuracy. The degradation of the dispersion quality began to appear in Fig. 6.17(c), measured using a 10× microscope objective with $f = 20$ mm as Bertrand lens. Here, a broadening of the lower polariton dispersion lines was observed. For the following measurement, presented in Fig. 6.17(d), performed with a 5× objective of $f = 40$ mm, the polariton lines were significantly broadened, and a reduction in signal visibility at higher wavevector values was evident. This objective had the longest focal length of all microscope objectives tested in this experiment. Nevertheless, it still allowed for reciprocal space imaging with reasonably high k-space resolution. The last optical element tested in the experimental setup with the microlens was a spherical bi-convex lens with $f = 25.4$ mm. Unlike microscope objectives, this lens lacked aberration corrections, which typically constitute a major advantage of microscope objectives, as they improve imaging fidelity and reduce distortions. The results obtained with the bi-convex lens are presented in Fig. 6.17(e). A pronounced broadening of the polariton lines was observed compared to the objective-based configuration, as well as a narrowing of the accessible wavevector range. Nevertheless, despite being a very simple optical element, the bi-convex lens used as a Bertrand lens still enabled the acquisition of polariton dispersion, while with much lower k-space resolution compared to microscope objectives. Another comment should be made on the signal visible at around 1.458 eV in Figs. 6.17(d,e), particularly intense at the map edges for large wavevectors. When using either the 5× objective or the bi-convex lens with $f = 25.4$ mm, the laser spot size exceeded the diameter of the microlens. As a result, the planar part of the microcavity was also excited in these measurements, producing emission at significantly lower energies than the polariton

modes excited using the microlens.

As expected, decreasing the magnification of the imaging optics resulted in reduced k-space resolution due to a smaller Fourier image being projected onto the camera, thus occupying fewer pixels. Nevertheless, clear polariton dispersion maps were still obtained even with the spherical lens. This demonstrated that, with the microlenses, high-quality momentum-resolved spectroscopy could be achieved without relying on bulky, high-NA microscope objectives, significantly simplifying the experimental setup and making it more compatible with cryogenic systems.

6.4.3. Parallel momentum-space mapping with microlens matrix

The results shown above demonstrated capturing of momentum-space resolved images using a single microlens. The purpose of the following research was to show that printed microlenses can not only replace conventional microscope objectives for wide-momentum reciprocal space imaging, but also enable simultaneous, parallel measurements across multiple spatial positions on a sample - a capability that, to the best of my knowledge, has not been demonstrated experimentally before.

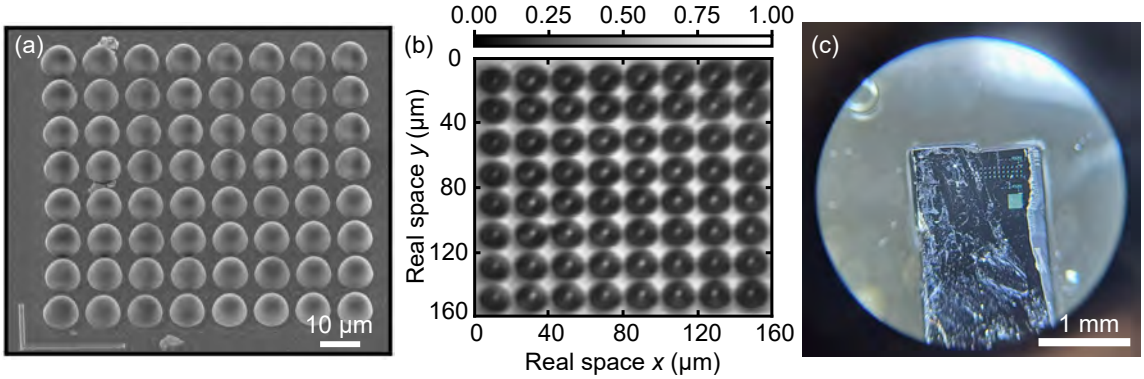

Figure 6.18: **Images of the printed array of microlenses for simultaneous imaging of 64 reciprocal spaces.** (a) SEM image of a test 8×8 microlens array printed on a silicon substrate. (b) Optical microscope image showing a top view of the printed microlens array. (c) Photograph of the array printed on the actual Sample B, captured through a standard laboratory microscope.

The main motivation for this approach is that each microlens provides momentum-space information from a well-localized region of the sample. By fabricating arrays of microlenses directly on the microcavity surface, it becomes possible to simultaneously probe multiple spatial positions and thus observe k-space dispersions from different regions in parallel. The compact size of individual microlenses, occupying only about 300–450 µm^2 of surface area each, further facilitates such integration, enabling scalable and multiplexed momentum-resolved measurements. Previous white-lamp transmission measurements performed on Sample A (presented in Fig. 6.15) had already shown that illuminating a few microlenses aligned in a row with a single broad beam allowed multiple dispersion relations to be captured simultaneously in a single spectrometer image. Building on this concept, the approach from an arrangement

of microlenses along one direction to two-dimensional array was extended, and demonstrated that photoluminescence measurements can also be performed in such a multi-microlens configuration.

To validate the fabrication process, a test matrix of 64 microlenses was first printed on a silicon substrate. As shown in Figs. 6.18(a,b), SEM and optical reflection imaging confirmed the successful and symmetric printing of all microlenses. In the next step, the same fabrication was repeated on the actual microcavity sample. After printing the matrix on Sample B, a photograph of the array was taken using a standard benchtop laboratory microscope with approximately 10× magnification, shown in Fig. 6.18(c).

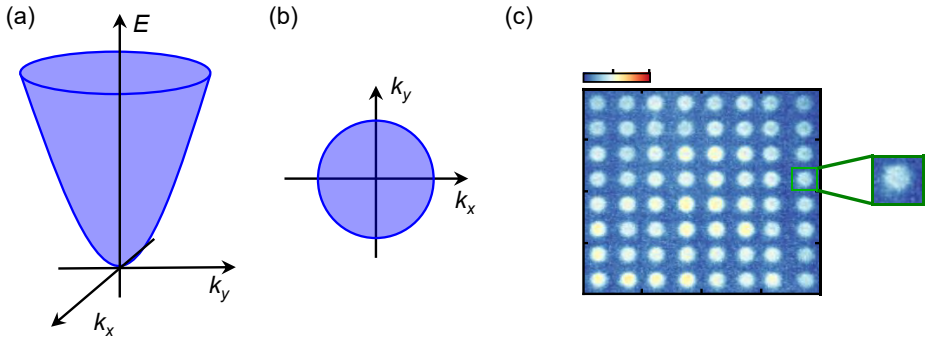

Figure 6.19: **Multiple reciprocal spaces mapping with a microlens array.** (a) Schematic three-dimensional dispersion relation of a parabolic mode. (b) Projection of the dispersion onto the (k_x, k_y) plane without energy resolution, forming a circle. (c) Experimental realization using Sample B with a microlens array. Simultaneous excitation of 64 microlenses produces an array of circles, each corresponding to a distinct reciprocal space image from an individual microlens.

To demonstrate what was achieved in the experiment, the following figures in this section present schemes illustrating the individual measurements. Figure 6.19(a) presents a schematic visualization of the two-dimensional dispersion relation for a mode with parabolic energy dependence. The x and y axes correspond to the wavevectors k_x and k_y, while the z-axis represents the energy. If such a two-dimensional dispersion is observed without energy resolution, its projection onto the (k_x, k_y) plane forms a circle, as illustrated in Fig. 6.19(b). Experimentally, such reciprocal space signals can be observed directly on the CCD camera. For this purpose, the Sample B with a printed array of 64 microlenses was cooled to 4.5 K in a cryostat and excited with a nonresonant laser beam. A lens was introduced into the optical path to expand the excitation beam into a Gaussian profile broad enough to uniformly illuminate the entire microlens array (approx. 160×160 µm). In this configuration, each of the 64 microlenses performed a Fourier transform of the local photoluminescence signal, producing 64 distinct Fourier planes corresponding to their spatial positions on the sample. These Fourier planes were then relayed through the detection optics, including the Bertrand and imaging lenses, and projected onto the CCD camera as simultaneously collected, separate polariton dispersions. A 10× microscope objective ($f = 20$ mm) was used as the Bertrand lens. As shown in Fig. 6.19(c), the simultaneous excitation of all 64 microlenses produced

an array of 64 circles, each representing an individual (k_x, k_y) space formed within a single microlens.

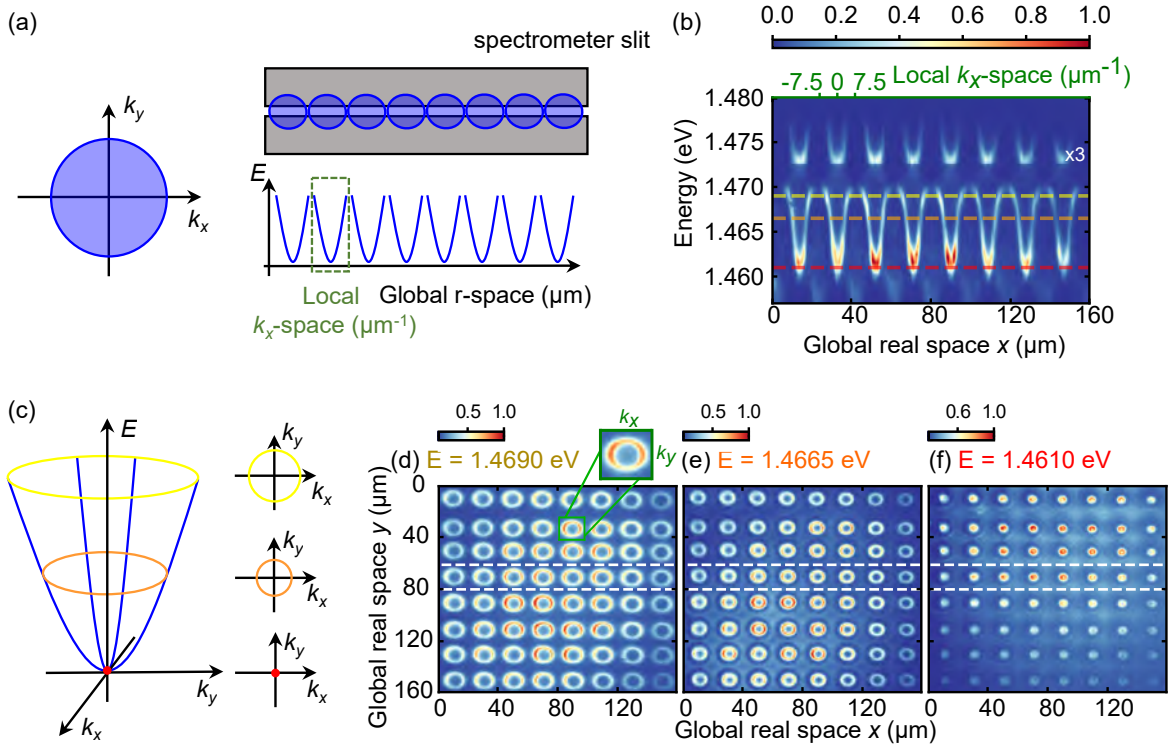

Figure 6.20: **Results demonstrating the use of microlenses to simultaneously capture multiple reciprocal spaces in a single measurement.** (a) A scheme showing how the reciprocal space (k_x, k_y) signal appears without spectral resolution, where the emission pattern takes the form of a circle, and each microlens produces its own such Fourier plane. The right side of panel presents eight of these reciprocal space images aligned vertically on the spectrometer slit, each positioned so that the center of its k_y-axis is located at the center of the slit. Each microlens produces a separate dispersion with its own local k-space axis, while the complete image, combining signals from multiple microlenses, is shown on the global real-space background. (b) Experimental result showing the dispersions collected with a spectrometer from eight independent locations on the sample, each covered by a separate printed microlens. (c) Schematic 3D visualization of the dispersion relation, with cross-sections taken at specific energies. Depending on the selected energy, the (k_x, k_y) cross-section appears either as a ring or as a single spot (at the dispersion minimum). (d)–(f) Experimental reciprocal space maps at constant energies. Those energies are also indicated by dashed yellow, orange, and red lines indicate in (b).

The physical interpretation of the signal outside the individual k-spaces is more complicated. Since the expanded laser beam was large enough to cover the full microlens matrix, it also excited the surrounding areas in a defocused manner. As a result, the collected image contained not only the 64 reciprocal space patterns but also a weak global background. For clarity, the axes in this image were labeled as "Global real space", similar to the description of the axis in

the measurement of transmission through a microlens (Fig. 6.15). Under full illumination of the microlens array, the real space of the sample was effectively observed, while focusing on a single circle provides access to the local (k_x, k_y) space generated by the corresponding microlens. This measurement demonstrated the feasibility of parallel observation of photoluminescence dispersions generated by the microlens array.

The next experimental concept was the simultaneous observation of multiple polariton photoluminescence signals from a microcavity with a printed microlens array, this time with energy resolution. This idea is illustrated schematically in Fig. 6.20(a). The left panel recalls the situation from the previous figure, where a single reciprocal space (k_x, k_y) image without energy resolution appears as a circle. When such a reciprocal space image is projected onto a spectrometer, the diffraction grating provides spectral resolution, allowing the measurement of energy-resolved reciprocal space. The right panel of Fig. 6.20(a) visualizes the case where, instead of a single reciprocal space image, several (in this case, eight) reciprocal space signals, each originating from a different microlens, are aligned along the entrance slit of the spectrometer. The top part of the sketch represents the spectrometer slit, with each violet circle corresponding to a reciprocal space image generated by a microlens. All eight circles are centered along the slit. The bottom part shows the expected spectrometer output: each circle should transform into a separate dispersion relation, so that the spectrometer simultaneously collects eight distinct polariton dispersions. As explained in the previous figure, each dispersion corresponds to a different location on the sample and is therefore described by its own "Local k-space" axes. However, when all dispersions are viewed together on the spectrometer, the horizontal axis is referred to as "Global r-space".

The experimental result with this configuration, obtained in a reflection geometry, is presented in Fig. 6.20(b). It was obtained by aligning eight microlenses along the spectrometer slit to simultaneously excite and collect emission from the microcavity in the strong coupling regime. The map clearly shows intense emission from eight lower polariton branches between 1.46 eV and 1.47 eV, as well as emission from the upper polariton branches above 1.473 eV. For better visibility, the part of the spectrum corresponding to the upper polaritons, i.e., above 1.473 eV, was multiplied by a factor of three. The weak signal between the individual polariton dispersions originates from polaritons relaxing from the minima of the dispersions modified by microlens-induced strains into the photonic potential minimum of the planar microcavity.

While energy resolution in reciprocal space imaging can be achieved with a spectrometer, here an alternative approach was applied to directly visualize constant-energy slices of the dispersion relation. Images at constant energy were collected at three characteristic energies: in the high-energy part of the lower polariton dispersion [yellow dashed line in Fig. 6.20(b)], at the center of the lower branch (orange dashed line), and at its minimum (red dashed line). This concept is illustrated in Fig. 6.20(c), which shows a schematic 3D view of the dispersion relation with cross-sections taken at specific energies, color-coded consistently with the map in Fig. 6.20(b). Depending on the selected energy, the (k_x, k_y) cross-section appears either as a ring or as a single spot (at the dispersion minimum). Short-pass and long-pass filters were used to obtain these energy slices, and the resulting single-energy reciprocal space maps were captured directly on a camera. As shown in Figs. 6.20(d)–(f), the first two slices revealed well-defined concentric circles of varying diameter, corresponding to different parts of the dispersion relation. As expected, at the dispersion minimum in Fig. 6.20(f), only small circular

spots were observed.

To verify the effectiveness of simplifying the detection optics, a similar experiment was conducted using a basic bi-convex lens with a $f = 25.4$ mm focal length as a Bertrand lens in place of the microscope objective. Despite the reduced resolution due to uncorrected aberrations, the main features of polariton dispersion were still observable, demonstrating that momentum-resolved reciprocal space measurements can be achieved using even the simplest optics, as shown in Figs. 6.21(a)–(d).

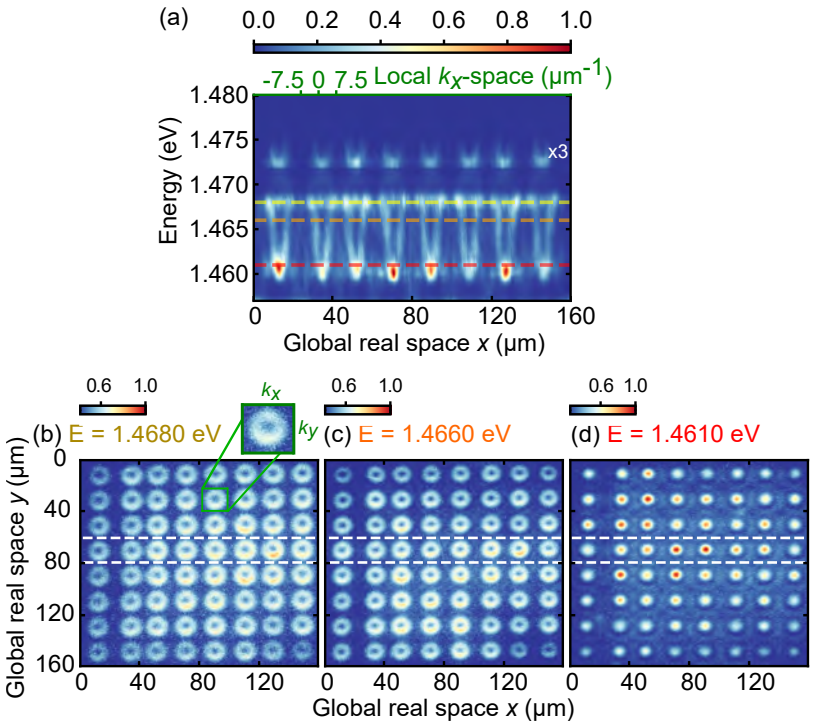

Figure 6.21: **Results demonstrating the feasibility of using only basic bi-convex lens as a Bertrand lens to image multiple reciprocal spaces within the same measurement.** (a) Experimental map of dispersions collected with a spectrometer from eight separate regions on the sample, each with a printed microlens, using a lens with $f = 25.4$ mm as the Bertrand lens. The yellow, orange, and red dashed lines mark the energies at which the experimental cross-sections were taken. (b)–(d) Cross-sections at selected energies through the dispersions. Depending on the chosen energy, the (k_x, k_y) cross-section is observed either as a ring or as a single spot located at the dispersion minimum.

Simultaneous imaging of arrays of independent polariton dispersions opens new experimental possibilities. It can significantly simplify the characterization of large samples, thanks to the straightforward capability to print multiple polymer structures across a large area. It is particularly promising for the study of heterostructures of transition metal dichalcogenides (TMDs), with Moiré patterns, patterned waveguides or photonic crystal arrays, where spatial variation plays a crucial role.

Additionally, adjusting the orientation of the microlens array relative to the spectrometer

slit allows collecting different cross-sections of the two-dimensional dispersion. As schematically illustrated in Fig. 6.22(a), in the conventional approach such a reconstruction is achieved by translating the final lens in the detection path, placed directly in front of the spectrometer slit. By translating this lens along the axis perpendicular to the slit, it becomes possible to acquire cross-sections of the full (k_x, k_y) dispersion relation. Specifically, as shown in Fig. 6.22(b), the spectrometer slit can be aligned to select different k_y values, in contrast to the standard case with $k_y = 0$, as represented by the two planes A and B to the left and right of $k_y = 0$. This procedure is visualized in Fig. 6.22(c) as the motion of the reciprocal space (k_x, k_y) image relative to the spectrometer slit. For a cross-section at plane A, the reciprocal space image is shifted to the right relative to the slit, and the dispersion minimum is observed at higher energy on the camera. When the (k_x, k_y) plane is aligned exactly with the slit, the dispersion with the true energy minimum is measured. Finally, when the reciprocal space image is shifted to the left, the observed dispersion minimum again appears at higher energy. In this way, reciprocal space tomography is performed by translating the lens in front of the spectrometer slit. Collecting multiple such maps and combining them into a single three-dimensional data cube enables a 3D reconstruction of the dispersion relation.

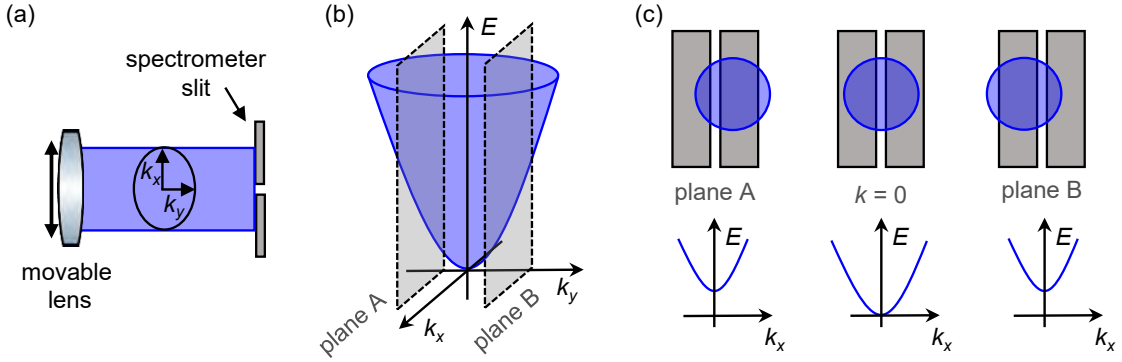

Figure 6.22: **Standard setup for reciprocal space tomography.** (a) Scheme showing how moving the final lens in the axis perpendicular to the spectrometer slit centers a different region of the (k_x, k_y) plane on the slit. (b) Parabolic dispersion with planes A and B marked on the left and right side of $k = 0$, corresponding to different selected wavevectors. (c) Illustration of how the (k_x, k_y) signal is positioned on the spectrometer slit for plane A, for $k = 0$, and for plane B, together with the corresponding shapes of the measured dispersion

Using a printed microlens array, different k_y parts of the polariton dispersion could be accessed simply by shifting the sample position. Because each microlens is integrated with the sample and acts as a miniature microscope objective, moving the sample therefore shifts the corresponding Fourier-plane image with respect to the spectrometer slit. This enables two-dimensional mapping of the dispersion. This concept is presented schematically in Fig. 6.23(a). To demonstrate this effect, a Dove prism was used to fine-tune the orientation of the image projected onto the spectrometer slit. This configuration is illustrated schematically in Fig. 6.23(b). The experiment began with all eight microlens reciprocal space (k_x, k_y) images aligned along the spectrometer slit so that each produced an identical dispersion pattern on the spectrometer. The sample position was then slightly shifted to move the microlens

signals away from the slit center, and the Dove prism was rotated to realign the microlens signals such that the last microlens was positioned at the slit center, while the first microlens corresponded to larger k_y wavevectors of the dispersion.

The resulting dataset in Fig. 6.23(c), shows the evolution of the dispersion appearance across consecutive PL maps from the microlenses. For better visibility of the upper polariton branch, the high-energy signal intensity was multiplied by a factor of three. The measurement was performed in a single acquisition, demonstrating that, as an alternative to moving the final lens in the detection path, it is possible to perform a tomography of the entire (k_x, k_y) dispersion by using an array of printed microlens. In these measurements, a 5× objective with $f = 40$ mm was used as the Bertrand lens, which limited the momentum resolution.

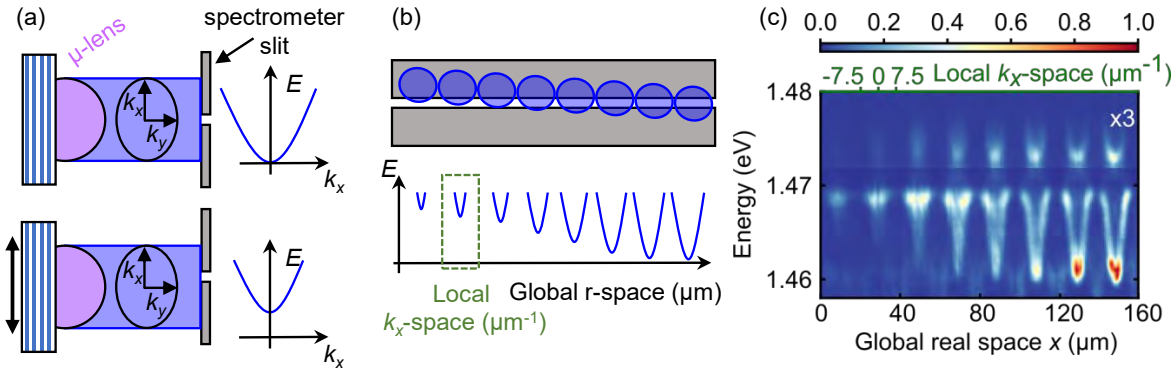

Figure 6.23: **Dispersion tomography performed using a microlens.** (a,b) Schematic illustration of the microlenses configuration used for a single accumulation (k_x, k_y) dispersion tomography measurement. (c) Experimental demonstration showing the evolution of dispersion from consecutive microlenses, collected in a single acquisition. This approach enables tomography of the full (k_x, k_y) dispersion, without moving the final lens in the detection path. In this measurement, a 5× objective ($f = 40$ mm) served as the Bertrand lens, resulting in limited resolution.

6.5. Microlenses for reducing energy required for achieving the condensation threshold

The measurements described in the previous section showed that polymer microlenses can operate at cryogenic temperatures (4.5 K) and are not damaged by exposure to pulsed picosecond laser excitation. Furthermore, their functionality in photoluminescence measurements had been confirmed, which motivated the extension of their application to another microcavity system operating under similar conditions. In the present study, the microlenses were printed on a new type of microcavity based on II-VI semiconductors, whose key feature is the ability to sustain exciton-polariton condensation, unlike the previously measured Sample B. An important characteristic of this structure, which supports the occurrence of the condensation, is the intrinsic photonic disorder, resulting from structural imperfections introduced during MBE growth. Although photonic disorder typically complicates the experiments, in the

context of non-equilibrium polariton condensates, it becomes advantageous as it enables localization of the condensate in photonic potential traps.

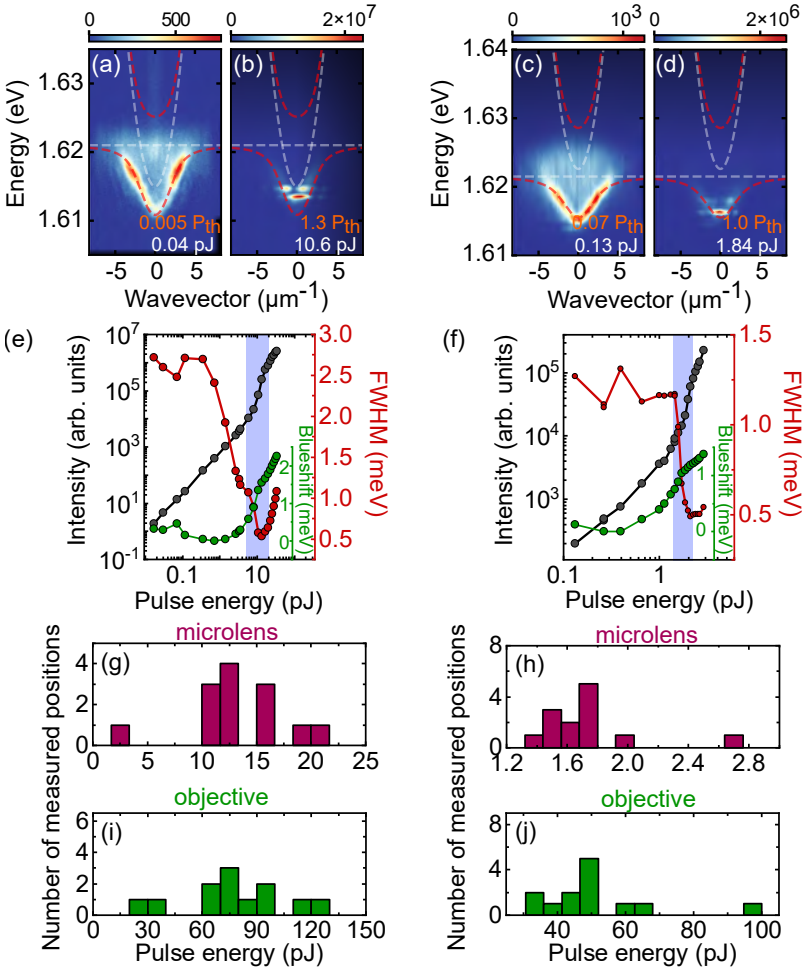

Figure 6.24: **The use of microlenses to reduce energy required for achieving the condensation threshold.** (a)–(d) Momentum-resolved PL spectra for two detunings in the CdTe-based sample, measured below and above the condensation threshold. Above threshold, emission localizes into discrete trap states, indicating condensation in potential minima. Dashed lines show applied coupled oscillator model. (e,f) Extracted from each dispersion and fitted with Lorentzian profiles condensate energy blueshift, linewidth (FWHM), and intensity with increasing excitation pulse energies. (g)–(j) Statistical analysis of condensation thresholds, dark green bars represent the standard configuration, pink bars correspond to the microlens configuration. Left panels show results for the first detuning, right panels for the second.

The studied sample was a microcavity based on CdTe, named Sample C.3. It consisted of two distributed Bragg reflectors made of alternating layers of CdZnMgTe and CdMgTe. Six CdTe quantum wells doped with Mn were placed between the mirrors. The detailed description

of the sample can be found in Appendix I, 7.1. The shape of the microlens was again designed using ray tracing simulations. Here, the microlenses were optimized for maximum excitation injection efficiency, resulting in the numerical aperture of this microlens close to 1. The obtained geometric parameters of the microlenses are: $a = 10.28$ μm, $b = 7.95$ μm, and $d = -0.21$ μm. This design allowed the excitation beam to be tightly focused close to the diffraction limit, where the large NA plays a role, making the system suitable for enabling the observation of a non-equilibrium Bose-Einstein condensate of exciton-polaritons at lower excitation powers.

Due to the significant spatial fluctuations of the photonic potential over small regions of the CdTe microcavity sample, the confirmation of the impact of microlenses on lowering the condensation threshold required a statistical approach. The studied microcavity had a thickness wedge along its entire length, which caused the detuning between the photonic and excitonic modes to vary with position. By selecting measurement regions perpendicular to the wedge direction, the detuning remained nearly constant, enabling the collection of statistical data under well-controlled conditions. Two representative detuning values were chosen [first detuning below and above the threshold is shown in Figs. 6.24(a,b), and second detuning is presented in Figs. 6.24(c,d)], and in each of these regions an array of microlenses was fabricated on the sample surface.

For each detuning, photoluminescence measurements were performed at 13 distinct positions using two excitation setups, a standard configuration, in which a microscope objective (NA = 0.55, 50× magnification) focused the excitation beam on the planar part near the microlens, and a microlens configuration, where the same objective served as a Bertrand lens while the excitation was focused by a microlens. The sample was excited with Coherent Mira-900 pulsed laser at wavelength $\lambda = 730$ nm (1.6984 eV), corresponding to the first Bragg minimum. For each site, a series of PL dispersions was measured with increasing excitation power, using the standard configuration and the microlens-based one. This procedure was repeated independently for the second detuning region, again collecting 13 pairs of datasets for each configuration.

In CdTe-based sample, the collected dispersions were less uniform than in GaAs-based structures. Furthermore, the strain introduced by the microlenses resulted in energy shifts of both: the cavity mode (by 0.6 meV) and exciton (by 1 meV), relative to the planar regions of the sample. As shown in Figs. 6.24(a)–(d), the coupled oscillator model was applied to dispersion relations for both detunings (parameters used for: first detuning: $E_{\mathrm{ph}} = 1.615$ eV, $E_{\mathrm{ex}} = 1.621$ eV, $\hbar\Omega_R = 0.013$ eV, $m^*_{\mathrm{ph}} = 1.1\times10^{-5}\ m_e$, and second detuning: $E_{\mathrm{ph}} = 1.6226$ eV, $E_{\mathrm{ex}} = 1.621$ eV, $\hbar\Omega_R = 0.013$ eV, $m^*_{\mathrm{ph}} = 1.1 \times 10^{-5}\ m_e$.). Above threshold, the emission clearly localizes into discrete trap states, indicating condensation in potential minima.

From each dispersion, a cross-section at $k = 0$ was extracted and fitted with a Lorentzian profile. This allowed to define the polariton energy blueshift, linewidth (FWHM), and intensity with increasing pump power, as shown in Figs. 6.24(e,f), as representative characteristics for both detunings. For every measurement, the signal was analyzed as a function of the laser pulse energy. The nonlinearity of the signal intensity with increasing laser pulse energy was then determined, and on this basis the condensation threshold was estimated for each measurement. The complete statistical analysis of the condensation thresholds for both detunings is presented in Figs. 6.24(g)–(j), where dark green bars correspond to the standard

configuration, and pink bars to the microlens configuration. The left panels show results for the first detuning, and the right panels for the second (x-axis scales differ between the microscope objective and microlens configurations).

The results confirm that microlens-based excitation reduces the energy required to reach the condensation threshold compared to the conventional setup. This improvement exceeds the reduction expected from simple diffraction-limited focusing: for the first detuning the threshold decreased approximately 7 times, and for the second 25 times. Under the diffraction-limited conditions, the excitation spot area is reduced from approximately 2.1 μm^2 for the NA = 0.55 objective to approximately 0.6 μm^2 for the high-NA microlens. While a substantial part of the threshold reduction is consistent with the smaller excitation area imposed by the diffraction limit (3.5×), the observed factors of 7× and 25× indicate additional mechanisms beyond pure geometric focusing. First, printed microlenses induce local strain, which shifts the cavity mode and exciton energies and thereby modifies the detuning. Second, unlike a microscope objective designed to focus in air, the microlens geometry is optimized for propagation through high refractive index DBR layers, providing improved focusing directly at the quantum-well plane. Third, the immersive properties of the microlenses can lower Fresnel reflection losses by providing an intermediate refractive-index layer, in place of high Δn air-semiconductor interface. The enhanced focusing efficiency, combined with the localization effects in the traps, makes microlenses promising platform for studying nonlinear polariton phenomena at excitation powers significantly lower than those required in standard microscopy configurations.

6.6. Summary

The aim of this Chapter was to introduce polymer microlenses as a tool for enhancing the excitation efficiency and improving the optical access to exciton-polariton microcavities. Both those properties are essential for exploring nonlinear effect, such as Bose-Einstein condensation at low excitation powers. The main goal was to develop an integrated optical platform enabling efficient excitation and light collection under cryogenic conditions, where conventional high-numerical-aperture objectives are limited. To achieve this, the specifically designed elliptical polymer microlenses were fabricated directly on the surface of semiconductor microcavities, offering a compact and efficient alternative for both excitation and reciprocal space imaging.

Ray-tracing simulations were used to optimize the microlens geometry to ensure access to a wide range of in-plane wavevectors while preserving the undistorted Fourier-plane mapping. The two-photon polymerization method provided reproducible fabrication of microlenses with controlled curvature and high optical quality.

Experimental measurements in various types of microcavities confirmed that the microlenses can not only replace bulky external microscope objectives but also extend the accessible k-space range, allowing observation of dispersion features that are otherwise inaccessible with standard optics. This improvement directly translates into improved control of excitation conditions and enhanced detection sensitivity, which are crucial for studying nonlinear polariton dynamics. Arrays of microlenses further expanded the experimental capabilities, allowing for the simultaneous collection of multiple dispersions, a concept referred to here as polariton multiplexing.

In the investigated CdTe-based cavities, the integration of microlenses resulted in a more efficient light extraction and a noticeable reduction of the excitation threshold for exciton-polariton condensation, confirmed by statistical measurements across varying exciton-photon detuning. This demonstrates that polymer microlenses are not only a practical solution for optical access but also a tool that enables new experimental regimes of low-power nonlinear polariton physics.

In summary, the work presented in this Chapter introduces a novel, energy-efficient optical platform that combines precise reciprocal space imaging with the ability to control polariton systems in ambient and cryogenic environments. The introduced approach opens new possibilities for exploring nonlinear phenomena and scalable polariton architectures where local optical elements define excitation, detection, and coupling in a single integrated structure.

Chapter 7

Summary

The dissertation is devoted to nonlinear effects in exciton-polariton condensates realized in CdTe-based semiconductor microcavities, demonstrating this II-VI material system as a versatile platform for exploring the interplay between light-matter coupling and material-specific characteristics. Across the Chapters, nonlinear effects are both the subject of investigation and a resource enabling more complex phenomena. Two main effects of non-equilibrium Bose-Einstein condensation and optical bistability, serve as key manifestations of polariton-polariton interactions and form the foundation of the presented studies. All developed methods and device architectures were conceived to either reveal or control these nonlinear behaviors, allowing exploration of regimes previously unreachable in exciton-polariton systems.

A defining feature of the II-VI microcavities is the intrinsic inhomogeneous photonic potential landscape originating from growth-related disorder. Rather than treating this as a limitation, the thesis demonstrates how it can be harnessed to facilitate polariton condensation by spatially localizing polaritons in natural photonic traps and to engineer coupling between them. This structural disorder can act as a natural environment for coupled polariton condnsates, offering an experimentally accessible route toward the creation of engineered polaritonic lattices and networks. Additionally, these localization and coupling properties are further explored in Appendix II, where interactions between three condensates trapped in separate potential minima are analyzed, providing insight into complex coupling geometries.

The thesis then introduces new types of optical bistabilities in transmissive CdTe-based microcavities. The first bistability featured a hysteresis loop with the conventional shape and direction known from other microcavities, although it emerged at an uncommon laser detuning, while the second, newly identified "triangular" hysteresis exhibited an unusual opposite switching direction. That observation was possible only because of the specific fabrication: a lift-off process, which allows transmission measurements not available in standard designs. Systematic power-dependent studies revealed bistable switching mechanisms associated with a thermally driven transition between the strong and weak coupling regimes. A proposed theoretical model that incorporates redshifts and Rabi splitting reduction reproduced the observed hysteresis and identified the physical origin of this unconventional bistability. This constitutes the first observation of bistability in a II-VI microcavity governed by a coupling-regime transition, in contrast to the established description based on Kerr-type nonlinearities. Moreover, the controllable transition between the strong and weak coupling regimes provided

access to an exceptional point in the polariton dispersion. Here, the experimental encircling of the exceptional point in the parameter space trajectories was used to trace the topology of the surrounding energy branches.

The dissertation further demonstrates magnetic-field control over the spatial parity of a polariton condensate supermode. It exploits the giant Zeeman effect in a semimagnetic CdTe microcavity with Mn-doped quantum wells. The magnetic field modifies the detuning and effective masses of the spin-polarized polariton branches, driving a transition between in-phase and anti-phase parity of condensate supermodes. The results expand the known means of controlling coherent coupling in light-matter systems. They reveal that external magnetic fields can reconfigure not only spin but also spatial symmetry of condensate modes as an important step toward magnetically tunable polaritonic architectures and reconfigurable optical elements.

A dedicated part of the dissertation presents the development of polymer microlenses printed directly on microcavity surfaces. Designed through custom ray-tracing simulations, these microlenses combine the focusing efficiency of high-numerical-aperture objectives with the compactness and applicability under cryogenic conditions. They enable local excitation, high-resolution and multiplexed reciprocal space imaging, from different spatial positions. Beyond expanding measurement capabilities, the microlenses reduce the energy needed to achieve condensation thresholds and enhance light extraction, providing an experimentally scalable route toward low-power polariton devices. The developed technology constitutes a new optical platform for spatial control over condensate sites, paving the way for the realization of interconnected polariton circuits and networks of coupled condensates.

Together, the dissertation establishes several original contributions to the understanding of nonlinear properties of exciton-polariton systems. It identifies new bistability mechanisms governed by transitions between the weak and strong coupling regimes on demand, demonstrates the feasibility of magnetic control over condensate spatial symmetry, and introduces integrated microlenses that enable energy-efficient access to nonlinear regimes. From a scientific perspective, these results deepen the understanding of how nonlinearity, and external control parameters intertwine in hybrid light-matter systems. From an application viewpoint, the developed methods open pathways toward energy-efficient, reconfigurable polaritonic devices, including optical switches, coupled-condensate networks, and magnetically controlled elements for information processing. The perspectives opened by this work include further exploration of band topology around exceptional points in non-Hermitian polariton systems, active control of condensate synchronization via local optical or magnetic fields, and the development of integrated architectures combining CdTe microcavities with on-chip microoptical elements. The demonstrated combination of material-specific advantages and purpose-built tools marks CdTe-based microcavities as a uniquely adaptable platform for studying and harnessing nonlinear phenomena in polariton condensates.

7.1. Appendix I: Description of the microcavity samples

This Appendix details the investigated samples. Depending on the material platform, the samples were divided into three groups: Sample A (dielectric SiO_2/TiO_2), Sample B (based on GaAs), and sample C (based on CdTe).

7.1.1. Sample A

Sample A was a dielectric stack composed of five pairs of SiO_2/TiO_2 Bragg layers that form the top and bottom reflectors grown on a transparent fused silica. The central cavity layer was made of SiO_2. Sample A did not contain an active emitter layer. It exhibited a well-defined cavity mode and allowed reliable reflectance and transmission measurements through the structure. The microcavity was designed for a central wavelength of $\lambda_0 = 732.77$ nm and operated at room temperature. This microcavity sample was grown using the electron-beam deposition technique, in which a high-energy electron beam is directed onto a target material, causing localized heating and evaporation. The resulting vapor then condenses on the substrate in a controlled manner, forming alternating dielectric layers that constitute the Bragg mirrors. The sample was grown by Dr. Janusz Kubrak from VIGO Photonics.

A schematic of the structure of sample A is shown in Fig. 7.1(a), while Fig. 7.1(b) presents a photograph of the cavity attached to a holder that enabled transmission measurements. This cavity was commonly used in experiments for the calibration of the optical setup, as its well-defined cavity mode allows characterization of the reciprocal space and the accessible k-vector range of a given microscope objectives. Specifically, it was used to calibrate the reciprocal space imaging system based on polymer microlenses, which is described in Chapter 6, "Polymer microlenses for optical microcavities."

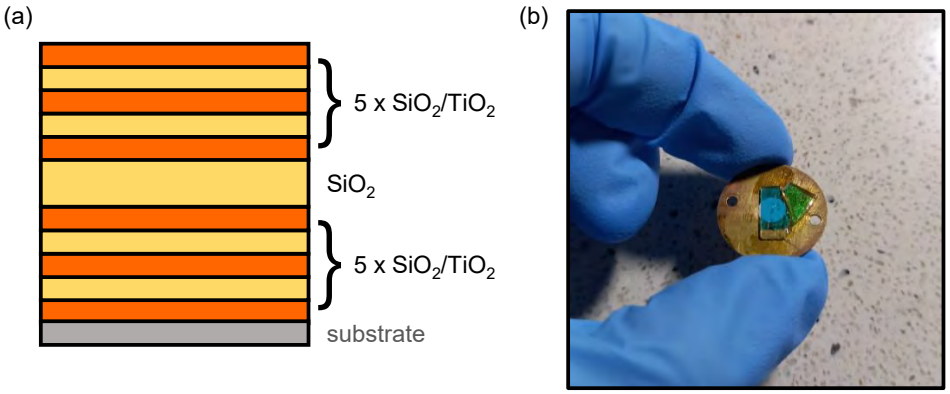

Figure 7.1: **Structure of Sample A dielectric microcavity.** (a) Schematic illustration of the SiO_2/TiO_2 cavity. (b) Photograph of the actual microcavity mounted on a holder enabling transmission measurements.

7.1.2. Sample B

GaAs-based Sample B was grown using MBE in the group of Prof. Benoit Deveaud at École Polytechnique Fédérale de Lausanne and was fabricated from group III-V semiconductors, mainly based on gallium arsenide (GaAs).

A scheme of Sample B is shown in Fig. 7.2(a) indicating the Bragg mirrors and quantum wells. Figure 7.2(b) presents a SEM image of the sample taken at the Centre of New Technologies, University of Warsaw, by Dr. Marta Bilska. The structure consisted of distributed Bragg reflectors (DBRs) made of alternating GaAs and AlAs layers. The bottom

DBR comprised 15.5 GaAs/AlAs pairs, while the top DBR contained 12 pairs. The GaAs cavity layer contained four groups of three $In_{0.05}Ga_{0.95}As$ quantum wells. The entire microcavity was designed for a central wavelength of $\lambda_0 = 860$ nm.

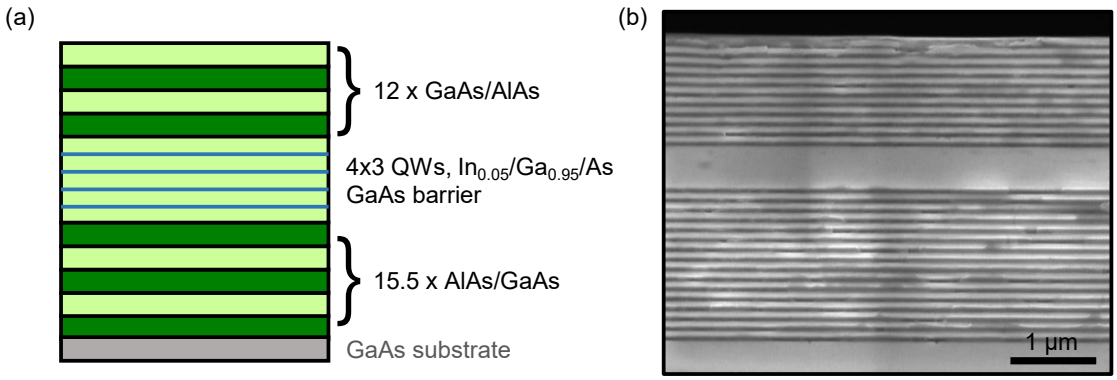

Figure 7.2: **Structure of Sample B microcavity.** (a) Schematic illustration showing the GaAs-based microcavity with a description of its composition. (b) SEM image of the sample, taken at the Centre of New Technologies, University of Warsaw by Dr. Marta Bilska.

7.1.3. Samples C.1, C.2 and C.3

The second type of semiconductor microcavities, denoted as Sample C.1, Sample C.2, and Sample C.3, was made of group II-VI compounds based on doped cadmium telluride (CdTe). These structures were designed and grown in the Molecular Beam Epitaxy (MBE) Laboratory at the Faculty of Physics, University of Warsaw, by Prof. Wojciech Pacuski and Dr. Bartłomiej Seredyński.

The structures of the CdTe-based microcavities are presented schematically in Figs. 7.3, 7.4, 7.5. These samples differ in their substrates, buffer layers, and mirror compositions, but share a common design principle with embedded CdTe:Mn quantum wells separated by appropriate barriers.

Figure 7.3 shows Sample C.1, which is a transmissive microcavity exfoliated onto a transparent Al_2O_3 substrate. The top mirror consisted of 20 pairs of $Cd_{0.88}Zn_{0.04}Mg_{0.08}Te/Cd_{0.52}Mg_{0.48}Te$ layers, while the bottom mirror consisted of 20 pairs of $Cd_{0.52}Mg_{0.48}Te/Cd_{0.88}Zn_{0.04}Mg_{0.08}Te$. Within the cavity, three double CdTe:Mn quantum wells were placed, separated by $Cd_{0.88}Zn_{0.04}Mg_{0.08}Te$ barriers. The design wavelength of this structure was $\lambda_0 = 820$ nm. This sample was characterized and used to measure the optical bistability effect, described in the Chapter 4, "Optical bistability in transmissive II-VI microcavities."

Figure 7.4 presents Sample C.2, a non-transmissive cavity grown on a 3-inch GaAs:Si (100) substrate. The structure included a GaAs buffer, followed by ZnSe and ZnTe buffers. The bottom Bragg mirror was composed of 19 pairs of $Cd_{0.35}Mg_{0.65}Te/Cd_{0.874}Zn_{0.033}Mg_{0.093}Te$ layers, while the top mirror contained 16 pairs of $Cd_{0.874}Zn_{0.033}Mg_{0.093}Te/Cd_{0.35}Mg_{0.65}Te$ layers. Within the cavity, three pairs of CdTe:Mn quantum wells were embedded, with $Cd_{0.874}Zn_{0.033}Mg_{0.093}Te$ barriers. The structure was designed for a central wavelength of

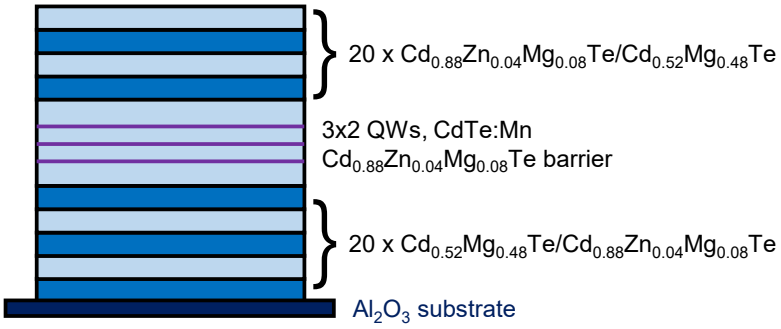

Figure 7.3: **Schematic structure of transmissive CdTe-based microcavity, Sample C.1.** CdTe-based microcavity exfoliated onto an Al_2O_3 substrate, designed for $\lambda_0 = 820$ nm.

$\lambda_0 = 780$ nm. This sample was characterized and used to measure ballistic condensates in a magnetic field, described in Chapter 5, "Magnetic field control of exciton-polaritons condensate supermode parity", and to investigate the interaction between three polariton condensates located in the photonic potential minima on the sample, described in Chapter 3, "Three coupled polariton condensates in complex potential landscapes."

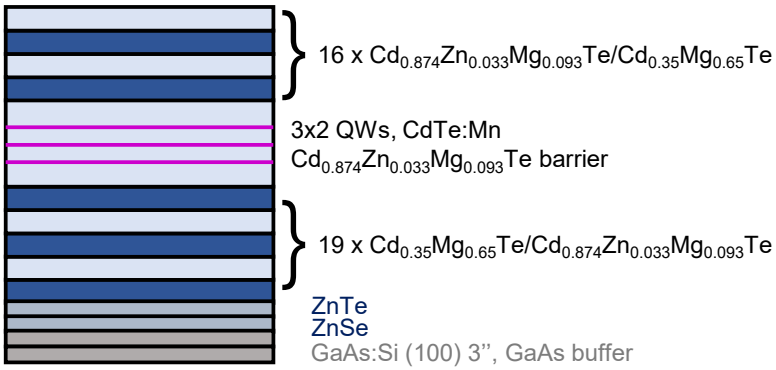

Figure 7.4: **Schematic structure of CdTe-based microcavity, Sample C.2.** Non-transmissive CdTe-based microcavity, designed for $\lambda_0 = 780$ nm.

Finally, Fig. 7.5 illustrates Sample C.3, which was grown on a 3-inch GaAs:Si (100) substrate with a GaAs buffer, followed by ZnSe, ZnTe, and $Cd_{0.95}Zn_{0.05}Te$ buffers. The bottom DBR consisted of 20 pairs of $Cd_{0.40}Mg_{0.60}Te/Cd_{0.88}Zn_{0.04}Mg_{0.08}Te$ layers, and the top mirror of 16 pairs of $Cd_{0.88}Zn_{0.04}Mg_{0.08}Te/Cd_{0.40}Mg_{0.60}Te$ layers. Inside the cavity, three pairs of CdTe:Mn quantum wells were incorporated, separated by $Cd_{0.88}Zn_{0.04}Mg_{0.08}Te$ barriers. The central design wavelength was $\lambda_0 = 820$ nm. This sample was used to measure the presence of strong coupling in temperature measurements in CdTe optical microcavity samples, described in Chapter 3, "Optical properties of CdTe-based semiconductor microcavities." It

was used to compare condensation thresholds with and without printed polymer microlenses on its surface, as described in Chapter 6, “Polymer microlenses for optical microcavities”.

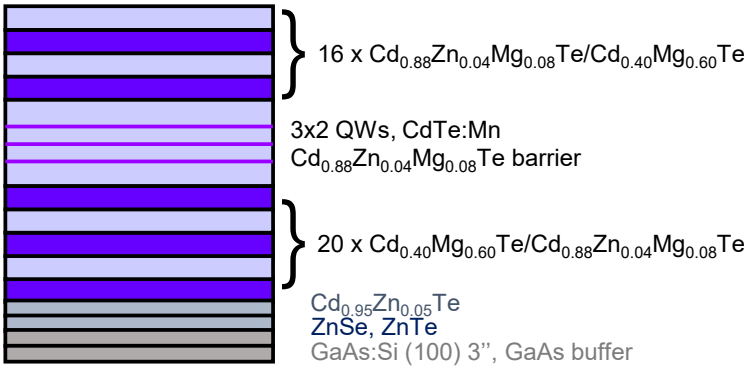

Figure 7.5: **Schematic structure of CdTe-based microcavity, Sample C.3.** Microcavity of CdTe, designed for $\lambda_0 = 820$ nm.

7.2. Appendix II: Three coupled polariton condensates in complex potential landscapes

The motivation for this study originated from a theoretical proposal suggesting the use of coupled non-equilibrium Bose-Einstein condensates for neuromorphic computations. In particular, the key characteristic feature under investigation is the strong nonlinear response of neighboring condensates to small variations in the excitation energy near the condensation threshold of each node in the network. This behavior results from the nonlinear coupling between the nodes.

To explore this concept experimentally, this research focused on the interaction of three condensates simultaneously formed in three potential minima of a CdTe-based microcavity, each excited by an independent laser spot. The difference between this project and the one discussed in Chapter 5 lies in the nature of the interactions: in Chapter 5 the condensates in a dyad synchronized through ballistic propagation, whereas in the present Appendix they interact via diffusive propagation.

As the results presented here are currently being used in ongoing theoretical work aimed at training a neural network based on the corresponding model, a separate chapter was not dedicated to this topic. Nevertheless, the experimental results obtained in this project are complete, the experimental part of the study has been concluded, and are consistent with the overall scope of this thesis. For this reason, the results are included in the Appendix as an illustration of another class of phenomena observable in CdTe-based microcavities, namely those arising from the nonlinear interactions of several (in this case, three) non-equilibrium Bose-Einstein condensates, enabled by the unique photonic potential landscape and the rich nonlinear properties of these structures.

7.2.1. Introduction to the topic of three coupled condensates

The preferential tight localization of the polariton condensates in a naturally occurring potential minima opens the question of interplay between multiple such sites. This section is devoted to the experimental investigation of the interactions between multiple polariton condensates formed in CdTe-based microcavities with an inhomogeneous photonic potential landscape. The focus is on exploring how such condensates couple and influence each other when confined to predefined positions within a disordered environment. To achieve that, a Spatial Light Modulator was employed as a tool to shape the excitation profile, providing a way to control condensates at the selected sites.

The measurements revealed that the strength and character of the interactions between the condensates depend sensitively on the shape of the local photonic potential. To demonstrate this effect, several representative regions of the sample were investigated, each corresponding to a distinct potential configuration and pump geometry. Together, these examples highlight the diversity of experimental conditions available in disordered CdTe-based microcavities.

The acquired dataset of condensate patterns formed within inhomogeneous photonic potentials provides a valuable foundation for further theoretical analysis, for example, as an experimental and realistic input for current simulation methods of coupled condensates, or potentially even as inspiration for alternative, neuromorphic or paradigm-shifting modeling approaches. Due to the inherent disorder of the potential landscape, the resulting data represent more complex and realistic scenarios, which can help improve the robustness and generalization capabilities of such models.

7.2.2. Realizations of three coupled condensates

To generate the desired excitation patterns, an experimental arrangement with a Spatial Light Modulator (SLM) was implemented. This setup allowed for precise shaping of the pump profiles, including multiple excitation spots with independently controlled intensities. This configuration enabled the controlled creation of three interacting condensates localized in the minima of the photonic potential. A schematic diagram of the experimental setup with the SLM is presented in Fig. 7.6.

The experiment was performed on a CdTe-based microcavity (Sample C.2), placed in a cryostat, in 4.5 K. The system was investigated under nonresonant excitation using a picosecond Coherent Mira-900 laser, with the wavelength tuned to the first Bragg minimum. In the following, the optical setup with the Spatial Light Modulator operating in amplitude modulation mode is described. The Gaussian laser beam was expanded with a lens and then passed through a polarizer and a half-wave plate, which together ensured the correct polarization orientation relative to the SLM axis. After reflection from the SLM, a second linear polarizer transmitted only the part of the (laser) beam whose polarization had been rotated by the SLM, thereby generating an amplitude-modulated pattern. This configuration enabled the SLM to impose a controlled spatial intensity distribution of the laser beam, which was then relayed by the optical system and imaged onto the sample plane by the microscope objective. In this way, the spatial pattern defined on the SLM matrix was directly reproduced on the surface of the microcavity in the form of the laser intensity distribution.

The aim of the experiment was to create three distinct polariton condensates coupled to

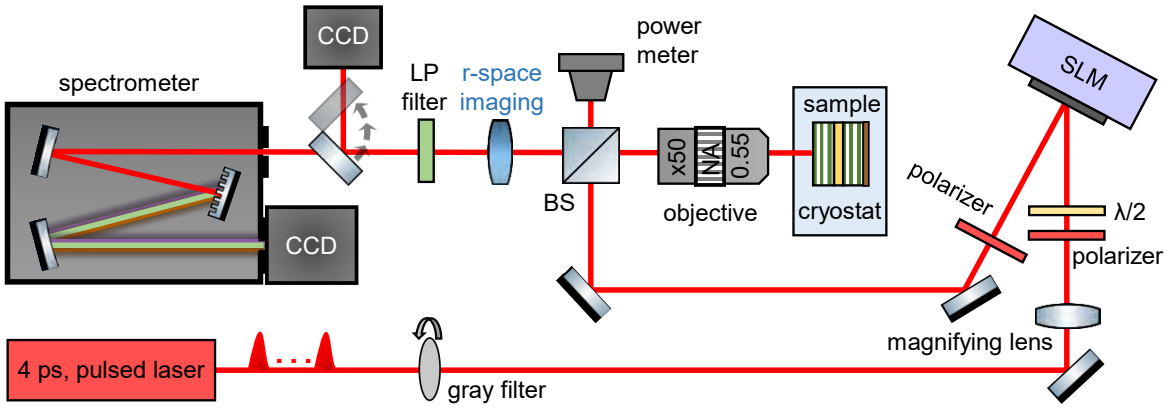

Figure 7.6: **Experimental setup with the Spatial Light Modulator (SLM).** A picosecond laser was used to excite the sample. Patterns were created using SLM in amplitude mode, which were then directed onto the sample.

each other on a disordered CdTe-based cavity sample. The SLM was computer-controlled via a custom Python software written together with Dr. Marcin Muszyński, that displayed predefined intensity profiles on its matrix. During the experiment, the grayscale values of the SLM were used to control the excitation power of each individual spot, while two additional parameters were adjusted: the relative positions and half-widths of three Gaussian beams. The positions and widths of the individual spots were chosen so as to excite three condensates localized in separate minima of the photonic potential without unwanted overlap. Independent power control through the grayscale scaling of the SLM was crucial, as it allowed precise tuning of the excitation intensity directly from the software, without the need for additional optical filters. The patterned laser beams were directed by a set of mirrors and focused onto the sample surface using a microscope objective. On the sample, this resulted in a laser intensity profile consisting of three Gaussian beams arranged at the vertices of a triangle, ensuring a non-collinear geometry.

The developed Python script allowed independent control of the power of the three excitation spots, enabling the excitation of polariton condensates that could exchange particles between neighbouring minima of the photonic potential. In this context, "interaction" was identified through mutual changes in the emission intensities of condensates located in neighbouring minima when the excitation power in one of them was varied. However, in many locations, only two condensates were visibly coupled. This limitation arose from the high potential barriers between the minima, which restricted particle exchange. In other cases, irregular disorder led to emission spreading into neighbouring sites even at low pump power from one laser beam.

Using the setup described above, the real-space emission from the sample was collected, and each location was examined. Initially, each of three laser spots was used individually to confirm that it excited emission from a single, spatially well-defined condensate. Subsequently, additional beams were added, and the changes in intensity at one position were monitored as the pump energy in neighbouring minima increased. In this way, three complete datasets were collected for three distinct regions of the sample. Each dataset was characterized by a different

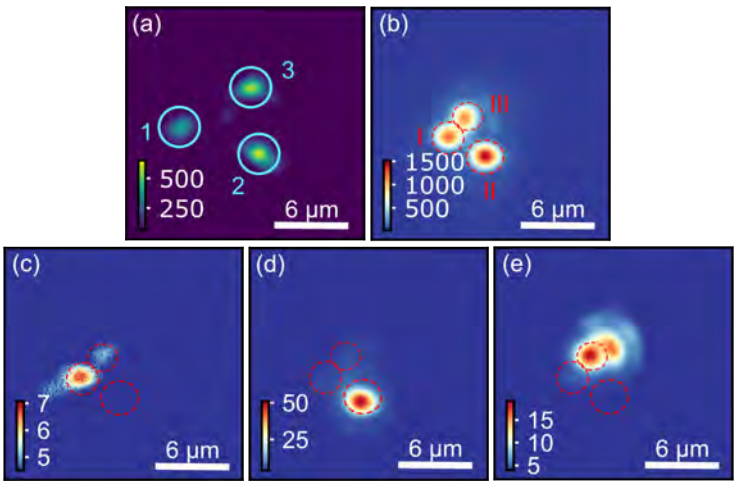

Figure 7.7: **Measurement results for the first location on the sample.** (a) Three laser beams, generated by the SLM and marked with turquoise circles numbered from 1 to 3. (b) Photoluminescence under simultaneous excitation with all three beams at maximum pulse energy. Emission regions are indicated with red dashed lines, and each emission spot is labelled with a Roman numeral corresponding to the respective beam. (c)–(e) Photoluminescence under excitation with each beam individually.

photonic potential landscape and relative beam arrangement. Figure 7.7 shows the results of the first dataset. Figure 7.7(a) illustrates the positions of the three laser spots, each with a half-width of approximately 2 µm. The excitation powers were chosen individually for each spot, and the corresponding emission behavior is discussed in the following panels. The beams, shaped by the SLM, are indicated by turquoise circles labelled from 1 to 3. Figure 7.7(b) presents the photoluminescence obtained under simultaneous excitation with the maximum pulse energies of all three laser spots. The emission regions are marked with red dashed lines, and each spot is labeled with a Roman numeral corresponding to the respective beam. It was observed that the emission did not always originate exactly at the pump position but was displaced by less than one micrometer toward the most favorable potential minimum. Figures 7.7(c)–(e) show the emission when each beam was used individually. The condensation thresholds for single beams were on the order of several to tens of picojoules per pulse.

The full three-dimensional dependence of the emission for the three interacting excitation spots is shown in Fig. 7.8. The pulse energy ranged from 0.05 pJ to 3.6 pJ for the first beam, from 0.01 pJ to 5.7 pJ for the second, and from 0.02 pJ to 7.6 pJ for the third. Each laser power range was divided into 12 steps. The measurements were performed systematically: starting with two beams turned off, the energy of the remaining beam was varied from minimum to maximum. Then, one of the other two beams was increased by one step, and the procedure was repeated. In total, $12\times12\times12 = 1728$ measurements were collected.

For each emission spot, the average intensity was extracted from a region marked with the dashed red circle. The extracted intensities were plotted on 3D graphs [Figs. 7.8(a),(c),(e)], which show the same sampling grid in 1st beam, 2nd beam, 3rd beam ($12\times12\times12$), while the point color encodes the intensity of a single emission spot: I_1 (from 1st beam), I_2 (from 2nd

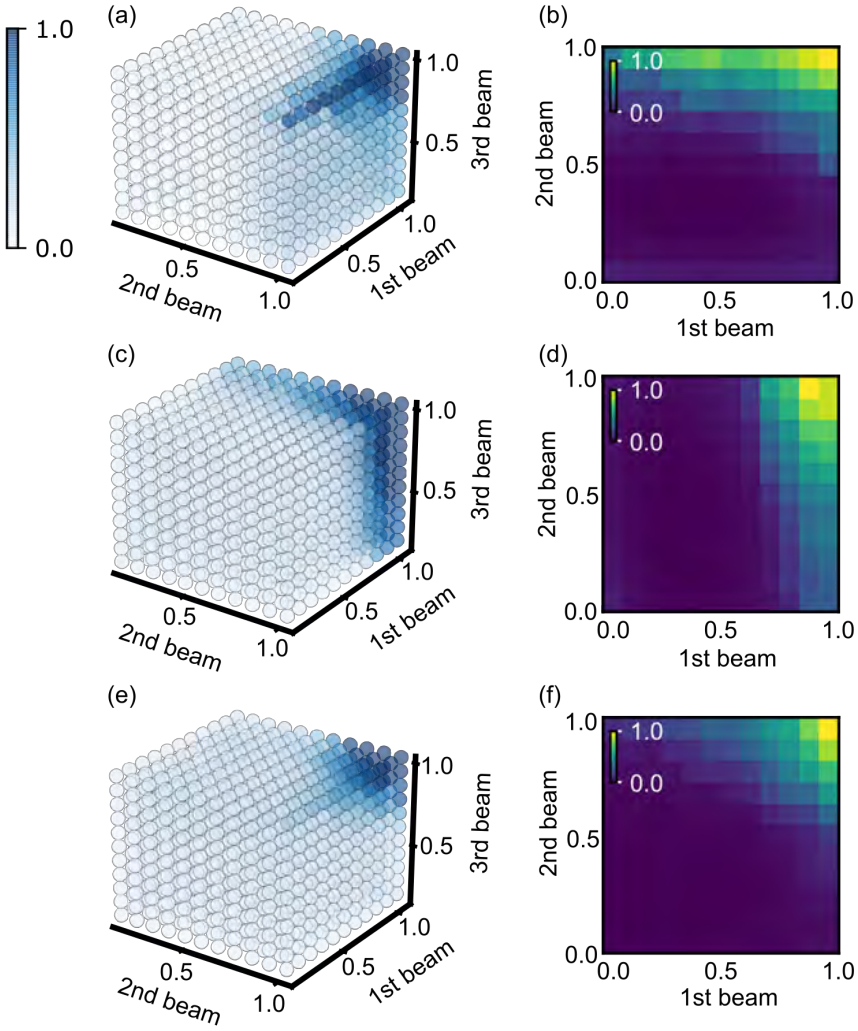

Figure 7.8: **Analysis of condensate interactions for the first position on the sample.** (a),(c),(e) The same 1st beam, 2nd beam, 3rd beam grid (12×12×12); color encodes I_1, I_2, and I_3, respectively (no special highlighting of point subsets). (b),(d),(f) Corresponding 1st beam, 2nd beam slices at fixed 3rd beam, showing how each intensity varies with the first and second beam.

beam), I_3 (from 3rd beam), respectively. All measurements are plotted uniformly, and the apparent structure comes from the color values. For example, Fig. 7.8(a) shows the (1st beam, 2nd beam, 3rd beam) grid colored by I_1, Fig. 7.8(c) by I_2, and Fig. 7.8(e) by I_3. To aid in interpretation, panels (b),(d),(f) present 2D slices through the same 3D dataset at a fixed value of the 3rd beam: specifically, fixed the 3rd beam to its 12th (highest) step (≈7.6 pJ in this dataset) and plotted intensity over the (2nd beam, 1st beam) plane (x = 2nd beam, y = 1st beam). Thus, panel (b) is indeed a cross-section of (a) at the 12th step, panel (d) is a cross-section of (c) at the 12th step, and panel (f) is a cross-section of (e) at 12th step. While there are 12 possible slices (one per 3rd-beam step), for brevity, one representative slice at

the highest step is shown; the remaining slices exhibit consistent trends (not shown). If the intensity was distributed uniformly along one axis of the plot, this indicated no interaction between the two locations. In contrast, if the intensity was concentrated near one corner, evenly covering the region corresponding to increasing pulse energy of both beams, this indicated interactions between condensates. An additional factor was whether the signal could be described by a nonlinear function, that is, whether the emission from the two points increased asymmetrically and nonlinearly. If so, this confirmed the presence of nonlinear effects between the condensates. Such signals were clearly visible in the 3D plots, while in 2D they were particularly evident at lower excitation energies.

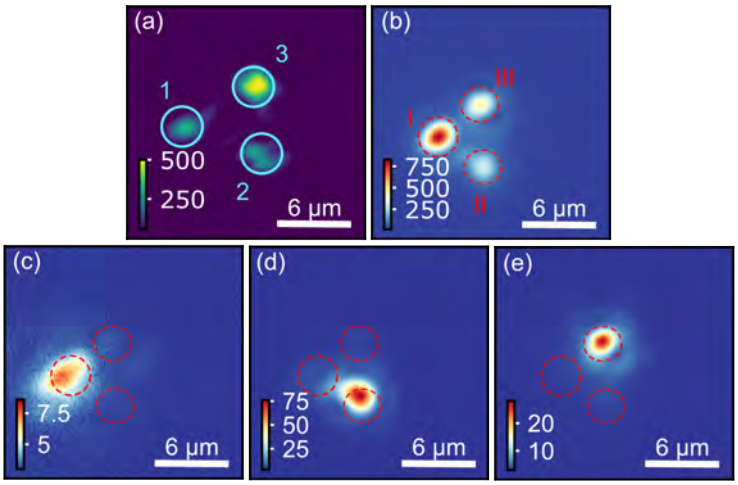

Figure 7.9: **Measurement results for the second analyzed location on the sample.** (a) Relative arrangement of the three laser beams, each position marked with turquoise circle. (b) Emission regions corresponding to individual condensates, outlined with red dashed circles used for averaging the signal intensity while varying the pulse energy. (c)–(e) Emission from each position under excitation with a single laser beam at the same low pulse energy.

Overall, the collected results suggest interactions among all three condensates: across the cases considered, the intensity tends to concentrate toward the high-high corner of the 2nd beam, 1st beam plane at fixed 3rd beam, which is consistent with a joint dependence on both beams. In addition, nonlinear behavior appears more pronounced in Figs. 7.8(a,b) and Figs. 7.8(c,d), and less evident in Figs. 7.8(e,f).

Analogous measurements were performed for the next two measured regions on the sample. Each analyzed location differed in the potential on the sample and the laser spots configuration. However, these differences provide additional datasets for training the neural network.

The next analyzed region of the sample was characterized by three condensates that were visually more separated from each other than in the first example, as shown in Fig. 7.9(b). Around each emission spot, a red dashed circle was drawn to define the area from which the signal was averaged during the measurement series with varying laser pulse energy. The relative arrangement of the beams is shown in Fig. 7.9(a). Although the third laser beam had the highest pulse energy, the emission signal from the corresponding location did not exhibit the highest intensity. The subsequent panels [Figs. 7.9(c)–(e)] present the emission from each

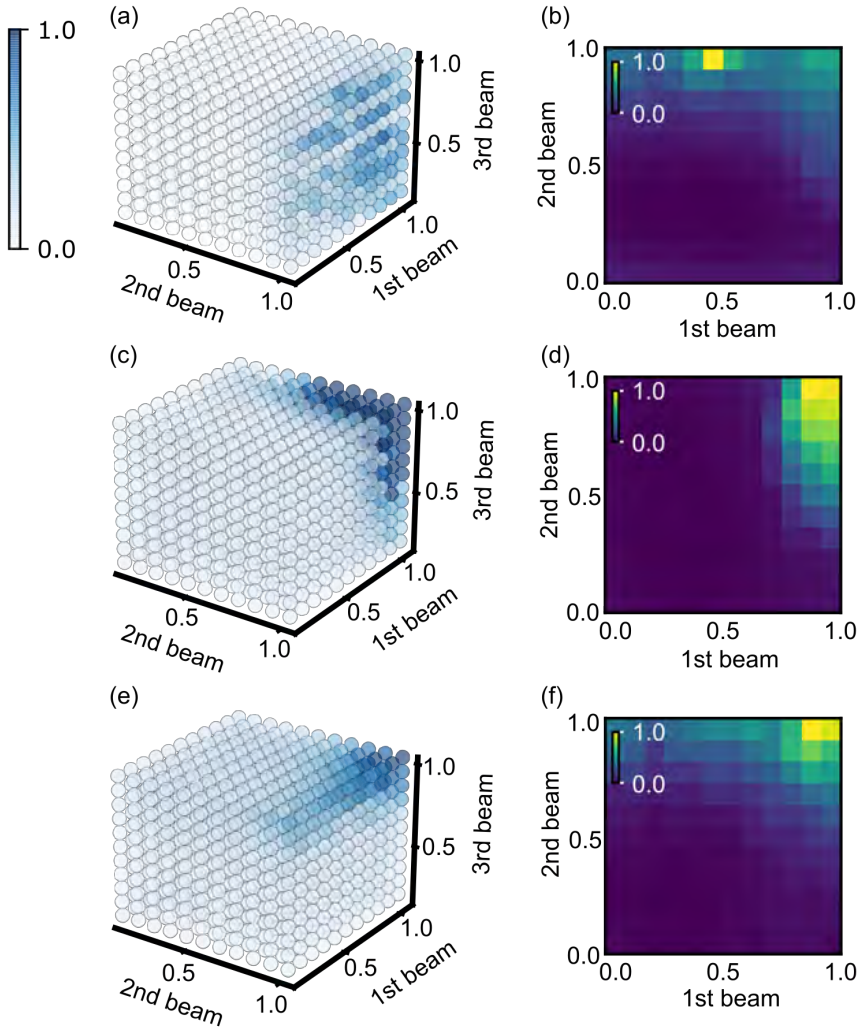

Figure 7.10: **Analysis of interactions between three neighbouring condensates in the second investigated region of the sample.** (a),(c),(e) Three views of the same 1st beam, 2nd beam, 3rd beam sampling grid, with color encoding I_1, I_2, I_3, respectively. (b),(d),(f) Corresponding 1st beam, 2nd beam slices at fixed 3rd beam that visualize how each intensity depends on the first and second beam.

location under excitation with a single laser beam at a low pulse energy value, kept the same for all these measurements.

Similarly to the previously analyzed location, the intensities of the condensate were extracted to investigate the mutual influence of emissions from three neighbouring regions of the sample, excited with increasing laser pulse energies in predefined sequences. The pulse energy ranges were as follows: for the first beam from 0.01 pJ to 5 pJ, for the second from 0.05 pJ to 6.7 pJ, and for the third from 0.1 pJ to 9.2 pJ. As previously, the energy was varied in 12 equal steps for each beam. Intensity values were normalized prior to plotting the final results. As previously, the energy was varied in 12 equal steps for each beam. Intensity

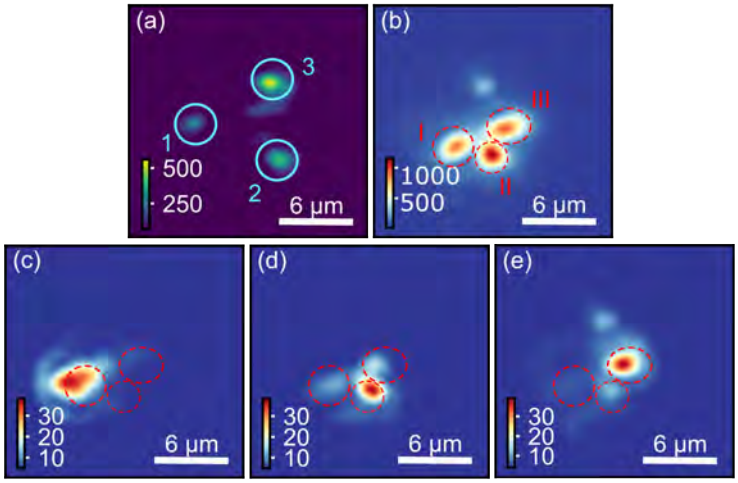

Figure 7.11: **Measurement results for the third analyzed location on the sample.** (a) Arrangement of the three laser beams, marked with turquoise circles and numbered. (b) Photoluminescence emission under simultaneous excitation with all three beams. (c)–(e) Photoluminescence maps for each beam excited individually. In panels (d) and (e), the strongest emission is observed in the region marked with a red dashed circle, with weaker emission also appearing from neighbouring potential minima.

values were plotted as measured (normalization was applied for the 3D/2D visualizations). As before, the results are shown as three 3D panels of the same 1st beam, 2nd beam, 3rd beam grid with color encoding I_1, I_2, I_3, respectively [Figs. 7.10(a),(c),(e)], and as 1st beam, 2nd beam slices at fixed 3rd beam [Figs. 7.10(b),(d),(f)]. In these maps, clear interactions were observed, manifested by stronger emission in the corners of the maps. Furthermore, all analyzed maps exhibited nonlinear behavior, the emission profile of two interacting points was non-uniform and could be described by a nonlinear function.

The last analyzed region more closely resembled the first studied area. Although the laser beams were clearly separated from each other [marked with turquoise circles and labeled with numbers in Fig. 7.11(a)], the observed emission originated from points located nearby but not directly beneath the excitation spots. The emission from three points under simultaneous excitation with all laser beams is shown in Fig. 7.11(b). Photoluminescence maps were also collected for each beam individually and are presented in Figs. 7.11(c)–(e). In particular, for the results shown in Figs. 7.11(d,e), it can be seen that the strongest emission occurs in the region indicated by the red dashed circle, although weaker emission from neighbouring potential minima was also observed.

Next, as for the previously analyzed locations, a three-dimensional grid consisting of 12×12×12 points was plotted, again showing the same 1st beam, 2nd beam, 3rd beam sampling grid in three panels, with color encoding I_1, I_2, I_3. These dependencies are presented in Figs. 7.12(a),(c),(e). Panels (b),(d),(f) show the corresponding 1st beam, 2nd beam slices at fixed 3rd beam. As in the previous measurement series, the results reveal not only the mutual interactions between the analyzed regions but also indications that these interactions may be nonlinear in nature.

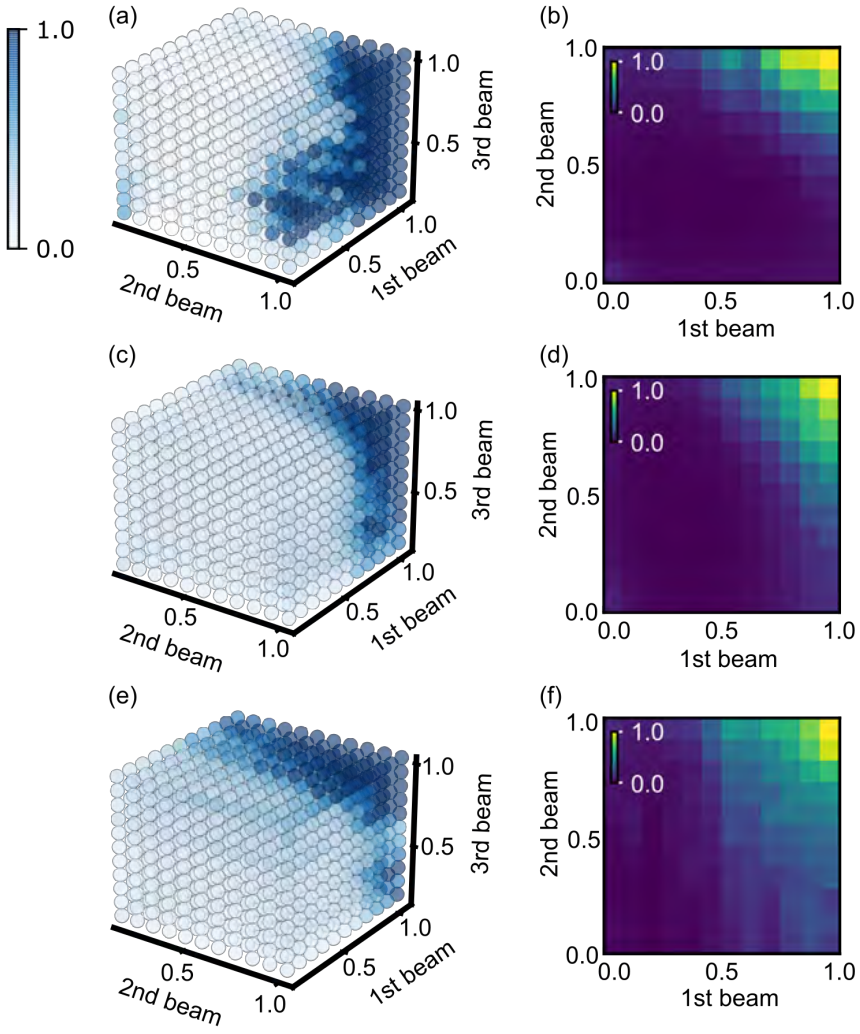

Figure 7.12: **Analysis of condensate interactions for the third investigated location on the sample.** (a),(c),(e) depict the identical sampling grid spanned by the 1st, 2nd, and 3rd beams, with point color representing I_1, I_2, and I_3, respectively. (b),(d),(f) show the matching slices in the (1st beam, 2nd beam) plane at a fixed 3rd-beam setting, illustrating how each intensity varies with the first and second beam.

The experiments not only allowed the observation of effects related to emission localization but also revealed the presence of nonlinear interactions between condensates. These experimental datasets provided a foundation for further analysis, including the training of a neural network designed to recognize and model the relationships between the excitation parameters and the observed emission signals.

In summary, the experimental results presented in this section demonstrate the interactions between three polariton condensates in CdTe-based microcavities with inhomogeneous photonic potential. By combining flexible beam-shaping using a Spatial Light Modulator with systematic measurements of emission profiles and interaction dependencies, it was possible to create a

data that captures both the localization properties of condensates and the nonlinear coupling between them. The significance of this approach lies not only in the observation of polariton dynamics in disordered structures but also in establishing an experimental basis for modeling.

Chapter 8

Publications of the author

Publications directly related to the dissertation:

1. **M. Furman**, M. Muszyński, P. Oliwa, Ł. Zinkiewicz, A. Bogucki, J. Szczytko, P. Wasylczyk, W. Pacuski, M. Król, B. Piętka,
"Multiplexed back focal plane imaging with on-chip integrated microlens array" (2025), arXiv, in review.

2. **M. Furman**, R. Mirek, M. Król, W. Pacuski, H. Sigurðsson, J. Szczytko, B. Piętka,
"Magneto-optical induced supermode switching in quantum fluids of light" (2023), *Communications Physics*, **6,** 196.

3. A. Opala, **M. Furman**, M. Król, R. Mirek, K. Tyszka, B. Seredyński, W. Pacuski, J. Szczytko, M. Matuszewski, B. Piętka,
"Natural exceptional points in the excitation spectrum of a light-matter system" (2023), *Optica* **10,** 8, pp. 1111–1117.

4. **M. Furman**, A. Opala, M. Król, K. Tyszka, R. Mirek, M. Muszyński, B. Seredyński, W. Pacuski, J. Szczytko, M. Matuszewski, B. Piętka,
"Inverted optical bistability and optical limiting in coherently driven exciton-polaritons" (2023), *APL Photonics*, **8,** 046105.

Further publications:

5. R. Mirek, **M. Furman**, A. Opala, M. Król, W. Pacuski, J. Szczytko, H. Sigurðsson, B. Piętka,
"Emission enhanced exciton-polariton condensates with optical feedback" (2025), *arXiv*, in review.

6. A. Opala, K. Tyszka, M. Kędziora, **M. Furman**, A. Rahmani, S. Świerczewski, M. Ekielski, A. Szerling, M. Matuszewski, B. Piętka,

"Room temperature exciton-polariton neural network with perovskite crystal" (2025), *Advanced Materials*, **2025,** e07612.

7. R. Mirek, **M. Furman**, M. Król, B. Seredyński, K. Łempicka-Mirek, K. Tyszka, W. Pacuski, M. Matuszewski, J. Szczytko, B. Piętka,
"Spin polarization of exciton-polariton condensate in a photonic synthetic effective magnetic field" (2023), *Physical Review B*, **107(12),** 125303.

8. M. Król, K. Łempicka-Mirek, K. Rechcińska, **M. Furman**, K. Nogajewski, R. Mazur, P. Morawiak, W. Piecek, W. Pacuski, J. Szczytko, B. Piętka,
"Universality of open microcavities for strong light-matter coupling" (2023), *Optical Materials Express*, **13,** 9, pp. 2651–2661.

9. R. Mirek, A. Opala, **M. Furman**, M. Król, K. Tyszka, B. Seredyński, W. Pacuski, J. Suffczyński, J. Szczytko, M. Matuszewski, B. Piętka,
"Neural Networks Based on Ultrafast Time-Delayed Effects in Exciton Polaritons" (2022), *Physical Review Applied*, **17,** 054037.

10. E. M. Łacińska, **M. Furman**, J. Binder, I. Lutsyk, P. J. Kowalczyk, R. Stępniewski, A. Wysmołek,
"Raman Optical Activity of 1T-TaS_2" (2022), *Nano Letters*, **22(7),** pp. 2835–2842.

11. K. Tyszka, **M. Furman**, R. Mirek, M. Król, A. Opala, B. Seredyński, J. Suffczyński, W. Pacuski, M. Matuszewski, J. Szczytko, B. Piętka,
"Leaky Integrate and Fire Mechanism in Exciton-Polariton Condensates for Photonic Spiking Neurons" (2022), *Laser & Photonics Reviews*, **17(1),** 2100660.

12. R. Mirek, A. Opala, P. Comaron, **M. Furman**, M. Król, K. Tyszka, B. Seredyński, D. Ballarini, D. Sanvitto, T. C. H. Liew, W. Pacuski, J. Suffczyński, J. Szczytko, M. Matuszewski, B. Piętka,
"Neuromorphic Binarized Polariton Networks" (2021), *Nano Letters*, **21(9),** 3715–3720.

13. M. Matuszewski, A. Opala, R. Mirek, **M. Furman**, M. Król, K. Tyszka, T. C. H. Liew, D. Ballarini, D. Sanvitto, J. Szczytko, B. Piętka,
"Energy-Efficient Neural Network Inference with Microcavity Exciton Polaritons" (2021), *Physical Review Applied*, **16,** 024045.

14. K. Łempicka, **M. Furman**, M. Muszyński, M. Król, A. Wincukiewicz, K. Rechcińska, R. Mazur, W. Piecek, M. Kamińska, J. Szczytko, B. Piętka,
"Exciton-Polaritons in a Tunable Microcavity with 2D-Perovskite" (2019), *International Photonics and OptoElectronics Meeting 2019 (OFDA, OEDI, ISST, PE, LST, TSA)*, (Optical Society of America, 2019) p. JW4A.66., Optica Publishing Group.

Chapter 9

Scientific conferences and scientific schools

9.1. Participation in scientific conferences

1. 25th International Conference on High Magnetic Fields in Semiconductor Physics (HMF-25), 16.09.2024 - 20.09.2024, title: " Changing the Parity of Polariton Dyad in External Magnetic Field ", poster;

2. 36th International Conference on the Physics of Semiconductors (ICPS), 28.07.2024 - 02.08.2024, title: "The Role of Magnetic Fields in Synchronization of Two Polariton Condensates", oral presentation;

3. 52nd International School & Conference on the Physics of Semiconductors "Jaszowiec 2024", Szczyrk, Poland, 15.06.2024 - 21.06.2024, title: " Spatial Control of Exciton-Polariton Condensates Properties Using External Magnetic Field", poster;

4. The International Conference on Nonlinear Optics and Excitation Kinetics in Semiconductors NOEKS.16, Fraueninsel, Germany, 17.09.2023 - 20.09.2023, title: "Spatially structuring exciton-polariton condensates with external magnetic fields", poster;

5. 51th International School & Conference on the Physics of Semiconductors "Jaszowiec 2023", Szczyrk, Poland, 17.06.2023 - 23.06.2023, title: "Natural Exceptional Points Appearing in Semiconductor Microcavity Systems", oral presentation;

6. SPIE Optics + Photonics, Emerging Topics in Artificial Intelligence (ETAI) 2022 San Diego, USA, 21.08.2022 - 25.08.2022, title: "Time-delayed nonlinear phenomena in exciton-polariton condensates for neuromorphic computing", oral presentation;

7. 50th International School & Conference on the Physics of Semiconductors "Jaszowiec 2022", Szczyrk, Poland, 04.06.2022 - 10.06.2022, title: "Optical Limiting in Coherently Driven Exciton-Polaritons", oral presentation;

8. 49th International School & Conference on the Physics of Semiconductors "Jaszowiec 2021", Warsaw, Poland, 01.09.2021 - 10.09.2021, title: "Time-delayed nonlinear phenomena in exciton-polariton condensate", oral presentation;

9. 2020 Virtual MRS Spring/Fall Meeting & Exhibit, Boston, USA, 27.11.2020 - 04.12.2020, title: “Strong Coupling of Light and Matter Observed in a Tunable Microcavity with 2D-Perovskites at Room Temperature”, poster;

10. 10th International Conference on Spontaneous Coherence in Excitonic Systems “ICSCE 10, 2020”, Melbourne, Australia, 28.01.2020 - 31.01.2020, title: "Tunable Room-Temperature Exciton-Polaritons in a Microcavity Containing 2D-Perovskites”, poster;

11. International Photonics and OptoElectronics Meetings “POEM 2019”, Wuhan, Chiny, 11.11.2019 - 14.11.2019, title: "Exciton-Polaritons in a Tunable Microcavity with 2D-Perovskite”, poster;

12. 48th International School & Conference on the Physics of Semiconductors "Jaszowiec 2019", Szczyrk, Poland, 08.06.2019 - 14.06.2019, title: "Two-dimensional optical trap producing exciton-polariton Bose-Einstein condensates in microcavity structures”, poster.

9.2. Participation in scientific schools

1. 9th Event of the International School of Nonequilibrium Phenomena, Course on Quantum Fluids of Light and Matter - QFLM2024, 15.11.2024 - 19.11.2024, Ettore Majorana Center, Erice, Italy;

2. International School of Physics "Enrico Fermi", Course on Quantum Fluids of Light and Matter - QFLM2022, Italian Physical Society, Italy, 01.07.2022 - 08.07.2022.

Bibliography

[1] Alexey Kavokin, Timothy CH Liew, Christian Schneider, Pavlos G Lagoudakis, Sebastian Klembt, and Sven Hoefling. Polariton condensates for classical and quantum computing. *Nat. Rev. Phys.*, 4(7):435–451, 2022.

[2] M Furman, A Opala, M Król, K Tyszka, R Mirek, M Muszyński, B Seredyński, W Pacuski, J Szczytko, M Matuszewski, et al. Inverted optical bistability and optical limiting in coherently driven exciton–polaritons. *APL Photonics*, 8(4), 2023.

[3] Rafał Mirek, Andrzej Opala, Paolo Comaron, Magdalena Furman, Mateusz Król, Krzysztof Tyszka, Bartłomiej Seredynski, Dario Ballarini, Daniele Sanvitto, Timothy CH Liew, et al. Neuromorphic binarized polariton networks. *Nano Lett.*, 21(9):3715–3720, 2021.

[4] Andrzej Opala and Michał Matuszewski. Harnessing exciton-polaritons for digital computing, neuromorphic computing, and optimization. *Opt. Mater. Express*, 13(9):2674–2689, 2023.

[5] Krzysztof Tyszka, Magdalena Furman, Rafał Mirek, Mateusz Król, Andrzej Opala, Bartłomiej Seredyński, Jan Suffczyński, Wojciech Pacuski, Michał Matuszewski, Jacek Szczytko, et al. Leaky integrate-and-fire mechanism in exciton–polariton condensates for photonic spiking neurons. *Laser & Photonics Reviews*, 17(1):2100660, 2023.

[6] Andrzej Opala, Riccardo Panico, Vincenzo Ardizzone, B Piętka, Jacek Szczytko, Daniele Sanvitto, Michał Matuszewski, and Dario Ballarini. Training a neural network with exciton-polariton optical nonlinearity. *Physical Review Applied*, 18(2):024028, 2022.

[7] Andrzej Opala, Krzysztof Tyszka, Mateusz Kędziora, Magdalena Furman, Amir Rahmani, Stanisław Świerczewski, Marek Ekielski, Anna Szerling, Michał Matuszewski, and Barbara Piętka. Perovskite microwires for room temperature exciton-polariton neural network. *Advanced Materials*, page e07612, 2025.

[8] M. Furman, M. Muszyński, P. Oliwa, Ł. Zinkiewicz, A. Bogucki, J. Szczytko, P. Wasylczyk, W. Pacuski, M. Król, and B. Piętka. Multiplexed back focal plane imaging with on-chip integrated microlens array. *arXiv*, 2025.

[9] Dimitris G Angelakis. Quantum simulations with photons and polaritons. *Quantum Science and Technology (Springer, 2017)*, 134, 2017.

[10] Natalia G Berloff, Matteo Silva, Kirill Kalinin, Alexis Askitopoulos, Julian D Töpfer, Pasquale Cilibrizzi, Wolfgang Langbein, and Pavlos G Lagoudakis. Realizing the classical XY Hamiltonian in polariton simulators. *Nat. Mater.*, 16(11):1120–1126, 2017.

[11] R Mirek, M Furman, M Król, B Seredyński, K Łempicka-Mirek, K Tyszka, W Pacuski, M Matuszewski, J Szczytko, and B Piętka. Spin polarization of exciton-polariton condensate in a photonic synthetic effective magnetic field. *Phys. Rev. B*, 107(12):125303, 2023.

[12] Magdalena Furman, Rafał Mirek, Mateusz Król, Wojciech Pacuski, Helgi Sigurðsson, Jacek Szczytko, and Barbara Piętka. Magneto-optical induced supermode switching in quantum fluids of light. *Commun. Phys.*, 6(1):196, 2023.

[13] Charles Kittel and Paul McEuen. *Introduction to solid state physics*. John Wiley & Sons, 2018.

[14] J Robertson, K Xiong, and SJ Clark. Band gaps and defect levels in functional oxides. *Thin Solid Films*, 496(1):1–7, 2006.

[15] Simon M Sze, Yiming Li, and Kwok K Ng. *Physics of semiconductor devices*. John wiley & sons, 2021.

[16] Harald Ibach and Hans Lüth. *Solid-state physics: an introduction to principles of materials science*. Springer Science & Business Media, 2013.

[17] PeterY Yu. *Fundamentals of semiconductors*. Springer, 2005.

[18] LJ Neuringer. Effect of pressure on the infrared absorption of semiconductors. *Phys. Rev.*, 113(6):1495, 1959.

[19] Z Dridi, B Bouhafs, and P Ruterana. Pressure dependence of energy band gaps for AlxGa1-xN, InxGa1-xN andInxAl1-xN. *New J. Phys.*, 4(1):94, 2002.

[20] B Gerlach, J Wüsthoff, MO Dzero, and MA Smondyrev. Exciton binding energy in a quantum well. *Phys. Rev. B*, 58(16):10568, 1998.

[21] Lowenna C Smith, James J Davies, Daniel Wolverson, Simon Crampin, RT Cox, Joel Cibert, H Mariette, VP Kochereshko, M Wiater, G Karczewski, et al. Motion-dependent magnetic properties of excitons in CdTe. *Phys. Rev. B*, 78(8):085204, 2008.

[22] NT Pelekanos, H Haas, N Magnea, H Mariette, and A Wasiela. Room-temperature exciton absorption engineering in ii-vi quantum wells. *Appl. Phys. Lett.*, 61(26):3154–3156, 1992.

[23] David AB Miller, DS Chemla, TC Damen, AC Gossard, W Wiegmann, TH Wood, and CA Burrus. Electric field dependence of optical absorption near the band gap of quantum-well structures. *Phys. Rev. B*, 32(2):1043, 1985.

[24] Jagdeep Shah. *Ultrafast spectroscopy of semiconductors and semiconductor nanostructures*, volume 115. Springer Science & Business Media, 2013.

[25] Robert N Hall, Gunther E Fenner, JD Kingsley, TJ Soltys, and RO Carlson. Coherent light emission from GaAs junctions. *Phys. Rev. Lett.*, 9(9):366, 1962.

[26] JP Van der Ziel, R Dingle, Robert C Miller, William Wiegmann, and WA Nordland. Laser oscillation from quantum states in very thin GaAs-Al0. 2Ga0. 8As multilayer structures. *Appl. Phys. Lett.*, 26(8):463–463, 1975.

[27] Haruhisa Soda, Ken-ichi Iga, Chiyuki Kitahara, and Yasuharu Suematsu. GaInAsP/InP surface emitting injection lasers. *Japanese Journal of Applied Physics*, 18(12):2329, 1979.

[28] Pochi Yeh. *Optical Waves in Layered Media*. Wiley, 2nd edition, 2005.

[29] Larry A. Coldren, Scott W. Corzine, and Milan L. Mašanović. *Diode Lasers and Photonic Integrated Circuits*. Wiley, 2nd edition, 2012.

[30] Alexey V. Kavokin, Jeremy J. Baumberg, Guillaume Malpuech, and Fabrice P. Laussy. *Microcavities*. Oxford University Press, 2nd edition, 2017.

[31] P. B. Johnson and R. W. Christy. Optical constants of the noble metals. *Phys. Rev. B*, 6(12):4370–4379, 1972.

[32] W Pacuski, C Kruse, S Figge, and D Hommel. High-reflectivity broadband distributed Bragg reflector lattice matched to ZnTe. *Appl. Phys. Lett.*, 94(19), 2009.

[33] Corné Koks and MP Van Exter. Microcavity resonance condition, quality factor, and mode volume are determined by different penetration depths. *Opt. Express*, 29(5):6879–6889, 2021.

[34] Cheng Zhang, Rami ElAfandy, and Jung Han. Distributed Bragg reflectors for GaN-based vertical-cavity surface-emitting lasers. *Appl. Sci.*, 9(8):1593, 2019.

[35] Pochi Yeh and Michael Hendry. Optical waves in layered media, 1990.

[36] Claude Weisbuch, Mr Nishioka, A Ishikawa, and Y Arakawa. Observation of the coupled exciton-photon mode splitting in a semiconductor quantum microcavity. *Phys. Rev. Lett.*, 69(23):3314, 1992.

[37] E. M. Purcell. Spontaneous emission probabilities at radio frequencies. *Phys. Rev.*, 69(11-12):681, 1946.

[38] Konstantinos Lagoudakis. *The physics of exciton-polariton condensates*. EPFL Press, 2013.

[39] Hui Deng, Hartmut Haug, and Yoshihisa Yamamoto. Exciton-polariton bose-einstein condensation. *Rev. Mod. Phys.*, 82(2):1489–1537, 2010.

[40] Iacopo Carusotto and Cristiano Ciuti. Quantum fluids of light. *Rev. Mod. Phys.*, 85:299–366, Feb 2013.

[41] H. Deng, G. Weihs, C. Santori, J. Bloch, and Y. Yamamoto. Condensation of semiconductor microcavity exciton polaritons. *Science*, 298(5591):199–202, 2002.

[42] J. Kasprzak, M. Richard, S. Kundermann, A. Baas, P. Jeambrun, J. M. J. Keeling, F. M. Marchetti, M. H. Szymańska, R. André, J. L. Staehli, V. Savona, P. B. Littlewood, B. Deveaud, and Le Si Dang. Bose-Einstein condensation of exciton polaritons. *Nature*, 443(7110):409–414, sep 2006.

[43] Konstantinos G Lagoudakis, Francesco Manni, Barbara Pietka, Michiel Wouters, Timothy Chi Hin Liew, Vincenzo Savona, Alexey V Kavokin, Régis André, and Benoit Deveaud-Plédran. Probing the dynamics of spontaneous quantum vortices in polariton superfluids. *Phys. Rev. Lett.*, 106(11):115301, 2011.

[44] Alberto Amo, Jérôme Lefrère, Simon Pigeon, Claire Adrados, Cristiano Ciuti, Iacopo Carusotto, Romuald Houdré, Elisabeth Giacobino, and Alberto Bramati. Superfluidity of polaritons in semiconductor microcavities. *Nat. Phys.*, 5(11):805–810, 2009.

[45] Iacopo Carusotto and Cristiano Ciuti. Quantum fluids of light. *Rev. Mod. Phys.*, 85(1):299–366, 2013.

[46] M. H. Anderson, J. R. Ensher, M. R. Matthews, C. E. Wieman, and E. A. Cornell. Observation of Bose-Einstein condensation in a dilute atomic vapor. *Science*, 269(5221):198–201, 1995.

[47] K. B. Davis, M.-O. Mewes, M. R. Andrews, N. J. van Druten, D. S. Durfee, D. M. Kurn, and W. Ketterle. Bose-Einstein condensation in a gas of sodium atoms. *Phys. Rev. Lett.*, 75(22):3969–3973, 1995.

[48] K. G. Lagoudakis, T. Ostatnický, A. V. Kavokin, Y. G. Rubo, R. André, and B. Deveaud-Plédran. Coherent oscillations in an exciton-polariton Josephson junction. *Nat. Phys.*, 6:860–864, 2010.

[49] KS Daskalakis, SA Maier, Ray Murray, and Stéphane Kéna-Cohen. Nonlinear interactions in an organic polariton condensate. *Nat. Mater.*, 13(3):271–278, 2014.

[50] Stéphane Kéna-Cohen and SR Forrest. Room-temperature polariton lasing in an organic single-crystal microcavity. *Nat. Photonics*, 4(6):371–375, 2010.

[51] Anton V Zasedatelev, Anton V Baranikov, Denis Sannikov, Darius Urbonas, Fabio Scafirimuto, Vladislav Yu Shishkov, Evgeny S Andrianov, Yurii E Lozovik, Ullrich Scherf, Thilo Stöferle, et al. Single-photon nonlinearity at room temperature. *Nature*, 597(7877):493–497, 2021.

[52] J. D. Plumhof, T. Stöferle, L. Mai, U. Scherf, and R. F. Mahrt. Room-temperature Bose–Einstein condensation of cavity exciton–polaritons in a polymer. *Nat. Mater.*, 13:247–252, 2014.

[53] R. Su, C. Diederichs, J. Wang, T. C. H. Liew, J. Zhao, S. Liu, W. Xu, Z. Chen, H. Deng, and Q. Xiong. Observation of exciton polariton condensation in a perovskite lattice at room temperature. *Nat. Phys.*, 16:301–306, 2020.

[54] Jun Wang, Rui Su, Jun Xing, Di Bao, Carole Diederichs, Sheng Liu, Timothy CH Liew, Zhanghai Chen, and Qihua Xiong. Room temperature coherently coupled exciton–polaritons in two-dimensional organic–inorganic perovskite. *ACS Nano*, 12(8):8382–8389, 2018.

[55] Rui Su, Carole Diederichs, Jun Wang, Timothy CH Liew, Jiaxin Zhao, Sheng Liu, Weigao Xu, Zhanghai Chen, and Qihua Xiong. Room-temperature polariton lasing in all-inorganic perovskite nanoplatelets. *Nano Lett.*, 17(6):3982–3988, 2017.

[56] X. Liu, T. Galfsky, Z. Sun, F. Xia, E. C. Lin, Y.-H. Lee, S. Kéna-Cohen, and V. M. Menon. Strong light–matter coupling in two-dimensional atomic crystals. *Nat. Photonics*, 9:30–34, 2015.

[57] Jie Gu, Biswanath Chakraborty, Mandeep Khatoniar, and Vinod M Menon. A room-temperature polariton light-emitting diode based on monolayer WS_2. *Nat. Nanotechnol.*, 14(11):1024–1028, 2019.

[58] A. Chernikov, T. C. Berkelbach, H. M. Hill, A. Rigosi, Y. Li, O. B. Aslan, D. R. Reichman, M. S. Hybertsen, and T. F. Heinz. Exciton binding energy and nonhydrogenic Rydberg series in monolayer WS_2. *Phys. Rev. Lett.*, 113(7):076802, 2014.

[59] John Wilfred Orton and Tom Foxon. *Molecular beam epitaxy: a short history.* Oxford University Press, 2015.

[60] J Sadowski, H Mariette, A Wasiela, R André, Y Merle d'Aubigné, and T Dietl. Magnetic tuning in excitonic bragg structures of (Cd, Mn) Te/(Cd, Zn, Mg) Te. *Phys. Rev. B*, 56(4):R1664, 1997.

[61] J.-G. Rousset, B. Piętka, M. Król, R. Mirek, K. Lekenta, J. Szczytko, W. Pacuski, and M. Nawrocki. Magnetic field effect on the lasing threshold of a semimagnetic polariton condensate. *Phys. Rev. B*, 96:125403, 2017.

[62] B. Seredyński, R. Mirek, K. Lekenta, J.-G. Rousset, M. Król, K. Łempicka-Mirek, K. Tyszka, M. Matuszewski, J. Szczytko, W. Pacuski, and B. Piętka. (Cd,Zn,Mg)Te-based microcavity on MgTe sacrificial buffer. *Phys. Rev. Mater.*, 2:043406, 2018.

[63] R. Mirek, M. Furman, M. Król, B. Seredyński, K. Łempicka-Mirek, K. Tyszka, W. Pacuski, M. Matuszewski, J. Szczytko, and B. Piętka. Spin polarization of exciton-polariton condensate in a photonic synthetic effective magnetic field. *Phys. Rev. B*, 107:125303, 2023.

[64] Mateusz Król, Rafał Mirek, Katarzyna Lekenta, Jean-Guy Rousset, Daniel Stephan, Michał Nawrocki, Michał Matuszewski, Jacek Szczytko, Wojciech Pacuski, and Barbara Piętka. Spin polarized semimagnetic exciton-polariton condensate in magnetic field. *Sci. Rep.*, 8(1):6694, 2018.

[65] R Mirek, M Król, K Lekenta, J-G Rousset, M Nawrocki, M Kulczykowski, M Matuszewski, J Szczytko, W Pacuski, and B Piętka. Angular dependence of giant Zeeman effect for semimagnetic cavity polaritons. *Phys. Rev. B*, 95(8):085429, 2017.

[66] Maciej Ściesiek, Krzysztof Sawicki, Wojciech Pacuski, Kamil Sobczak, Tomasz Kazimierczuk, Andrzej Golnik, and Jan Suffczyński. Long-distance coupling and energy transfer between exciton states in magnetically controlled microcavities. *Commun. Mater.*, 1(1):78, 2020.

[67] M Król, R Mirek, D Stephan, K Lekenta, J-G Rousset, W Pacuski, AV Kavokin, M Matuszewski, J Szczytko, and B Piętka. Giant spin Meissner effect in a nonequilibrium exciton-polariton gas. *Phys. Rev. B*, 99(11):115318, 2019.

[68] Mark Steger, Gangqiang Liu, Bryan Nelsen, Chitra Gautham, David W Snoke, Ryan Balili, Loren Pfeiffer, and Ken West. Long-range ballistic motion and coherent flow of long-lifetime polaritons. *Phys. Rev. B*, 88(23):235314, 2013.

[69] Andrzej Opala, Magdalena Furman, Mateusz Król, Rafał Mirek, Krzysztof Tyszka, Bartłomiej Seredyński, Wojciech Pacuski, Jacek Szczytko, Michał Matuszewski, and Barbara Piętka. Natural exceptional points in the excitation spectrum of a light–matter system. *Optica*, 10(8):1111–1117, 2023.

[70] Hyatt Gibbs. *Optical bistability: controlling light with light*. Elsevier, 2012.

[71] Robert W Boyd, Alexander L Gaeta, and Enno Giese. Nonlinear optics. In *Springer Handbook of Atomic, Molecular, and Optical Physics*, pages 1097–1110. Springer, 2008.

[72] A. Szöke, V. Daneu, J. Goldhar, and N. A. Kurnit. Bistable optical element and its applications. *Appl. Phys. Lett.*, 15(11):376–379, dec 1969.

[73] H. M. Gibbs, S. L. McCall, and T. N. C. Venkatesan. Differential gain and bistability using a sodium-filled Fabry-Perot interferometer. *Phys. Rev. Lett.*, 36:1135–1138, May 1976.

[74] E Abraham and SD Smith. Optical bistability and related devices. *Rep. Prog. Phys.*, 45(8):815, 1982.

[75] DAB Miller. Optical bistability and differential gain resulting from absorption increasing with excitation. *J. Opt. Soc. Am. B: Opt. Phys.*, 1(6):857–864, 1984.

[76] N. K. Dutta, G. P. Agrawal, and M. W. Focht. Bistability in coupled cavity semiconductor lasers. *Appl. Phys. Lett.*, 44(1):30–32, jan 1984.

[77] Rajarshi Roy and L. Mandel. Optical bistability and first order phase transition in a ring dye laser. *Opt. Commun.*, 34(1):133–136, jul 1980.

[78] Peter Jung, George Gray, Rajarshi Roy, and Paul Mandel. Scaling law for dynamical hysteresis. *Phys. Rev. Lett.*, 65:1873–1876, Oct 1990.

[79] Amitabh Joshi, Andy Brown, Hai Wang, and Min Xiao. Controlling optical bistability in a three-level atomic system. *Phys. Rev. A*, 67:041801, Apr 2003.

[80] Subhadeep Gupta, Kevin L. Moore, Kater W. Murch, and Dan M. Stamper-Kurn. Cavity nonlinear optics at low photon numbers from collective atomic motion. *Phys. Rev. Lett.*, 99:213601, Nov 2007.

[81] Hannes Gothe, Tristan Valenzuela, Matteo Cristiani, and Jürgen Eschner. Optical bistability and nonlinear dynamics by saturation of cold Yb atoms in a cavity. *Phys. Rev. A*, 99:013849, Jan 2019.

[82] H. M. Gibbs, S. L. McCall, T. N. C. Venkatesan, A. C. Gossard, A. Passner, and W. Wiegmann. Optical bistability in semiconductors. *Appl. Phys. Lett.*, 35(6):451–453, 1979.

[83] Marin Soljačić, Mihai Ibanescu, Chiyan Luo, Steven G Johnson, Shanhui Fan, Yoel Fink, and John D Joannopoulos. All-optical switching using optical bistability in nonlinear photonic crystals. In *Photonic crystal materials and devices*, volume 5000, pages 200–214. SPIE, 2003.

[84] Arka Majumdar and Armand Rundquist. Cavity-enabled self-electro-optic bistability in silicon photonics. *Opt. Lett.*, 39(13):3864–3867, Jul 2014.

[85] H. Kawaguchi. Bistable laser diodes and their applications: state of the art. *IEEE J. Sel. Top. Quantum Electron.*, 3(5):1254–1270, 1997.

[86] Christopher F. Marki, Douglas R. Jorgesen, Haijiang Zhang, Pengyue Wen, and Sadik C. Esener. Observation of counterclockwise, clockwise and butterfly bistabilty in 1550 nm vcsoas. *Opt. Express*, 15(8):4953–4959, Apr 2007.

[87] Antonio Hurtado, Ana Quirce, Angel Valle, Luis Pesquera, and Michael J. Adams. Power and wavelength polarization bistability with very wide hysteresis cycles in a 1550nm-VCSEL subject to orthogonal optical injection. *Opt. Express*, 17(26):23637–23642, Dec 2009.

[88] Hongchao Xie, Shengwei Jiang, Jie Shan, and Kin Fai Mak. Valley-selective exciton bistability in a suspended monolayer semiconductor. *Nano Lett.*, 18(5):3213–3220, 2018.

[89] Changjun Min, Pei Wang, Chunchong Chen, Yan Deng, Yonghua Lu, Hai Ming, Tingyin Ning, Yueliang Zhou, and Guozhen Yang. All-optical switching in subwavelength metallic grating structure containing nonlinear optical materials. *Opt. Lett.*, 33(8):869–871, Apr 2008.

[90] Alexey Kavokin, Jeremy J. Baumberg, Guillaume Malpuech, and Fabrice P. Laussy. *Microcavities*. Oxford University Press, 5 2017.

[91] Alessandro Tredicucci, Yong Chen, Vittorio Pellegrini, Marco Börger, and Franco Bassani. Optical bistability of semiconductor microcavities in the strong-coupling regime. *Phys. Rev. A*, 54:3493–3498, Oct 1996.

[92] Lucia Cavigli and Massimo Gurioli. Optical bistability and laserlike emission in a semiconductor microcavity. *Phys. Rev. B*, 71(3):035317, 2005.

[93] A. Baas, J. Ph. Karr, H. Eleuch, and E. Giacobino. Optical bistability in semiconductor microcavities. *Phys. Rev. A*, 69:023809, Feb 2004.

[94] F. Claude, M. J. Jacquet, R. Usciati, I. Carusotto, E. Giacobino, A. Bramati, and Q. Glorieux. High-resolution coherent probe spectroscopy of a polariton quantum fluid. *Phys. Rev. Lett.*, 129:103601, Aug 2022.

[95] N. A. Gippius, S. G. Tikhodeev, V. D. Kulakovskii, D. N. Krizhanovskii, and A. I. Tartakovskii. Nonlinear dynamics of polariton scattering in semiconductor microcavity: Bistability vs. stimulated scattering. *Europhys. Lett.*, 67(6):997, sep 2004.

[96] Daniele Bajoni, Pascale Senellart, Esther Wertz, Isabelle Sagnes, Audrey Miard, Aristide Lemaître, and Jacqueline Bloch. Polariton laser using single micropillar GaAs-GaAlAs semiconductor cavities. *Phys. Rev. Lett.*, 100(4):047401, 2008.

[97] A. Baas, J.-Ph. Karr, M. Romanelli, A. Bramati, and E. Giacobino. Optical bistability in semiconductor microcavities in the nondegenerate parametric oscillation regime: Analogy with the optical parametric oscillator. *Phys. Rev. B*, 70:161307, Oct 2004.

[98] H Ulmer-Tuffigo, F Kany, G Feuillet, R Langer, J Bleuse, and JL Pautrat. Magnetic tuning of resonance in semimagnetic semiconductor microcavities. *J. Cryst. Growth*, 159(1-4):605–608, 1996.

[99] Murielle Richard, J Kasprzak, R André, R Romestain, Le Si Dang, G Malpuech, and A Kavokin. Experimental evidence for nonequilibrium Bose condensation of exciton polaritons. *Phys. Rev. B*, 72(20):201301, 2005.

[100] D Pereda Cubian, M Haddad, Régis André, R Frey, G Roosen, JL Arce Diego, and C Flytzanis. Photoinduced magneto-optic Kerr effects in asymmetric semiconductor microcavities. *Phys. Rev. B*, 67(4):045308, 2003.

[101] J-G Rousset, Barbara Piętka, Mateusz Król, Rafał Mirek, Katarzyna Lekenta, Jacek Szczytko, Jolanta Borysiuk, J Suffczyński, Tomasz Kazimierczuk, Mateusz Goryca, et al. Strong coupling and polariton lasing in te based microcavities embedding (Cd, Zn) Te quantum wells. *Appl. Phys. Lett.*, 107(20), 2015.

[102] Denis Scalbert, Masha Vladimirova, Adalberto Brunetti, Steeve Cronenberger, Michal Nawrocki, Jacqueline Bloch, AV Kavokin, IA Shelykh, Régis André, Dimitri Solnyshkov, et al. Polariton spin beats in semiconductor quantum well microcavities. *Superlattices Microstruct.*, 43(5-6):417–426, 2008.

[103] Catherine Gourdon, G Lazard, Vincent Jeudy, Christophe Testelin, EL Ivchenko, and G Karczewski. Enhanced Faraday rotation in CdMnTe quantum wells embedded in an optical cavity. *Solid State Commun.*, 123(6-7):299–304, 2002.

[104] B Seredyński, P Starzyk, and W Pacuski. Exfoliation of epilayers with quantum dots. *Mater. Today:. Proc.*, 4(7):7053–7058, 2017.

[105] B Seredyński, M Król, P Starzyk, R Mirek, M Ściesiek, K Sobczak, J Borysiuk, D Stephan, J-G Rousset, J Szczytko, et al. (Cd, Zn, Mg) Te-based microcavity on MgTe sacrificial buffer: Growth, lift-off, and transmission studies of polaritons. *Phys. Rev. Mater.*, 2(4):043406, 2018.

[106] Lee W. Tutt and Thomas F. Boggess. A review of optical limiting mechanisms and devices using organics, fullerenes, semiconductors and other materials. *Prog. Quantum Electron.*, 17(4):299–338, January 1993.

[107] Reena Gadhwal and Ambika Devi. A review on the development of optical limiters from homogeneous to reflective 1-D photonic crystal structures. *Opt. Laser Technol.*, 141:107144, 2021.

[108] Reena Gadhwal, Parul Kaushik, and Ambika Devi. A review on 1D photonic crystal based reflective optical limiters. *Crit. Rev. Solid State Mater. Sci.*, 48(1):93–111, 2023.

[109] Matthias Heinrich, Falk Eilenberger, Robert Keil, Felix Dreisow, Eric Suran, Frédéric Louradour, Andreas Tünnermann, Thomas Pertsch, Stefan Nolte, and Alexander Szameit. Optical limiting and spectral stabilization in segmented photonic lattices. *Opt. Express*, 20(24):27299–27310, Nov 2012.

[110] U. Kuhl, F. Mortessagne, E. Makri, I. Vitebskiy, and T. Kottos. Waveguide photonic limiters based on topologically protected resonant modes. *Phys. Rev. B*, 95:121409, Mar 2017.

[111] Saima Husaini, Huayu Teng, and Vinod M. Menon. Enhanced nonlinear optical response of metal nanocomposite based photonic crystals. *Appl. Phys. Lett.*, 101(11):111103, 2012.

[112] Jarrett H. Vella, John H. Goldsmith, Andrew T. Browning, Nicholaos I. Limberopoulos, Ilya Vitebskiy, Eleana Makri, and Tsampikos Kottos. Experimental realization of a reflective optical limiter. *Phys. Rev. Applied*, 5:064010, Jun 2016.

[113] A. A. Ryzhov. Optical limiting performance of a GaAs/AlAs heterostructure microcavity in the near-infrared. *Appl. Opt.*, 56(21):5811, jul 2017.

[114] Daniele Sanvitto and Stéphane Kéna-Cohen. The road towards polaritonic devices. *Nat. Mater.*, 15(10):1061–1073, jul 2016.

[115] Scott Dufferwiel, Stefan Schwarz, Freddie Withers, Aurélien AP Trichet, Feng Li, Maksym Sich, Osvaldo Del Pozo-Zamudio, Casper Clark, Anton Nalitov, Dmitry D Solnyshkov, et al. Exciton–polaritons in van der waals heterostructures embedded in tunable microcavities. *Nat. Commun.*, 6(1):8579, 2015.

[116] N. S. Voronova, A. A. Elistratov, and Yu. E. Lozovik. Detuning-controlled internal oscillations in an exciton-polariton condensate. *Phys. Rev. Lett.*, 115:186402, Oct 2015.

[117] Amir Rahmani, David Colas, Nina Voronova, Kazem Jamshidi-Ghaleh, Lorenzo Dominici, and Fabrice P. Laussy. Topologically driven Rabi-oscillating interference dislocation. *Nanophotonics*, 11(12):2909–2919, 2022.

[118] Amir Rahmani and Lorenzo Dominici. Detuning control of Rabi vortex oscillations in light-matter coupling. *Phys. Rev. B*, 100:094310, Sep 2019.

[119] Lorenzo Dominici, David Colas, Antonio Gianfrate, Amir Rahmani, Vincenzo Ardizzone, Dario Ballarini, Milena De Giorgi, Giuseppe Gigli, Fabrice P. Laussy, Daniele Sanvitto, and Nina Voronova. Full-Bloch beams and ultrafast Rabi-rotating vortices. *Phys. Rev. Research*, 3:013007, Jan 2021.

[120] OA Egorov, Dmitry V Skryabin, AV Yulin, and F Lederer. Bright cavity polariton solitons. *Phys. Rev. Lett.*, 102(15):153904, 2009.

[121] Valentin Goblot, Hai Son Nguyen, Iacopo Carusotto, Elisabeth Galopin, Aristide Lemaître, Isabelle Sagnes, Alberto Amo, and Jacqueline Bloch. Phase-controlled bistability of a dark soliton train in a polariton fluid. *Phys. Rev. Lett.*, 117(21):217401, 2016.

[122] Ivan Iorsh, Alexander Alodjants, and Ivan A. Shelykh. Microcavity with saturable nonlinearity under simultaneous resonant and nonresonant pumping: multistability, Hopf bifurcations and chaotic behaviour. *Opt. Express*, 24(11):11505–11514, May 2016.

[123] E. Cancellieri, F. M. Marchetti, M. H. Szymańska, and C. Tejedor. Multistability of a two-component exciton-polariton fluid. *Phys. Rev. B*, 83:214507, Jun 2011.

[124] L. Dominici, M. Petrov, M. Matuszewski, D. Ballarini, M. De Giorgi, D. Colas, E. Cancellieri, B. Silva Fernández, A. Bramati, G. Gigli, A. Kavokin, F. Laussy, and D. Sanvitto. Real-space collapse of a polariton condensate. *Nat. Commun.*, 6(1):8993, Dec 2015.

[125] Christoph Lange, Emiliano Cancellieri, Dmitry Panna, David M Whittaker, Mark Steger, David W Snoke, Loren N Pfeiffer, Kenneth W West, and Alex Hayat. Ultrafast control of strong light–matter coupling. *New J. Phys.*, 20(1):013032, jan 2018.

[126] C Ciuti, P Schwendimann, and A Quattropani. Theory of polariton parametric interactions in semiconductor microcavities. *Semicond. Sci. Technol.*, 18(10):S279–S293, sep 2003.

[127] Iacopo Carusotto and Cristiano Ciuti. Probing microcavity polariton superfluidity through resonant Rayleigh scattering. *Phys. Rev. Lett.*, 93:166401, Oct 2004.

[128] Hui Deng, Hartmut Haug, and Yoshihisa Yamamoto. Exciton-polariton Bose-Einstein condensation. *Rev. Mod. Phys.*, 82:1489–1537, May 2010.

[129] I. Yu. Chestnov, T. A. Khudaiberganov, A. P. Alodjants, and A. V. Kavokin. Heat-assisted self-localization of exciton polaritons. *Phys. Rev. B*, 98:115302, Sep 2018.

[130] Dario Ballarini, Igor Chestnov, Davide Caputo, Milena De Giorgi, Lorenzo Dominici, Kenneth West, Loren N. Pfeiffer, Giuseppe Gigli, Alexey Kavokin, and Daniele Sanvitto. Self-trapping of exciton-polariton condensates in GaAs microcavities. *Phys. Rev. Lett.*, 123:047401, Jul 2019.

[131] Ryo Hanai, Alexander Edelman, Yoji Ohashi, and Peter B. Littlewood. Non-Hermitian Phase Transition from a Polariton Bose-Einstein Condensate to a Photon Laser. *Phys. Rev. Lett.*, 122:185301, May 2019.

[132] Jacob B. Khurgin. Exceptional points in polaritonic cavities and subthreshold Fabry–Perot lasers. *Optica*, 7(8):1015–1023, Aug 2020.

[133] G Tosi, G Christmann, NG Berloff, P Tsotsis, T Gao, Z Hatzopoulos, PG Savvidis, and JJ Baumberg. Sculpting oscillators with light within a nonlinear quantum fluid. *Nat. Phys.*, 8(3):190–194, 2012.

[134] Sebastian Klembt, TH Harder, OA Egorov, K Winkler, R Ge, MA Bandres, M Emmerling, L Worschech, TCH Liew, M Segev, et al. Exciton-polariton topological insulator. *Nature*, 562(7728):552–556, 2018.

[135] Sergey Alyatkin, Helgi Sigurdsson, Alexis Askitopoulos, Julian D Töpfer, and Pavlos G Lagoudakis. Quantum fluids of light in all-optical scatterer lattices. *Nat. Commun.*, 12(1):5571, 2021.

[136] Julian D Töpfer, Helgi Sigurdsson, Lucinda Pickup, and Pavlos G Lagoudakis. Time-delay polaritonics. *Commun. Phys.*, 3(1):2, 2020.

[137] Qi Yao, Evgeny Sedov, Shouvik Mukherjee, Jonathan Beaumariage, Burcu Ozden, Ken West, Loren Pfeiffer, Alexey Kavokin, and DW Snoke. Ballistic transport of a polariton ring condensate with spin precession. *Phys. Rev. B*, 106(24):245309, 2022.

[138] Julian D Töpfer, Ioannis Chatzopoulos, Helgi Sigurdsson, Tamsin Cookson, Yuri G Rubo, and Pavlos G Lagoudakis. Engineering spatial coherence in lattices of polariton condensates. *Optica*, 8(1):106–113, 2021.

[139] Hamid Ohadi, RL Gregory, T Freegarde, YG Rubo, AV Kavokin, NG Berloff, and PG Lagoudakis. Nontrivial phase coupling in polariton multiplets. *Phys. Rev. X*, 6(3):031032, 2016.

[140] Sergey Alyatkin, JD Töpfer, Alexis Askitopoulos, Helgi Sigurdsson, and PG Lagoudakis. Optical control of couplings in polariton condensate lattices. *Phys. Rev. Lett.*, 124(20):207402, 2020.

[141] Dmitriy Dovzhenko, Denis Aristov, Lucinda Pickup, Helgi Sigurðsson, and Pavlos Lagoudakis. Next-nearest-neighbor coupling with spinor polariton condensates. *Phys. Rev. B*, 108(16):L161301, 2023.

[142] L Pickup, H Sigurdsson, J Ruostekoski, and PG Lagoudakis. Synthetic band-structure engineering in polariton crystals with non-Hermitian topological phases. *Nat. Commun.*, 11(1):4431, 2020.

[143] Timur Shegai, Vladimir D. Miljković, Kui Bao, Hongxing Xu, Peter Nordlander, Peter Johansson, and Mikael Käll. Unidirectional broadband light emission from supported plasmonic nanowires. *Nano Lett.*, 11(2):706–711, February 2011.

[144] Lukas Novotny and Niek van Hulst. Antennas for light. *Nat. Photonics*, 5(2):83–90, February 2011.

[145] Wenqi Zhu, Dongxing Wang, and Kenneth B. Crozier. Direct observation of beamed Raman scattering. *Nano Lett.*, 12(12):6235–6243, November 2012.

[146] Zhipeng Li, Feng Hao, Yingzhou Huang, Yurui Fang, Peter Nordlander, and Hongxing Xu. Directional light emission from propagating surface plasmons of silver nanowires. *Nano Lett.*, 9(12):4383–4386, September 2009.

[147] Jon A. Schuller, Sinan Karaveli, Theanne Schiros, Keliang He, Shyuan Yang, Ioannis Kymissis, Jie Shan, and Rashid Zia. Orientation of luminescent excitons in layered nanomaterials. *Nat. Nanotechnol.*, 8(4):271–276, March 2013.

[148] Mauro Brotons-Gisbert, Raphaël Proux, Raphaël Picard, Daniel Andres-Penares, Artur Branny, Alejandro Molina-Sánchez, Juan F. Sánchez-Royo, and Brian D. Gerardot. Out-of-plane orientation of luminescent excitons in two-dimensional indium selenide. *Nat. Commun.*, 10(1), September 2019.

[149] Luca Sortino, Jonas Biechteler, Lucas Lafeta, Lucca Kühner, Achim Hartschuh, Leonardo de S Menezes, Stefan A Maier, and Andreas Tittl. Atomic-layer assembly of ultrathin optical cavities in van der Waals heterostructure metasurfaces. *Nat. Photonics*, pages 1–8, 2025.

[150] Armando Genco, Cristina Cruciano, Matteo Corti, Kirsty E McGhee, Benedetto Ardini, Luca Sortino, Ludwig Huttenhofer, Tersilla Virgili, David G Lidzey, Stefan A Maier, et al. k-space hyperspectral imaging by a birefringent common-path interferometer. *ACS Photonics*, 9(11):3563–3572, 2022.

[151] M. Andreas Lieb, James M. Zavislan, and Lukas Novotny. Single-molecule orientations determined by direct emission pattern imaging. *J. Opt. Soc. Am. B: Opt. Phys.*, 21(6):1210, June 2004.

[152] Adam S. Backer and W. E. Moerner. Extending single-molecule microscopy using optical Fourier processing. *J. Phys. Chem. B*, 118(28):8313–8329, May 2014.

[153] Saman Jahani and Zubin Jacob. All-dielectric metamaterials. *Nat. Nanotechnol.*, 11(1):23–36, January 2016.

[154] Bo Wang, Wenzhe Liu, Maoxiong Zhao, Jiajun Wang, Yiwen Zhang, Ang Chen, Fang Guan, Xiaohan Liu, Lei Shi, and Jian Zi. Generating optical vortex beams by momentum-space polarization vortices centred at bound states in the continuum. *Nat. Photonics*, 14(10):623–628, July 2020.

[155] Nolan Lassaline, Raphael Brechbühler, Sander J. W. Vonk, Korneel Ridderbeek, Martin Spieser, Samuel Bisig, Boris le Feber, Freddy T. Rabouw, and David J. Norris. Optical Fourier surfaces. *Nature*, 582(7813):506–510, June 2020.

[156] Yang Chen, Jiangang Feng, Yuqing Huang, Weijin Chen, Rui Su, Sanjib Ghosh, Yi Hou, Qihua Xiong, and Cheng-Wei Qiu. Compact spin-valley-locked perovskite emission. *Nat. Mater.*, 22(9):1065–1070, April 2023.

[157] Oriol Arteaga, Shane M Nichols, and Joan Antó. Back-focal plane Mueller matrix microscopy: Mueller conoscopy and Mueller diffractrometry. *Appl. Surf. Sci.*, 421:702–706, 2017.

[158] Jonathan A. Kurvits, Mingming Jiang, and Rashid Zia. Comparative analysis of imaging configurations and objectives for Fourier microscopy. *J. Opt. Soc. Am. A*, 32(11):2082, October 2015.

[159] Arun Jaiswal, Chandresh Kumar Rastogi, Sweta Rani, Gaurav Pratap Singh, Sumit Saxena, and Shobha Shukla. Two decades of two-photon lithography: Materials science perspective for additive manufacturing of 2D/3D nano-microstructures. *Iscience*, 26(4), 2023.

[160] Martin Schumann, Tiemo Bückmann, Nico Gruhler, Martin Wegener, and Wolfram Pernice. Hybrid 2D–3D optical devices for integrated optics by direct laser writing. *Light Sci. Appl.*, 3(6):e175–e175, 2014.

[161] Aleksander Bogucki, Łukasz Zinkiewicz, Wojciech Pacuski, Piotr Wasylczyk, and Piotr Kossacki. Optical fiber micro-connector with nanometer positioning precision for rapid prototyping of photonic devices. *Opt. Express*, 26(9):11513–11518, 2018.

[162] Julian Schulz, Sachin Vaidya, and Christina Jörg. Topological photonics in 3D micro-printed systems. *APL Photonics*, 6(8), 2021.

[163] Rui Zhou, Yansong Wang, Ziyu Liu, Yongqiang Pang, Jianxin Chen, and Jie Kong. Digital light processing 3D-printed ceramic metamaterials for electromagnetic wave absorption. *Nano-Micro Lett.*, 14(1):122, 2022.

[164] Kun Peng Zhang, Yan Fei Liao, Bin Qiu, Yue Kun Zheng, Ling Ke Yu, Gong Han He, Qin Nan Chen, and Dao Heng Sun. 3D printed embedded metamaterials. *Small*, 17(50):2103262, 2021.

[165] Shahin Bagheri, Ksenia Weber, Timo Gissibl, Thomas Weiss, Frank Neubrech, and Harald Giessen. Fabrication of square-centimeter plasmonic nanoantenna arrays by femtosecond direct laser writing lithography: effects of collective excitations on seira enhancement. *ACS Photonics*, 2(6):779–786, 2015.

[166] Aleksander Bogucki, Łukasz Zinkiewicz, Magdalena Grzeszczyk, Wojciech Pacuski, Karol Nogajewski, Tomasz Kazimierczuk, Aleksander Rodek, Jan Suffczyński, Kenji Watanabe, Takashi Taniguchi, et al. Ultra-long-working-distance spectroscopy of single nanostructures with aspherical solid immersion microlenses. *Light Sci. Appl.*, 9(1):48, 2020.

[167] Guo-qiu Jiang, Qi-hang Zhang, Jun-yi Zhao, Yu-kun Qiao, Zhen-Xuan Ge, Run-ze Liu, Tung-Hsun Chung, Chao-yang Lu, and Yong-heng Huo. Comprehensive measurement of the near-infrared refractive index of GaAs at cryogenic temperatures. *Opt. Lett.*, 48(13):3507, June 2023.

[168] Xiaoqin Zhou, Yihong Hou, and Jieqiong Lin. A review on the processing accuracy of two-photon polymerization. *AIP Adv.*, 5(3):030701, 03 2015.

[169] Fabian Niesler and Martin Hermatschweiler. Two-photon polymerization—a versatile microfabrication tool: From maskless lithography to 3D printing. *Laser Tech. J.*, 12(3):44–47, 2015.

[170] Dwight W. Berreman. Optics in stratified and anisotropic media: 4×4-matrix formulation. *J. Opt. Soc. Am.*, 62(4):502–510, Apr 1972.

[171] Mathias Schubert. Polarization-dependent optical parameters of arbitrarily anisotropic homogeneous layered systems. *Phys. Rev. B*, 53:4265–4274, Feb 1996.